Increasing Faradaic Efficiency and Current Density for the Lithium-Mediated Ammonia Synthesis

Li, Katja

Publication date:
2023

Document Version
Publisher's PDF, also known as Version of record

Citation (APA):
Li, K. (2023). *Increasing Faradaic Efficiency and Current Density for the Lithium-Mediated Ammonia Synthesis*. Department of Physics, Technical University of Denmark.

DTU Physics
Department of Physics

Increasing Faradaic Efficiency and Current Density for the Lithium-Mediated Ammonia Synthesis

Katja Li

Supervisor: Prof. Ib Chorkendorff
Co-Supervisor: Prof. Jakob Doganli-Kibsgaard

Ph.D. Thesis
Technical University of Denmark
Department of Physics
Surface Science and Catalysis
January 2023

Cover image generated by DALL·E 2
Prompt: "Making fertilizer out of solar and wind, digital art"

Abstract

Ammonia, being one of the most produced chemicals worldwide with 180 Mio. ton per year, plays an important role in our society. It‘s main use is as fertilizer and it is predicted that without the industrial scale production of ammonia via the Haber-Bosch process, we would not be able to feed half of the current global population. With continuous global population growth the role of ammonia will be even more important in the future. Moreover, ammonia is a precursor for many chemicals both in the polymer industry as well as in the pharmaceutical industry. As important and positive the influence of ammonia is, it also leaves a negative impact on the environment. With steam reforming from methane as a main contribution, the Haber-Bosch process is responsible for around 340 Mt CO_2 emissions per year. Ammonia is hereby the chemical with the largest green house gas emission, with ethylene (140 Mt CO_2) in a far second place.
Hence, it is important to mitigate the negative impact of the Haber-Bosch synthesis by more sustainable processes, such as electrochemical nitrogen reduction (NRR) powered by renewable electricity sources. The NRR field is relatively young and therefore scattered with a lot of false positive results, since the measured concentrations are often in the sub-ppm regions. Several protocols have been published how to vigorously prove the ammonia production from nitrogen and since then the field has moved in the right direction by revisiting and even subtracting previously published results. The most promising method so far is the lithium-mediated electrochemical ammonia synthesis (LiMEAS), which has been successfully reproduced by several labs. The success and industrial relevance of an electrochemical reaction is usually quantified by values such as Faradaic efficiency (FE), energy efficiency (EE) and current density. The goal of this thesis is to increase both the Faradaic efficiency and current density to levels where the reaction can be considered for scale-up.

The FE was increased significantly from 25 to around 80 % by the addition of small amounts of oxygen (0.6 - 0.8 mol.%) into the reaction atmosphere at 20 bar total nitrogen pressure. This result was quite unexpected, since oxygen was initially believed to hinder the reaction due to competing oxygen reduction reaction (ORR) and Li_2O formation. However, the data presented here prove the opposite, that oxygen greatly enhanced the FE at the right concentrations. At higher concentrations however, the FE dropped rapidly to 0 %. The explanation of this unusual effect was by modification of the solid electrolyte interphase (SEI) by oxygen. From literature it

is already known that oxygen modifies the SEI layer and previous work from our group predicts that the FE is strongly depending on the diffusion rates of the reactants through the SEI layer. To support this hypothesis, air-free characterization (X-ray photoelectron spectroscopy, XPS, X-ray diffraction, XRD) of the SEI layer was conducted at different concentrations of oxygen. With experimental results and theoretical predictions combined, the modification of the SEI layer through O_2 was proven.

To increase the current density, high surface area copper electrodes were synthesized by electrodeposition at high overpotentials via the hydrogen bubble template (HBT) method. Then the electrolyte had to be optimized for high current application. Namely the concentration of the electrolyte had to be increased from 0.3 M to 2 M to increase the conductivity and therefore minimize iR losses. Furthermore, higher concentrations lead to a thinner double-layer, which increases the electrochemical surface area (ECSA). Lastly, the ECSA was determined by capacitive cycling in the same solvent as LiMEAS. With these electrodes, the current density was increased to -100 mA/cm^2_{geo}. Further optimization of the HBT method and electrolyte lead to a current density of -1 A/cm^2_{geo} with FE of 71 ± 3 %.

The last focus in this thesis is to elucidate the role of ethanol (EtOH) in the system. It was initially predicted to be the proton source, but that does not seem to be it‘s only role. Experiments where the electrolyte was switched from containing EtOH to non containing EtOH electrolyte showed even higher FE than with EtOH. The conclusion from these experiment was that EtOH has an important role to play in the beginning to built the SEI layer, but in the sequential run does not serve as proton source and ammonia can be formed with tetrahydrofuran (THF) as proton source.

Resumé

Ammoniak, værende et af de mest producerede kemikalier på verdensplan med 180 millioner ton per år, spiller en vigtig rolle i vores samfund. Det bliver hovedsagligt brugt til gødning, og det estimeres, at vi ikke vil kunne brødføde halvdelen af jordens befolkning, uden industrielt produceret ammoniak via Haber-Bosch processen. Med en fortsat befolkningsvækst kommer ammoniak til at spille en endnu større rolle i fremtiden. Desuden er ammoniak en forløber for mange kemikalier, både i polymer- samt i farmaci-industrien. På trods af vigtigheden og den positive indflydelse af ammoniak, efterlader det også negative indtryk på miljøet. Med dampreformering fra metan som hovedbidrag, er Haber-Bosch processen ansvarlig for at udlede omkring 340 Mt CO_2 om året. Ammoniak er hermed det kemikalie med størst aftryk af drivhusgas, hvor ethylen (140 Mt CO_2/år) kommer ind på en andenpladsen.
Det er derfor vigtigt at imødekomme den negative effekt af Haber-Bosch syntesen gennem en mere bæredygtig proces, såsom elektrokemisk nitrogen reduktion (NRR) drevet af vedvarende kilder af elektricitet. NRR-feltet er relativt ungt og derfor også spredt med mange falske positive resultater, da de målte koncentrationer ofte er lavere end ppm (milliontedele). Flere protokoller er blevet publiceret for hvordan man korrekt kan bevise produktion af ammoniak fra nitrogen, og sidenhen har feltet flyttet sig i den rigtige retning, hvor tidligere publicerede resultater er blevet testet igen og nogle endda trukket tilbage. Den mest lovende metode indtil nu er den lithium-medierede elektrokemiske ammoniak syntese (LiMEAS), som succesfuldt er blevet reproduceret af flere laboratorier. Succes og industriel relevans af en elektrokemisk reaktion bliver typisk kvantificeret ved værdier som Faradaisk effektivitet (FE), energieffektivitet (EE) og strømtæthed. Målet for denne afhandling er at øge både den Faradaiske effektivitet og strømtætheden, til niveauer hvor reaktionen kan blive taget i betragtning til opskalering.

FE blev signifikant forøget fra 25 til 80 % ved at tilføje små mængder oxygen (0.6 – 0.8 mol.%) til reaktionsatmosfæren ved 20 bars nitrogentryk. Dette resultat var ganske overraskende, da oxygen førhen var forventet at begrænse reaktionen grundet konkurrerende oxygen reduktionsreaktion (ORR) og formation af Li_2O. De præsenterede resultater beviser dog det modsatte, at oxygen i høj grad forbedrer FE ved de helt rigtige koncentrationer. Dog falder FE hurtigt til 0 % ved for høje koncentrationer. Forklaringen til denne usædvanlige effekt var modificering af det faste elektrolyt-overgangs-lag (SEI), hvor forudgående arbejde fra vores gruppe forudsiger at

FE er stærkt afhængig af diffusionsraterne af reagenterne gennem dette SEI-lag. For at understøtte denne hypotese, blev luftfri karakterisering (røntgenfotoelektron spektroskopi, XPS, og røntgendiffraktion, XRD) af SEI-laget udført ved forskellige koncentrationer af oxygen. Ved at sammenholde de eksperimentelle resultater samt teoretiske forudsigelser, blev modificeringen af SEI-laget ved O_2 bevist.

For at øge strømtætheden blev elektroder med stort overfladeareal fremstillet ved elektrodeponering med høje overpotentialer via hydrogenboble-skabelon (HBT) metoden. Herefter skulle elektrolytten optimeres til brug ved høj strøm. Hertil blev elektrolytkoncentrationen nødt til at blive øget fra 0.3 til 2 M, for at øge konduktiviteten og dermed minimere iR tab. Derudover ledte høje koncentrationer til et tyndere dobbeltlag, hvilket øger det elektrokemiske overfladeareal (ECSA). Slutteligt blev ECSA fastsat ved kapacitive cyklusser i samme solvent som LiMEAS. Med disse elektroder blev strømtætheden øget til -100 $mA/cm^2{}_{geo}$. Yderligere optimering af HBT metoden samt elektrolytten ledte til strømtætheder på -1 $A/cm^2{}_{geo}$ med en FE på 71 ± 3 %.

Det sidste fokus i denne afhandling er at belyse rollen af ætanol (EtOH) i systemet. Det var oprindeligt forudsagt at fungere som protonkilde, men det tyder ikke på at være dets eneste rolle. Eksperimenter hvor elektrolytten blev udskiftet fra hhv. at indeholde EtOH til efterfølgende ikke at indeholde EtOH, viste endnu højere FE end hvis elektrolytten altid indeholdte EtOH. Konklusionen fra disse forsøg var, at EtOH spiller en vigtig rolle i begyndelsen med at opbygge SEI-laget, men i det efterfølgende forløb ikke agerer som protonkilde, og ammoniak her kan blive dannet med tetrahydrofuran (THF) som protonkilde.

Preface

The work for this thesis was carried out at the Technical University of Denmark, Department of Physics, Section of Surface Physics and Catalysis (SurfCat) between December 2019 and November 2022. Some measurements were taken at the European Synchrotron Radiation Facility (ESRF) in collaboration with the beamline scientists in Grenoble. However, these experiments will not be part of this thesis. My experimental work was carried out in close collaboration with other students and postdocs at SurfCat, especially in the ammonia team.

Throughout this thesis, I use the pronoun "I" to highlight the parts of the work carried out by myself, while "we" is used where no clear distinction between my work and ideas, and those of my colleagues can be made. The contributors to the work in the different parts of this thesis are stated in the respective chapters.

Katja Li
November 2022

Acknowledgments

The work that was carried out in this thesis was partly funded by Villum Center for the Science of Sustainable Fuels and Chemicals (V-SUSTAIN grant 9455), Innovationsfonden (E-ammonia grant 9067-00010B) and the European Research Council (ERC) under the European Union's Horizon 2020 research and innovation program (grant agreement no. 741860).

Firstly, I want to thank my supervisors Prof. Ib Chorkendorff and Prof. Jakob Doganli-Kibsgaard for providing me with the opportunity to work on this project. Their guidance over the last three years allowed me to have a great and fruitful experience here at DTU. Moreover, I would like to thank Prof. Peter Vesborg and Prof. Jens Nørskov for their collaboration on the ammonia project and interesting insights and discussions in the weekly meetings.

I thank the whole SurfCat and CatTheory group for creating a enjoyable working atmosphere and being very approachable in times of need. Especially, I want to express my gratitude to the floor and labmanagers, Brian Knudsen, Patrick Strøm-Hansen, Jakob Ejler and Jacqueline McAnulty for keeping the lab in order and enabling all of us to conduct our work. They are our daily super-heroes. I also want to thank the theory collaborators from CatTheory, Vanessa Jane Bukas, Yuanyuan Zhou and Aoni Xu for the interesting input and discussions.

Most importantly, I want to thank the entire ammonia team, for providing continuous support during the years and for reading through my thesis. Especially, the ammonia members that were there from the beginning, Suzanne Zamany Andersen, Jakob Brunn Pedersen, Mattia Saccoccio and Kevin Krempl helped me a lot to get used to the project. Suzanne's encouraging words were the reason I joined the ammonia team, otherwise I would have done OER and missed on the chance to collaborate with her on the oxygen project. To Mattia I owe all my Swagelok abilities and I thank him for the patience he had teaching me way to correctly build gas lines, which I enjoy doing now very much. Big thanks also to Jakob who helped me with the Danish part of my thesis. I thought in the beginning it would be easy to learn Danish if I know German but I was very wrong in that. I also want to thank Rokas Sazinas, who started at a similar time with me and with whom I could share the initial learning curve. His knowledge in organic chemistry and funny stories were always a pleasure to listen to. I was lucky enough that even more members joined the team during my time here. I had the pleasure of working together with Sarah Groot Shapel for a while and during that time working and discussion felt more like a fun thing to do than usual. I also learned a lot from the new post-docs Shaofeng Li and

Xianbiao Fu and enjoyed very much the collaboration with them. Unfortunately, I could not spend a lot of time with the newest additions to the team Jon Bjarke Valbæk Mygind and Niklas Deißler, but I think I crammed in some quality time with them during the beamline we had in October, where I am actually currently sitting at 3 am. During this beamline we were joined by our collaborators from Stanford, Valerie Niemann and Peter Benedek whom also made it more fun than work, which I am very grateful for. Moreover, I also want to acknowledge the great expertise of our beamline scientists Valentin Vinci and Jakub Drnec and would like to thank them for their time and interest in this project. The time and experience at a synchrotron source at ESRF was definitely some of the most interesting time in my PhD and made me re-realise how cool science can be. A special thanks also to my colleague Tim Trichter for introducing and explaining me the basics of DRT analysis.

Aside from the ammonia team, I was lucky enough to also make countless other friends in SurfCat that I will for sure keep contact with even after leaving. I especially got along well with the members of the CO_2 group, Tugce, Clara, Yu, Wanyu, Carlos, Sahil, Asger, Quicheng and Esperanza (Yes I added you to the CO_2 team, hope you don’t mind). Surprisingly, I even learned things about CO_2 reduction, who knows when that will come in handy. I also made friends with Yanxin, Tobias and Edwin in the Atomicar team, both my neighbors in office and in lab. I also can’t forget to thank Degenhart, who suggested me to come to SurfCat in the first place. This place was honestly the best I could have done my PhD in and I am very grateful for the suggestion. Another big part of my social life here at SurfCat was my Chinese community. The many hot pot evenings I had with Yanxin, Chao, Yu, Wanyu, Quicheng, Shaofeng, Xianbiao, Yarong, Yuanyuan and Ke will be missed. I would say that I improved my Chinese speaking skills quite a bit and especially in the technical aspect. I never would have dreamed of saying "electrolyte" in Chinese, I think even my parents don’t know this word. As a foreigner here in Denmark all you guys gave me a feeling of family and I will remember all the dinners and small weekend trips fondly. Lastly, I want to thank my family for their continuous support and letting me complain during the harder times. They might think I am a huge nerd but I can still feel that they are proud of me. During the past 3 years it was hard to return to China to see my extended family but I hope I can go back in the near future.

List of Publications

First Author:

Paper 1

Enhancement of Li-mediated ammonia synthesis by addition of oxygen
K. Li[*], S. Z. Andersen[*], M. J. Statt[*], M. Saccoccio, V. J. Bukas, K. Krempl, R. Sazinas, J. B. Pedersen, K. Krempl, V. Shadravan, Y. Zhou, D. Chakraborty, J. Kibsgaard, P. C. Vesborg, J. Nørsvov and I. Chorkendorff
Science, **2021**, 374, 1593-1597.
[*] these authors contributed equally

Paper 2

Increasing current density of Li-mediated ammonia synthesis with high surface area copper electrodes
K. Li, S. G. Shapel, D. Hochfilzer, J. B. Pedersen, K. Krempl, S. Z. Andersen, R. Sazinas, M. Saccoccio, S. Li, D. Chakraborty, J. Kibsgaard, P. C. Vesborg, J. Nørsvov and I. Chorkendorff,
ACS Energy Letters, **2022**, 7, 36-41.

Co-Author:

Paper 3

Towards understanding of electrolyte degradation in lithium-mediated non-aqueous electrochemical ammonia synthesis with gas chromatography-mass spectrometry
R. Sažinas, S. Z. Andersen, K. Li, M. Saccoccio, K. Krempl, J. B. Pedersen, J. Kibsgaard, P. C. K. Vesborg, D. Chakraborty and I. Chorkendorff
RSC Advances, **2021**, 11, 31487-31498.

Paper 4

Oxygen-Enhanced Chemical Stability of Lithium-Mediated Electrochemical Ammonia Synthesis

R. Sažinas, K. Li, S. Z. Andersen, M. Saccoccio, S. Li, J. B. Pedersen, J. Kibsgaard, P. C. K. Vesborg, D. Chakraborty and I. Chorkendorff

The Journal of Physical Chemistry Letters, **2022**, 13, 4605-4611.

Paper 5

Electrosynthesis of ammonia with high selectivity and high rates via engineering of the solid-electrolyte interphase

S. Li*, Y. Zhou*, K. Li, M. Saccoccio, R. Sažinas, S. Z. Andersen, J. B. Pedersen, X. Fu, V. Shadravan, D. Chakraborty, J. Kibsgaard, P. C. Vesborg, J. Nørskov and I. Chorkendorff

Joule, **2022**, 3, 2083-2101.

* these authors contributed equally

Paper 6

Electrosynthesis of ammonia from nitrogen reduction coupled with hydrogen oxidation in a continuous-flow reactor

X. Fu*, J.B. Pedersen*, Y. Zhou*, M. Saccoccio, S.Li, R. Sažinas, K. Li, S. Z. Andersen, A. Xu, N.H. Deissler, J.B.V. Mygind, C. Wei, J. Kibsgaard, P. C. Vesborg, J. Nørskov and I. Chorkendorff

Submitted

* these authors contributed equally

Contents

List of Figures

List of Tables

Nomenclature

Latin Symbols

b	Intercept with y-axis	–
C	Capacitance	F
c	Concentration	mol/L
d	Thickness	cm
E	Potential	V
E^0	Standard reduction potential	V
E^{cell}	Cell potential	V
F	Faraday constant	96 485.33 A s/mol
FE	Faradaic efficiency	%
G	Gibbs free energy	kJ/mol
H	Enthalpy	kJ/mol
I	Intensity	W/m^2
I	Current	A
i	Current	A
i	Imaginary number	–
L	Crystal size	nm
m	Mass	g
m	Slope	–
n	Amount of substance	mol
p	Pressure	bar
Q	Charge	A s
R	Ideal gas constant	8.314 J/(K mol)
R	Resistance	Ω
s	Error	–
T	Temperature	K
t	Time	s
V	Potential	V
Z	Impedance	Ω
z	Amount of electrons	–
z	Charge	–

Greek Symbols

β	Full width half maximum	°
ε	Extinction coefficient	m^2/mol
η	Efficiency	%
Θ	Angle	°
γ	Distribution function of relaxation times	Ω
λ	Wavelength	nm
ν	Scan rate	mV/s
ϕ	Work function	J
σ	Charge density	C/cm^2
τ	Time constant	s
ω	Angular frequency	Hz

Subscript

b	Intercept with y-axis
bin	Binding
ct	Charge transfer
d	Diffuse
dl	Double layer
i	Inner
kin	Kinetic
M	Metal
m	Slope
p	Photon
r	Real
S	Solution
spec	Specific
W	Warburg

Abbreviations

AEL	Alkaline electrolyzer
BET	Brunauer-Emmet-Teller
BSE	Back scattered electrons
CA	Chronoamperometry
CE	Counter electrode
CP	Chronopotentiometry
CV	Cyclic voltametry
DMSO	Dimethylsulfoxide
DRT	Distribution of relaxation times
ECSA	Electrochemical surface area
EDX	Energy dispersive X-ray spectroscopy
EE	Energy efficiency
EIS	Electrochemical impedance spectroscopy
EDL	Electrical double layer
FE	Faradaic efficiency
GEIS	Galvanostatic electrochemical impedance spectroscopy
GC	Gas chromatography
HB	Haber-Bosch
HBT	Hydrogen bubble template
HER	Hydrogen evolution reaction
HOMO	Highest occupied molecular orbital
HOR	Hydrogen oxidation reaction
IC	Ion Chromatography
IHP	Inner Helmholtz plane
LiMEAS	Li-mediated electrochemical ammonia synthesis
LUMO	Lowest unoccupied molecular orbital
LSV	Linear sweep voltametry
MFC	Mass flow controller
MS	Mass spectrometry
NRR	Nitrogen reduction reaction
OCV	Open circuit voltage
OER	Oxygen evolution reaction
OHP	Outer Helmholtz plane
ORR	Oxygen reduction reaction
PC	Propylene carbonate
PEIS	Potentiostatic electrochemical impedance spectroscopy
PEMEL	Proton exchange membrane electrolyzer
PTFE	Polytetrafluorethylene
QMS	Quadrupol mass spectrometer

RE	Reference electrode
RHE	Reversible hydrogen electrode
SE	Secondary electrons
SEI	Solid electrolyte interphase
SEM	Scanning electron microscopy
SHE	Standard hydrogen electrode
SOC	State of charge
SOEL	Solid oxide electrolyzer
TEM	Transmission electron microscopy
THF	Tetrahydrofuran
UHV	Ultra high vacuum
WE	Working electrode
XPS	X-ray photoelectron spectroscopy
XRD	X-ray diffraction

1 Introduction

Ammonia is unarguably one of the most important chemical feedstocks in our society. Its main use is as fertilizer, with around 97 % of the fertilizers being derived from ammonia [1]. It is also an important starting material in the polymer industry as well as used as refrigerant [2]. Predictions show that our demand for ammonia is even expected to rise 2.3 % per year in the future [3]. To satisfy the huge industrial demand of ammonia, it is produced in big facilities from its elements by the so-called Haber-Bosch process (HB), which utilizes high temperatures and pressures in combination with an Fe-based catalyst. With this, 180 Mio. tonnes of ammonia can be produced per year and distributed worldwide. The following sections will discuss the evolution of the Haber-Bosch synthesis in detail along with its benefits and repercussions on the society. Afterwards, the role of ammonia in the future as power storage is analyzed and compared to the hydrogen economy. Lastly, electrochemical ammonia synthesis as a more renewable alternative to the thermal equivalent is introduced and the challenges thereof discussed.

1.1 The Two Sides of Industrial Ammonia Production

The synthesis of ammonia from nitrogen and hydrogen was invented by Fritz Haber in the early twentieth century [4] and was implemented industrially by Carl Bosch in 1931 [5], which awarded them both a Nobel prize each [6, 7]. It is believed to be one of the most important inventions at the time since it allowed billions of people to be fed by the fertilizers produced from this process. An estimate of the population growth with and without the Haber-Bosch process can be seen in Fig. 1.1

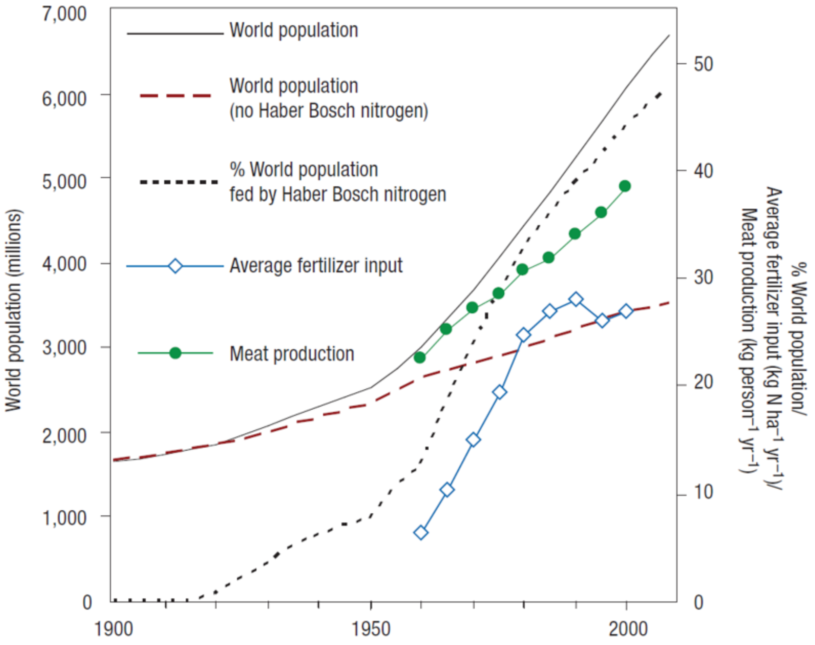

Figure 1.1: World population growth in the twentieth century with Haber-Bosch (black) and without (red-dashed) [8].

The data shows that around 40 % of the current population is fed by the Haber-Bosch process [8]. Since the beginning of the industrial application the energy and production costs also decreased immensely from more than 110 kW h/kg to 7.7 kW h/kg though developments in engineering as well as scaling-up the facilities [5], making the energy efficiency (EE) increase from 36 to 62 %, which is the number based on best available techniques and can not be optimized much further [9]. The factories where ammonia is produced nowadays can deliver up to 6000 tonnes of ammonia per day and are several hectares in size. Knowing all this, shows that the Haber-Bosch synthesis has certainly had a huge positive influence in the technological and social development the last century, but these do not come without caveats. The Haber-Bosch process has been leaving a huge environmental impact on our earth since its invention due to its high energy demand and large CO_2 emissions. The need for its high energy demand can be explained by a look at the simple reaction equation in (1.1):

$$N_2 + 3\,H_2 \rightleftharpoons 2\,NH_3 \qquad \Delta H = -92.4\,\frac{\mathrm{kJ}}{\mathrm{mol}} \tag{1.1}$$

As the reaction enthalpy is negative the reaction should be spontaneous, but this is limited by the slow kinetics caused by the strong N–N triple bond. To circumvent that issue high temperatures (650-750 K) in addition to an active Fe-catalyst are employed, which however shifts the equilibrium to the side of the educts. To mitigate that, high pressures (50-200 bar) need to be used in this process, making the process heavily energy consuming [10]. In fact, the Haber-Bosch process is believed to be responsible for about 1.4 % of the total annual energy consumption [11]. In the last 20 - 30 years the improvements in EE have slowed dramatically, making it obvious that without groundbreaking achievements in technology the efficiency can not be improved anymore [9]. The CO_2 emission of some of the most produced chemicals are given in Fig. 1.2:

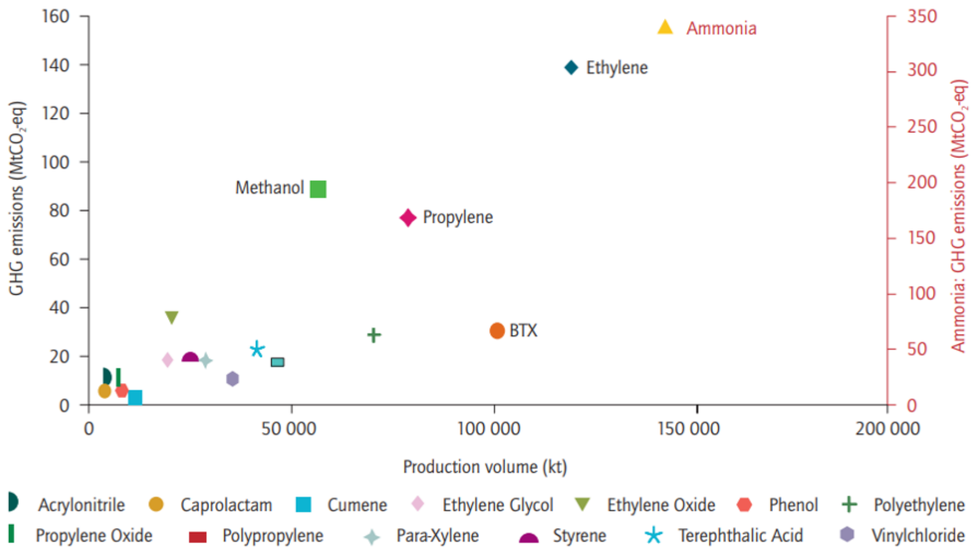

Figure 1.2: CO_2 emissions of industrially produced chemicals. Note that ammonia is on a separate y-axis. Source: DECHEMA 2013

It has to be noted that ammonia is on a separate y-axis here, making it by far the chemical that emits the largest amount of CO_2 per equivalent of product. Since climate change, and the issues that come along with it, is the biggest issue we face as a whole community, the large CO_2 footprint is concerning. From (1.1) it is not directly visible where the emission come from but the H_2 from the Haber-Bosch process is made by steam reforming (see (1.2)), which then results in the total reaction equation seen in (1.3). Another part of methane is burned to generate the necessary heat for the process. Some plants use coal instead of natural gas (1.4), leading to an even higher CO_2 output. In average, one Haber-Bosch plant produces 1.6 - 2.9 tons of CO_2 per ton of NH_3 [5], not considering the emissions resulting from the building of these facilities.

$$CH_4 + H_2O \rightleftharpoons 3\,H_2 + CO \qquad \Delta H = 206\,\frac{kJ}{mol} \tag{1.2}$$

$$3\,CH_4 + 6\,H_2O + 4\,N_2 \longrightarrow 8\,NH_3 + 3\,CO_2 \tag{1.3}$$

$$3\,C + 6\,H_2O + 2\,N_2 \longrightarrow 4\,NH_3 + 3\,CO_2 \tag{1.4}$$

Furthermore, large amounts of NO_X are produced in the process, and the removal thereof is very costly [1]. All these facts make it clear that the current ammonia synthesis via Haber-Bosch is not sustainable in the future and new ways of ammonia production have to be found to satisfy the demands.

1.2 Ammonia Economy in the Future

Many people believe that ammonia, aside from its important role as fertilizer, might be a better energy storage medium than hydrogen. This is due to its relative high energy density and easier storage than hydrogen, since ammonia is easily liquified [1, 12]. When the energy is needed ammonia would then be electrochemically converted in a fuel cell to hydrogen and nitrogen again, while delivering energy in form of electricity. Some even believe in ammonia as a fuel for boats or cars [12].

To accommodate the vast amounts of ammonia needed in this future, it is obvious that other alternative ways of ammonia synthesis need to be realized that are environmentally friendly. In general, three options are discussed and each come with their own advantages and disadvantages. The optimal solution would be direct electrochemical nitrogen reduction in aqueous medium with water as the hydrogen source at ambient pressures and temperatures. This would not only be the most energy efficient way but also most environmentally friendly way since only renewable energy sources would be used and the process would leave no carbon footprint. However, this dream is far from realization and in the following all three options are explored and the role of ammonia in the future discussed.

1.2.1 Ammonia as Energy Storage and Source

In searching for a new way of storing the energy from renewable sources, batteries were the first choice, since they offer a direct method to store the electrical energy. However, this way does not seem to be sustainable since batteries can not accommodate the capacity required for large and long time energy storage [13]. The only way to avoid as many losses as possible in long time energy storage is by chemical ways via hydrogen or other carbon free mediums [14]. One of the most promising options is ammonia, and its possible role in an carbon free future is depicted in Fig. 1.3. It shows the whole life cycle of ammonia as an energy carrier and source. In this scenario ammonia is used in various applications such as in the medical industry, as transportation fuel and as fertilizer where it is converted back to nitrogen, which is harmless for the environment.

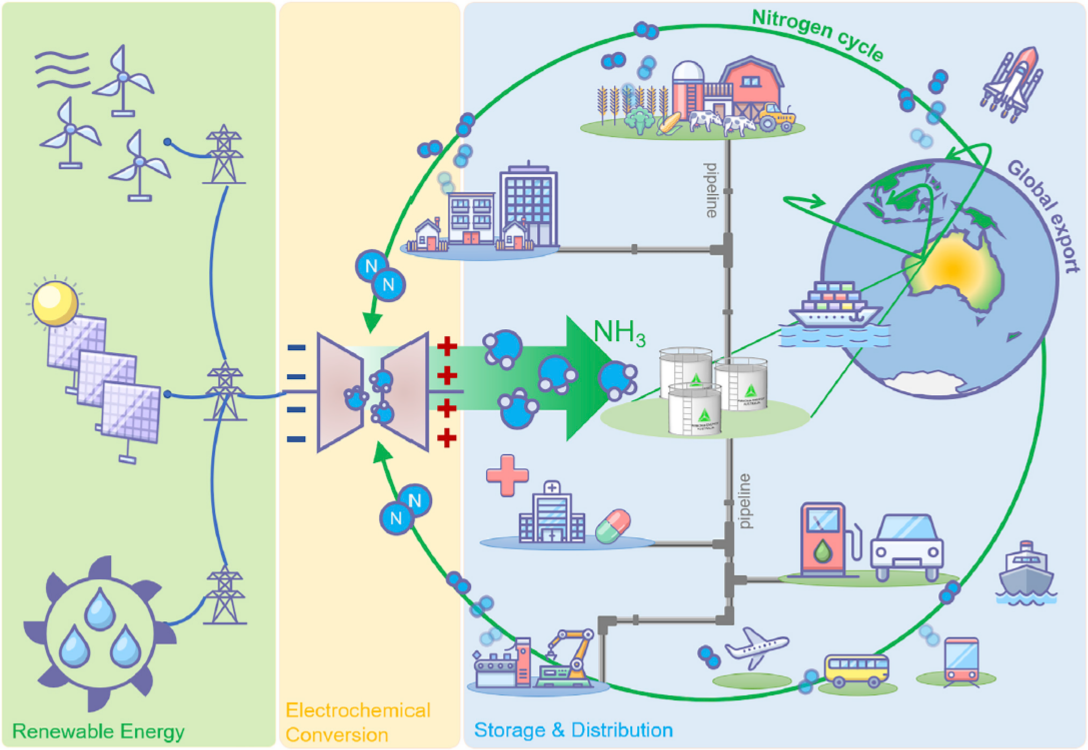

Figure 1.3: Role of ammonia in the future as energy carrier. [12]

Ammonia is a promising candidate because of several more reasons. First of all, its energy density is comparable to those of fossil fuels with 22.5 MJ/kg and the storage cost per unit energy is low at 0.54 \$/kg-H_2 compared to that of pure hydrogen (14.95 \$/kg-H_2) [1]. Moreover, it can be transported more conveniently than hydrogen as shown in Fig.1.3. It is easily liquefied by compression to 10 bar [12] or can even be transported as solid in form of metal nitrate salts. Hexa-ammine-magnesium chloride has been considered for that role, as it is made from the abundant and cheap magnesium chloride and can be compressed into pellets that then give a similar volumetric ammonia content of 615 kg-NH_3/m^3 as liquid ammonia [15]. The distribution of either liquid or solid ammonia derivatives would also be no problem since the required infrastructure is already present due to the demands today. It is also discussed to use ammonia directly as fuel for transportation in ships or cars [16, 17]. However, the technologies are still in the beginning stages and only the future will show if ammonia will assert oneself as a replacement of fossil fuels.

Using ammonia as an energy storage medium and source not only comes with technological challenges but also concerns about health and safety. Our current economy is optimized for fossil fuels and so are our technologies like heat engines, turbines and fuel cells. Since ammonia is corrosive and incompatible with certain materials such as copper and zinc, new machines need to be developed and adapted to ammonia [1]. With the corrosive nature of ammonia comes also other health and safety concerns, which could lead to issues in public acceptance. The risks of ammonia needs to be portrayed clearly to the public before it can be used in large scales. Ammonia by itself might be categorized as toxic, however it is not as dangerous when compared to other fossil fuels. The risk of explosion is also lower since ammonia is hard to ignite and explosion is only possible at high pressures and temperatures when there is an ignition source [1]. Ammonia itself might not be explosive but a lot of its derivatives in form of nitrates, amines and nitro-compounds are. If an explosion of ammonia or its derivatives happens, the consequences might be fatal, since large amounts of NO_x will be released. In general the risk of NO_x exposure is a huge concern and ways to remove it efficiently and effectively need to be developed.

In summary, ammonia is one of the most promising carbon-free alternatives both for energy storage and source. This is reflected in the countless funds worldwide going into research and industry regarding this topic. Its potential is vast but safety issues and technologies need to be adapted. Nevertheless, first round-trip efficiency values for residential (40-50 %) and automotive applications (20-30 %) seem promising [14].

1.2.2 Alternative Ammonia Synthesis Methods

The most obvious and easiest option is to implement a modified Haber-Bosch process where the H_2 comes from water splitting instead of steam reforming. This would decrease CO_2 emissions, making the ammonia much more sustainable. However, this alternative would still rely on big centralized plants, which require huge capital costs and make the developing countries reliant on the richer countries. A way to mitigate this is by electrochemical nitrogen reduction with a coupled water splitting device as hydrogen source. This option is not only carbon free but can be powered solely by renewable energy from electricity from solar cells or wind mills. The last possibility, and the most energy efficient and environmentally friendly way, would be direct electrochemical nitrogen reduction in aqueous medium without a separate water splitting device.

Water splitting coupled with Haber-Bosch - e-Haber-Bosch

To obtain the necessary H_2 for the ammonia synthesis, the current Haber-Bosch plants utilize a methane steam reforming reactor (see (1.2)), followed by a water gas shift reactor (1.5), an CO_2 removal unit and lastly a mechanization unit, to recover as much CO_2 as possible.

$$\mathrm{CO} + \mathrm{H_2O} \rightleftharpoons \mathrm{CO_2} + \mathrm{H_2} \qquad \Delta H = -41\,\frac{\mathrm{kJ}}{\mathrm{mol}} \tag{1.5}$$

The steam methane reforming reactor uses a lot of energy since the temperatures are in the order of 900 °C. The energy required for the heating is gained from methane combustion, which again emits CO_2 [9]. The mixture of resulting CO, H_2 and unreacted educts is then introduced to a water gas shift reactor, where the CO is reacting with the steam to form H_2 and CO_2. The remaining CO is converted back to CH_4 to avoid poisoning of the catalyst. Knowing these procedures, it is clear now that the H_2 production alone leads to an enormous amount of CO_2 emissions as well as energy input. The use of a water electrolysis unit as H_2 source would mitigate all these emissions. A comparison of a methane powered and electrically powered Haber-Bosch process is shown in Fig. 1.4

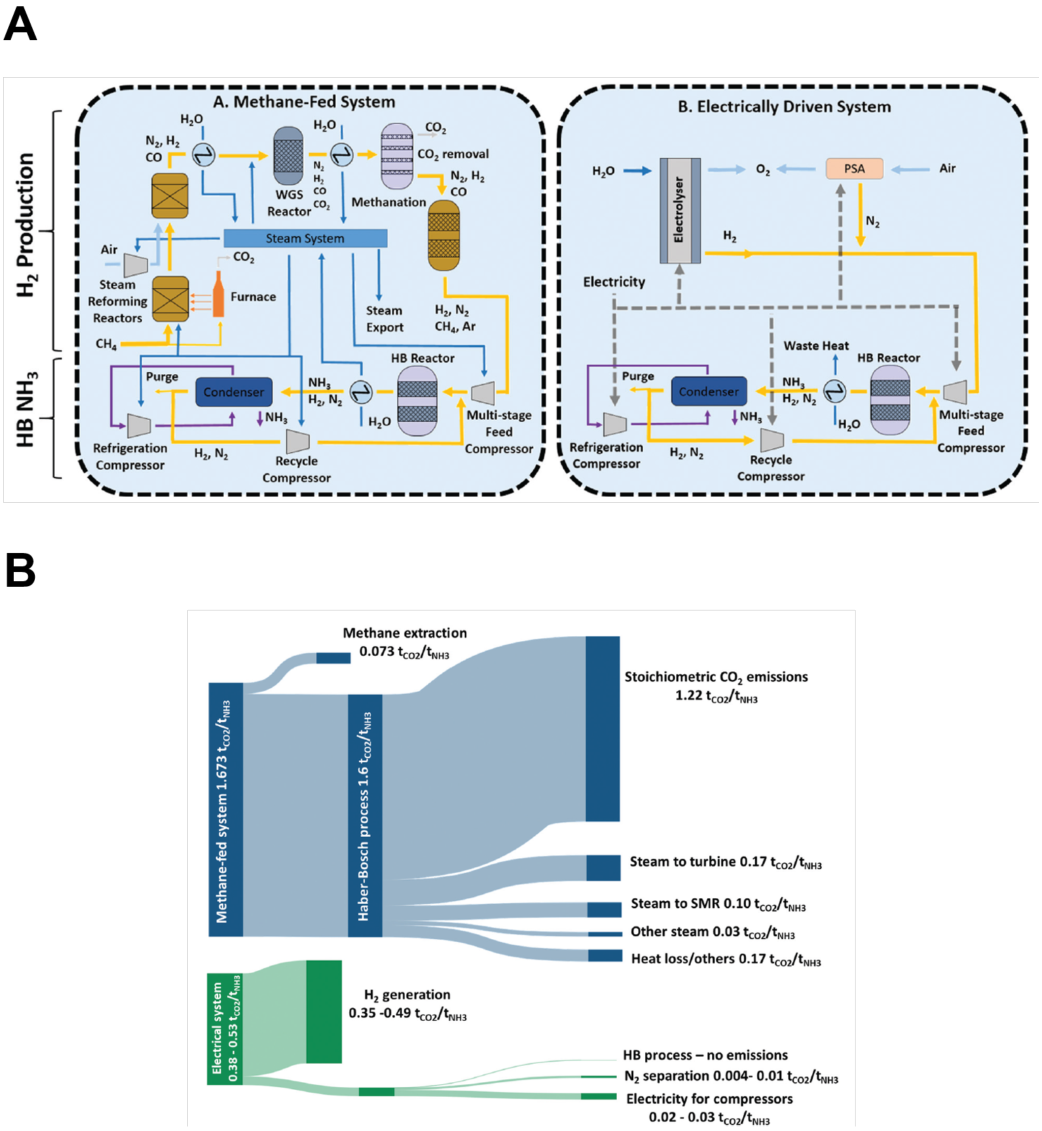

Figure 1.4: Comparison of methane powered and partially electrical powered Haber-Bosch process. **A**: Schematic diagram of both alternatives. **B**: CO_2 emissions of both alternatives. [9]

The electrically driven system in Fig1.4 **A** looks far more simple in construction with less inputs of steam (dark blue lines) and more electrical energy input (dashed gray lines). This would possibly reduce capital costs and hence would make it possible to install smaller more flexible facilities, also in developing countries. The CO_2 emissions for both alternatives are given in

Fig.1.4 **B** in a Snakey chart. It is seen that a water splitting coupled Haber-Bosch plant would decrease the CO_2 emissions from 1.67 to 0.38 - 0.53 t_{CO2}/t_{NH3} leading to a 68 - 77% reduction of the emissions [18]. The Snakey chart makes it clear that most of the emissions do not come from the actual synthesis of ammonia but mostly from the production of H_2. It is predicted that this new electrically driven Haber-Bosch process would require 1.6 kg of water per kg of produced NH_3 and would produce 1.4 kg of highly pure O_2, which could be used elsewhere [9]. The commercialization potential of the electrical driven Haber-Bosch process depends largely on the efficiency of the electrolyzer component. The most promising electrolyzers can be separated into alkaline electrolyzers (AEL), proton exchange membrane electrolyzers (PEMEL) and solid oxide electrolyzers (SOEL) [19]. The energy efficiencies of AEL and PEMEL are in the order of 50-60 %, whereas the SOEL has higher efficiencies of over 80 % [20]. However, the SOEL are expensive and not as durable. PEMEL have the advantage of archiving higher current densities, which would lead to smaller stacks than AEL, however are also more expensive. A techno-economic analysis performed by Zhang et al. calculated the total EE of a Haber-Bosch plant coupled with an SOEL to be 74%, which is higher than the current 61% of methane driven plants. The drawback there are the costs which would lead to an ammonia price of around 400\$/t_{NH3} [21]. However, with the continuous progress in the electrolyzer field and the predicted drop in electricity cost, the realization of these electrical Haber-Bosch plants might be possible in the near future. A smaller scale plant has already been realized in a collaborative work by Siemens plc, Cardiff University, the University of Oxford and the Science & Technology Facilities Council in a wind turbine driven electrical Haber-Bosch plant that makes 30 kg of NH_3 daily and uses an AEL [22]. A bigger project is planned by Thyssenkrupp who plan to complete their green ammonia plant in 2023 [23]. They promise a ammonia production of 50 tonnes per day with their AEL coupled to a low pressure Haber-Bosch plant which is catalyzed by a cobalt-promoted magnetite catalyst.

Water Splitting Coupled with Electrochemical Nitrogen Reduction

The electrified Haber-Bosch synthesis might be more environmentally friendly, but there is still the issue of centralization and intermittency. Since the Haber-Bosch plant itself requires very big facilities and is best run continuously, the capital costs are still high and the electrolyzer needs to either run consistently, which is not always possible with renewable energy sources, or would need a hydrogen tank, which brings more safety issues. A solution to these problems would be to eliminate the Haber-Bosch component entirely and substitute it with an electrochemical process. The electrochemical reduction of N_2 to NH_3 is a 6 e^- process and should theoretically happen at very mild potentials in both acidic and basic solutions as shown in (1.6) & (1.8) [24].

$$N_{2(g)} + 6H^+_{(aq)} + 6e^- \rightleftharpoons 2\,NH_{3(aq)} \qquad E^0 = 0.092\,\mathrm{V}\ vs\ RHE \tag{1.6}$$

$$2H^{+}{}_{(aq)} + 2e^{-} \rightleftharpoons H_{2(g)} \qquad E^{0} = 0.0\,\mathrm{V}\ vs\ RHE \tag{1.7}$$

$$N_{2(g)} + 6H_{2}O_{(aq)} + 6e^{-} \rightleftharpoons 2\,NH_{3(aq)} + 6OH^{-}{}_{(aq)} \qquad E^{0} = 0.092\,\mathrm{V}\ vs\ RHE \tag{1.8}$$

$$2H_{2}O_{(l)} + 2e^{-} \rightleftharpoons H_{2(g)} + 2\,OH^{-}{}_{(aq)} \qquad E^{0} = 0.0\,\mathrm{V}\ vs\ RHE \tag{1.9}$$

The main competitor for the NRR is the hydrogen evolution reaction (HER) which happens at similar potentials seen in (1.7) & (1.9). Thermodynamically NRR is supposed to happen before HER, which in praxis is not the case. The problem lies in the very stable N_2 triple bond (941 kJ/mol) and the resulting slow kinetics and large activation barriers. Researchers agree that the first part of splitting the triple bond requires the most energy and could happen in a one or two electron process shown in (1.10) & (1.11) [24].

$$N_{2} + 2H^{+} + 2e^{-} \rightleftharpoons N_{2}H_{2(g)} \qquad E^{0} = -1.19\,\mathrm{V}\ vs\ RHE \tag{1.10}$$

$$N_{2} + e^{-} \rightleftharpoons N_{2}^{-}{}_{(aq)} \qquad E^{0} = -4.16\,\mathrm{V}\ vs\ NHE \tag{1.11}$$

These large activation barriers, especially in the one electron case, shows the need for a catalyst to circumvent the sluggish kinetics. The catalyst that could achieve this feat is yet to be found but theoretical calculations suggest that potentials of at least -1.0 to -1.5 V vs SHE would be needed [25]. This would correspond to a total cell voltage of the same value since the potential contribution of the HOR counter electrode reaction is negligible. Even though such a process does not yet exist, the Department of Energy has set a goal in the REFUEL program on the specific targets the NRR has to fulfill to be industrial relevant. They predict a minimum FE of 90 % and an EE of 60 % at a current density of $-300\,\mathrm{mA/cm^2}$ are needed [26]. Aside from the advantage of being adaptable to the energy input of the renewable energy sources, this fully electrified process would also not need big facilities, which makes it possible to have smaller ammonia production plants. Moreover, this process might not need as pure of a N_2 feed as the Haber-Bosch process, where the catalyst is poisoned by ppm of O_2 [27]. In summary, the NRR process coupled with a water splitting device has a lot of advantages over an electrified Haber-Bosch process and could be even more energy efficient, however the current technologies, especially on the NRR side, are still in the initial developing phases.

Direct Nitrogen Reduction in Aqueous Medium

To even further simplify the ammonia production, the electrolyzer part can be combined with the NRR into a single reaction cell, where the counter electrode reaction is oxygen evolution reaction (OER), shown in (1.12). The total reaction is seen in (1.13) and would optimally achieve a cell potential of around 2.6 V, considering the standard reduction potentials for the half cell reactions in addition to 200 mV overpotential.

$$2\,H_2O_{(l)} \rightleftharpoons O_{2(g)} + 4\,H^+{}_{(aq)} + 4\,e^- \qquad E^0 = 1.23\,\mathrm{V}\ \mathit{vs}\ \mathit{RHE} \tag{1.12}$$

$$N_{2(g)} + 3\,H_2O_{(aq)} \longrightarrow 2\,NH_{3(g)} + 1.5\,O_{2(g)} + 4\,e^- \qquad E^{\mathrm{cell}} \approx 2.6\,\mathrm{V} \tag{1.13}$$

As stated above, the limiting factor is the cathode reaction, for which no electrocatalyst has been found so far. Nevertheless, feasibility study have been conducted and this direct NRR has been compared to the e-HB and the currently fossil fuel based HB. With aggressively optimistic assumptions in the NRR part, the study conducted by Hochmann et al. [28] show that direct NRR is more efficient and convenient than both Haber-Bosch alternatives. The only advantage of the conventional HB is that it is not as depended on the fluctuating electricity prices as e-HB and NRR which of course will have a huge influence on the cost of ammonia. The effect is more critical for e-HB, since it has to run continuously because of the HB part, whereas the NRR plants can just lower production when the prices rise. This reason could make the NRR more economically relevant than e-HB even though the EE is lower.

1.3 Thesis Outline

Chapter 2 will include a short introduction to electrocatalysis in general, with a focus on the current state-of-the-art in non-aqueous electrochemical ammonia synthesis. In Chapter 3 the experimental setups and methods that were used throughout the thesis are explained.

The next two Chapters 4 and 5 will focus on the improvement of the Li-mediated ammonia synthesis in therms of faradaic efficiency and current density, respectively. The results from Chapter 4 were published in Paper 1 and Paper 4, explaining the surprisingly positive influence of small amounts of O_2 in the system. The results from Chapter 5 were published in Paper 2 and 5 and showcase high surface area electrodes that allow high current density application.

Chapter 6 will give a more fundamental look into the LiMEAS by investigating the role of EtOH in detail. The results will be published in the future, as it is currently in preparation.

Lastly, the limitations of the LiMEAS are discussed and concluding remarks given in Chapter 7.

2 Electrocatalysis and Nitrogen Reduction

The first part of this chapter will cover the basics of electrochemistry and electrocatalysis. These are the fundamentals which this whole thesis is based on, however due to lengths restraints they will only be covered shortly. The main part of this chapter will be the challenges and current state of electrochemcial ammonia synthesis. The state of the art and developments of the LiMEAS so far will be listed and explained.

2.1 Electrocatalysis and Electrochemistry

In general, electrochemistry is the study of reactions that are induced by electricity, like electrolysis, corrosion or electrophoresis. In the times of digitalisation electrochemistry has found many applications such as sensors, fuel cells and most importantly batteries. According to IUPAC a catalyst is a substance that lowers the activation barrier of a reaction without being consumed and hence improves the kinetics of a reaction [29]. It can be separated into two categories, heterogeneous and homogeneous. In electrocatalysis the catalyst is most often a metal or solid immersed in an liquid electrolyte, which makes them a heterogeneous catalyst. In contrast to thermal catalysis, the energy needed to overcome the activation barrier comes from electrons rather than temperature. A schematic of a catalyzed and not catalyzed reaction is shown in Fig.2.1 **A**.

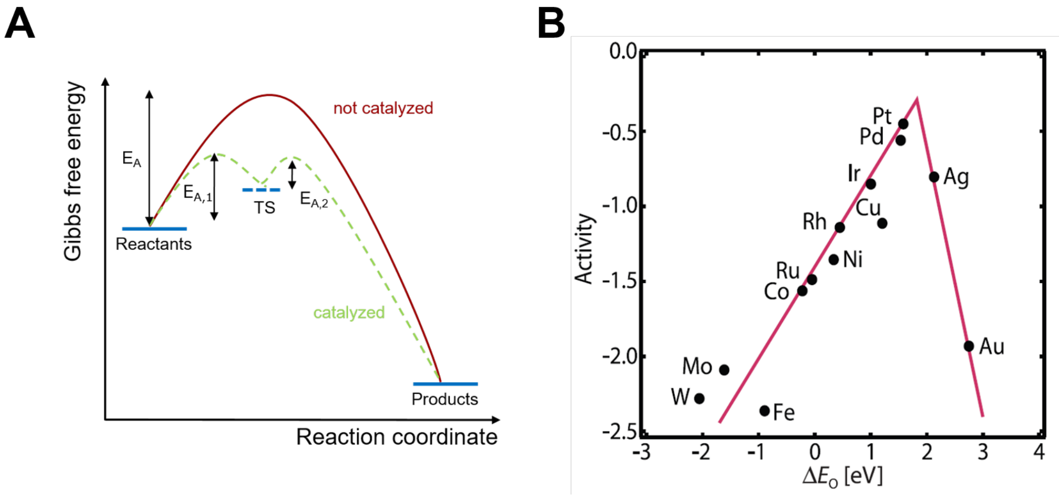

Figure 2.1: **A** Schematic of a catalyzed and not catalyzed reaction, with E_A, being the activation barrier and *TS* the transition state. **B** Calculated volcano plot for ORR [30].

A good catalyst has to bind the substrate just right. If it binds it too strongly, the product is hard to desorb, and if it binds it too weekly the molecule will not react. This principle is called the Sabatier principle and is visualized in so-called volcano plots where the binding strength of a certain metal is plotted against the activity of that catalyst [31]. A volcano plot of oxygen reduction reaction (ORR) catalysts is shown in Fig. 2.1 **B**. The most active catalyst that binds the substrate not too weakly nor too strongly is seen at the top of the volcano plot, which is Pt in this case.

2.1.1 Electrochemical Setup and Charge Transfer

A typical electrochemical cell consists of at least two electrodes that are in contact with an electrolyte, and a power source. A schematic of such a cell is shown in Fig. 2.2.

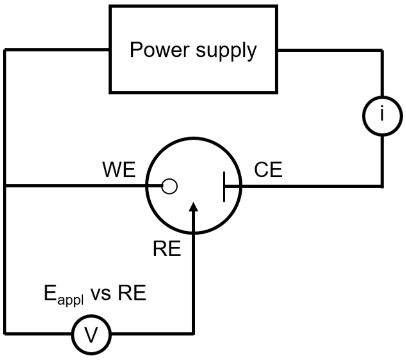

Figure 2.2: Schematic of a typical electrochemical cell with three electrode setup.

On an electrode two different reactions can happen, namely an oxidation or reduction. During an oxidation reaction the reactant loses electrons and during a reduction, the reactant receives electrons which decreases the oxidation number of a specific element. The electrode where a reduction takes place is called the cathode and the electrode where an oxidation takes place is the anode. One can not happen without the other, but normally only one of these reactions is investigated in detail, whose electrode is then called the working electrode (WE) and the other electrode is named counter electrode (CE). Combining both of these half reactions will result in a redox reaction. For an electrochemical reaction these two electrodes are needed, which then gives a two electrode setup. To determine the absolute potentials at which the reduction and oxidation reactions happen, a reference electrode (RE) is needed, whose potential is stable during the operation. the potentials are then referred to as vs. RE. When the electrical circuit is closed and zero current or open circuit voltage (OCV) is applied no net reaction is taking place. The measured OCV is an indication of the equilibrium potentials of the reactants in the electrolyte. As soon as a bias, which is the driving force, is applied reactions can take place. [32]

An illustration of the electrical processes that takes place between the electrode and electrolyte is given in Fig. 2.3.

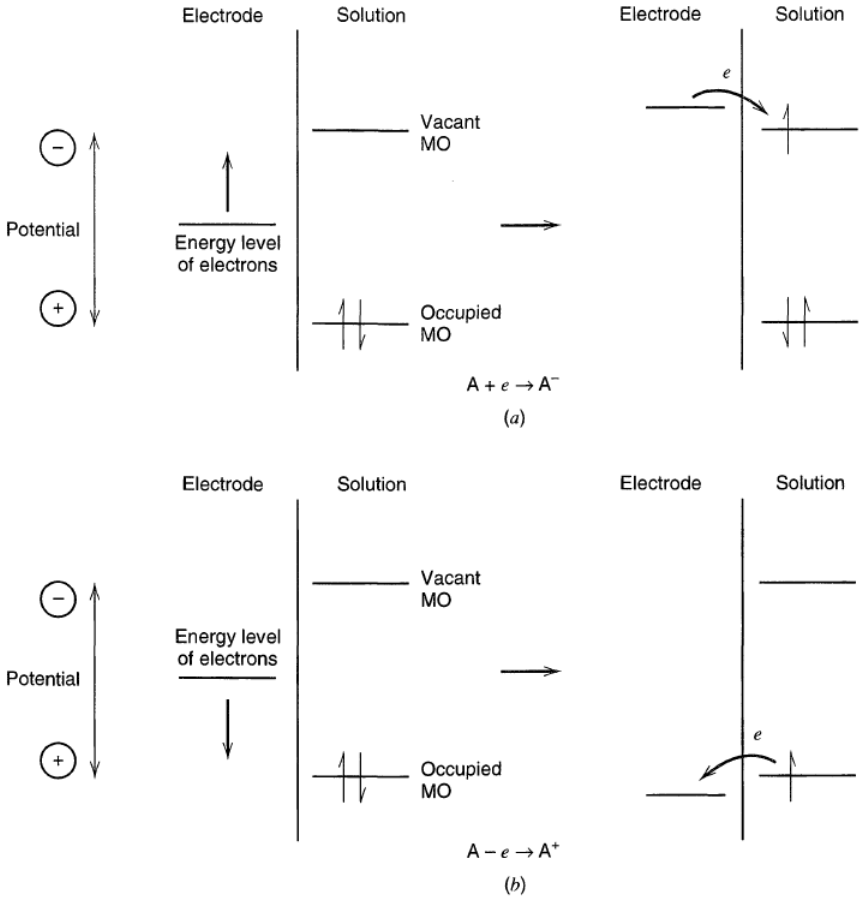

Figure 2.3: Illustration of electrochemical oxidation (bottom) and reduction (top) reactions. [33]

A reduction takes place on the side where a negative bias is applied which raises the energy levels of the electrons. If the level is raised further than the lowest unoccupied molecular orbital (LUMO) of a reactant the electron can jump from the electrode to the reactant and reduce it. The opposite happens during an oxidation where the energy level of the electrons are lowered below the highest occupied molecular orbital (HOMO) which makes it then possible for the anode to accept an electron from the reactant. [33]

Oxidation and reduction reactions obey Faraday's law, which states that the amount of reaction happening is proportional to the passed charge. Aside from charge transfer reactions occur non-faradaic reactions like adsorption or desorption can take place. One has to remember that both faradaic and non-faradaic reactions take place simultaneously during an electrode reaction, even tough in most cases the faradaic reactions are of greater interest.

2.1.2 Electrode Electrolyte Interface

The electrical double layer (EDL) is a description of the electrode electrolyte interface and can be depicted as an capacitor which is governed by following equation:

$$\frac{Q}{E} = C \tag{2.1}$$

Each capacitor has a certain capacity C it can contain. When a potential E is applied, current will flow until a certain charge Q is passed that fulfills the equation 2.1. In case of the EDL the charges can be seen as an access of charge at the metal electrode (Q_M) and an opposite charge of the same magnitude in the solution (Q_S). The EDL is generally very thin (around 0.1 Å) and has capacitance values of 10 to 40 mF/cm^2, which is very dependent on the electrolyte and electrode material. [33] As seen in the schematic of the EDL in Fig. 2.4 **A**, the EDL is made out of two layers. On the first layer, also called inner Helmholtz plane (IHP), solvent molecules or ions are specifically adsorbed to the electrode and the total charge density from these adsorbed molecules is σ_i. Solvated ions of the opposite charge can form the second layer in the outer Helmholtz plane (OHP) and are therefore non-specifically adsorbed with a charge density of σ_d. The total accumulated charge density σ_S is then the sum of σ_i and σ_d. The range of the second layer, often also called diffuse layer, can range into the bulk of the electrolyte and is dependent on the electrolyte concentration. It is thinner for higher electrolyte concentrations and less than 100 Å for electrolyte concentrations above 0.2 M. From the voltage profile shown in Fig. 2.4 **B** is is clearly seen that the EDL induces a potential drop close to the electrode surface, meaning that the reactants experience a diminished potential in contrast to what was applied on the electrode. [33, 34]

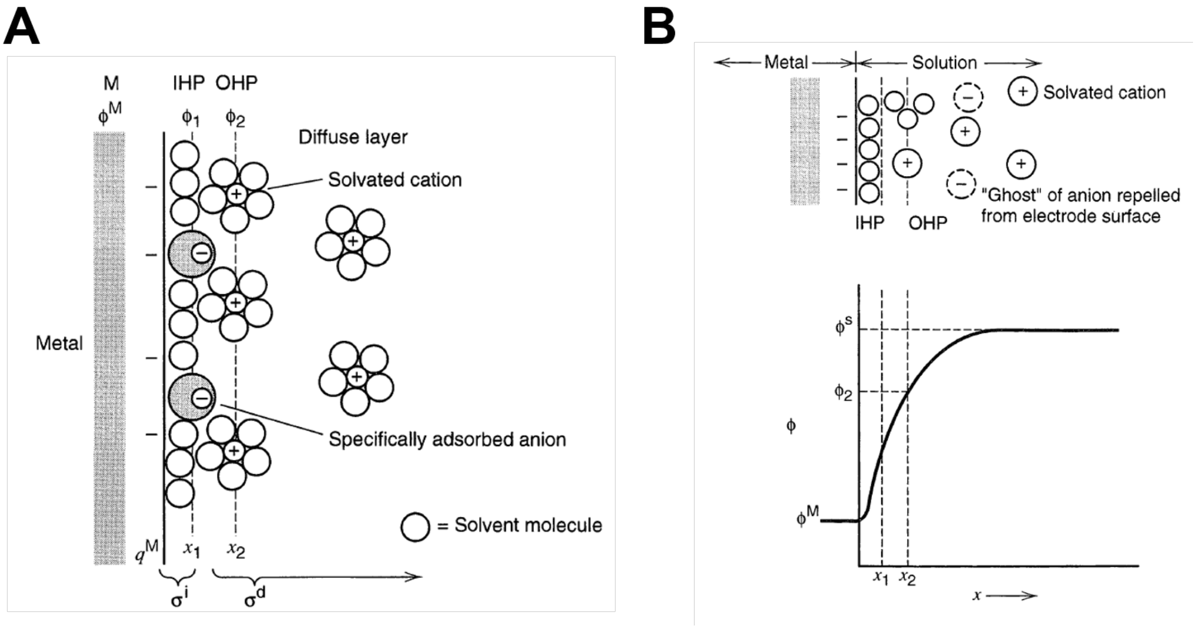

Figure 2.4: A Proposed schematic of the electrochemical double layer. **B** Potential profile across the electrochemical double layer. [33]

Since the capacitive current has nothing to do with faradaic reactions and more with the electrical interface, it is most often neglected when investigating electrochemical reactions. However, in some cases it is important for measuring the electrochemical active surface area (ECSA) by capacitive cycling, which will be explained in later sections.

2.1.3 Role of Potential

The potential of a reaction is determined by referencing it versus a reference electrode, whose potential should be stable during the reaction. In aqueous solutions the standard hydrogen electrode (SHE) or reversible hydrogen electrode (RHE) are commonly used. The reactions and conditions are shown below:

$$\mathrm{SHE}: 2\,\mathrm{H}^+ + 2\,\mathrm{e}^- \rightleftharpoons \mathrm{H}_2 \qquad E = 0.0V \qquad \text{Pt, 1atm H}_2\text{, a}_{\mathrm{H}+}\text{=1, pH=0} \tag{2.2}$$

$$\mathrm{RHE}: 2\,\mathrm{H}^+ + 2\,\mathrm{e}^- \rightleftharpoons \mathrm{H}_2 \qquad E = 0.0V \qquad \text{Pt, 1atm H}_2\text{, a}_{\mathrm{H}+}\text{=1} \tag{2.3}$$

The pH dependent RHE scale can be obtained from the SHE scale with following relation:

$$E_{RHE} = E_{SHE} - 0.059 \cdot pH \tag{2.4}$$

In this thesis a pseudo reference Pt wire electrode was used, since it is hard to find reference electrodes in non-aqueous environments that do not contaminate the electrolyte. It is even harder to define the potential, because in our case we know that the bulk electrolyte changes during the duration of an experiment through solvent oxidation at the anode. Hence, we are aware that the reference potential can shift and we advise to take the potentials with a grain of salt. In some of the studies the potentials were referenced vs Li/Li^+ whose potential was determined before a reaction with the onset of Li plating in a linear sweep voltametry (LSV).

2.2 The Current State of (non-aqueous) Electrochemical Ammonia Synthesis

As outlined in the previous section, the future of renewable ammonia production is heavily dependent on the establishment and improvement of electrochemical nitrogen reduction reaction. The reason why this important issue has not been solved is mainly threefold. For once, the activation of the stable triple bond in N_2 is a challenge as already stated. Another issue is the competition of NRR with HER in aqueous systems. Due to scaling relations, HER is always favored over NRR on all transition metal surfaces [35], which makes industrially relevant electrochemical ammonia synthesis very hard, if not impossible. These two points are also the reason why currently most of the NRR publications show low FE and ammonia formation rates. The synthesized ammonia is in concentrations of ppm or even ppb and hence very prone to contamination. It has been shown that a huge amount of published data is measuring on contamination, instead of N_2 derived ammonia [36]. All these challenges and their possible solutions will be further evaluated with a focus on the non-aqueous ammonia synthesis, which is the basis of this thesis.

2.2.1 Challenges in Electrochemical Ammonia Synthesis

As trustworthy experimental data on electrochemical ammonia synthesis is still lacking, one has to rely heavily on theoretical calculations and simulations to understand the difficulty of NRR. In principle the NRR can happen in two ways, namely associativity, where the N-N bond is broken at the end or and dissociatively where the first step is breaking the N-N bond. Both mechanisms can be seen in Fig. 2.5.

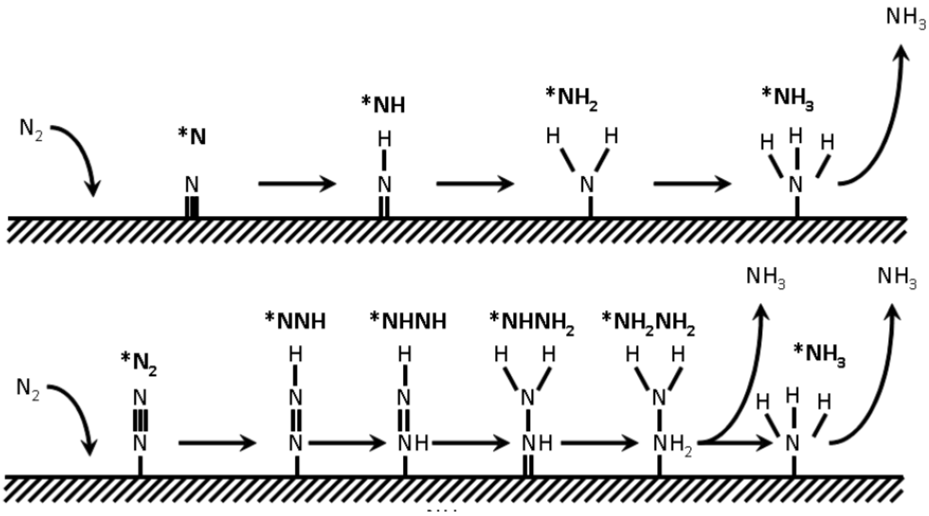

Figure 2.5: Associative (bottom) and dissociative (top) nitrogen reduction mechanism on metal surfaces. [11]

It has been calculated that the N-binding energy of the catalyst is responsible for the pathway which N_2 activation takes place. At strong binding surfaces such as Zr, W and Mo the dissociative pathway is prevailing, which is also the mechanism in the HB process. And in turn, at intermediate N-binding surfaces the associative pathway dominates on transition metals such as Cu, Pt or Pd [11, 25]. The conclusion of the study was that the most promising NRR catalyst would be in the strong binding regime and the predicted potential would be around -1 to -1.5 V vs SHE [25]. The commonly agreed reason why no suitable catalyst has been found so far is because of the scaling relations between the two intermediates $*N_2H$ and $*NH_2$, where the * denotes an active site on the catalyst. Optimally, the catalyst would bind the former strongly but the latter weakly to allow the desorption of NH_3, however because they scale linearly this is not possible. Due to this, Van der Ham et al. predicted a minimum overpotential of 0.4 V to be necessary [11]. A proposed way to circumvent this scaling relation is by having dual metal active sites [37].

Once the activity problem is solved, the selectivity problem must be addressed. As seen in the volcano plots in Fig. 2.6, the HER always requires less negative potentials than NRR on flat and stepped surfaces alike.

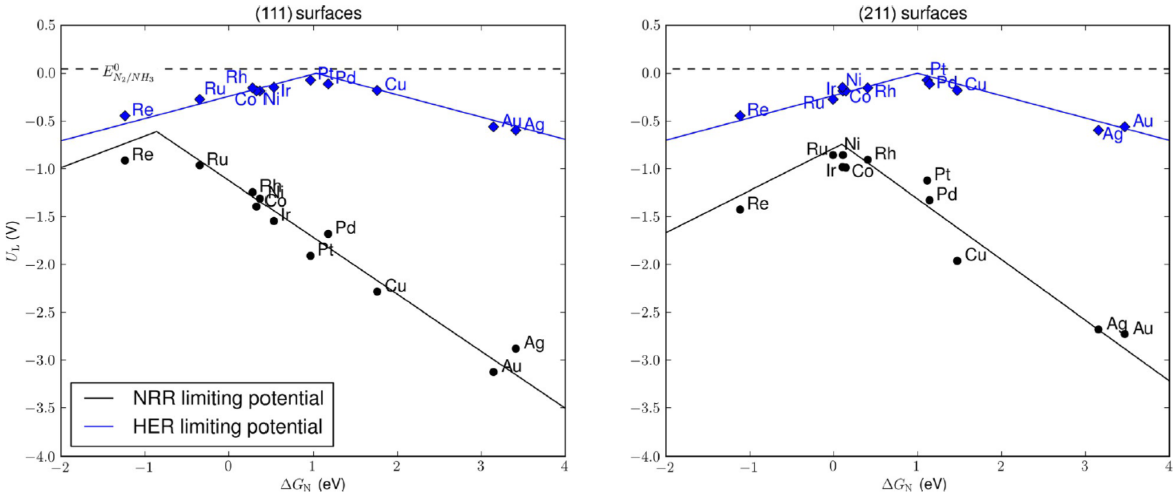

Figure 2.6: Comparison of HER and NRR limiting-potential in volcano plots. [37]

Strategies to suppress HER in relation to NRR is to reduce the availability of the reactants of HER, which are protons and electrons. Ways to reduce proton availability is to either dilute an aqueous solvent with a polar aprotic solvents such as DMSO or completely switch to non-aqueous solvents such as THF or propylene carbonate (PC). Strategies to slow down electron transfer include applying a thin layer of insulator on the catalyst where the electrons need to tunnel through or utilizing a photoabsorber to achieve the same effect [38].

After both activity and selectivity issues are solved the last step is to correctly evaluate the catalyst. As simple as this sounds, it is not so trivial in the very low ammonia concentrations most papers claim to produce. Several groups have come up with rigorous protocols to be followed to guarantee NH_3 production from N_2 activation [36, 39–42]. All of them follow the same goal to identify sources of activated nitrogen contamination such as different NO_X compounds that come from the chemicals that were used in the experiments. Furthermore, NH_3 contamination can come directly from human breath or the nitrile gloves. The sources of false positives are wide and a definite proof, as was stated by several of these protocols, are quantitative isotope experiments with $^{15}N_2$ [43]. The goal thereby is to prove that one can produce as much $^{15}NH_3$ as $^{14}NH_3$ over several points. A detailed method how to quantify the isotope labeled ammonia was published in [44]. Due to all these meticulous instructions, scientists in the field started to publish more critical work [45, 46] or even retracted previous publications, which is a step in the right direction.

2.2.2 Non-Aqueous Ammonia Synthesis - The Li-mediated Pathway

To avoid the selectivity issues mentioned in the previous section, H^+ availability can be limited in non-aqueous electrolytes. Currently, the only proven method to synthesize ammonia electrochemically is the Li-mediated pathway, which uses the reactive metal Li to break the stable N triple bond [47–50]. The history of the LiMEAS can be dated back to Fichter et al. in 1930 [51] where they used alcohols as solvent. Several decades later in the early 1930s Tsuneto et al. investigated the process more sophistically in THF [52, 53]. We have based our findings heavily on the findings of Tsuneto and still use a very similar electrolyte composition as they did. Aside from our group, it has gained great interest in the past years and has been reproduced by many groups worldwide [40, 49, 54–58].

The exact mechanism is yet to be elucidated but it is agreed that it consists of three major steps:

$$\text{Li plating}: \mathrm{Li^+ + e^- \longrightarrow Li} \qquad E^0 = -3.04\,\mathrm{V} \tag{2.5}$$

$$\mathrm{N_2}\text{fixation}: \mathrm{Li + N_2 \longrightarrow Li_3N \text{ or } LiN_xH_y} \qquad \mathit{\Delta H} < 0 \tag{2.6}$$

$$\text{Protonation}: \mathrm{Li_3N + H^+ \longrightarrow NH_3 + Li^+} \qquad \mathit{\Delta H} < 0 \tag{2.7}$$

The first step seen in (2.5) is the only electrochemical step which is a reduction of Li^+ ions from solution into metallic Li. It requires large negative potentials of over -3 V since the $2s^0$ state of Li^+ is much more stable than $2s^1$. The last two steps are purely chemical and exothermic in nature. Since Li is such a reactive metal, it is possible to split the N triple bond while forming a Li-N or Li-N-H containing species. The exact reaction product has not been characterized yet since it is only possible to measure it *in situ*. This species will then be protonated to form NH_3. It was initially believed that the protons are coming from EtOH [49, 55], but Krempl et al. proved that THF can also be a proton source, since they saw an acidification of the electrolyte over time even without EtOH present [59]. They hypothesized that the acidification is due to the oxidation of THF on the anode which leads to formation of dihydrofuran and two H^+. This species was also confirmed by GC-MS measurements of the electrolyte after electrochemistry [60]. Furthermore, the decomposition and further polymerization of THF on Pt anodes was also observed elsewhere [61].

Since finding a stable reference electrode in a non-aqueous system is not trivial, especially in the LiMEAS case where the electrolyte changes over time, galvanostatic methods are used rather than potentiostatic ones. A typical chronopotentiometry (CP) of a LiMEAS reaction at ambient pressures and temperatures is given in Fig. 2.7.

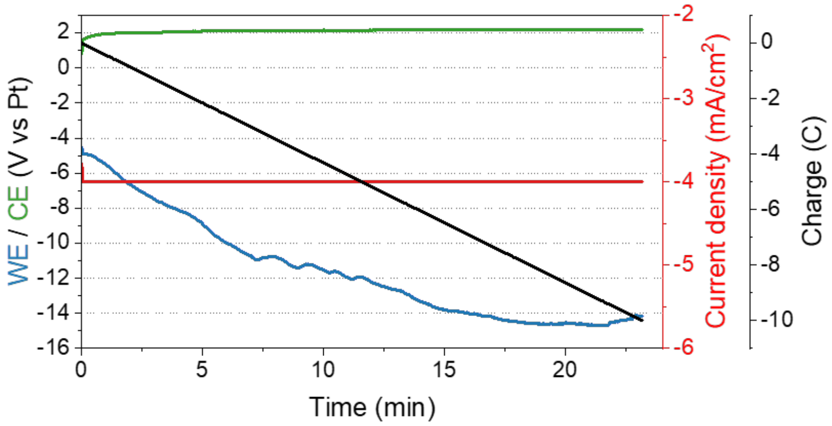

Figure 2.7: Typical chronopotentiometry of a LiMEAS reaction at ambient pressure and temperatures at −4 mA/cm^2. The WE was a Mo foil and the CE was a Pt mesh. The reaction was performed in 0.5 M LiClO$_4$ with 0.17 M EtOH in THF.

At these ambient conditions the LiMEAS exhibits FE of around 5 % and its operation is unstable with the WE dropping to potentials of below −10 V in a few minutes. This is of course not sustainable and a solution was found by Andersen et al. by cycling the applied current between zero current and operation current [62]. This allows the freshly deposited Li to react away during the resting phase before deposition of new Li. Hence, the accumulation of unreacted Li and possible other non-conductive decomposition products is avoided. With this cycling method the system stays stable for days.

To boost the rather low FE, several groups have tried to increase the N_2 availability, which was proven by Tsuneto et al. to have a positive impact on the FE [52]. One way to achieve that is by increasing the N_2 pressure in a batch cell type setup [55, 62]. Another way is to apply a gas diffusion electrode (GDE) in a flow cell [56], which allows for ambient N_2 pressures. Both strategies indeed increased the FE, proving that the LiMEAS is N_2 limited.

The work of Lazouski et al. [56], which successfully implemented the GDE, was also the first to address the reaction at the anode. As stated above the anode reaction is believed to be solvent oxidation, but in their work HOR was utilized at the anode by flowing H_2 at the anode. This not only improved the stability of the electrolyte but also, in theory, should lower the total cell potential due to the less positive potentials needed at the anode, however their reaction was not stable over time and ran at cell potentials of over 20 V. Suryanto et al. improved upon the H^+ transport by introducing a phosphonium-based proton shuttle to carry the protons from the anode to the cathode [55]. The same group also investigated the HOR in non-aqueous electrolytes further and saw a fast poisoning of the standard HOR catalyst Pt [54]. They concluded that a bifunctional catalyst would be the solution for a stable HOR operation.

Another important aspect of the LiMEAS is the solid electrolyte interphase (SEI) layer which is formed on top of the metallic Li. This term is borrowed from the battery literature and describes an ionically conductive but electrically insulating layer that forms from decomposition products of Li with the electrolyte [63, 64], and was first described by Dey in 1977 [65]. This layer protects the metallic Li underneath from further reactions with the solvent and in the case of LiMEAS also regulates the availability of the reactants Li^+, N_2 and H^+ at the electrode surface. Since the SEI layer is very sensitive to moisture and air it is very hard to probe and still not very well understood. One can argue that the SEI layer changes as soon as there is no potential applied anymore, which makes in-situ characterization the only way to investigate this layer. Nevertheless, some effort was put into analyzing the SEI layer in the LiMEAS community. Cyo-transmission electron microscopy (TEM) was used to characterize the SEI layer after electrochemistry and revealed that EtOH has a strong influence of the SEI morphology [66]. Without it, the SEI layer seems thin and compact with crystalline Li underneath it but with EtOH in Ar atmopshere, the SEI layer is thicker and the Li beneath is formed in islands and not distributed equally. Under LiMEAS conditions, meaning with EtOH and in N_2 atmosphere, the SEI layer is still thick but no metallic Li was detected underneath. The authors concluded that EtOH makes the SEI layer more penetrable, which leads to more favorable reaction conditions of Li with N_2. The only in-situ characterization so far was conducted by Blair et al. with neutron reflectometry [67]. They confirmed a residual layer on top of a Mo cathode after CP and prolonged OCV, which is believed to be the SEI layer consisting of components such as Li_2O, LiOH and $LiClO_4$.

2.3 Aims of this Thesis

At the start of this PhD project in December 2019 not many articles were published on LiMEAS since it has only gained interest through the publication by Andersen et al. [40]. As stated in the last section, since then several groups have started to investigate this and the advances were very steep since it is currently the only tangible hope of a green and renewable ammonia synthesis.
The main goal of this thesis was to scale up the current densities and hence ammonia production rates for a more industrially relevant operation. In addition to that, a more fundamental understanding of the process was also a focus in this work.
The specific aims of this thesis are listed in the following:

1.) Is O_2 as harmful to the LiMEAS as it is to the HB process? This question lead to a surprising result that is both of great importance scientifically and industrially. The results will be shown in Chapter 4.

2.) How can we archive higher current densities in this system? The synthesis of high surface area electrodes and optimization of the electrolyte are presented in Chapter 5.

3.) What exactly are the roles of EtOH and how can we prove it? It was clear from the beginning that EtOH is essential to making NH_3 but what we believe the role of EtOH was has changed significantly over the past three years. This development will be outlined in Chapter 6.

4.) How far are we from our goal of renewable and decentralized fertilizer production? Chapter 7 will give some insights and challenges the LiMEAS community needs to face in the future.

3 Experimental Methods

This chapter will give an insight into the different setups that were used in this thesis as well as the electrochemical methods that were applied. Most of the experimental and characterization methods used in this thesis are standard techniques, which is why they will only be explained briefly. A strong focus and an important basis for the thesis is the detection of ammonia given the importance of correct quantification. Due to our non-aqueous system the detection is not as straightforward as in aqueous systems and the difficulties and pitfalls of the two quantification methods will be discussed in detail in section 3.3.

3.1 Electrochemical Setups and Gas Cleaning and Mixing

The experiments in this thesis were conducted either at ambient pressured in a single compartment glass cell for more fundamental studies or in a pressurized autoclave. The pressure vessel was custom build in our lab and designed by Mattia Saccoccio and Suzanne Zamany Andersen. The gasses used in all experiments were purified in our gas cleaning setup and also properly mixed for the O_2 experiments described in Chapter 4.

3.1.1 Single Compartment Cell

The single compartment glass cell is the easiest electrochemical setup and was used for the EtOH exchange experiments in Chapter 6. Fig 3.1 shows a photograph and a schematic of the cell used in this thesis.

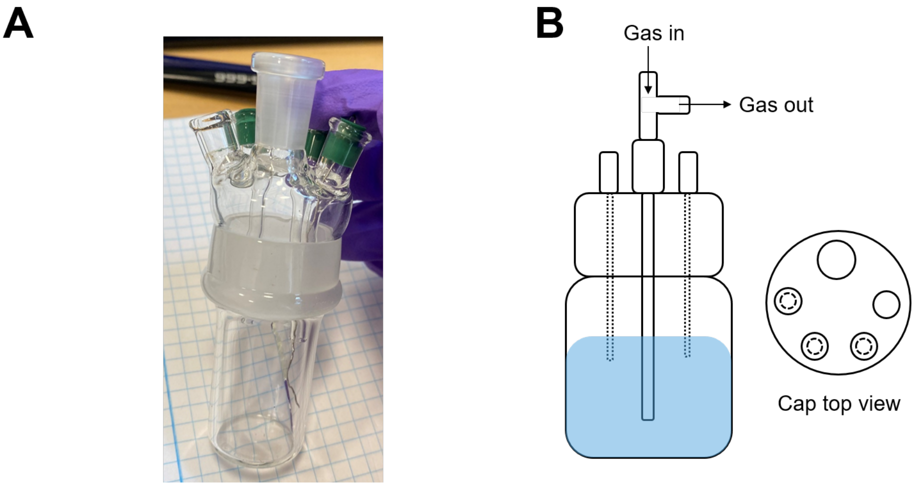

Figure 3.1: **A** Photograph and **B** schematic of the custom made single compartment glass cell, which was used in this work.

The cell lid is custom made and has five openings. Three openings are for the WE, CE and RE and have thin glass tubes attached to guide the metal wires. This allows a more stable and reproducible positioning of the electrodes. The positioning of the electrodes is more important in non-aqueous electrolytes due to the higher resistances. One opening is for introducing and taking out the electrolyte. These for openings can be sealed of with a cylindrical rubber to make the cell air-tight. The last opening is for a gas bubbler. Since our reaction requires gasses like N_2 or Ar, such a gas bubbler is needed. This makes the cell air tight with the only in and outlets at the bubbler. However, these openings are not completely sealed, which is why experiments in a fumehood can still lead to O_2 or H_2O contamination. Therefore all the glass cell experiments were conducted inside a glovebox.

3.1.2 High Pressure Autoclave Setup

A home built autoclave was used for the O_2 experiments in Chapter 4 and the high current density experiments in Chapter 5. The operation pressures were mostly kept at 10 and 20 bar, since higher pressures would make it industrially expensive to apply. Inside the pressure vessel sits a one compartment glass cell, very similar in build as the one described in the previous section 3.1.1, with the exception that there is a bigger hole in the lid to allow faster gas atmosphere exchange. Fig 3.2 **A** and **B** show a photograph of the glass cell with the electrode alignment and the autoclave, respectively. A horizontal electrode aliment was chosen to allow stirring in the glass cell. The WE, CE and RE electrodes were placed as close together as possible to avoid huge iR drops. Fig. 3.2 **C** is a 3D rendering of the glass cell inside the autoclave. The hole in the lid is clearly visible in the front. Fig. 3.2 **D** shows a schematic of the autoclave with the in-operando electrolyte sampling mechanism.

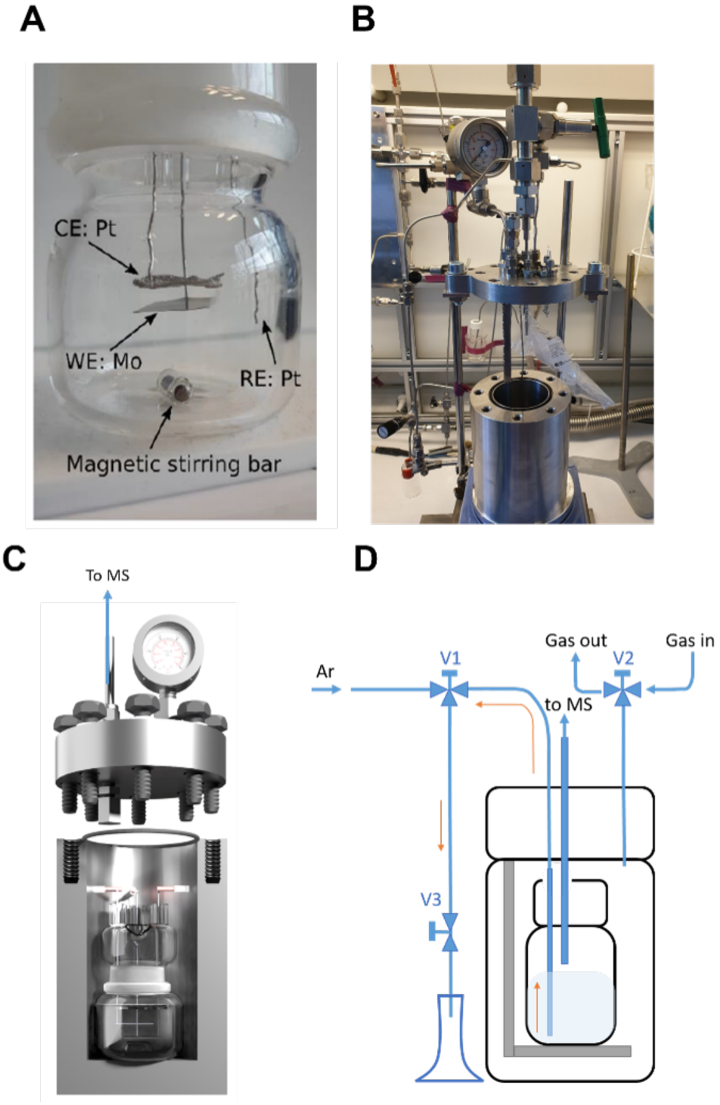

Figure 3.2: Custom built pressure vessel for electrochemical ammonia synthesis. **A** Photograph of the glass cell inside the autoclave. **B** Photograph of the pressure vessel inside a fumehood. **C** Rendering of the autoclave with glass cell and inlet to mass spectrometer. **D** Schematic of the autoclave with electrolyte sampling mechanism.

For the in-operando sampling a polytetrafluorethylene (PTFE) tube is placed inside the big hole in the lid to the bottom of the cell. This PTFE tube is then connected to a 1/16 inch stainless steel tube that goes thorough the lid of the autoclave and then to a three way valve (V1). When the valve is opened to the glass cell, the whole tube is filled with electrolyte up to V3 due to the pressure inside the autoclave. The tube diameter and length were chosen that there is about 1 mL of volume inside. Then the valve V1 is closed and opened to an Ar line which flushes out the electrolyte when V3 is opened inside a small measurement cylinder. The cell is also connected to a mass spectrometer through a 1 µm orifice that is drilled into a 1/8 inch tube, which is also introduced into the cell. The orifice separates the reaction pressure from the ultra high vacuum (UHV) inside the mass spectrometer (MS).

3.1.3 Gas Mixing and Cleaning Setup

Correct gas cleaning and mixing is a very important prerequisite in the field of NRR. Studies have shown that false positive NH_3 signals can stem from NO_x impurities inside the feed gas, which is why the N_2 needs to be purified [36]. To avoid these issues we have implemented a gas cleaning and mixing setup that can be seen in Fig 3.3.

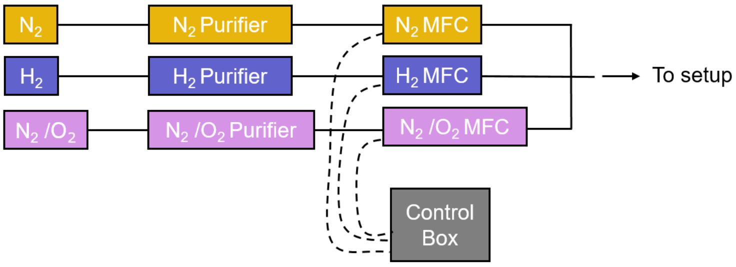

Figure 3.3: Schematic of the gas cleaning and mixing setup.

The gasses are cleaned in conventionally available purifiers from NuPure for N_2, H_2 and synthetic air, which can clean NO_x up to ppt levels. For the O_2 experiments in Chapter 4 we have mixed pure N_2 with synthetic air (20% O_2 in N_2), to get the right O_2 contents. The mixing was done with mass flow controllers (MFC, Brooks) whose flows are controlled by a control box. The N_2 flow was held constant at 5 L/min and the synthetic air flow was then adjusted. To confirm the actual gas atmosphere in the autoclave, the gas composition was measured by a MS (OmniStar GSD 320, Pfeiffer Vacuum). The measured amount deviated slightly from the calculated amount due to possible imperfect gas mixing or communication issues with the control box. This will be discussed in detail in Chapter 4.

3.2 Electrochemical Methods

During this thesis many standard electrochemical methods were used like, cyclic voltametry (CV), linear sweep voltametry (LSV) or impedance measurements. This chapter will briefly describe these techniques and explain for what reason they were used in this work. Specifically, it will be discussed why chronopotentiometry (CP) is preferred in this system compared to chronoamperometry (CA). Moreover, the methods how to make and measure the high surface area metal electrodes are explained in detail.

3.2.1 Cyclic Voltametry and Linear Sweep Voltametry

The potential of the WE is scanned from one potential to another and back at a specific scan rate in CVs. The resulting current response is plotted against the WE potential for analysis. The LSV is basically the same, just that the potential is not scanned back to the starting potential. These methods are generally used to gain information about the different reactants in a system. When reaching a specific potential where a reaction can happen, the current increases and decreases again when the reaction becomes mass transport limited, resulting in a peak shape. The CV can give information about the composition of the reactants through the Nernst equation, when knowing the standard reduction potential (E^0) of the reaction Ox → Red [68]:

$$E = E^0 + \frac{RT}{zF} \cdot ln\left(\frac{Ox}{Red}\right) \tag{3.1}$$

A typical CV and LSV recorded in the LiMEAS system is shown in Fig. 3.4.

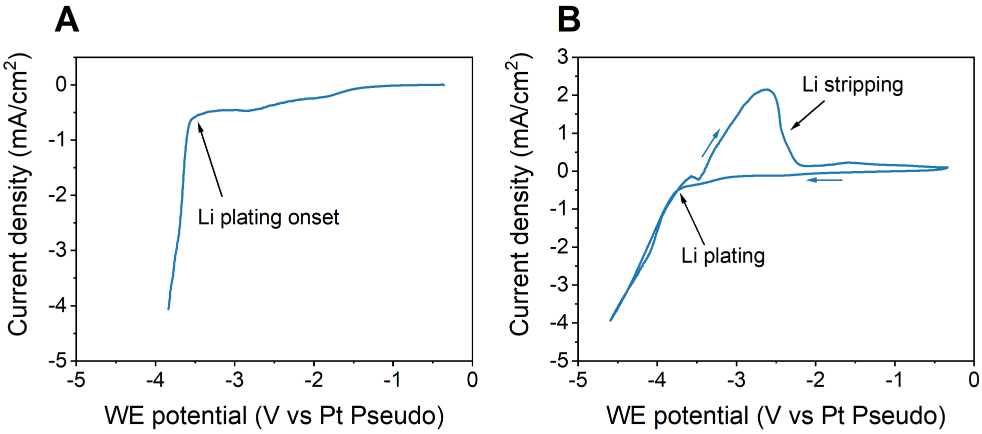

Figure 3.4: Representative **A** CV and **B** LSV in LiMEAS. The WE was Mo, CE and RE were Pt. The electrolyte for both was a 0.3 M $LiClO_4$ with 0.17 M EtOH in THF.

The LSV was used in this work to determine the onset potential of Li plating E_{Li}, which was then used to convert the WE potential from vs Pt (E_{vsPt}) to vs Li/Li$^+$ (E_{vsLi}) in a simple way:

$$E_{vsLi} = E_{vsPt} - E_{Li} \tag{3.2}$$

The onset is quite sharp and does not exhibit a peak shape since the concentration of Li$^+$ ions in the electrolyte is so high that the system is not mass transport limited. The CV in Fig.3.4 **B** gives more information in the back-scan. Not only is the Li plating visible but in the oxidative scan direction another broad peak appears which is related to the reversible reaction of metallic Li stripping off the surface. When comparing the charges of both processes it is possible to see how much Li is lost in this process. This is important for Li metal batteries, however in this work it is not investigated further.

3.2.2 Chronopotentiometry

CP and CA are both techniques that are used to investigate the stability and time dependence of a reaction, as the names already imply. For CP a constant current is chosen and the voltage observed and vice versa for CA. Since there is no stable RE in the LiMEAS system, as discussed in Chapter 2.1.3, it is not viable to do constant potential measurements. The disadvantage of constant current experiments however is, that double-layer charging effects are more prominent and hard to deconvolute [33]. In the future, when a stable and reliable RE is found, the chronoamperometry (CA) might be more favored. In this work CP was used exclusively to produce NH_3. A typical CP is given in Fig. 3.5.

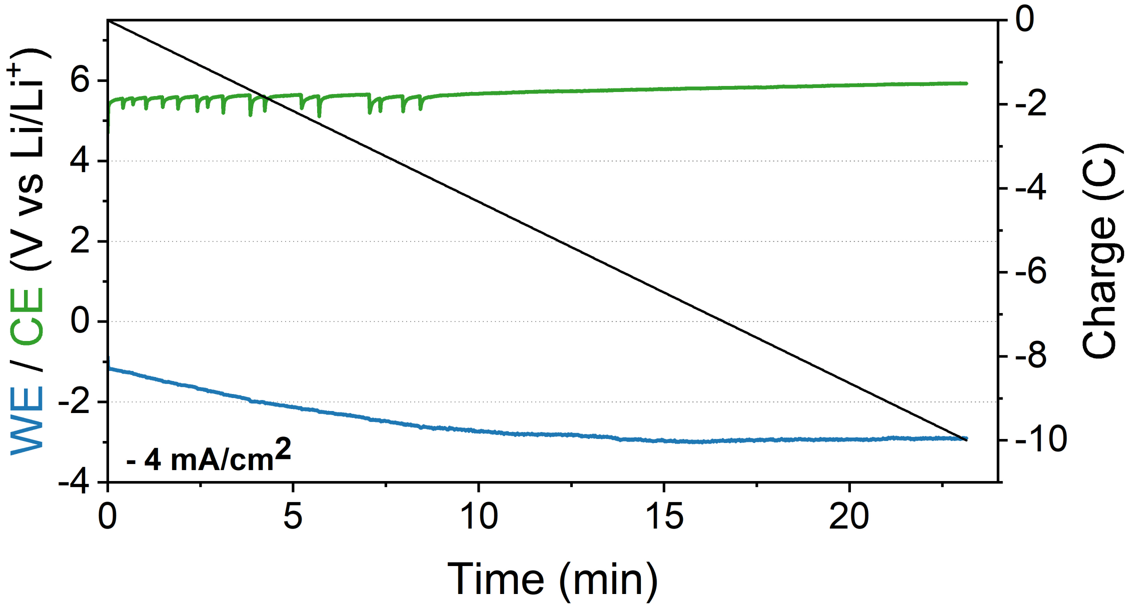

Figure 3.5: Representative CP in LiMEAS at current density of −4 mA/cm^2. The WE was Mo, CE and RE were Pt. The electrolyte was a 0.5 M $LiClO_4$ with 0.17 M EtOH in THF.

Since the current is set at a constant value, the charge accumulates linearly over time. The WE potential is below Li plating, which is indicated by the negative potentials vs Li/Li$^+$. The potential decreases over time and shows that the system is not stable. This will be discussed in detail in the following chapters. In contrast, the CE is stable during the duration of the experiment.

NH_3 is produced mainly during the CP and the charge passed in the CP (Q) is needed to calculate the efficiency of ammonia production. There are several ways to define efficiency but the most commonly used value is Faradaic efficiency (FE) or current efficiency. It determines how much charge goes towards making the desired products versus the total passed charge. To calculate the FE one must know the mole of produced NH_3, n_{NH3}, and z, the moles of electrons needed to make one mole NH_3, which in this case is 3:

$$FE_{NH3} = \frac{z \cdot F \cdot n_{NH3}}{Q} \cdot 100\% \tag{3.3}$$

Another way to represent efficiency is through energy efficiency (EE, η) and is not as straightforward to calculate as FE. The first ones to attempt a EE definition in LiMEAS are the group of Karthish Manthiram [49, 56], which our team then also adapted to stay comparable. They define the EE with the amount of energy obtained from NH_3 from oxidation to water versus the total electric energy put in to make the NH_3:

$$\eta = \frac{E_{out}}{E_{in}} = \frac{\Delta G_{R,NH3} \cdot n_{NH3}}{\int E_{cell}(t)dt \cdot Q} \tag{3.4}$$

$\Delta G_{R,NH3}$ in this case is 339 kJ/mol$_{\mathrm{NH3}}$ or 19.9 kJ/g$_{\mathrm{NH3}}$. The denominator is the total electrical energy being put into the system and consists of the cell potential integrated over time, times the total charge. While this way of calculation gives a first approximation of the EE, it is lacking in several aspects. It does not account for the energy needed to produce H_2 from H_2O, nor does it incorporate the fact that in the current LiMEAS the H^+ source is sacrificial. However, it is still a useful measure and together with a FE gives a fuller view on the total efficiency of the LiMEAS. Hereon, another EE is described labeled η_{new}, which will incorporate the energy needed for making H_2. This will be discussed in detail in the upcoming publication of Paper 6 [69].

$$\eta_{new} = \frac{E_{out}}{E_{in}} = \frac{E_{out}}{E_{in}^{H2} + E_{in}^{NH3}} \tag{3.5}$$

The energy input for making H_2 can be obtained from the EE of an electrolyzer η_{H2}, which is somewhere between 70 - 90 %:

$$\eta_{H2} = \frac{\Delta G_{R,H2} \cdot n_{H2}}{E_{in}^{H2}} \tag{3.6}$$

so that the total η_{new} is:

$$\eta_{new} = \frac{\Delta G_{R,NH3} \cdot n_{NH3}}{\frac{\Delta G_{R,H2} \cdot n_{H2}}{\eta_{H2}} + E_{in}^{NH3}} \tag{3.7}$$

The sacrificial H^+ donor EtOH can be incorporated in E_{in}^{NH3}, however, the goal should be to use HOR on the CE as H^+ source so that this will not be necessary. Regardless, the EE of the LiMEAS will never achieve high values, since the plating potential of Li at -3.04 V is much higher than the theoretical necessary potential for splitting the N_2 triple bond (-1.19 V vs RHE).

This point is also made clear when looking at Fig. 3.6, which shows the energy losses in the LiMEAS.

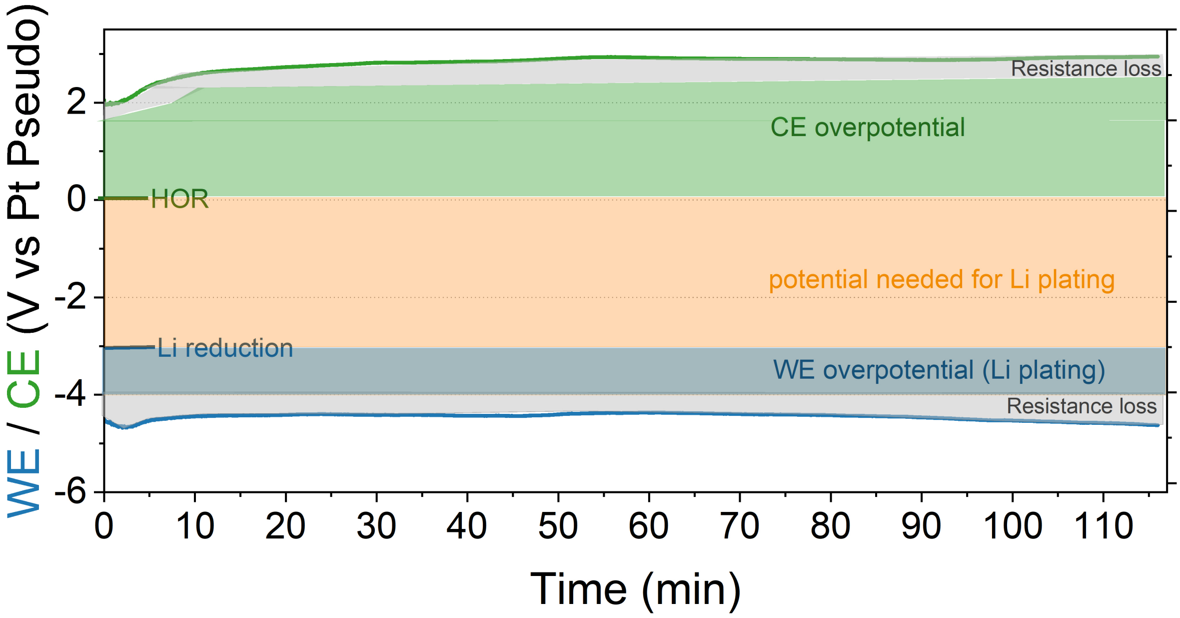

Figure 3.6: Visualization of the energy losses in LiMEAS. This CP was conducted at 20 bar in 0.3 M $LiClO_4$ + 0.17 M EtOH in THF at a current density of –4 mA/cm^2 on a Mo WE with Pt as CE and RE. Data from Paper 4 [70].

The total cell potential in this representative CP is 7.25 V, with 2.8 V vs Pt on the CE and –4.45 V vs Pt at the WE. The gray parts visualize resistance losses due to the high resistance of the non-aqueous electrolyte and account for approximately 0.5 V. Since theoretically HOR is possible at the CE instead of solvent oxidation, the rest of the CE potential can be described as overpotential and is in the range of 2.3 V. On the WE side the overpotential for Li plating is around 0.9 V, when using Li plating as the WE reaction but 2.8 V when referencing to N_2 bond splitting. If only regarding the WE potential E_{WE}, the voltage efficiencies η^V can then be defined as:

$$\eta^V_{NRR} = \frac{-1.19V}{E_{WE}} = \frac{-1.19V}{-4.45V} = 26.7\% \tag{3.8}$$

$$\eta^{ViR}_{NRR} = \frac{-1.19V}{E_{WE}} = \frac{-1.19V}{-3.95V} = 30.1\% \tag{3.9}$$

$$\eta^V_{LiMEAS} = \frac{-3.04V}{E_{WE}} = \frac{-3.04V}{-4.45V} = 68.3\% \tag{3.10}$$

$$\eta^{ViR}_{LiMEAS} = \frac{-3.04V}{E_{WE}} = \frac{-3.04V}{-3.95V} = 77.0\% \tag{3.11}$$

η^{ViR} is the voltage efficiency considering iR compensation. However, these values need to be taken with a grain of salt since due to the pseudo reference potential it is not possible to give exact overpotentials. This voltage efficiency times the FE would also be a reasonable proxy to evaluate the LiMEAS.
In this work all EE values given are by the calculation method of (3.4), however in the future our group will implement (3.7) or other better alternatives.

3.2.3 Electrochemical Impedance Spectroscopy (EIS)

In electrochemical impedance spectroscopy (EIS), an electrochemical system is perturbed by a small oscillating potential or current in a range of different frequencies. From the resulting current or potential response the impedance, $Z(\omega)$, can be calculated [71]:

$$Z(\omega) = \frac{\widetilde{V}(\omega)}{\widetilde{I}(\omega)} = \left|\frac{\widetilde{V}(\omega)}{\widetilde{I}(\omega)}\right| \cdot (cos\phi(\omega) + jsin(\omega)) = Z_r + jZ_j \tag{3.12}$$

As seen from (3.12) the impedance is dependent on the angular frequency (ω) and consists of a real part Z_r, which is the resistance, and an imaginary part Z_j, which is called the reactance. To gain valuable information from the measurement, equivalent circuit fitting needs to be performed and the data is often plotted in a Nyquist plot. Fig. 3.7 shows a Randles circuit with the corresponding Nyquist plot.

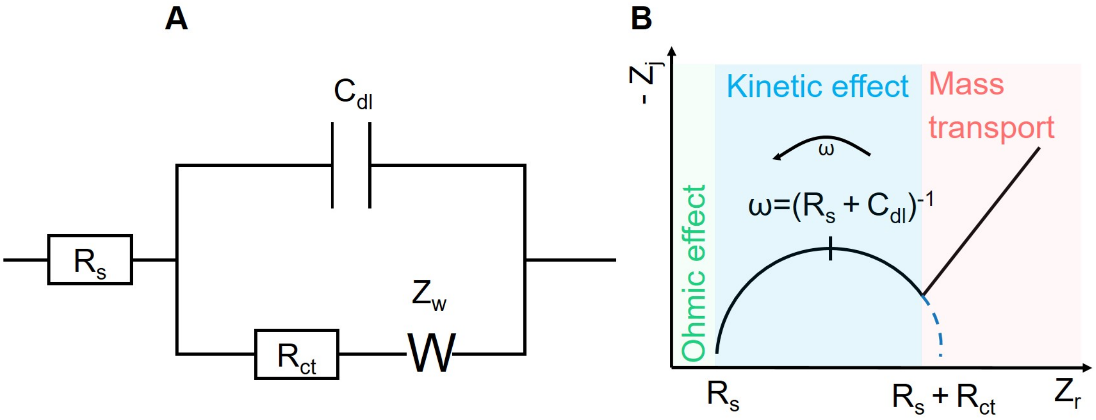

Figure 3.7: A Randles circuit and **B** the corresponding Nyquist plot.

The Randles circuit seen in Fig. 3.7 **A** is often used to describe electrochemical processes with the solution resistance R_s being connected in series with a parallel combination of a double layer capacitance C_{dl} and a faradaic reaction [72]. The faradaic reaction consists of a charge transfer resistance R_{ct} in series with a Warburg impedance Z_w that symbolizes diffusion resistance and is a constant phase element with the phase of 45°, which is why the line in the Nyquist plot at the low frequency regime goes off at that angle. The values of the different resistances and the double payer capacity can be determined from the Nyquist plot shown in Fig. 3.7 **B**. The solution resistance only has a real term and is therefore the first cross section with the x-axis. The second cross section is $R_s + R_{ct}$. Lastly, C_{dl} can be obtained from the middle of the half circle.

Since the LiMEAS is not straightforward to model this way, with the SEI layer and different electrochemical and chemical steps in series, the main use of EIS in this work was to determine the solution resistance for iR correction purposes. Since the solution resistance is non-negligible in non-aqueous electrolytes, it is important to know that the measured WE potential is not the actual potential at the WE. Hence, wherever possible potentiostatic EIS (PEIS) was used to measure the solution resistance and the values lie somewhere between (50-400 Ω) depending on the system and electrolyte used. In this work, the CPs are not iR corrected to give an undiluted image of the potentials. The actual potential at the WE E_{WE} can however be easily obtained from the measured potential E_{meas}, using following formula:

$$E_{WE} = E_{meas} - iR_s \tag{3.13}$$

Distribution of Relaxation Times (DRT)

As already mentioned, one needs to fit the EIS data to an equivalent circuit model to gain any valuable information. This however is not always possible since it must be known how many and which processes take place in a process to not over-fit the data. A model free approach that can still give information about the number of processes and time scales thereof is the distribution of relaxation time (DRT) analysis. It allows the interpretation of EIS data in the time domain through a Fourier transform from the frequency domain. In the conventional Nyquist plot, electrode processes can overlap and are hard to distinguish, but they could be resolved in the time domain. [73]

The first step of the DRT analysis is to fit the EIS data with an infinite number of in row RC elements, whose impedance in described in (3.14):

$$Z_{RC} = \frac{R}{1 + j\omega\tau_{RC}} \tag{3.14}$$

τ is the relaxation time constant in s. This makes the fitted DRT impedance [74]:

$$Z_{DRT} = R_{pol} + \int_0^\infty \frac{\gamma(\tau)}{1+j\omega\tau} d\tau \tag{3.15}$$

Finding the distribution function of relaxation times $\gamma(\tau)$ is a non trivial problem and many different practices exist. One of the most common approaches is by Tikhonov regularization, which allows a simplification of the problem and is related to the method of least squares. The exact method to obtain $\gamma(\tau)$ is beyond the scope of this thesis but more information can be found in [73, 75]. $\gamma(\tau)$ can then be plotted versus $\log(\tau)$. DRT is limited in the frequency domain it is accurate in. At very high or low frequencies the data is inaccurate and often has to be removed [73]. Another pitfall is that DRT analysis requires high frequency resolution and is very perceptive to noise and hence a lot of smoothing of the data can be required, depending on the quality of the measured data. Nevertheless, it is a powerful tool if applied carefully and can be applied in battery literature to investigate Li plating and SEI related phenomena [76]. An example of a DRT spectrum of a Li-ion battery during fast charging is given in Fig. 3.8

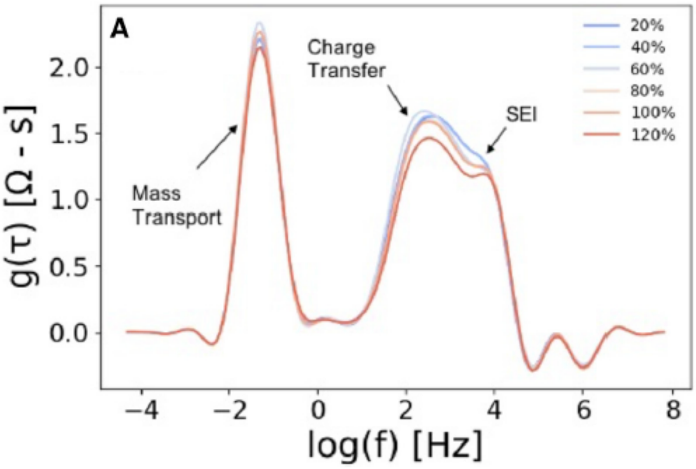

Figure 3.8: DRT spectra of Li-ion battery at OCV after being charged at a C/5 rate to different state of charges. [76]

In this publication the authors investigated a fast charged Li-ion battery at different state of charges (SOC) with DRT. They could changes in the SEI layer resistance at 10^4 Hz and also Li plating around 10^2 Hz.

In this work DRT analysis is performed in a typical LiMEAS system with the hopes to gain information and deconvolute SEI related phenomena and Li plating.

3.2.4 Capacitive Cycling

There are many different ways to measure the ECSA, such as CO-stripping, metal oxide reduction, H-adsorption or under potential deposition. After careful consideration it was decided to use capacitive cycling in an electrolyte that is similar to our reaction electrolyte to determine the ECSA of our high surface area Cu electrodes. This method is not only applicable to a lot of materials, in contrast to CO-stripping, but also allows us to determine the ECSA under our specific electrolyte conditions.
The only prerequisite for this method is that a capacitive region exists in the CV where only double layer charging is occurring without any faradaic reactions.

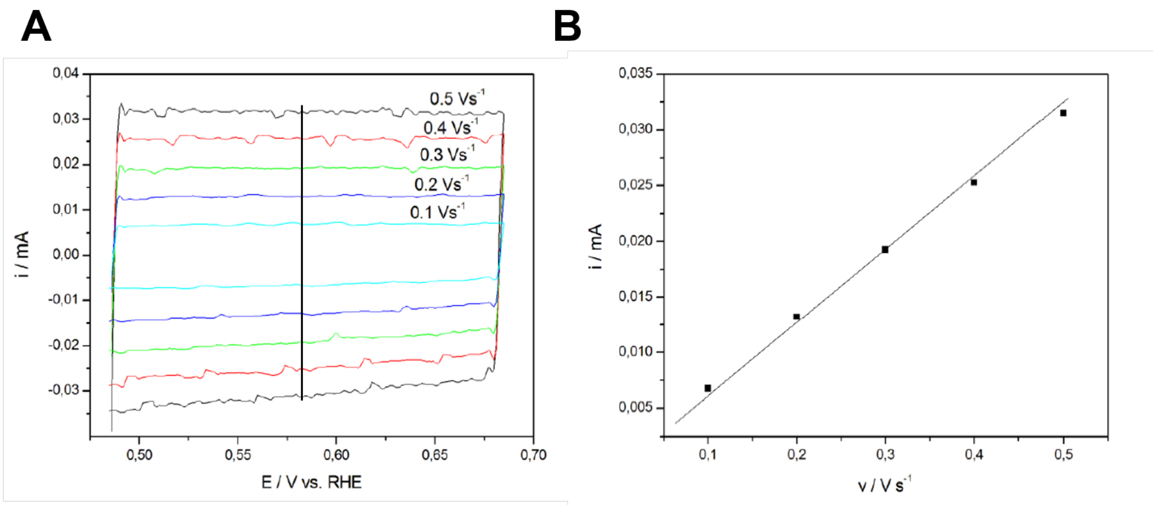

Figure 3.9: **A** Cyclic voltammetry in the double layer region with different scan rates for Pt in 0.5 M H_2SO_4. **B** Dependence of double layer charging current on scan rate for Pt in 0.5 M H_2SO_4. [77]

Since only double layer charging is taking place in this non-faradaic region, and the double layer current is proportional to the scan rate, one can determine the double layer capacity C_{dl} when measuring CVs at different scan rates as seen in Fig. 3.9 **A** and (3.16).

$$i = \frac{dQ}{dt} = \frac{dQ}{dE} \cdot \frac{dE}{dt} = C_{dl} \cdot v \tag{3.16}$$

Experimentally, one would plot the change of current dI, determined by taking half of the charge and discharge current at each scan rate in the middle of the potential range, versus the scan rate v, like in Fig. 3.9 **B**. The slope of the resulting linear line is then the double layer capacity

C_{dl}. To obtain the ECSA, the obtained double layer capacitance must be divided by the specific capacitance C_{spec} of the material in that electrolyte.

$$ECSA = \frac{C_{dl}}{C_{spec}} \tag{3.17}$$

This C_{spec} value is generally between 20 and 40 µF/cm^2 [78] but varies a lot with the investigated material and electrolyte and has to be determined separately if one wants to avoid large errors. [77]
The ECSA determination by capacitive cycling was also validated for non-aqueous solvents in a publication by Yoon et al. where they measured C_{spec} for a wide range of materials in 0.15 M KPF_6/MeCN electrolyte. Interestingly, they observed that most materials in this case exhibit similar C_{spec} values of 11 ± 5 µF/cm^2 [79].

3.2.5 High Surface Area Electrode Deposition

To synthesize high surface area Cu electrodes, a method called hydrogen bubble template (HBT) was applied. The method is based on applying a large overpotential for metal deposition in acidic electrolyte, which allows rigorous HER to occur simultaneously with metal deposition. The metal is then deposited around the resulting H_2 bubbles and after the bubbles disappear a porous metal structure is left behind. A depiction of this process is seen in Fig. 3.10.

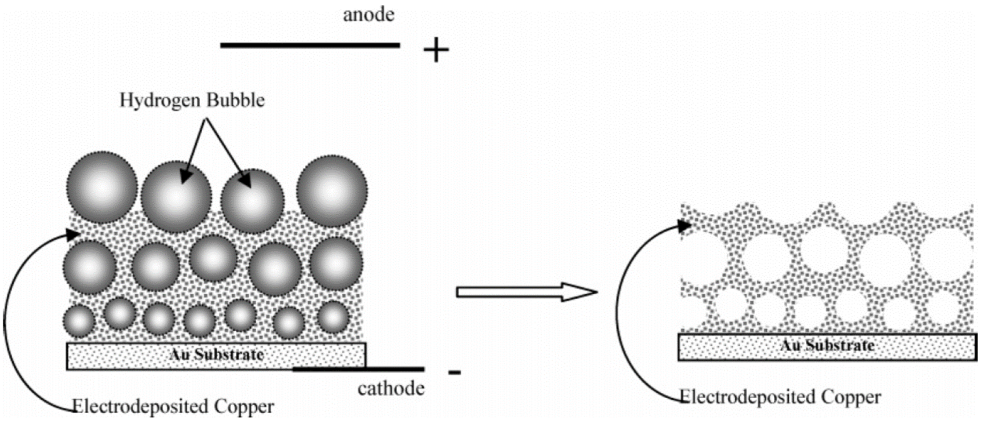

Figure 3.10: Schematic of hydrogen bubble template of Cu on Au. [80]

The further up in the deposition the more the H_2 bubbles have coalesced, resulting in larger pores on top of the deposition [81]. The pores are generally in the 10 - 100 µm size and exhibit dendrite like nano-structures as seen in Fig.3.11. In literature, Cu is mostly used for HBT, but other metals such as Pd, Pt. Rh or Ni are also reported, as well as alloys [82].

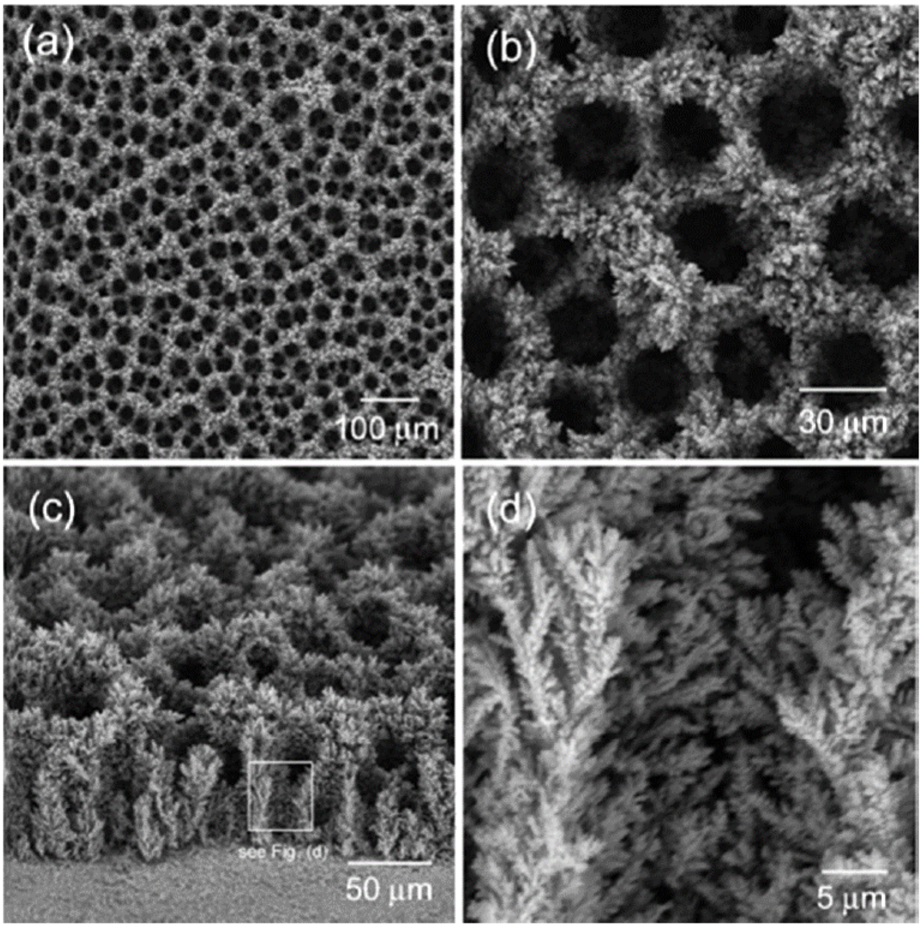

Figure 3.11: SEM of hydrogen bubble template of Cu. Deposition conditions were 20 s in the electrolyte of 0.4 M $CuSO_4$ + 1.5 M H_2SO_4 + 0.1 M CH_3COOH at current densities of −3 A/cm^2 [83].

The method is highly adaptable and deposition features can be tuned by varying the applied current, potential or time. Additionally, the pore size can be adapted by adding surfactants or additives such as ethylene glycol, CTAB or sodium sulfate [82]. For our Cu electrodes we used a electrolyte consisting of 0.4 M $CuSO_4$ in 1.5 M H_2SO_4 and applied a constant current density of around −5 A/cm^2 for different amount of times ranging from 15 s to 5 min. During deposition, the working electrode was sandwiched between a split Pt mesh counter electrode to ensure even current density distribution on both sides of the working electrode. A schematic of the setup and photographs of the deposited Cu electrodes on different substrates is shown in Fig. 3.12. For the experiments presented here either Ni foam or stainless steel mesh were chosen as a substrate for the deposition. Both were spot welded on a Cu wire to ensure good electrical connection.

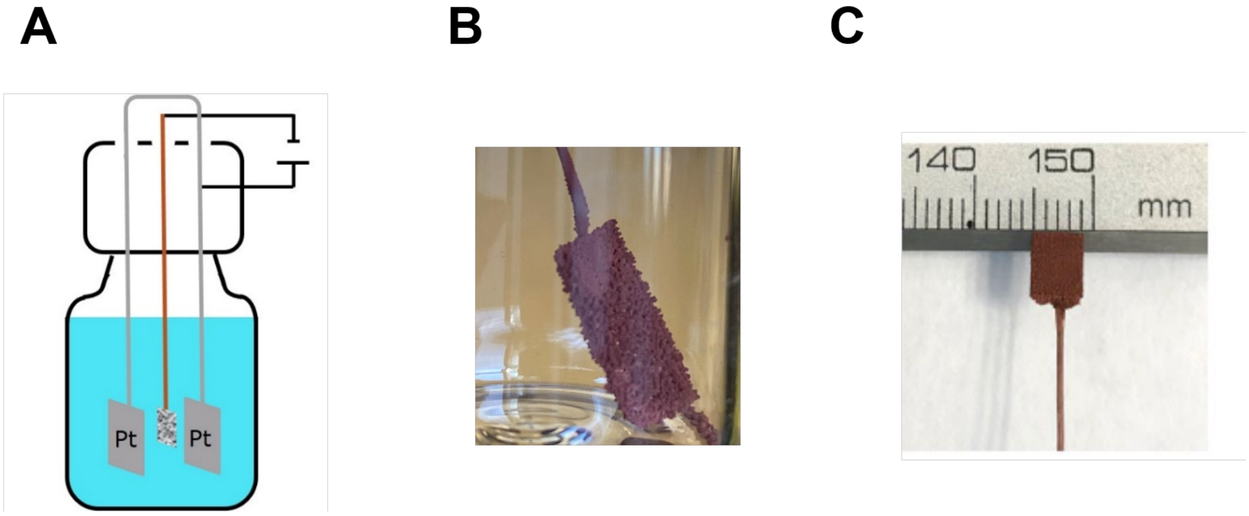

Figure 3.12: **A** Hydrogen bubble template setup with split Pt mesh counter electrode. **B** Deposited high surface area Cu on Ni foam (HBTCu). The geometric surface area of one side was 0.5 cm^2. **C** Deposited high surface area Cu on stainless steel mesh (HBTCuSS). The geometric surface area of one side was 0.2 cm^2

3.3 Ammonia Quantification

The correct quantification of ammonia is essential in this work and not as straightforward as it might sound. Since at some reaction conditions the expected ammonia content can be in the sub ppm levels the detection methods have to be sensitive and accurate in our non-aqueous conditions. Throughout this work two main detection methods were used, namely colorimetric quantification via the indophenol blue method and ion chromatography (IC). Both methods will be critically tested for application in the LiMEAS and their advantages and disadvantages discussed herein. Other quantification methods used in our team include mass spectrometry [84] and nuclear magnetic resonance spectroscopy (NMR) [44]. These two methods can distinguish between isotopes and are necessary for quantitative isotope measurements, which is still a requirement for any new catalyst in NRR. However, in this work they were not extensively used and hence not further discussed in detail.

3.3.1 UV-Vis Indophenol Blue

The indophenol blue method is based on the Berthelot reaction, which forms a blue indophenol dye from ammonia. Since this reaction is quantitative it is possible to use this reaction to measure the amount of ammonia in aqueous solutions with UV-Vis. The four steps of the reaction are shown in (3.18) – (3.21):

$$NH_3 + H_2O \rightleftharpoons NH_4^+ + OH^- \tag{3.18}$$

$$NH_3 + OCl^- \longrightarrow NH_2Cl + OH^- \tag{3.19}$$

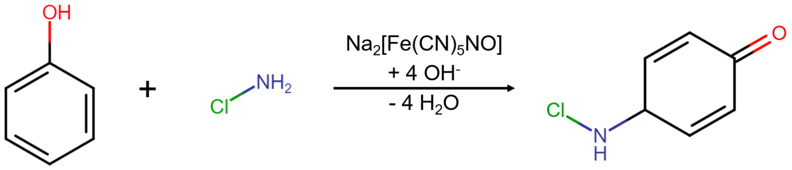

(3.20)

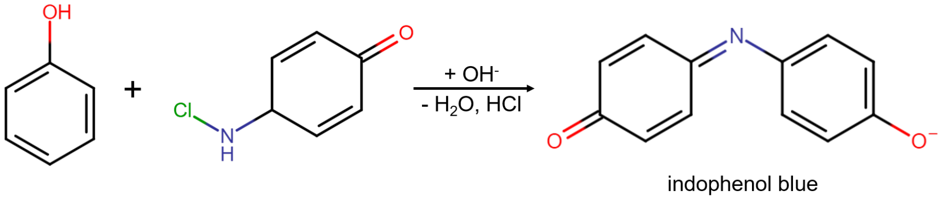

(3.21)

The equation in (3.18) shows the equilibrium of ammonia in aqueous solutions. Depending on the pH value of the solution the equilibrium can be shifted towards ammonia or ammonium. In our samples we suspect an acidic environment, since protons are produced on the CE. To shift the equilibrium towards ammonia, alkaline hypoclorite solution is added. The hypochlorite reacts with the ammonia to monochloroamin as seen in (3.19). Afterwards, a phenol nitroprusside solution is added, where the nitroprusside acts as a catalyst for the phenol and monochloroamin to react and form a C–N bond. The resulting compound will react with another phenol molecule to finally form the indophenol dye seen in (3.21), which is present in its anionic form in alkaline media.

The quantitative conversion of ammonia to indophenol is the precondition to determine the concentration via UV-Vis. The relationship between concentration and absorption intensity was discovered by Pierre Bouguer [85] and Johann Heinrich Lambert [86] and described in the Lambert-Beer law seen in (3.22) [87]:

$$E_\lambda = log_{10}\left(\frac{I_0}{I}\right) = \varepsilon_\lambda \cdot c \cdot d \tag{3.22}$$

The extinction E_λ is defined as the logarithm of the intensity of the light source I_0 versus the transmitted light I, which is equal to the extinction coefficient ε_λ times the concentration c and thickness of the solution d. The relation is limited mostly by chemical and instrumental factors and holds best at low concentrations or at absorbance ranges between 0.2 – 0.5. At higher concentrations the analyte will have inter-molecular interactions, which influence the band structure and therefore the absorption behavior, making the relationship between absorbance and concentration not linear anymore. Even with considering all chemical and technical influences, there are still phenomena that can not be explained by the law. In samples which are reflective, constructive and destructive interference could take place that convolute the intensity measurement [88]. Hence, the Lambert Beer law can be a strong tool in optical spectroscopy, but one has to be careful with the limitations.

A calibration is usually required to obtain the extinction coefficient ε_λ. To make a calibration curve for our non-aqueous samples we developed a procedure that is stated in detail in [40, 89]. We have made this procedure to ensure that the calibration is as close as possible to the way we actually measure our samples. In short, we prepare standard solutions of different ammonia contents in a solvent that represents our electrolyte (in this case 0.2 M $LiClO_4$ in THF). Then we acidify the samples to trap all ammonia in form of ammonium and evaporate the THF in a water bath at 60°C until only salt residue is left. Afterwards, we add 2 mL of water, and 0.5 mL of each akaline hypochlorite and phenol nitroprusside. Then we let the indophenol color develop for 30 min in the dark before measuring the UV-Vis spectra. This is the same procedure we follow when measuring actual experimental samples. The UV-Vis spectra of the calibration with the calibration curve is seen in Fig. 3.13. The y-axis of the calibration curve does not represent the peak absorbance of the UV-Vis spectra, but the peak minus the absorbance at 860 nm. This is to account for the background that might be different from experiment to experiment. Some of our electrolytes after reaction are turbid or have a slight color change because of decomposition products from the counter electrode. These compounds will shift the UV-Vis spectra upwards, which makes the measurement of ammonia unprecise.

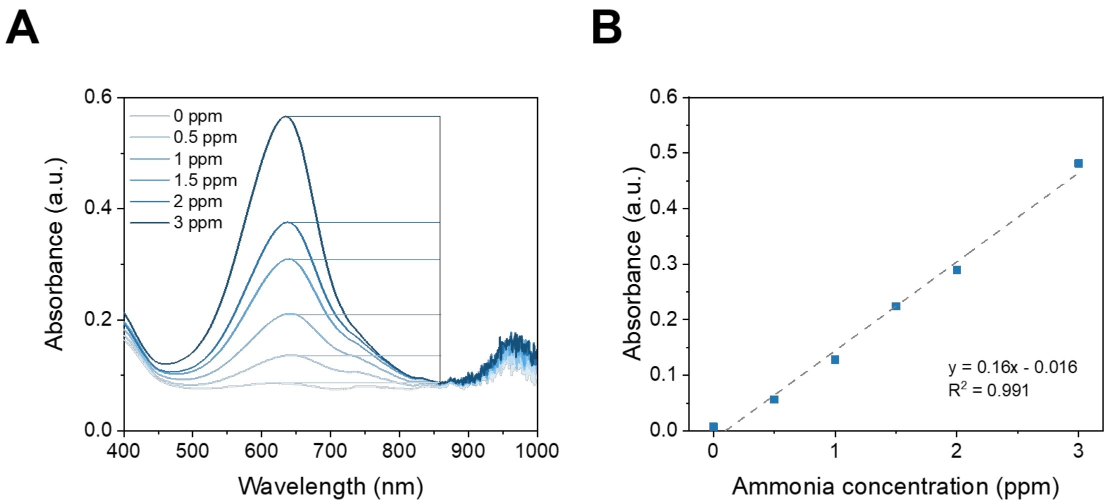

Figure 3.13: Calibration of ammonia from non-aqueous solution by Indophenol method. **A** UV-Vis spectra of the calibration solutions. **B** Calibration curve of ammonia from non-aqueous solution.

Even with this countermeasure, ammonia detection might be questionable due to drifts in the UV-Vis itself or different batches of indophenol reagents. A method to mitigate these issues is by standard addition. This was used in literature to detect ammonia by Suryanto et al. [55]. To measure the ammonia content of you sample c_0, several samples are taken and to all except one an increasing amount of ammonia c_a is added. Then the absorbance is plotted versus the added amount of ammonia, as seen in Fig. 3.14.

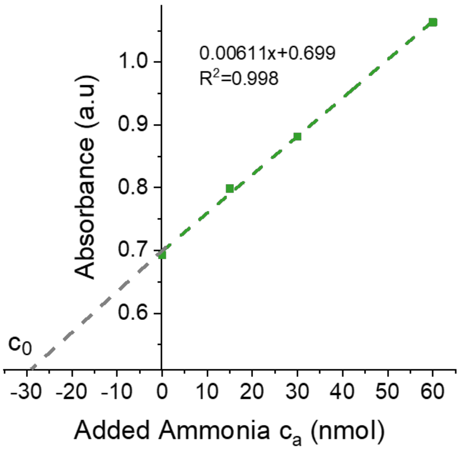

Figure 3.14: Standard addition method for ammonia detection with UV-Vis.

The intercept with the x-axis is the unknown ammonia content of your sample c_0 and can be determined by the slope m and intercept with the y-axis b, as seen in 3.23. The error s_c can be calculated by error propagation from the error of b (s_b) and m (s_m), which are obtained from linear regression.

$$c_0 = -\frac{b}{m} \tag{3.23}$$

$$s_c = \sqrt{c_x^2 \cdot \left(\frac{s_b}{b}\right)^2 c_x^2 \cdot \left(\frac{s_m}{m}\right)^2} \tag{3.24}$$

The big advantage of the standard addition method is that it takes into account fluctuations from the UV-Vis equipment, the indophenol reagents and most importantly the electrolyte itself. Different reaction conditions like salt concentration or decomposition might influence the formation of the indophenol dye. This makes the standard addition method much more trustworthy than a simple calibration curve.

To test the performance of the standard addition method in our non-aqueous system, two measurements were performed. One, with a sample of known ammonia content of 120 nmol and one with a sample from an actual experiment of unknown ammonia content. Both should ideally give the same slope. The results of the UV-Vis measurements and the relative error from the calibration measurement are shown in Fig. 3.15 and Table 3.1, respectively.

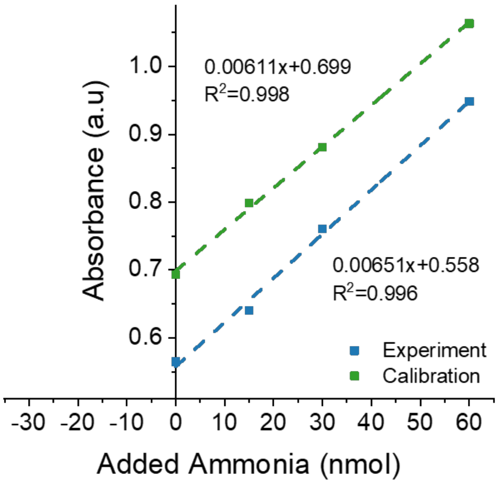

Figure 3.15: Implementation of standard addition method to the Indophenol measurement. The green curve is a measurement performed only with known calibration liquids, whereas the blue curve is a measurement of an actual unknown concentration of an experiment.

Table 3.1: Relative error of standard addition method.

Added ammonia [nmol]	Measured Ammonia [nmol]	Rel. Error [%]
120	114 ± 0.003	6

As seen in n Fig. 3.15, the slope of both measurements vary slightly from each other. This might be due to the influence of the electrolyte residuals like Li^+ ions and decomposition products from THF. In fact, it was observed in literature before that metal cations as well as organic solvents have an effect on the indophenol measurement [90]. In this study the authors also investigated the performance of the indophenol method by measuring calibration liquids in a vast range of concentrations.

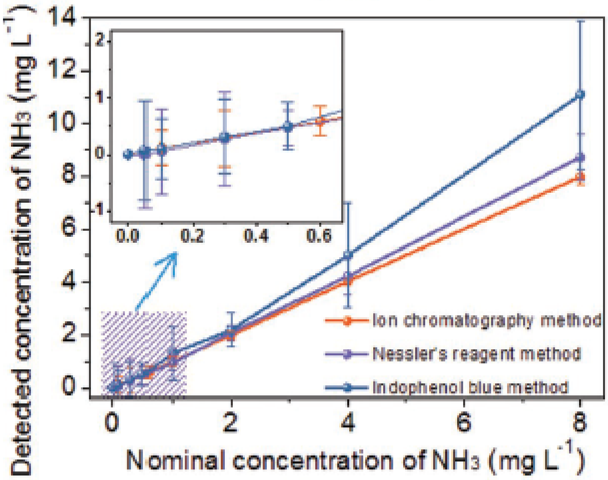

Figure 3.16: Performance of indophenol method for detection of ammonia and comparison to Nessler method and ion chromatography [90].

The data in Fig. 3.16 shows clearly that indophenol is only accurate in a small concentration window of around 0.5 - 2 ppm. All these facts, and the relative high error seen in Table 3.1 lead to the conclusion that the detection of ammonia via the indophenol method is not the most robust and has to be used carefully.

3.3.2 Ion Chromatography

Another way to quantify ammonia, or in this case ammonium, is through IC. As already seen in Fig. 3.16 the IC is more accurate than the indophenol method in a wider concentration range. The schematic of a typical ion chromatograph is shown in Fig. 3.17.

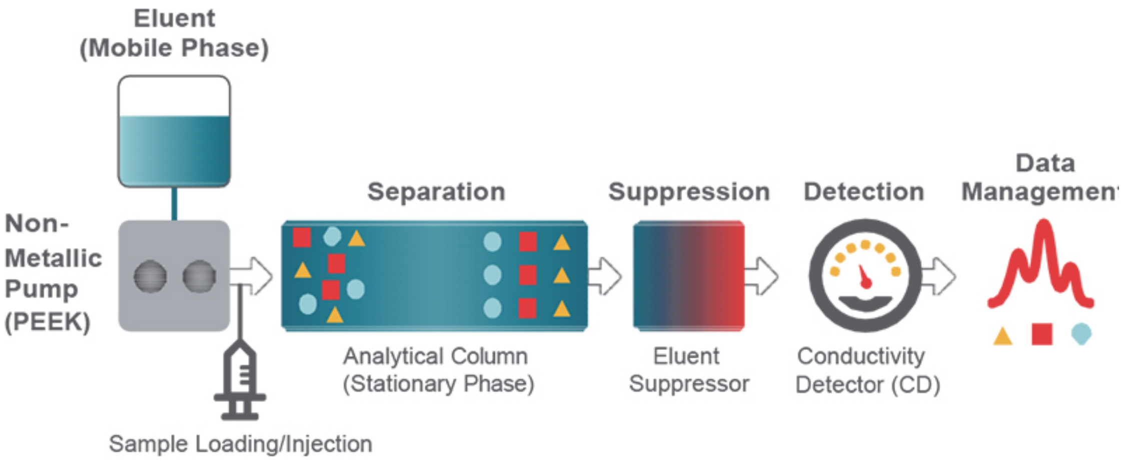

Figure 3.17: Schematic of a typical ion chromatograph [91].

Chromatography in general describes a separation method where the substance of interest is carried in a mobile phase and separated in a stationary phase. Examples of methods include gas-chromatography, high performance liquid chromatography, thin-layer chromatography and ion chromatography [92]. IC was first introduced by Small *et al*. in 1975 [93] and has since then become an important method in analytic chemistry to separate ions. The component responsible for the separation is the stationary phase, or column in IC, due to different strength of adsorption and hence time of desorption of the analytes. Therefore, it is important to chose the right column for the substances that one needs to separate. In our case we were interested in ammonium, which is a cation that is why we chose a cation-exchange column with carboxyl groups and particle size of 5 µm (Metrohm, Metrosep C6 6.1051.XX0). This column has a high resolution to distinguish between ammonium, lithium and sodium ions. As is seen from Fig. 3.17, the sample is carried by the eluent, in our case 3.3 mM HNO_3 with 10 vol.% acetone. After the separation in the column, the solvent signal is suppressed and the detection of the separated ions are conducted in a conductivity detector. Finally, the chromatogram is given as conductivity versus time.

Since the IC and the column was optimized for aqueous samples, it was necessary to check if our organic solvent THF will have an influence on the measurement. For that, an aqueous 10 ppm solution of ammonium was tested without THF and with 10 vol.% added THF. The effect of THF was clearly visible as shown in Fig. 3.18 **A**. THF causes a upward shift of the whole chromatogram, causing the ammonia peak at 7.9 min to become unreliable. To solve this issue an organic solvent can be added to the eluent, which helps to flush out THF more quickly from the column. As seen in Fig. 3.18 **B** the addition of 10 vol.% acetone helped to diminish the effect of THF.

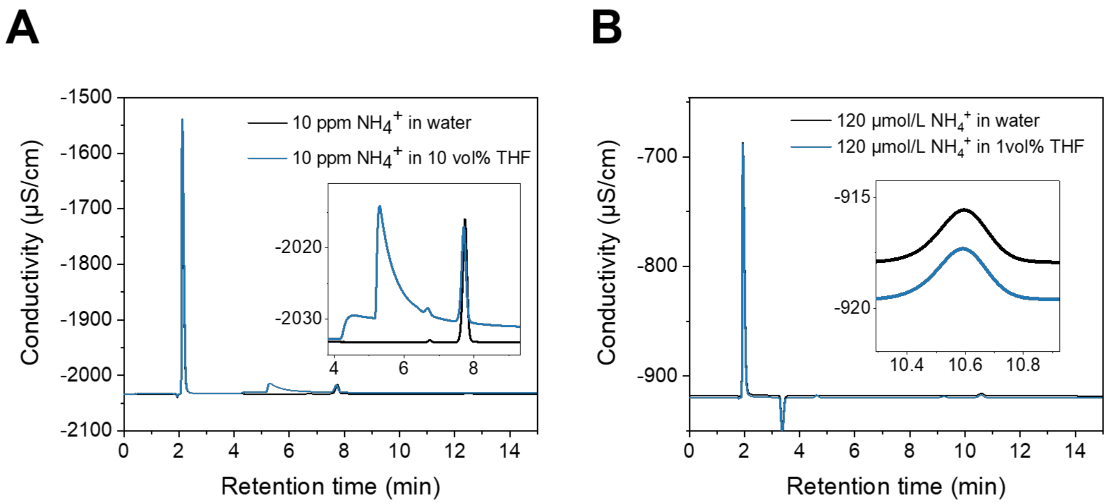

Figure 3.18: Effect of eluent on ammonia signal. **A** Influence of THF on the chromatogram with a 3.3 mM HNO_3 eluent. **B** Influence of THF on the chromatogram with a 3.3 mM HNO_3, 10 vol.% acetone eluent.

With the optimized eluent, an aqueous calibration of ammonia was performed, with the results shown in Fig. 3.19. The calibration curve in Fig. 3.19 **B** is obtained by integrating the peaks of the chromatogram and plotting it versus the known ammonium content. As seen from the R^2 factor, the IC gives very accurate data in aqueous solutions. To confirm that the calibration curve is always accurate, a standard solution of ammonium should be tested regularity about once a month.

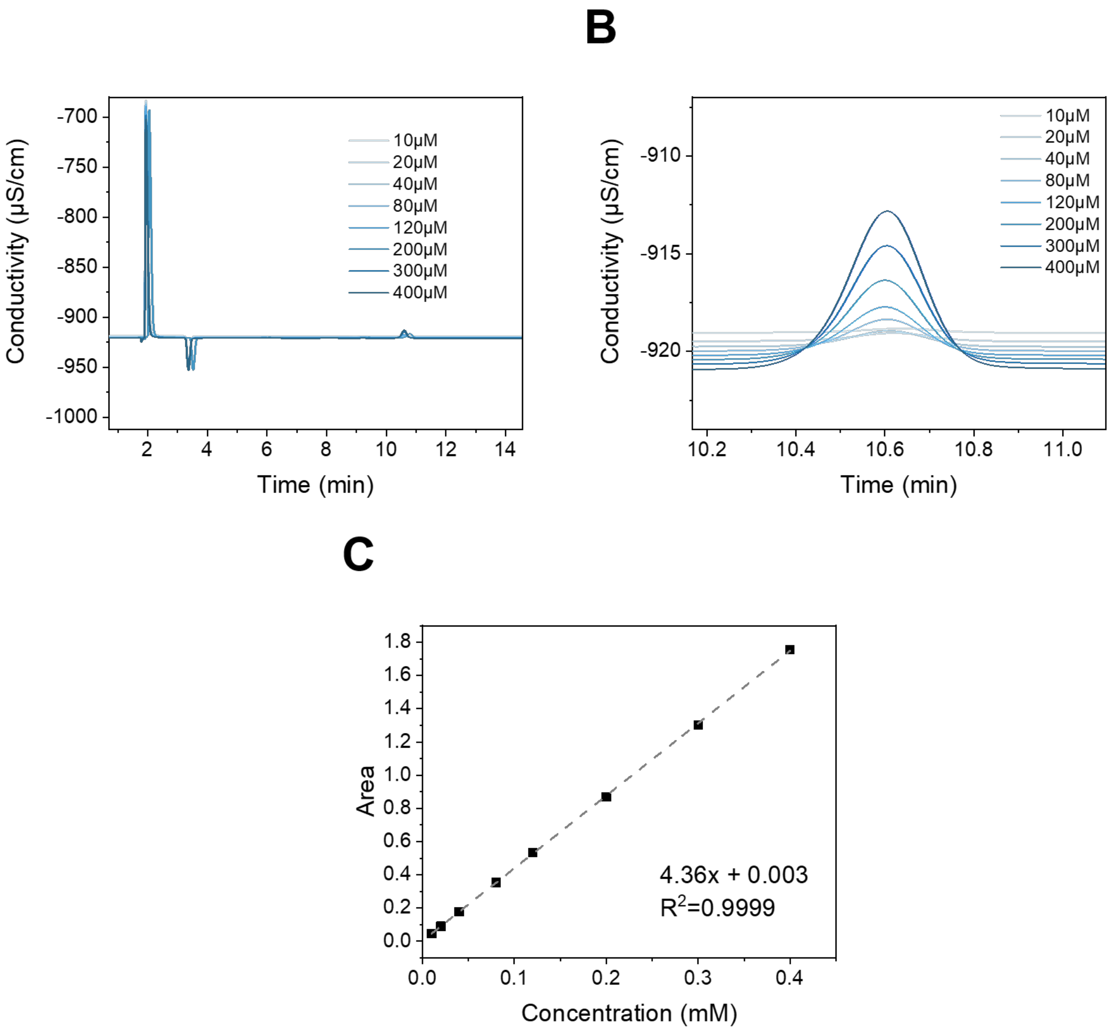

Figure 3.19: Calibration of ammonium in aqueous solution by ion chromatography. **A** Chromatogram of the calibration with the insert on the ammonium peak in **B**. **C** Calibration curve of ammonium in aqueous solution.

Before we were able to use the IC for ammonium detection in our system we have to make sure that the IC measures accurately in our non-aqueous electrolytes. Our standard electrolytes are typically a THF based electrolyte with 0.3-1M Li salt concentration. Therefore, we needed to analyse the effect of both THF and Li salt on the ammonium measurement. For that we prepared an aqueous ammonium stock solution with the concentration of 120 µM (Stock), a solution A (0.1 mL THF + 9.9 mL Stock) and solution B (1 mL 1 M $LiBF_4$ in THF + 9 mL Stock). Then different amounts of A and B were added into Stock and the measured area compared to the expected area of ammonium calculated with the calibration curve in Fig. 3.19 **C**. The exact procedure is listed in Table 3.2 and 3.3 and the results are shown in Fig. 3.20.

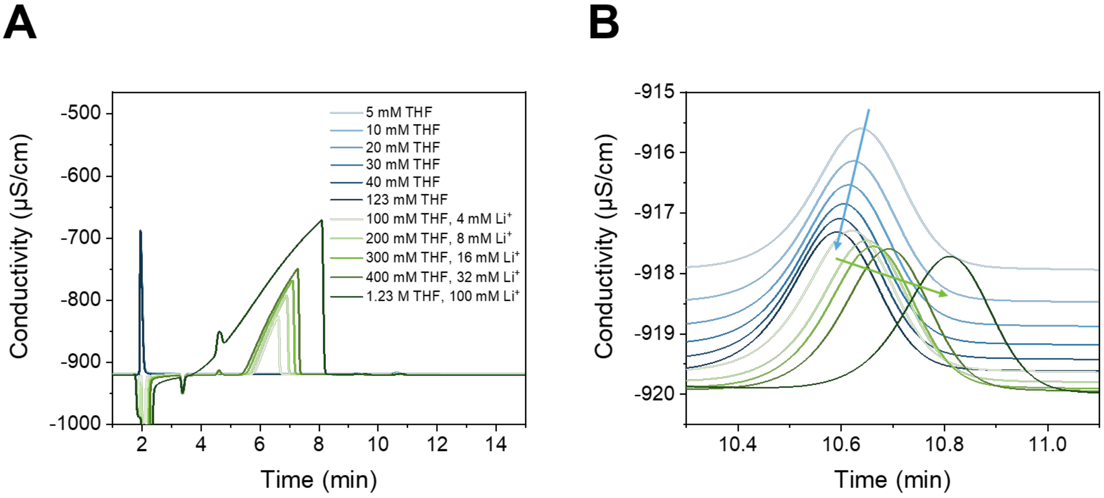

Figure 3.20: Calibration of ammonium in non-aqueous solution by ion chromatography. **A** Chromatogramm of the calibration with the insert on the ammonium peak in **B**. The effect of THF (blue) and Li-salt (green) on the chromatogramm are analyzed.

Table 3.2: Relative error of addition of THF into the IC sample.

Added Stock [mL]	Added A [mL]	Expected area	Measured area	Rel. Error [%]
4.8	0.2	0.518	0.517	0.2
4.6	0.4	0.518	0.515	0.5
4.2	0.81	0.517	0.513	0.8
3.8	1.22	0.517	0.513	0.7
3.4	1.62	0.516	0.512	0.8
0	5	0.513	0.506	1.3

Table 3.3: Relative error of addition of THF and Li salt into the IC sample.

Added Stock [mL]	Added B [mL]	Expected area	Measured area	Rel. Error [%]
4.6	0.40	0.514	0.509	1
4.2	0.81	0.510	0.503	1.3
3.8	1.22	0.505	0.502	0.7
3.4	1.62	0.501	0.497	0.9
0	5	0.466	0.469	-0.6

The blue lines in Fig. 3.20 show the effect of THF on the ammonium measurement. It is seen that increasing amounts of THF shifts the ammonium peak slightly to earlier retention times but the area stays the same, with the relative errors shown in Table 3.2. The effect of Li-salt in addition to THF is seen in the green lines in Fig. 3.20. A big peak due to Li^+ is seen around 6 min, which however does not interfere with out ammonium peak at 10.6 min. The detail chromatogram in Fig. 3.20 **B** shown that the increasing Li^+ content shifts the ammonium peak to more positive retention times, but does not influence the area. In conclusion, these results confirm that we can measure our non-aqueous samples as long as they are diluted by a factor of 10 or more.

3.4 Characterization Methods

Several characterization techniques were used throughout the thesis, most of which were for the *ex-situ* characterization of the electrode after reaction to identify the deposition and SEI layer. It must be noted here that the SEI layer can only be correctly characterized *in-situ*, since it will already change once the applied current or potential has stopped. However, because during the duration of the PhD it was not feasible to do *in-situ* experiments, several air and water free characterization methods were applied to gain information about the SEI layer.

3.4.1 X-ray Photoelectron Spectroscopy (XPS)

X-ray Photoelectron Spectroscopy (XPS) is a technique that can identify and quantify the elements and chemical states thereof in a sample, with the exception of H and He. It is based on the photoelectric effect, which describes the emission of photo-electrons upon radiation. During the measurement the sample is hit with X-rays of a known energy (E_{ph}), which remove electrons out of the different orbitals of the elements, whose kinetic energy (E_{kin}) is then measured. When accounting for the instrument specific work function ϕ, the element specific binding energies E_{bin} can be calculated as follows [94]:

$$E_{bin} = E_{ph} - E_{kin} - \phi \tag{3.25}$$

The measurement must take place in ultra high vacuum (UHV) since otherwise the electrons could not travel to the detector. This is also the reason why this method is so surface sensitive (< 2nm), since only the electrons emitted from the topmost layers can reach the detector [95]. Not only is this method able to determine the elemental composition of the sample, it can also give information about the neighboring elements and oxidation state through the shift in E_{bin}. The binding energies of the electrons will shift to higher values if close to a more electro-negative element or with increasing oxidation state and vice versa. The sensitivity is highly dependent on the cross section of the specific element, which generally increases with atom number. Overall, the detection limits are around the ppt - ppm levels and can be tuned by changing the measurement conditions such as dwell time or scan number.

In this work XPS was used to characterize the composition of the SEI layer and electrode deposit through an air and moisture free transfer arm. Furthermore, the purity of electrodeposited porous Cu electrodes was checked with this method.

3.4.2 X-ray Diffraction (XRD)

X-ray diffraction can qualify crystalline phases through identification of their crystal structures and lattice parameters. In this measurement X-rays with wavelength of λ are irradiated upon the sample and scattered elastically. Only if the Bragg equation in (3.26) is fulfilled will the X-rays interfere constructively, which will lead to a detectable signal:

$$n\lambda = 2d \cdot sin\Theta \tag{3.26}$$

The Bragg equation is visually depicted in Fig. 3.21.

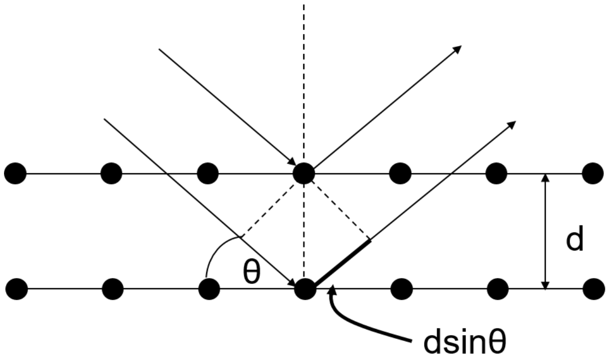

Figure 3.21: Schematic of constructive interference of X-rays according to Braggs law.

Since this method is based on the periodicity of the lattice, only crystalline samples will give sharp peaks. The peak position (in θ) can then be used to calculate the lattice spacing d, which is characteristic for different materials. In addition to the different crystal phases in a sample, the crystal size L can also be determined through the width (β) of the reflections. This relation is governed by the Scherrer equation [96]:

$$L = \frac{K\lambda}{\beta cos\Theta} \tag{3.27}$$

K is a constant that is often set as 1 [95]. From the Scherrer equation it is clear that smaller crystals give wider peaks and vice versa. This method is a good approximation of crystal size, however should be confirmed with other methods.

Similar with the XPS, XRD was used to identify species in the SEI layer and deposit of the WE after reaction without exposure to air and moisture. Since XPS can determine elemental composition and XRD can characterize crystal phases these measurements are complimentary.

3.4.3 Scanning Electron Microscopy - Energy Dispersive X-ray Spectroscopy (SEM-EDX)

In scanning electron microscopy (SEM) the morphology of a conductive sample can be investigated through irradiation with an electron beam of typically 1-30 keV which gives a depth resolution in the nm - µm regime [97]. The interaction of the electron beam with the sample and the resulting detectable signals is seen in Fig. 3.22.

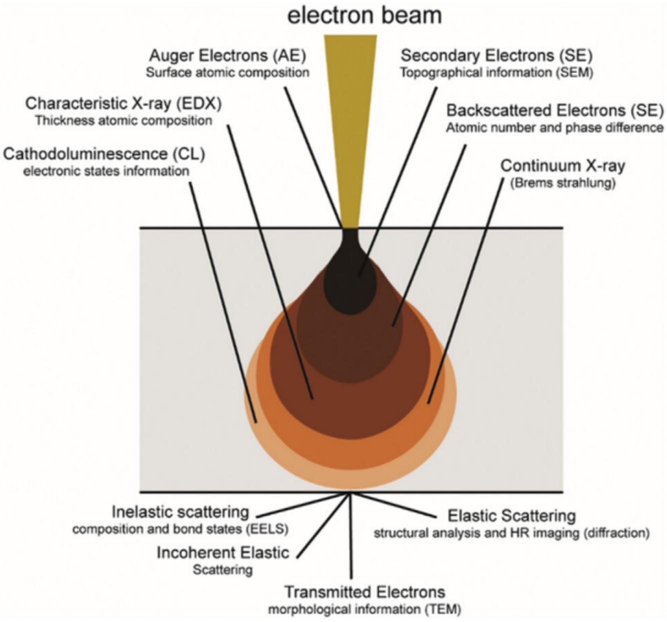

Figure 3.22: Interaction of an electron beam with a sample and the resulting detectable signals. [97]

The microscope can either be run in secondary electron (SE) or backscattered electron (BSE) mode. The first gives topographical information since the detected electrons come from the surface region of the sample, whereas the latter contains information about the atomic number, since heavier atoms scatter more efficiently and appear therefore brighter. The resolution of both lie in the low nm regime [95]. Additionally, information about the elemental composition of the sample can be gained though detection of the characteristic X-rays in the energy dispersive X-ray (EDX) mode. There the incoming electrons will excite an electron sitting in the inner shell of an element. The resulting hole will then be filled with electrons from outer shells and during the process X-rays with characteristic energies are released [98].

To check the morphologies of the high surface area electrodes, SEM was applied in this work. Moreover, the degree of deposition coverage was confirmed by EDX.

3.4.4 Quadrupol Mass Spectrometry (QMS)

A quadropol mass spectrometer analyses the mass of the incoming charged species through separation of their $\frac{m}{z}$ ratio. It can also be coupled to a chromatogram, where the sample is already separated, like in a GC-MS. A schematic setup of a QMS analyzer is shown in Fig. 3.23. The mass selecting component is the quadrupole, which is made out of four cylindrical metal rods. The rods opposite to each other are electrically connected, in which one pair is connected to a positive direct voltage source U and the other pair to a negative one. In addition, a modulated high-frequency potential $V_0 \cdot cos\omega t$ is applied to each pair. If the ions enter the quadrupole along the z-axis they start to oscillate in the x- and y-directions. Depending on the applied potentials only ions with a certain $\frac{m}{z}$ ratio can reach the detector, whereas the other ions are screened out. [99]

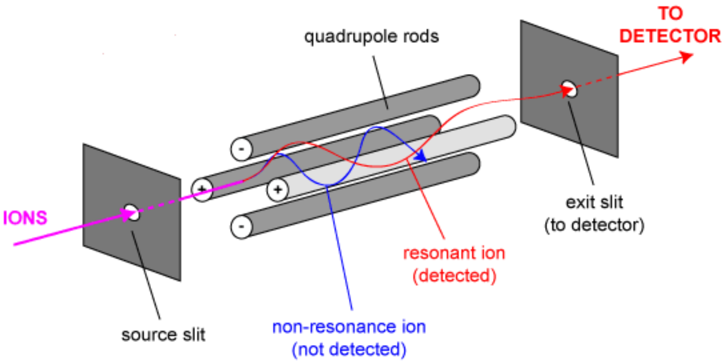

Figure 3.23: Schematic setup of a quadrupole mass analyzer. [100]

The total ion current represents the amount of ions detected across the entire range of masses at each time. The additional information of the nature of the components are gained from the mass spectra, which shows the intensity of the ions of different $\frac{m}{z}$ ratio. Each component showcases an unique fragmentation pattern, which is used to identify the substance. Most analysis softwares contain a database with which it is possible to compare the recorded spectra with and therefore obtain the information about the nature of one analyte.

The QMS was used in two different ways in this thesis. For once a QMS was attached to the autoclave setup described in section 3.1 to analyse the gas composition. Additionally, a QMS was attached to a GC to determine the organic decomposition products in the electrolyte after reaction.

4 Effect of Oxygen on the Li-mediated Ammonia Synthesis

Small amounts of O_2 and H_2O are detrimental for the industrial Haber-Bosch synthesis as it poisons the catalyst [27]. To investigate the effect of O_2 in our LiMEAS system, small amounts of O_2 were added in the gas feed of the autoclave setup and the exact concentration was measured with a MS. This chapter will discuss the extraordinary finding that little amounts of O_2 in the gas feed is increasing the FE of the process. This is very counter-intuitive, since one would think that O_2 will decrease the FE by forming Li_2O or by inducing oxygen reduction reaction (ORR). The whole study on the effect on O_2 lead to two published works, namely Paper 1 [101] and Paper 4 [70], which will be discussed in this chapter. Paper 1 was a collaboration between several people in the ammonia team, but I want to highlight the contribution of Suzanne, who saw this effect initially and did the experimental work together with me, and Mattia, who helped with designing the set-up and doing the air free XPS measurements. Moreover, I want to emphasize the contribution of the theory collaborators Michael, Vanessa and Yuanyuan, whose data were essential on explaining the effect of O_2.

The second publication was lead by Rokas, who evaluated the effect of O_2 on the decomposition products of the electrolyte, which can be seen as a follow up to the previous publication of decomposition without O_2 in different solvents [60]. The following sections will firstly cover all the information that was published in Paper 1 [101] and then discuss the results from Paper 4 [70].

4.1 Effect of Oxygen on the Faradaic Efficiency

All experiments were conducted in the autoclave at 10 or 20 bar reaction pressure with the gas mixing setup previously shown in 3.1. The WE used was a Mo foil of 1.8 cm^2 with a Pt mesh CE and Pt wire RE. 0.3 M $LiClO_4$ with 0.17 M EtOH in THF was used as a electrolyte and the applied current was $-4\,mA/cm^2$ until 50 C were reached or the cell potential exceeded the limit of the potentiostat. For a more detailed description of the experimental procedure please see the supplementary information of Paper 1 [101], which is given in the Appendix B.2. Fig.

4.1 shows the resulting FE as function of molar O_2 content X_{O2} and O_2 partial pressure p_{O2} that were calculated as follows:

$$\mathrm{X_{O2}} = \frac{\mathrm{I_{O2}}}{\mathrm{I_{O2}} + \mathrm{I_{N2}}} \tag{4.1}$$

$$\mathrm{p_{O2}} = \mathrm{X_{O2}} \cdot \mathrm{p_{tot}} \tag{4.2}$$

with I_{O2} and I_{N2} being the ion currents of the MS of mass 32 and 28, respectively and p_{tot} being the total reaction pressure of either 10 or 20 bar.

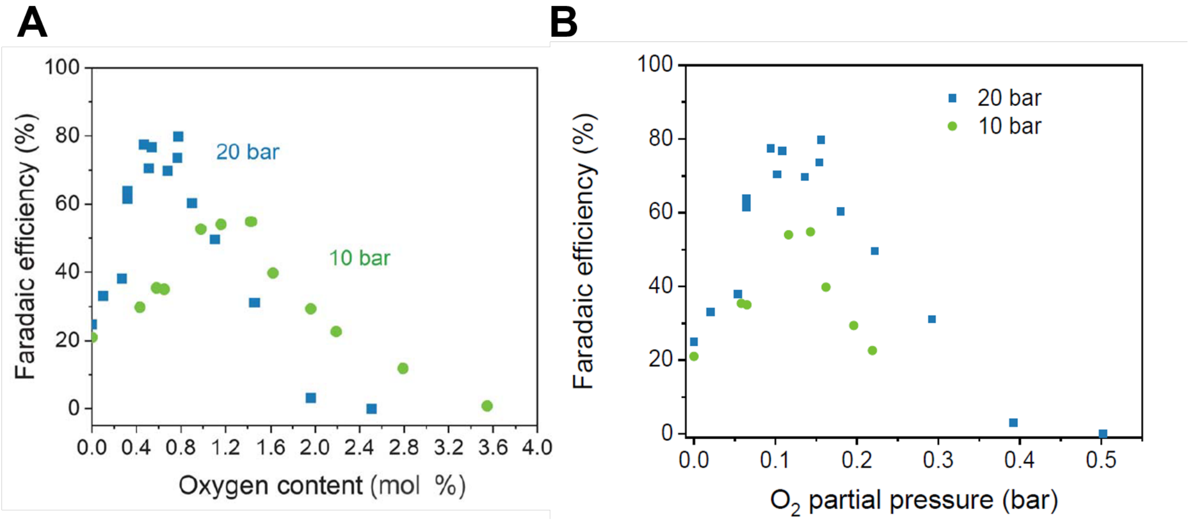

Figure 4.1: Effect of **A** molar oxygen content **B** oxygen partial pressure on the faradaic efficiency of LiMEAS at 10 and 20 bar. Data from Paper 1 [101].

It is clearly visible that small amounts of O_2 have a largely positive impact on the FE at both pressures. The optimum at 20 bar lies around 0.7 - 0.8 mol % and at around twice that value for the experiments at 10 bar. If plotted against the partial pressure, the optimum O_2 content aligns for both reaction pressures at around 0.15 bar. This shows that the concentration of O_2 is more important to determine the optimum O_2 content rather than the molar ratio. Moreover, the highest achievable FE is higher at 20 bar at around 78 ± 1.3 %, whereas at 10 bar it is lower at 53.8 ± 1.1 %, most likely due to N_2 mass transport limitations. This leads to a maximum EE of 11.7 ± 0.5 % at 20 bar.

After the peak, the FE drops rapidly until it reaches 0 % which is in accordance with earlier work by Tsuneto et al., where they observed 0 % FE when using synthetic air (20 % O_2) at 50 bar [52].

4.2 Effect of Oxygen on the Stability

Additionally to the positive effect of O_2 on the FE, it also exhibits an influence on the overall stability of the system. It is well established that the LiMEAS is unstable due to the overloading of the WE potential over time [56, 62]. It is hypothesized that this destabilization is caused by rapid and uncontrolled Li plating on the WE, which leads to a larger amount of reactive Li being plated than N_2 is available. This favors Li to react with other molecules, like THF or EtOH to form passivating side products, which then lead to these immensely negative potentials [62]. Hence, balancing the Li deposition rate with the incoming rate of N_2 and H^+ is a key factor for the success of LiMEAS. This will be later discussed in more detail.

As seen in Fig. 4.2 **A**, the WE without O_2 starts to destabilize immediately and decreases by 10 V after 20 min of operation. Since the CE potential stays quite stable, independent from the O_2 content, only one representative line for the CE potential is shown in Fig. 4.2 **A**. To better quantify the stability we came up with the measure of t_{stable}, which is defined as the time where the WE potential remains within 1 V of the starting potential. The relation between t_{stable} and molar O_2 content is given in Fig. 4.2 **B**.

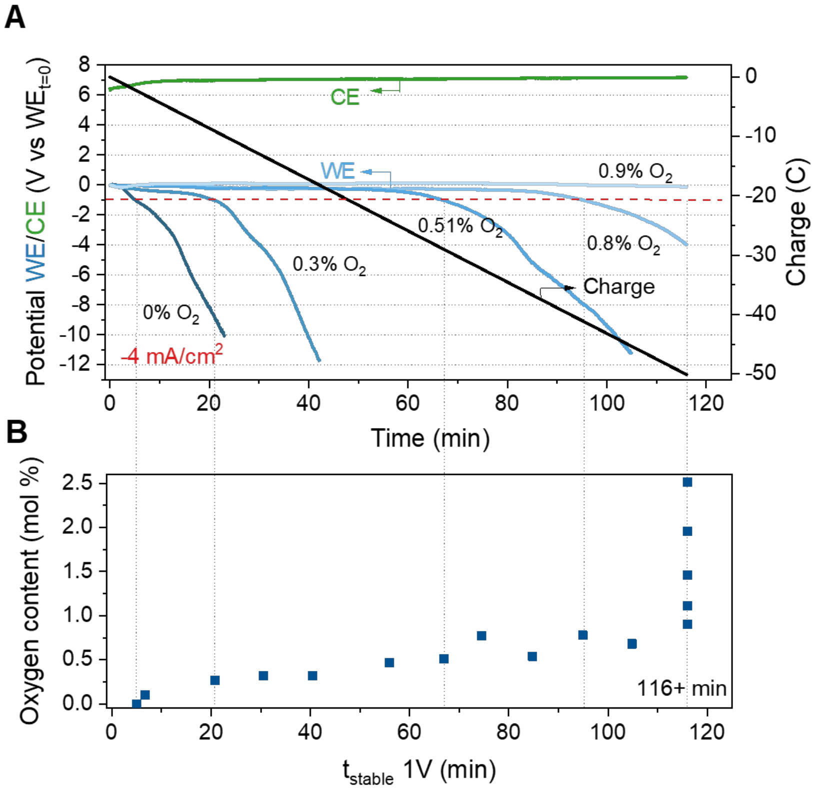

Figure 4.2: Effect of O_2 on the **A** WE potential and **B** t_{stable} at 20 bar. Data from Paper 1 [101].

A clear linear trend can be observed between stability and O_2 content with all the experiments being stable over 0.9 mol % O_2, which is why those points are summarized in t_{stable} 116+ min.

Therefore, it can be concluded that O_2 must play a role in on the WE and more specifically make the Li on the WE more stable against decomposition to passivating substances.
It should be noted here that the word stable is used in a relative sense. Since the experiments only lasted for 116 min, we have no way of predicting the long time stability (days). However, a previous published cycling strategy, where the Li was plated for 1 min, followed by a 3 min resting phase at OCV achieved stability over days and was also applied to our system with added O_2. The details will be shown below in section 4.4.

4.3 Importance of correct gas mixing

As the whole study depends on the correct measure of O_2 content, a large emphasis needs to be put on the correct gas mixing and measuring procedure. At the beginning of the study we did not have the MFC setup and solely relied on the MS to get the correct O_2 content. To fill in the gas in that case, purified 6.0 N_2 was used to pump and purge the autoclave 10 times, to remove all residual air. Then the reactor was filled again with 6.0 N_2 to a certain pressure and topped off with synthetic air (20 % O_2 in N_2) to reaction pressure to achieve the desired O_2 content that was determined by the MS after 20 min of equilibration time. With the MFC setup the procedure stays the same with the only difference that the pump and purge process was already done with the correct N_2 / O_2 gas mixture instead of pure N_2 and also filled to reaction pressure with that mixture. This, in theory should allow a homogeneous distribution of O_2 in N_2 not only in the gas phase but also in the electrolyte phase, whereas the "incorrect" mixing without MFC would lead to a relatively higher amount of N_2 being dissolved in the electrolyte than O_2.

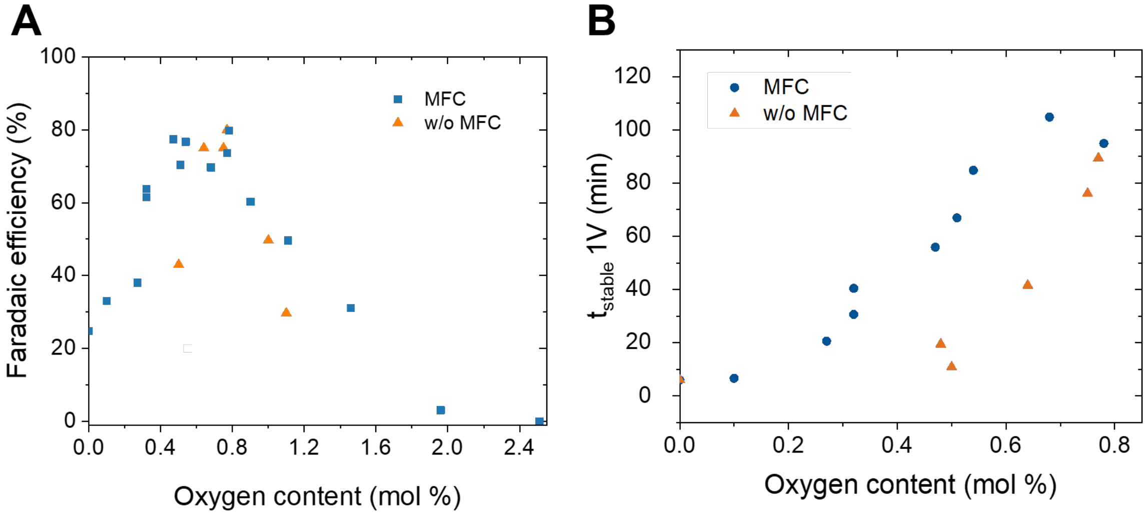

Figure 4.3: Effect of correct gas mixing with mass flow controllers on the FE **A** and t_{stable} **B**. Data from Paper 1 [101].

To compare the differences between these two procedures, Fig. 4.3 shows the effect of gas mixing with and without MFC on the FE and t_{stable}. It seems like the difference in gas mixing did not have a huge influence on the obtained FE. This could be caused by the fact that during the duration of the experiment the O_2 is being distributed homogenously in the electrolyte, aided by the stirrer induced mass transport. However, a bigger difference is seen in Fig. 4.3 **B** in the t_{stable} with and without MFC. The WE potential seems less stable at similar measured O_2 contents in the gas phase, suggesting that the O_2 in the electrolyte phase is less than in the gas phase in the case of incorrect gas mixing, due to the reasons given above. Therefore, it seems that t_{stable} is more dependent on the O_2 content at the beginning of the experiment in the electrolyte phase, which is a hint to the role of O_2 in the system. This will be discussed in the section regarding the role of O_2 in the system.

Even with the MFC setup it was not possible to get the exact desired O_2 contents every time. The differences between set O_2 content by the MFC and measured O_2 content by the MS is seen in Fig. 4.4 and the relative errors are given in Tab 4.1.

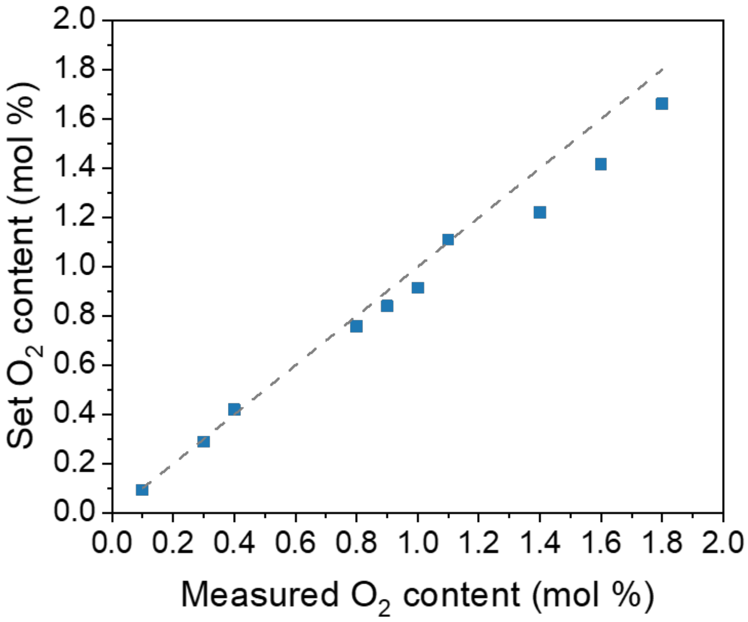

Figure 4.4: Difference between set O_2 content by MFCs and measured O_2 content by MS.

Table 4.1: Relative error of set O_2 content by MFCs and measured O_2 content by MS.

Set O_2 content [mol %]	Measured O_2 content [mol %]	Rel. Error [%]
0.1	0.09	10.00
0.3	0.29	3.33
0.4	0.42	-5.00
0.8	0.76	5.00
0.9	0.84	6.67
1.0	0.91	9.00
1.1	1.11	-0.91
1.4	1.22	12.86
1.6	1.42	11.25
1.8	1.66	7.78

There is both a negative and positive error with a trend towards larger errors at the higher oxygen content side. Due to these discrepancies it is not possible to get the exact O_2 content than what is desired, which makes reproducing the exact same experiment hard. That is why, instead of repeating the same O_2 content experiments several times, we opted to conduct several experiments in a smaller O_2 content window, especially at the optimum region.

This off-set could be due to imperfect gas mixing in the tubes, especially since the N_2 gas flow is much higher than the synthetic air flow, or due to uncertainties caused by the control box, which is an older model and might not be entirely compatible with the MFCs. Nevertheless, the measured value by the MS is deemed accurate and trustworthy and therefore used throughout the whole work. A typical MS spectrum is shown in Fig. 4.5, including the initial pump and purge process.

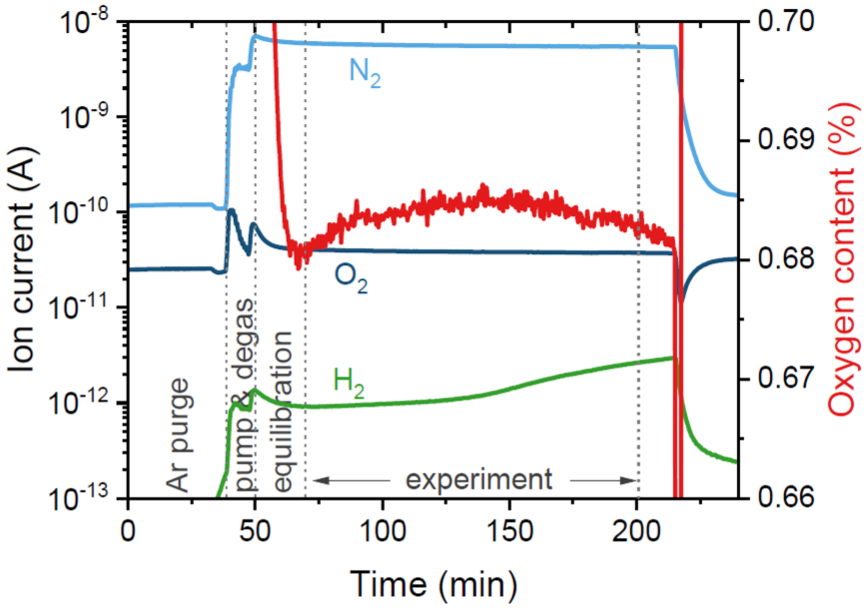

Figure 4.5: Mass spectrum of a typical O_2 enhanced LiMEAS experiment at 20 bar. Data from Paper 1 [101].

First, the autoclave containing an empty glass cell is purged with Ar to remove air. Then the electrolyte is introduced, the lid closed and the reactor is filled to 10 bar and released to 3 bar 10 times with the correct reaction gas mixture, to change out all the gas in the autoclave. Then the system is given time to equilibrate for 20 min at OCV to get a stable MS signal and the exact O_2 content is recorded at this time. During the duration of the experiment the O_2 and N_2 signals do not vary significantly and hence the O_2 content also stays constant. An increase in the H_2 is observed due to HER though the exact onset can not be determined, since the H_2 needs to diffuse though the electrolyte and to the orifice, which takes an unknown amount of time. It is proven however, that HER takes place as simultaneously to NH_3 formation. A detailed electrochemical mass-spectrometry study with high time resolution has been done by Krempl et al. [102]. The MS also does not show an NH_3 signal, since the produced NH_3 is mainly in the electrolyte phase and is dissolved as NH_4^+ due to electrolyte acidification from the counter electrode reaction [59]. To prove this further, we have released the gas for some experiments through an acid trap and measured no significant ammonia.

4.4 Explanation of the enhancing effect of Oxygen

After observing the counter-intuitive positive effect of small amounts of O_2 we have tried to reasonably explain this phenomenon. The right side of the maximum, where FE falls with increasing O_2 content is easy to explain. This could be due to two side reactions, namely ORR or Li_2O formation. Since water is formed during ORR, the water content was measured before and after reaction with a Karl-Fisher titrator and the results are plotted in Fig 4.6.

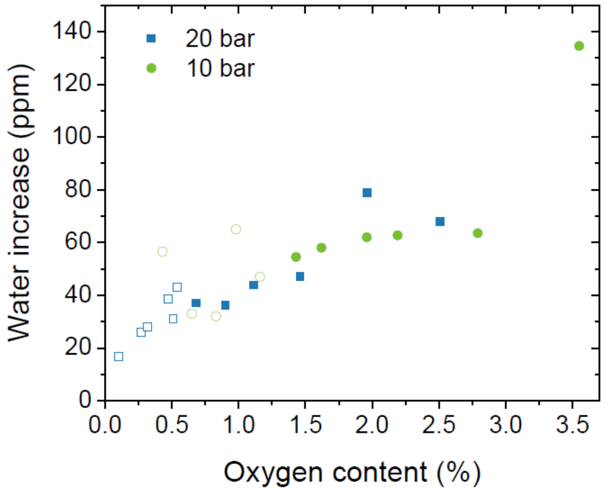

Figure 4.6: Increase of H_2O content at different oxygen concentrations at 10 and 20 bar. Data from Paper 1 [101].

Since water is also made during an experiment without added O_2, due to possible ClO_4^- reduction to ClO_3^- or other side reactions, it is important to compare the points that have run the same amount of time. The hollow points represent experiments that overloaded before reaching 50 C and hence did not run the whole 116 min. All filled points ran until 50 C and therefore the same amount of time. With these data points it is clear that there is a linear relationship between added O_2 and water increase, which can be caused by ORR and proves our first suspicion of the role of O_2 in the system. The hypothesis of Li_2O formation will be discussed in the later part of electrode characterization.

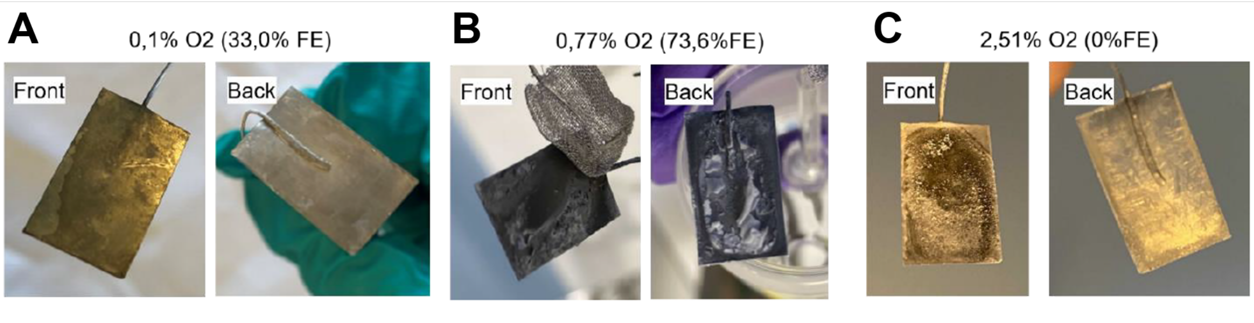

Figure 4.7: Front and back images of the Mo electrode after electrochemistry for **A** 0, **B** 0.8 and 3 mol % oxygen. Data from Paper 1 [101].

The more difficult part is to explain why small amounts of O_2 enhances the FE towards NH_3. From the previous section we already know that O_2 has an influence on the WE rather than CE and probably effects the Li deposition in making the Li more resistant to side reactions. This fact is solidified when looking at the images in Fig. 4.7, which show the front and backside of the Mo WE after electrochemistry for different O_2 contents. The front side is the side which faces the CE and the backside is the side that faces away from the CE. In Fig. 4.7 **A**, on the left side of the optimum O_2 content, little to no physical deposit can be seen on either front or backside. At the optimum O_2 content in Fig. 4.7 **B** a thick grayish deposition is observed on both sides of the electrode. And lastly, on the right side of the optimum the backside is blank again but a black deposit can be observed on the front side. These differences show clearly that O_2 has an influence on the deposition behavior of Li, making it more stable at the optimal O_2 content and most likely changing the composition completely at the higher O_2 content side.
The component that stabilizes Li towards decomposition in organic electrolytes is commonly known as solid electrolyte interphase layer (SEI) in the battery literature, which was described in chapter 2.2.2. All these above stated observations hint towards the fact that O_2 in a way influences the SEI layer in making metallic Li more stable and therefore more accessible to react with N_2, instead of participating in side reactions with the electrolyte. As the SEI layer is known to be built in the initial phase of Li deposition, our observation that O_2 content in the electrolyte in the beginning of an experiment has a huge effect also supports this hypothesis.To prove the SEI modification through addition of O_2 we consulted Li metal battery literature and found the work by Wang et al. which state that the SEI layer with O_2 forms a homogenous SEI layer that allows even and consistent Li deposition [103]. The effect is visually depicted in Fig. 4.8.

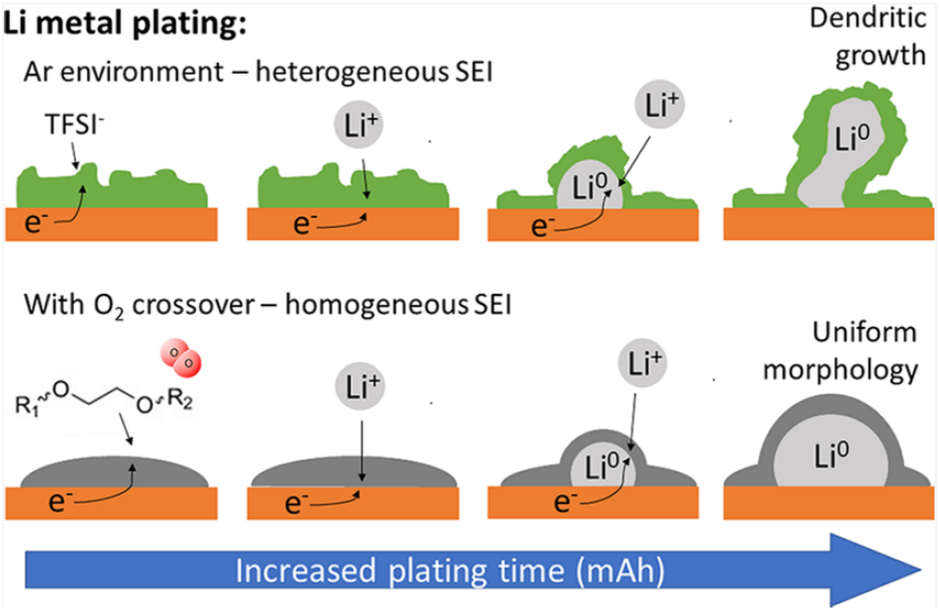

Figure 4.8: Effect of O_2 on the SEI and Li plating behavior in Li metal batteries. [103]

They observe better cycling performance of their Li-metal batteries in O_2 containing atmosphere and attribute this to a LiOH rich SEI layer. This SEI layer is responsible for having more even and less porous Li deposition, which they observed with SEM. Albeit the slight differences in electrolyte (1M LiTFSI in tetraglyme) our systems are quite comparable, having a Li salt in an ether based electrolyte, hence transferring their observations and explanations to our system is not too far-fetched. In their follow-up work, they investigated the O_2-modified SEI layer further, by putting the SEI layer in contact with the radical (2,2,6,6-Tetramethylpiperidin-1-yl)oxyl (TEMPO) [104]. Then they measured the concentration of this radical by *in-operando* electron paramagnetic resonance (EPR) spectroscopy and the decomposition products of TEMPO with *ex-situ* solid-state and solution nuclear magnetic resonance (NMR) spectroscopy. They found that the TEMPO concentration with O_2-modified SEI is more stable and shows less decomposition in comparison to a SEI layer formed under Ar. This means that the diffusion of TEMPO through the O_2-modified SEI layer is hindered or slowed down and therefore keeps the Li more protected from the electrolyte, which is in accordance to our hypothesis.

Our long time cycling experiments with added O_2 are further evidence of our theory. The cycling procedure developed by Andersen et al. [62] cycles between Li plating currents and resting phases at OCV. This improves the stability, since it avoids unwanted accumulation of highly reactant Li on the WE surface. Furthermore, it enhances the FE due to the fact that Li reacts during OCV with N_2 to form ammonia. At the same conditions as the 20 bar O_2 enhancement experiments, the cycling method improved the FE from 24.7 ± 0.5 % without cycling to 40.9 ± 2.3 % FE with cycling. We applied the same cycling procedure to two different O_2 contents and the results are shown in Fig. 4.9.

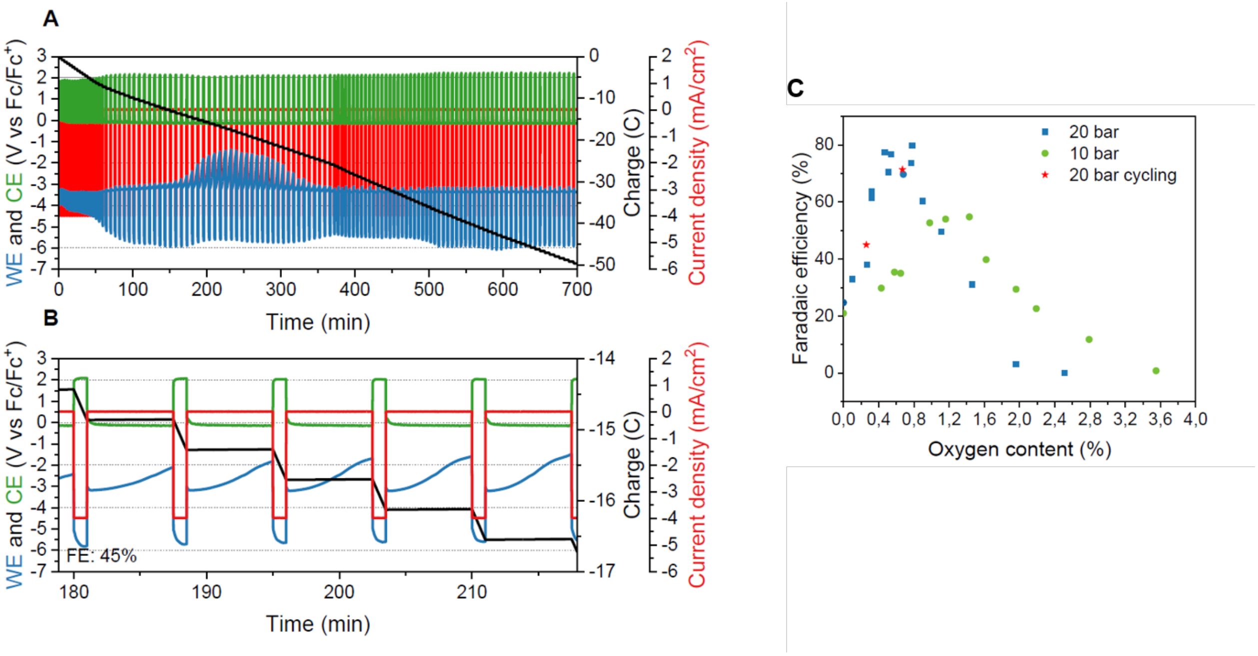

Figure 4.9: **A** Full CP and **B** insert of a cycling experiment with optimum concentration of O_2 at 20 bar. **C** Effect of cycling on the faradaic efficiency. Data from Paper 1 [101].

The CPs in Fig 4.9 **A** and **B** show that the WE potential can be kept sable for a longer period of time, but more interestingly the graph in Fig 4.9 **C** shows that the cycling method does not significantly improve the FE. This means that during the resting time the Li on the surface does not additionally react with N_2 to form more NH_3, since N_2 diffusion is likely being slowed down by the modified SEI layer.

4.4.1 Theoretical Explanation of the Effect of O_2

To further solidify our claim, our theory collaborators Michael, Vanessa and Yuanyuan applied our gained experimental knowledge to their previously established mikro-kinetic model [62]. This model assumes that the diffusion of reactants (Li^+, H^+ and N_2) to the electrode surface is rate limiting. This assumption is fair, given the fact that both electrochemical and chemical reaction steps should proceed at a higher rate, because of the highly negative potentials and reactivity of metallic Li [105, 106]. Plotting the relative diffusion rates of $\frac{r_{H+}}{Li}$ and $\frac{r_{N2}}{Li}$ as a function of the FE results in the heatmap seen in Fig. 4.10.

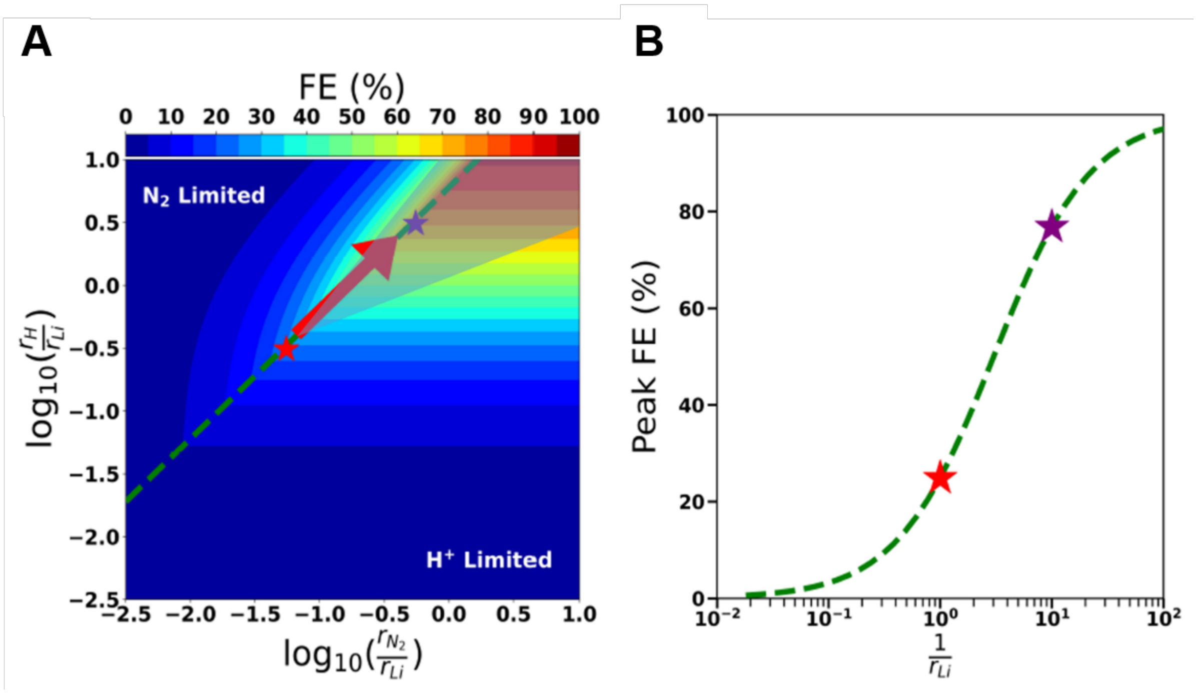

Figure 4.10: **A** Heatmap of the predicted FE as a function of the ratio of nitrogen to lithium (x-axis) and proton to lithium (y-axis) diffusion rates. **B** Faradaic efficiency dependence on Li^+ diffusion rate. Data from Paper 1 [101].

The dashed green line separates the N_2 and H^+ limited regime. In the N_2 limited regime, for example at 1 bar, decreasing the H^+ availability by reducing the concentration of the H^+ source (moving vertically down in the heatmap) or increasing the N_2 pressure (moving horizontally right) would lead to higher FE. However, the large increase in FE can not be explained by horizontal or vertical movements in the heatmap. A diagonal movement is more likely, which is shown in the shaded area, is needed to achieve a FE increase from 25 % (red star) to 80 % (purple star). This diagonal movement can only be achieved when the rate of Li^+ diffusion, r_{Li+}, is slowed down relative to the diffusion rates of H^+, r_{H+}, and N_2, r_{N2}. This conclusion again is consistent with our claim. Moreover, the heatmap also correctly predicts the observed behavior at different pressures, giving it further credibility. In the N_2 limited regime (10 bar) moving diagonally with the same slope results to lower maximum FE than at 20 bar. The maximum FE is also predicted here to be concentration or rather O_2 partial pressure dependent, since it is a competition between ORR and NRR.

4.4.2 Measuring the Oxygen Modified Solid Electrolyte Interphase

Now with our hypothesis strongly supported both by experimental results and theoretical modeling, it is necessary to also find direct prove experimentally by probing the SEI layer. As stated earlier, investigating the SEI layer is not trivial due to its water and air sensitivity, however we tried to analyze it to the best of our ability within our own facilities. The methods used here were XPS and XRD, both made as air and moisture free as possible. For the XPS investigations the reactions were performed in an autoclave that is inside the glovebox. After the reaction the WE was put inside a transfer arm that can be seen in Fig. 4.11.

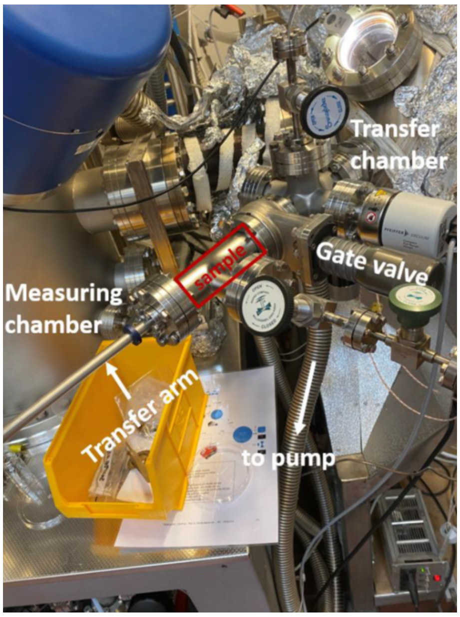

Figure 4.11: Home-built XPS transfer arm attached to the transfer chamber. Picture from Paper 1 [101].

The transfer arm with the sample was attached to the transfer chamber and then the arm was quickly pumped down to pressures below 2 · 10^{-5} mbar and introduced to the measuring chamber which had pressures below 9 · 10^{-10} mbar. Therefore, the sample only experienced Ar atmosphere or UHV. The sample was not Ar sputtered to avoid any damage of the SEI layer. In total three different O_2 conditions were investigated, below the optimum, at the optimum and above the optimum O_2 concentration. The discussion here will solely focus on the detail spectra but the whole survey spectra is provided in the Appendix B.2. The exact measurement conditions and parameters are provided in the supplementary information of Paper 1 [101], which is given in the Appendix B.2.

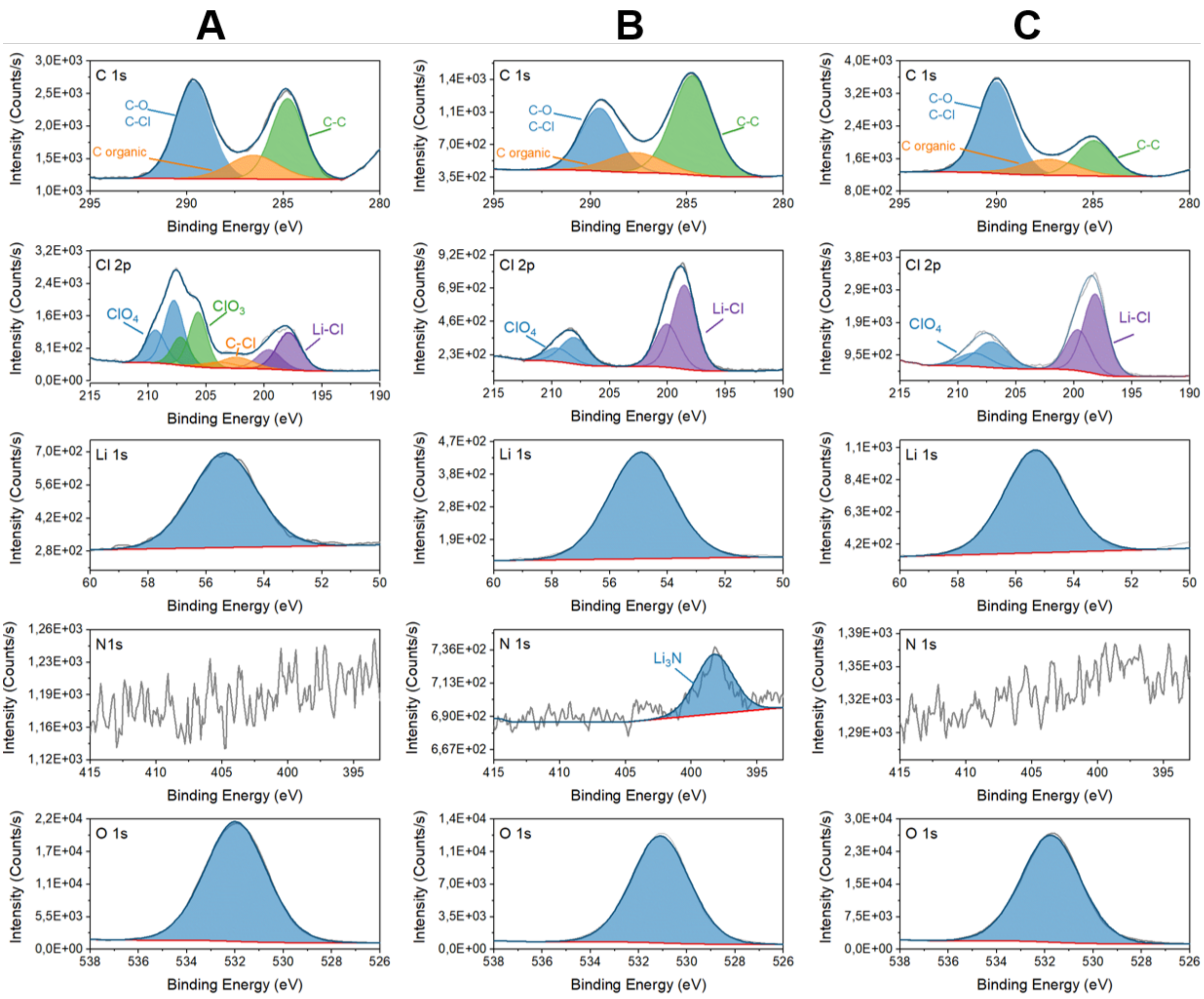

Figure 4.12: XPS detail spectra of the Mo electrode after electrochemistry for **A** 0, **B** optimum 0.8 and **C** 3 mol % oxygen at 20 bar. Data from Paper 1 [101].

The most interesting feature is seen in the N 1s spectra, where only a peak is visible in the case of optimum 0.8 mol % O_2. This aligns with the fact that we have the highest ammonia formation rate under these conditions. Due to the predicted reaction mechanism we attribute this peak to Li_3N. The peak position also corresponds well with values observed in literature

[107, 108], being shifted to lower binding energies, which hint towards metal nitrides. However, other species such as $Li_xN_yH_z$ can not be disregarded. The fact that we only see a N 1s feature in the optimum O_2 conditions shows that the reaction of Li with N_2 is more favored under these conditions. Hence, N_2 diffusion through the SEI layer might be favored compared to H^+ diffusion with this SEI layer.

The C1s spectra in all three cases looks similar, with C-C single bonds, which are partly due to adventitious C. More interestingly, the spectra shows a broad signal that belongs to organic carbon species, which might be the SEI layer or other decomposition of THF and/ or EtOH. Additionally, the shifted signal to higher binding energies hint towards C-X bonds with neighboring atoms of higher electro-negativity. In this case C-Cl or C-O bonds are both possible and could be part of the SEI layer. The same C1s peaks are also seen in the work of Wang et al. [103] where they observe a broad C=O signal at 288 eV and Li_2CO_3 at 290 eV. The initials of a peak at 280 eV can be assigned to the Cl 2s signal of ClO_4^-.

Some visible differences can also be seen in the Cl 2p spectra of the three different experiments. The spectra with pure N_2 as reaction atmosphere exhibits more species than the other two, namely some C-Cl and ClO_3 peaks. These additional substances could be the reason for the destabilization of the working electrode. For the experiments with 0.8 and 3.0 mol % O_2 it seems like only the salt $LiClO_4$ is present at the surface.

All the Li 1s and O 1s spectra are showing only one broad peak with no clear differences. Since a lot of Li-X and O-X bonds are in the same binding energy regime [109–111], it is hard to gain any meaningful conclusions from these spectra.

For the XRD investigation we used a holder that was fitted with a polyetheretherketone (PEEK) dome which is tightened onto an o-ring leading to an air-tight configuration. A picture of this setup together with the tool to fasten it is given in Fig. 4.13 **A**. The sample preparation was similar to the previous one, where the experiment was conducted in an autoclave within the glovebox and the electrode was then attached to the sample holder using a piece of carbon tape. Then the PEEK dome was tightened around the holder and the assembled setup was brought to the XRD measuring device. We chose PEEK since it only has few Bragg reflections. The XRD patterns are seen in Fig. 4.13 **B**.

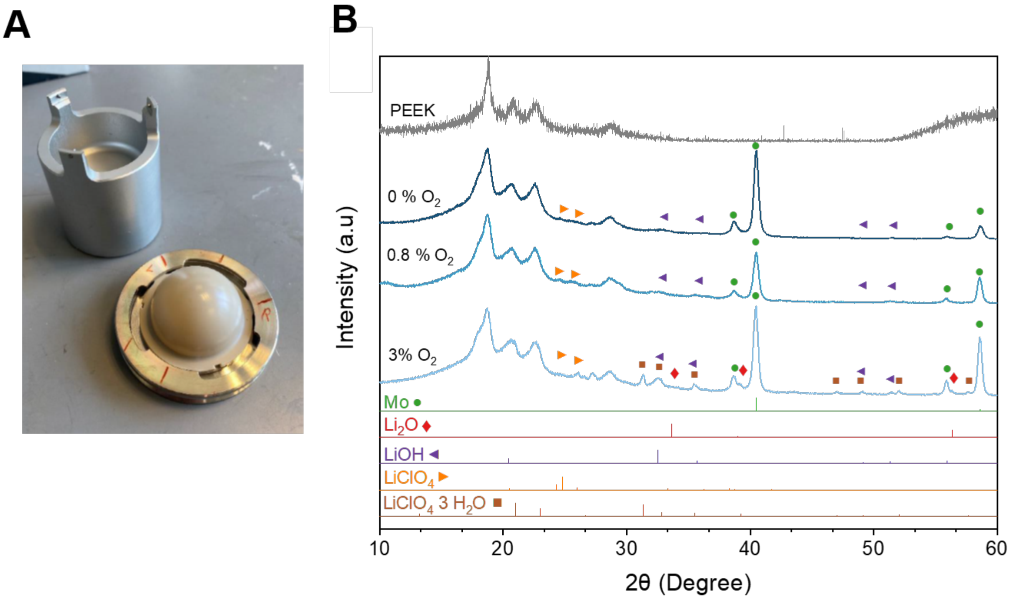

Figure 4.13: XRD pattern of the electrode after electrochemistry for **A** 0, **B** optimum 0.8 and 3 mol % oxygen at 20 bar. Data from Paper 1 [101].

All three samples show clear patterns of Mo and $LiClO_4$, which are expected but have no relation to the SEI layer. The other substance that is clearly visible in the samples with 0.8 and 3 mol % O_2, but only faintly visible in the sample without added O_2, is LiOH. LiOH has been previously observed in SEI layers of Li-O_2 batteries [112]. The peaks are more pronounced in the sample with the highest O_2 content of 3 mol %, which is also in accordance to literature, that predicts LiOH formation due to O_2 crossover [103, 113]. Moreover, Zheng et al. calculated that the diffusion barrier of Li^+ through LiOH is relatively high and therefore Li^+ diffusion is hindered, which supports our hypothesis. A pattern of hydrated $LiClO_4$ can only be observed in the 3 mol % O_2 sample due to the increased amount of H_2O formed by ORR. Most interestingly, the phase of Li_2O is also obtained in the highest O_2 amount sample, as was predicted in the previous section 4.4 and explains the rapid decrease of FE at higher O_2 contents.

4.5 Effect of O_2 on the electrolyte decomposition products

The evaluation of the decomposition products at different O_2 contents gives further insights into the role of O_2 in the LiMEAS. For this, O_2 enhancement experiments were conducted the same way as mentioned above and the electrolyte was analyzed immediately afterwards in the GC-MS with minimal air and moisture exposure. Moreover, the deposit was also analysed by NMR to characterize the species in the deposit. For a detailed experimental procedure of the electrochemistry and analysis, please find the supplementary information of Paper 4 in the

Appendix B.2.
The NMR results of the dissolved WE deposit in $CDCl_3$ are shown in Fig. 4.14.

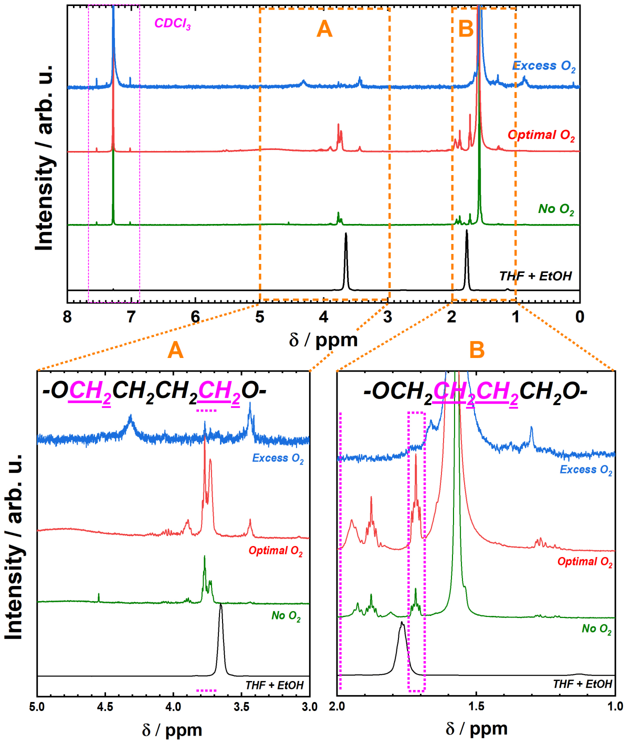

Figure 4.14: NMR of the dissolved deposit after electrochemistry at **A** 0, **B** optimum 0.8 and 3 mol % oxygen at 20 bar. Data from Paper 4 [70].

Based on the NMR results, the main organic compound of the deposit is polyTHF. The CH_2 groups next to an O atom are at higher chemical shifts of 3.7 ppm and the CH_2 with further distance to the O atom are at 1.7 ppm, as was also shown in literature [61, 114]. Interestingly, the polyTHF signal disappears at an excess of 3 mol % added O_2. Most likely, the deposit in that case is mainly dominated by $Li_xO_yH_z$ species. The GC-MS results give more insights into the various decomposition products in the electrolyte and are summarized in Fig. 4.15 **A**.

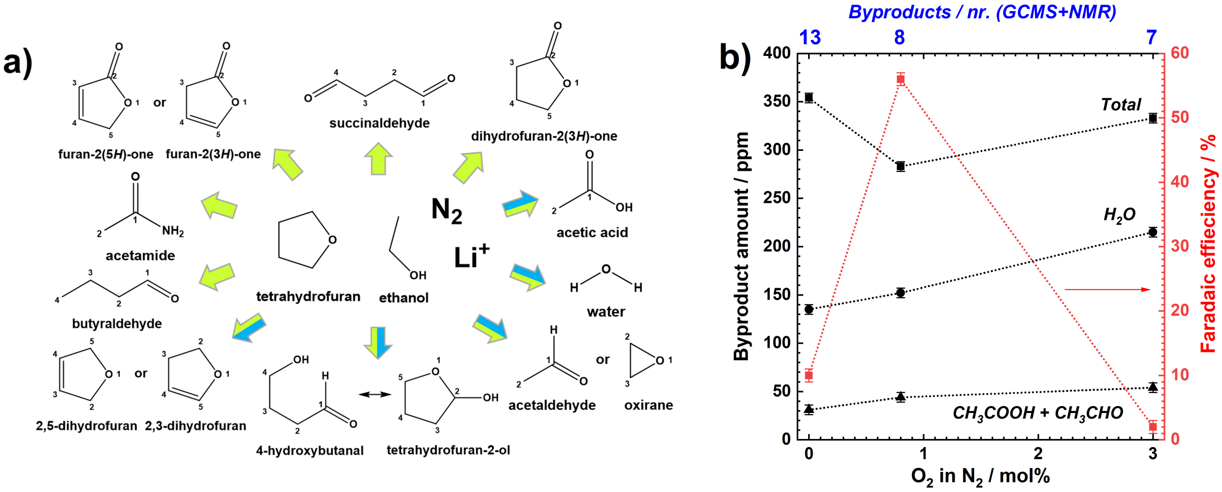

Figure 4.15: Effect of O_2 on the electrolyte decomposition products. **A** Detected decomposition products without O_2 (green) and with added O_2 (blue). **B** Number and amount of byproducts as a funtion of O_2 content. Data from Paper 4 [70].

The detected products without added O_2 are indicated with green arrows and the ones with added O_2 are shown with blue arrows. Different molecules such as oxirane and acetaldehyde are counted as two products but mesomeric structures like 2,5-dihydrofuran or 4,5-dihydrofuran are counted as one. The results clearly show that the addition of O_2 diminishes the number of side products significantly from 12 to 7. This could also be an explanation for the increase in WE potential stability that was shown before. The concentration of O_2 does not seem to matter in the number of byproducts detected, but after quantification of the byproducts, it does change the total amount of products as indicated in 4.15 **B**. The number of byproducts entails polyTHF that was previously detected with NMR, so that the total number is minimized at highest O_2 content but the concentration of decomposition products is lowest at optimum O_2 contents of 0.8 mol %. However, this total amount also accounts for water, which increases proportionally to the O_2 concentration due to ORR.

4.6 Summary

The effect of O_2 on the LiMEAS was carefully investigated with real world application in mind, where O_2 contamination can occur. The results are not only scientifically interesting but also have a positive impact on future industrial application. With the combined experimental and computational effort we reached following conclusions:

- Small amounts of O_2 (0.6-0.8 mol %) increase the FE of LiMEAS at 20 bar reaction pressure from 24.7 ± 0.5 % to 78 ± 1.3 %, leading to an EE of 11.7 ± 0.5 % . The same experiments at 10 bar show that the optimal O_2 content is dependent on the O_2 partial pressure and not molar O_2 content.

- At higher than optimum O_2 concentrations the FE falls rapidly and reaches 0 % due to Li_2O formation and ORR. The formation of Li_2O was verified by air and moisture free XRD, where only at high O_2 contents of 3 mol % the pattern of Li_2O was observed. ORR was confirmed by measuring the water content for varying O_2 concentrations, which gave a linear correlation.

- O_2 also increases the stability of the WE, most likely due to modification of the SEI layer, which in turn influences plating behavior of Li.

- With theoretical modeling and literature research we conclude that the enhancement in FE is due to the modification of the SEI through O_2 which slows down Li^+ diffusion relative to H^+ and N_2 transport to the electrode surface.

- The SEI layer was investigated by air and moisture free XRD and XPS, which show that the LiOH content is increased with O_2. Furthermore, only at the optimum of 0.8 mol % O_2, a N 1s signal was observed, meaning that under these conditions reaction of Li with N_2 is more favored.

- Lastly, the decomposition products in the electrolyte were investigated with NMR. The results show that at the optimum of 0.8 mol % O_2 the total amount of decomposition byproducts is at its lowest, which might also explain the increased stability of the WE.

5 Increasing Current Density and Rate

Before starting the project, the highest reported current density was –25 mA/cm^2 [56], however the overall cell potentials were very high (> 20 V) and the experiment only lasted for a few minutes. The goal in our team was to develop high surface area electrodes that can sustain a current density of at least -100 mA/cm^2 with reasonable cell potentials and stability. In the beginning, I tested various substrates with surface structuring of different sizes such as Ni-foam (structures in mm size), shrink film derived Mo (μm) [115] and oxide-derived Cu (nm) [116, 117]. The only prerequisite is that the material should work for LiMEAS, which means it should not form an alloy with Li. After some initial troubles I found a method that seems promising, called the hydrogen bubble template (HBT) method, that was described in section 3.2.5, which deposits porous Cu, or also other metals, on substrates of ones choosing.

This chapter will be divided into two parts. The first part is the verification of the HBT method for LiMEAS, where this porous Cu was deposited on Ni foam as a substrate and tested for NH_3 formation at -100 mA/cm^2. The results were published in Paper 2 [118]. For this work I want to acknowledge Degenhart Hochfilzer for the discussions, especially in the beginning of this project, and Sarah Groot Shapel who joined me for parts of the experiments.

The second part will cover the optimization of the HBT electrodes by electrolyte design and changing the substrate for deposition. This work was a result of collaboration between theoreticians and experimentalists, which lead to the publication of Paper 5 [119]. For this section I want to credit Shaofeng Li for the experimental and Yuanyuan Zhou for the theoretical part.

5.1 Verification of Hydrogen Bubble Template Method

To test if the HBT Cu electrode work for LiMEAS, they were synthesized according to procedures from the literature [80] and characterized by SEM, SEM-EDX and XPS. After the purity was confirmed, the ECSA was determined by capacitive cycling, which was described in section 3.2.4. Then the electrodes were tested at 20 bar for LiMEAS and the results documented. For the sake of continuity all electrodes that were used for Paper 2, which this section is based on, will be named HBTCu, as was the case in the publication [118].

Before starting with the results it is of great importance to define some terms that are necessary to understand this chapter. Since the focus lies on high surface area electrodes we need to strictly define the terms geometric surface area, real surface area and ECSA, which is the most relevant for us. The geometric surface area is what one can measure with a simple ruler and does not account for porosity or surface morphology. The real surface area accounts for all these features and can be measured by Brunauer–Emmett–Teller (BET) isotherms. In our case, we are interested in the area that is electrochemically active. As stated in section 3.2.4 there are many ways to measure the ECSA and in this context we chose capacitive cycling. All current densities hereon will be given as mA/cm_{geo}^2, unless otherwise specified.

5.1.1 Synthesis and Characterization of Cu Deposited on Ni Foam

The deposition method was briefly explained in chapter 3.2.5. For a more detailed description please find the supporting information of Paper 2 [118] in B.2. After the deposition the electrodes were characterized with SEM to see the high surface area structures. The images of the substrate Ni foam before and after HBT deposition are given in Fig. 5.1.

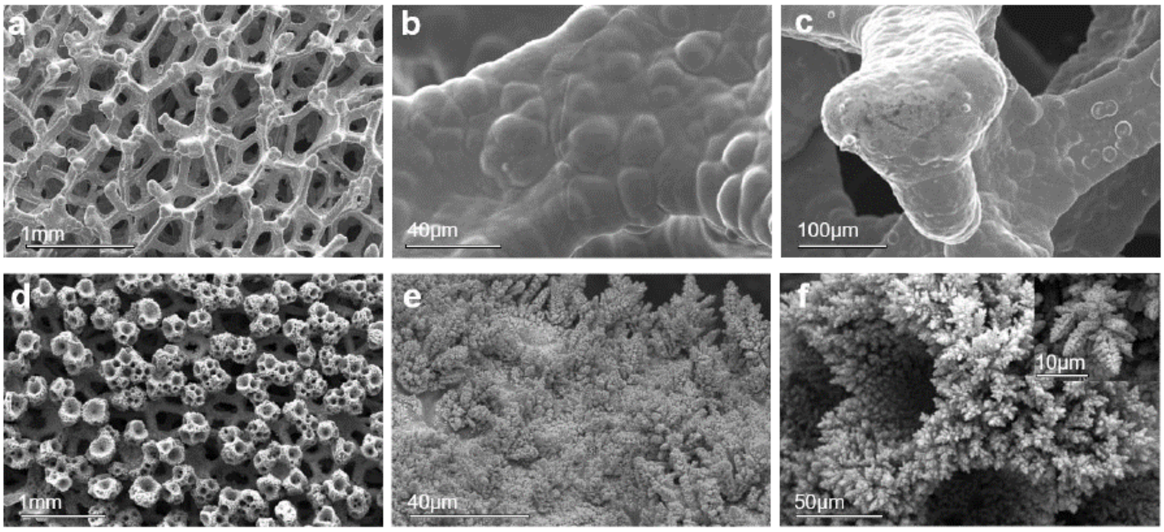

Figure 5.1: SEM images of the Ni foam (a-c) before and (d-f) after hydrogen bubble template with Cu. The deposition conditions were 15 s in an electrolyte of 0.4 M $CuSO_4$ + 1.5 M H_2SO_4 at a current of −5 A. Data obtained from Paper 2 [118].

Even before deposition Ni foam itself has a porous structure with features in the mm regime. The three-dimensional construct can be roughly divided in two different areas, one being the topmost round features seen in Fig. 5.1 **C** and the other one being the inner planes seen in Fig. 5.1 **B**. After deposition of porous Cu the real surface area is visibly enhanced with deposition morphology considerably different on both of these sub-structures. A closer look on the morphologies is given in Fig. 5.2.

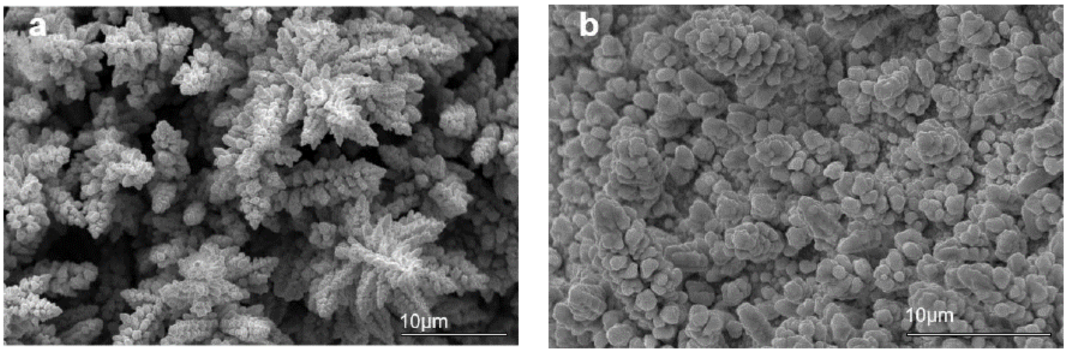

Figure 5.2: SEM images of the morphologies of HBTCu on the (a) ball-like top section and (b) inner surface section. The deposition conditions were 15 s in an electrolyte of 0.4 M $CuSO_4$ + 1.5 M H_2SO_4 at a current of −5 A. Data obtained from Paper 2 [118].

Here it is clear that the Cu grows differently on both sections of the Ni foam. This is most likely due to the inhomogeneous current density distribution, which is higher on the top, and probably also mass transport limitations. The Cu^{2+} concentration inside of the Ni foam will be reduced more quickly and hence the concentration changes and more HER will occur over time. These are issues that will be addressed in the later part, where the substrate for deposition was changed.

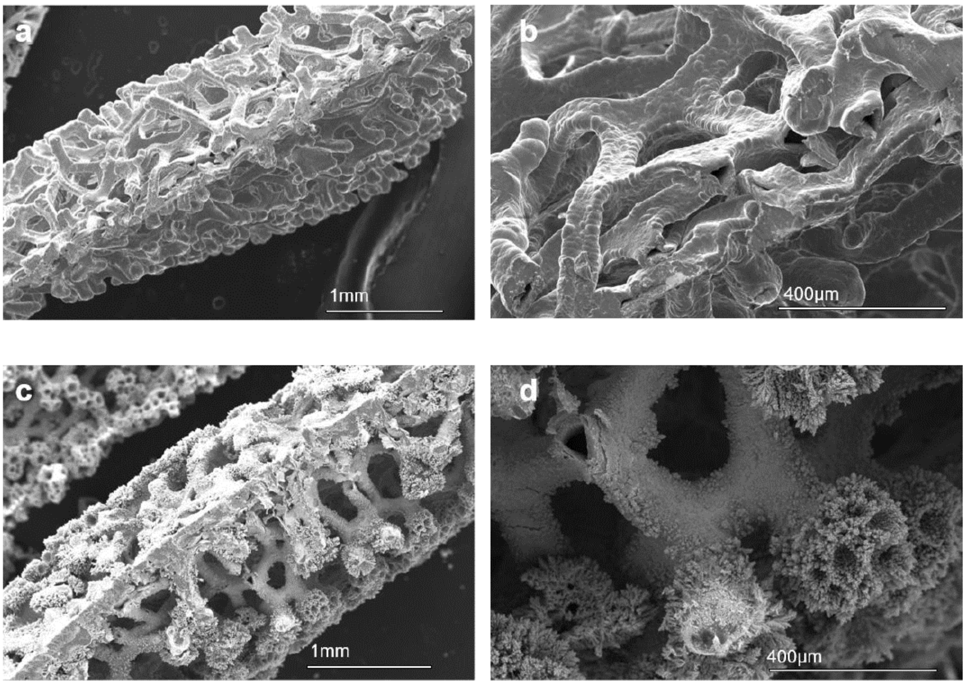

Figure 5.3: SEM images of the cross sections of Ni foam (a-b) before and (c-d) after hydrogen bubble template with Cu. The deposition conditions were 15 s in an electrolyte of 0.4 M $CuSO_4$ + 1.5 M H_2SO_4 at a current of −5 A. Data obtained from Paper 2 [118].

To confirm that the Ni foam was fully covered in Cu, SEM of the cross sections were taken to observe the inner most parts of the electrode. For that, the electrode was cut in half and taped standing up with carbon tape before putting it into the microscope. The images are seen in Fig. 5.3. From Fig. 5.3 **d** it is clear that the whole Ni foam is completely covered with porous Cu. There is a significant difference between the surface structure of pure Ni foam (Fig. 5.3 **b**) and Cu deposited on Ni foam.

Since SEM is only a visual confirmation of the complete coverage of Cu on Ni, the next step was to check the purity of the electrode with more thorough techniques. Hence, the electrodes were measured by SEM-EDX (Fig. 5.2) and XPS (Fig. 5.5).

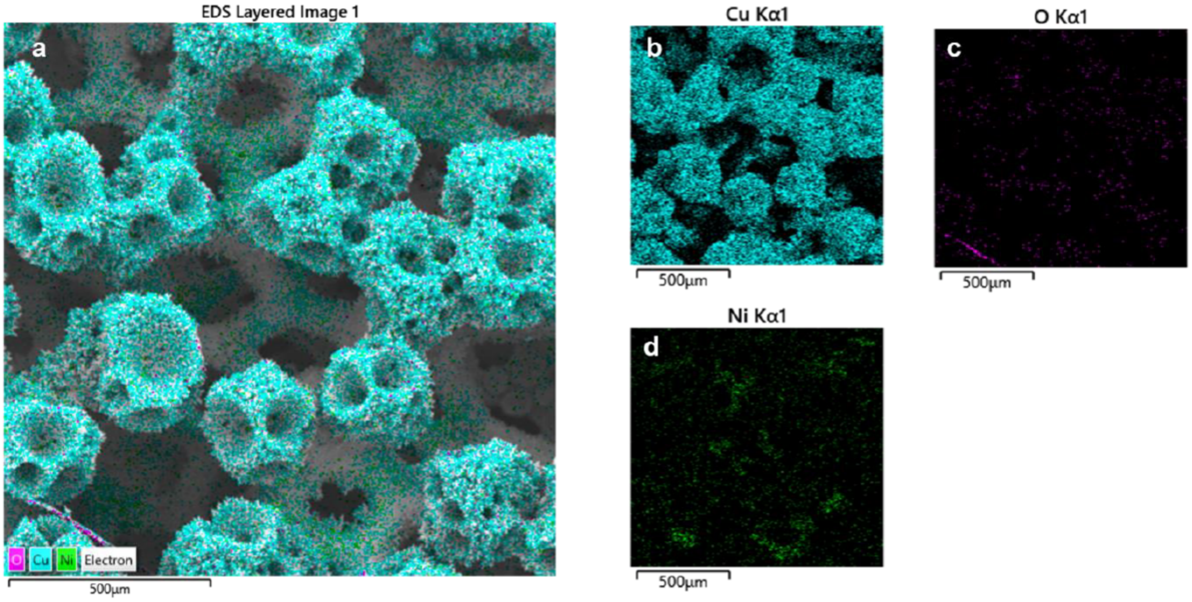

Figure 5.4: SEM-EDX images of the Ni foam after hydrogen bubble template with Cu. Data obtained from Paper 2 [118].

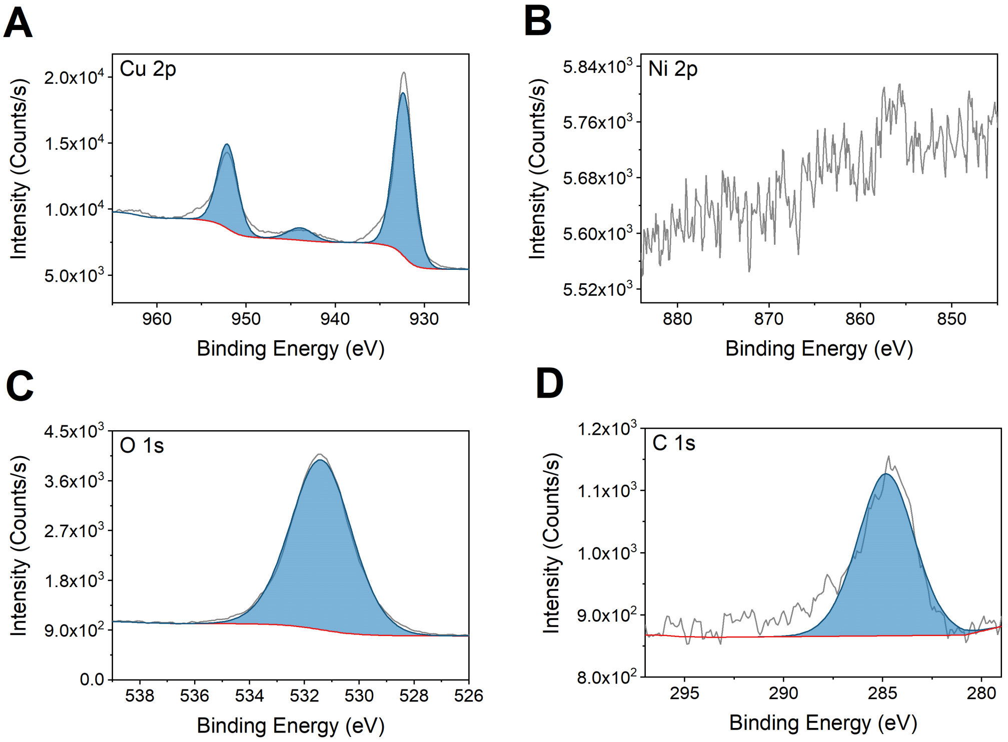

Figure 5.5: **A** Cu 2p, **B** Ni 2p, **C** 1s and **D** C1s XPS spectra of the Ni foam after hydrogen bubble template with Cu. Data obtained from Paper 2 [118].

The SEM-EDX revealed mostly Cu with some Ni shining through. The small Ni signal in Fig. 5.2 **d** is due to the fact that EDX is not a surface sensitive measurement (sensitivity low μm) [120]. Under these deposition conditions, the thickness of the deposited Cu film is normally in the low μm regime as well [82], hence some Ni can be seen. The more surface sensitive method XPS (sensitivity low nm) [121] does not depict any Ni on the surface, as is seen from Fig. 5.5. The full survey spectra can be seen in Fig. B.2 in the Appendix B.1.2.

Capacitive cycling was chosen to determine the ECSA. The method was briefly explained in 3.2.4. As was explained there, it is necessary to know the specific capacitance C_{spec} of the material, in this case Cu, in the electrolyte. Since we will use a 2 M $LiClO_4$ with 0.17 M EtOH in the LiMEAS, a 2 M $LiClO_4$ electrolyte was chosen for the capacitive cycling measurement. The exact details of the experimental procedure can be found in the supplementary information of Paper 2 [118] in the Appendix B.2. Briefly, to determine C_{spec} of Cu, a Cu stub of known area (0.2 cm^2) was polished until the roughness factor is close to 1. Then CVs were measured in the potential range from 0 to −200 mV vs OCV at scan rates between 10 - 60 mV/s. Since in our system we only have a pseudo reference Pt electrode, the OCV was chosen as a reference potential. We found that other groups also used OCV as a reference to measure capacitive cycling [79]. We determined a C_{spec} value of 17 µF/cm^2, which is in accordance with predicted values from literature [79]. The electrochemical data of the C_{spec} is shown in Fig. 5.6. The same procedure was repeated to determine the ECSA of HBTCu. This was done three separate times on three different HBTCu electrodes and the resulting ECSA was 66.5 ± 7.1 cm^2. Since the HBTCu electrode was 0.5 cm^2_{geo} in size, the roughness factor is 66.5 when considering both sides of the electrode. This means that if one can normally apply a current density of around -2 mA/cm^2_{ECSA} on foils, the HBTCu electrodes should sustain a current density of around -130 mA/cm^2_{geo}

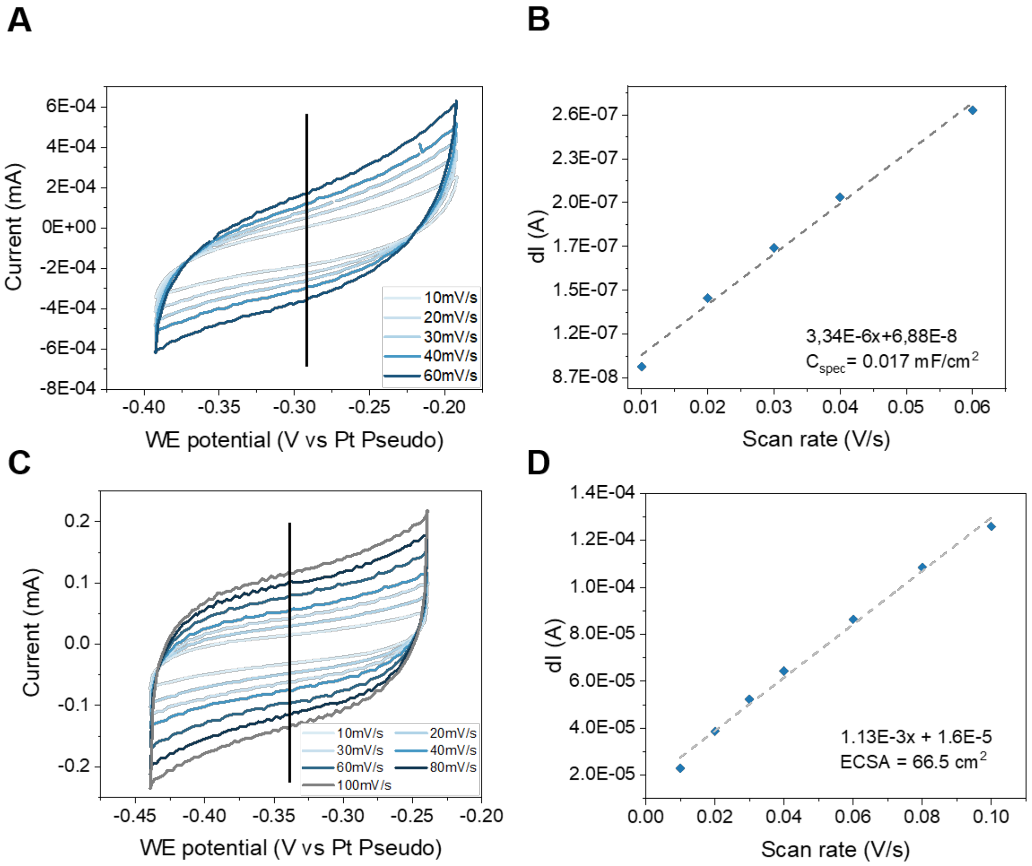

Figure 5.6: Determination of specific capacitance of Cu and ECSA of HBTCu in 2 M LiClO4 in THF electrolyte with capacitive cycling.**A** CVs at different scan speeds around 0 to -200 mV vs OCV. of Cu. **B** Change in current versus scan speed of Cu. **C** CVs at different scan speeds around 0 to -200 mV vs OCV. of HBTCu. **D** Change in current versus scan speed of HBTCu. Data obtained from Paper 2 [118].

5.1.2 Experimental Prove of Concept

Up to this point, the standard electrolyte used was 0.3 - 0.5 M Li salt solution in THF with 0.17 M EtOH. However, to utilize high surface area HBTCu electrodes to their fullest potential, the salt concentration needed to be increased. From literature it is known that the EDL becomes thinner at higher salt concentrations, which enables the probing of the whole ECSA. This is phenomenon is depicted in Fig. 5.7 **A**.

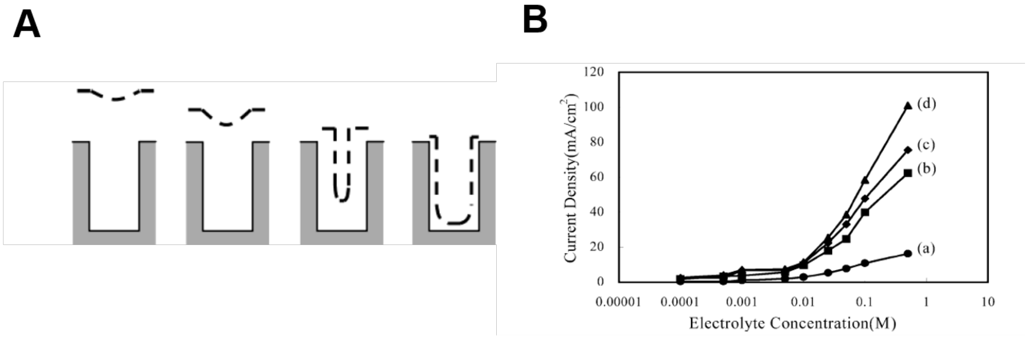

Figure 5.7: **A** Visual depiction of thickness of EDL as function of the electrolyte salt concentration. From low concentration (1 mM, left) to high concentration (1 M, right). **B** The results of chronoamperometry of ORR at (a) flat and (b-d) mesoporous Pt electrodes at various electrolyte concentrations. [122]

At lower electrolyte concentrations the thickness of the EDS might cover parts of the surface structures and render them invisible and hence decrease the ECSA. Therefore, less current can be achieved, which is shown in Fig. 5.7 **B** where Boo et al. measured the current density of ORR on mesoporous Pt at different electrolyte salt concentrations. Clearly the achievable current density is proportional to the salt concentration. With this in mind we increased our salt concentration to 2 M. Another reason for increasing the molarity is to reduce the ohmic resistance in our setup. Due to the non-aqueous solvent the resistances are quite high (100-300 Ω) and coupled with the high currents this would lead to an increased cell potential due to iR drop.

The testing of the HBTCu electrodes for LiMEAS was conducted in the autoclave setup previously described in 3.1. For a more detailed experimental procedure please find the supplementary information of Paper 2 [118] in the Appendix B.2. The electrochemical data from HBTCu was compared to plain Cu foil and to previous publications on Mo foil [62]. The resulting FE, EE and NH_3 formation rates of HBTCu and Cu are listed in Tab. 5.1

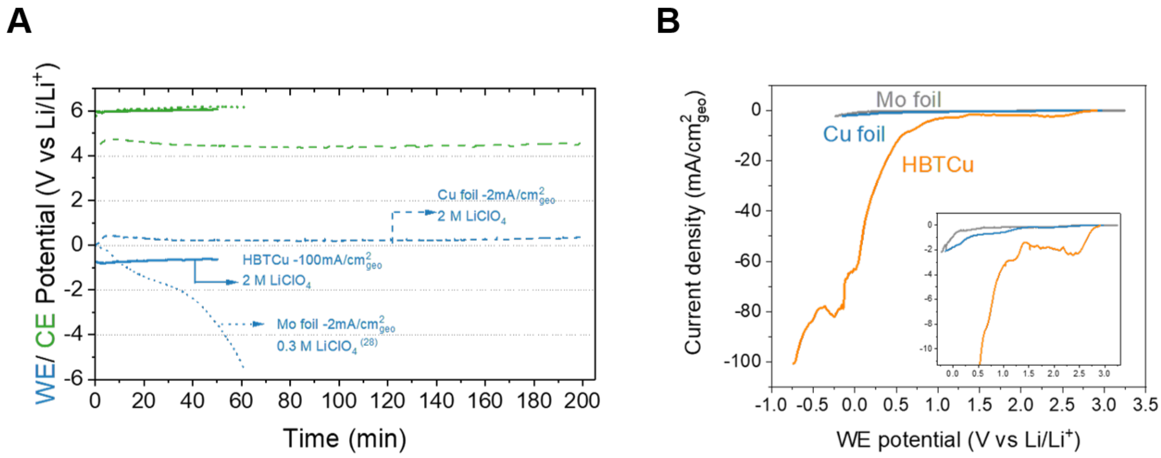

Figure 5.8: **A** Chronopotentiometry and **B** Linear sweep voltammetry of Cu foil, Mo foil and HBTCuNi in the LiMEAS at 20 bar. The electrolyte was 2 M $LiClO_4$ + 0.17 M EtOH in THF. Data obtained from Paper 2 [118]. The Mo reference data was taken from [62].

Table 5.1: FE, EE and NH_3 formation rates of HBTCu and Cu under the same reaction conditions. Data obtained from Paper 2 [118].

Electrode	FE [%]	EE [%]	NH_3 formation rate $\left[nmol/\left(s \cdot cm^2{}_{geo}\right)\right]$
Cu foil	13.6 ± 1.0	3.9 ± 0.3	1.0 ± 0.1
HBTCu	13.3 ± 2.0	2.3 ± 0.3	46.0 ± 6.8

Already from the LSV in Fig. 5.8, the current density increase is clearly visible. Both Cu and Mo foil have similar current densities at comparable potentials but HBTCu exhibits far larger current densities. The differences in the CP in Fig. 5.8 **A** can also be explained. The discrepancy in the cell potentials of HBT Cu and Cu foil are mainly due to iR drops since the applied current for HBTCu was −50 mA and for Cu foil only −1 mA. With measured resistances of around 20 - 30 Ω the iR drop would be around 1.25 V and 25 mV, respectively. Secondly, both measurements conducted in 2 M $LiClO_4$ electrolyte have stable potentials, whereas the measurement in 0.3 M $LiClO_4$ has an unstable WE potential under the otherwise same reaction conditions (20 bar N_2, -2 $mA/cm^2{}_{geo}$). We can most likely rule out the possibility that this is due to the different WE materials since Cu and Mo both were used interchangeably in literature [40, 49, 62]. More likely the stability increase arises from the increased salt concentration. This is also believed by Westhead et al. [123], who attribute the stability to a more inorganic SEI layer. It is well known in battery literature that an increase in salt concentration leads to a more inorganic SEI layer, since Li gets in contact more with the salt anions which make the main part of the inorganic SEI layer [124]. Moreover, a more stable Li metal cycling behavior was also previously observed at high Li salt concentration, which the authors ascribe to a more uniform SEI layer [125]. Hence, not only is the higher salt concentration beneficial for utilizing high surface area electrodes, it

is also improving the stability of the process.
One must also consider the "salting-out" effect, which lowers the solubility of gases in liquids at higher salt concentrations [126]. Given the already low N_2 solubility in THF of 3.3 mM [127, 128], this might be an issue. This could be an explanation as to why the overall FE of both HBTCu and Cu foil are quite low at around 13 %. However, the ammonia formation rates are increased almost by a factor of 50 when comparing the Cu foil to the HBTCu electrodes. This result verifies the HBT method for synthesizing high surface area electrodes for the LiMEAS.

5.2 Optimizing Conditions for High Current Density

As already mentioned in the previous section Ni foam does not seem to be the ideal substrate, because of the uneven current density distribution. Furthermore, the HBTCu electrodes are also mechanically quite unstable and some Cu particles can fall off, if handled too roughly. In the following chapter, together with Shaofeng Li, we deposited the Cu on stainless steel mesh, which seems a much better substrate for the HBT and LiMEAS. This together with the electrolyte optimization suggested by theoretical calculations from Yuanyuan Zhou, lead to high FE of 71 ± 3 % at current densities of -1 A/cm^2_{geo}, which makes the LiMEAS closer to industrially relevant applications. These results were published in Paper 5 [118].

5.2.1 Stainless Steel Mesh as Electrode Substrate

The experimental procedures to synthesize and measure the ECSA of the HBT electrodes on stailess steel mesh, heron called HBTCuSS, are the same as the previous section and briefly described in section 3.2.5 and 3.2.4. For more details please see Paper 5 [118] in the appendix B.2. Fig. 5.9 shows the SEM images of the stainless steel substrate before and after HBT in addition to the ECSA determination data from capacitive cycling.

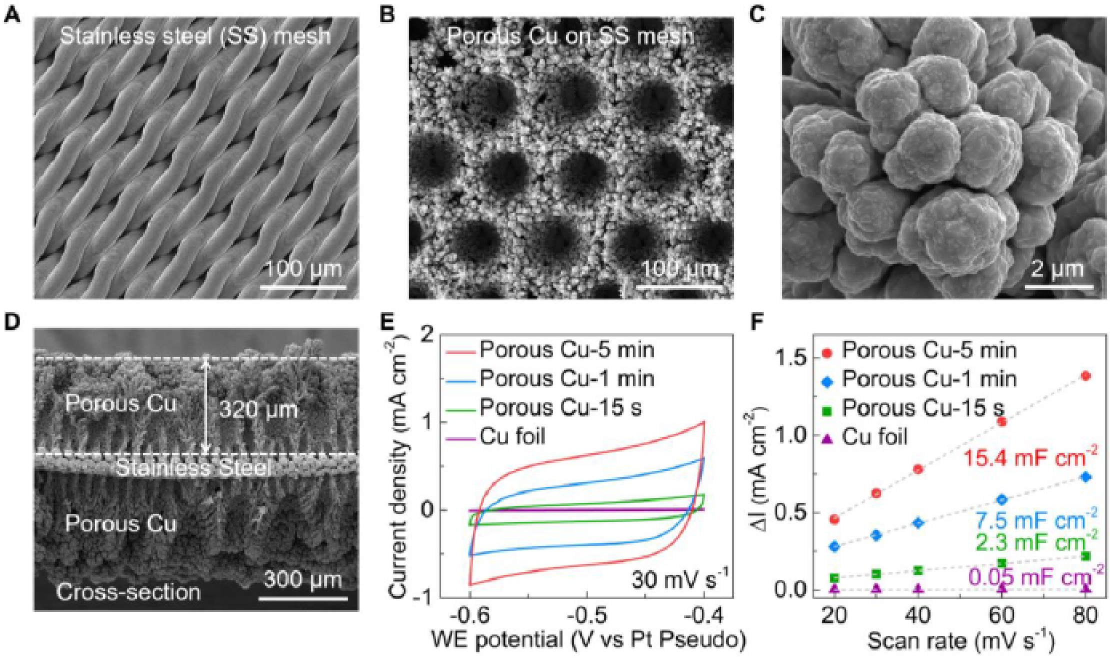

Figure 5.9: **A-D** SEM images of the stainless steel mesh before and after HBT. The deposition were performed in an electrolyte of 0.4 M $CuSO_4$ + 1.5 M H_2SO_4 at a current of −5 A. **E-F** ECSA determination of HBTCuSS with capacitive cycling in 2 M $LiClO_4$. Data obtained from Paper 5 [119].

The SEM images in Fig. 5.9 **B-D** reveal a more evenly distributed deposition, since stainless steel mesh does not have different surface features like Ni foam does. It can be in a way described as more of a 2D structure than 3D. This also leads to a better mechanical stability as Cu particles do not fall off the electrode easily. The thickness and hence the ECSA can be tuned by varying the deposition time, with longer deposition time of 5 min leading to a deposition thickness of 320 μm. When looking at the capacitive cycling data in Fig. 5.9 **F**, the resulting ECSA increases from Cu foil to HBTCuSS-5min by a factor of 308. At -3 mA/cm^2_{ECSA} the current density per geometric surface area would be around -1 A/cm^2_{geo}.

5.2.2 Theoretical Prediction on Optimal Solid Electrolyte Interphase Layer

Since the electrode was now optimized for high current density application, the next step was to increase the FE and hence NH_3 formation rate. The theory collaborators suggested, similarly to the O_2 case, a modification of the SEI layer. Hence, Yuanyuan first calculated which of the inorganic SEI compounds could be stable at Li plating potentials and then evaluated their respective Li^+ conductivity. For this only compounds that are not soluble in THF were considered since otherwise their concentration in the SEI would be negligent. The results are given in Fig. 5.10.

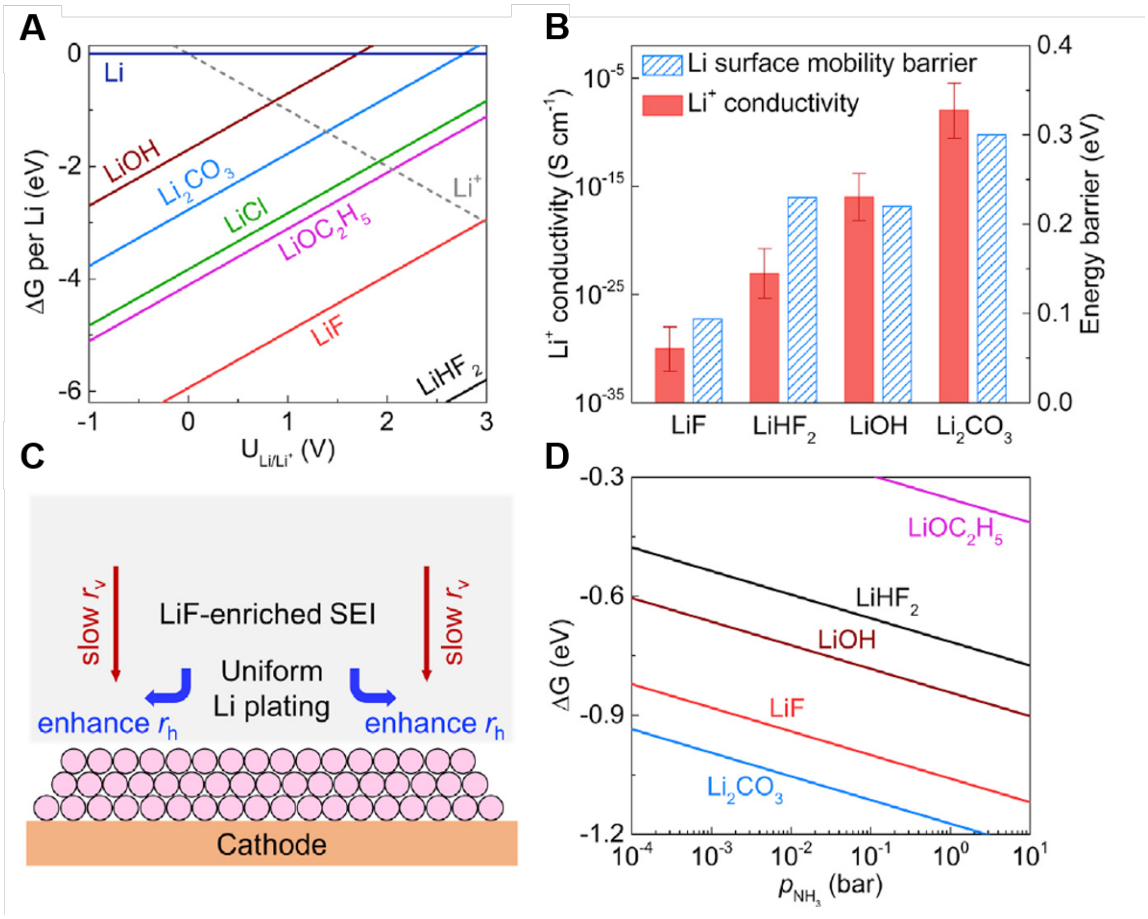

Figure 5.10: **A** Calculated Gibbs free energy of formation of different Li compounds as a function of potential. **B** Predicted Li surface mobility barriers and Li^+ conductivities of different SEI components. **C** Schematic of Li^+ surface mobility barriers and conductivities of different SEI components. **D** Gibbs free energy of adsorption of NH_3 on different Li containing SEI compounds. Data obtained from Paper 5 [119].

From the Pourbaix diagram in Fig. 5.10 **A** it is seen that with $LiClO_4$ as electrolyte salt, the two most stable compounds are $LiOC_2H_5$ and Li_2CO_3, since LiCl is soluble in THF [129]. Both are more likely to result from decomposition of Li with EtOH instead of the ClO_4^- anion. When using a F-containing salt like $LiBF_4$ or $LiPF_6$, the most likely SEI components are then LiF and $LiHF_2$. Next, the Li surface mobility barrier and Li^+ conductivity were estimated in Fig. 5.10 **B**. The difference between these two values is visualized in Fig. 5.10 **C**. The Li surface mobility barriers describes how well Li can be distributed horizontally (blue arrows). A low Li surface mobility barrier is desired, since it would result in a more homogeneous Li plating. The substance with the lowest surface mobility barrier is LiF. This result was also previously reported in [112], where Zheng et al. suggested LiF as a beneficial constituent of the SEI as well. In contrast to the surface mobility barrier, the Li^+ conductivity vertically thorough the

SEI layer (red arrows) should be low, as was already discussed in the O_2 enhancement section. This is because Li^+ also competes for electrons and uncontrolled or wasted Li deposition that does not react with N_2 lowers the FE. Again, the F-containing constituents seem to be more beneficial compared to LiOH and Li_2CO_3 due to their low Li^+ conductivity.
Moreover, the theoretical data in Fig. 5.10 **D**, which shows the Gibbs free energy of adsorption of NH_3 on different SEI components, suggests that the formed NH_3 can also be trapped inside the SEI layer. This issue was never before raised and will be addressed carefully in this work. Hence, the conclusions gained from the theoretical calculations are twofold. Firstly, it was concluded that flourinated substances, especially LiF, are desirable components for the SEI layer. Secondly, it was hypothesized that a non-negligible amount of formed NH_3 could be trapped on the electrode, which has to be accounted for in the FE calculations. To test this hypothesis, the experiments were conducted with three different Li salts: $LiClO_4$, which can not form a LiF rich SEI layer, and $LiBF_4$ and $LiPF_6$ that can form LiF. The electrodes after electrochemistry are also washed with water and the NH_3 content determined.

5.2.3 Solid Electrolyte Interphase at High Current with Different Li-salts

To test the maximal sustainable current density, the electrode with the highest ECSA, which is HBTCuSS-5min, was employed in a range of experiments varying the Li-salt and current density. The electrolyte consisted always of a 2 M Li salt solution in THF with 0.17 M EtOH and the experiment was conducted in the autoclave at 20 bar pure N_2. For more detailed experimental procedure see Paper 5 [119] in Appendix B.2. The electrodes were tested at -100, -200, -500 and -1000 mA/cm^2_{geo} and the results are shown in Fig. 5.11.

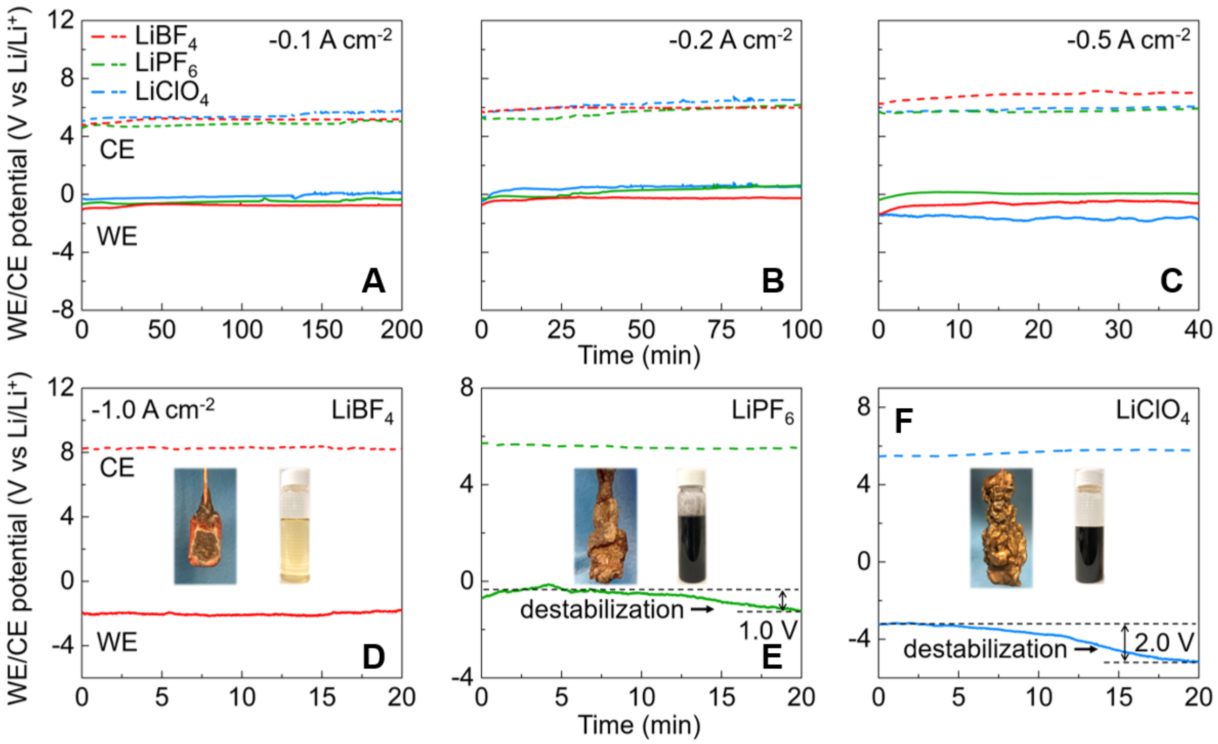

Figure 5.11: Chropnopotentiommetry of HBTCuSS-5min at current densities of **A** -100, **B** -200, **C** -500 and **D-F**, -1000 mA/cm$^2_{geo}$ at 20 bar with different Li-salts. Data obtained from Paper 5 [119].

The CPs ran different amount of times so that the total passed charge stays constant at 240 C. The voltage profiles of -100, -200 and -500 mA/cm$^2_{geo}$ look very stable for the three different Li-salts, which suggests a stable operation. A slight difference of cell potentials is due to the difference in resistance of the system depending on the used electrolyte salt. The resistance increased in the following order: $LiPF_6 < LiClO_4 < LiBF_4$. Representative PEIS measurements are shown in Fig. B.3 in the Appendix B.1.2.

At -1 A/cm$^2_{geo}$ the WE potentials of the experiments with $LiPF_6$ and $LiClO_4$ start to destabilize around 1 and 2 V from start to end of the CP, respectively. The inserts in Fig. 5.11 **D-F** also show the WE and the electrolyte after electrochemistry. Clearly the electrolyte is not stable and is being oxidized at the CE, which is not sustainable for long time operation. After letting the electrolyte stand for one day it polymerizes to a gel state, proving the oxidation and polymerization of THF. Only the electrolyte with $LiBF_4$ used as the salt still remains relatively clear and does not polymerize, making it the most stable out of these three electrolytes. It is known that $LiPF_6$ is not stable at elevated temperatures above 60 °C [130] and hence it could be that during the mixing of the electrolyte, which emits heat due to solvation, the electrolyte already starts to decompose. Additionally, the P-F bond is very susceptible to hydrolysis, even with trace amounts [131]. Similarly, $LiClO_4$ is unstable as it is a strong oxidant that can react with the solvent, especially at elevated temperatures and high currents [131–133]. In contrast, $LiBF_4$

is not only anodically relative stable but also thermally [134–136]. However, in battery literature it is not favored because of its low ion mobility and conductivity [131].

Another stark difference that shows the beneficial use of $LiBF_4$ is the amount of deposit that stays on the WE after electrochemistry. A very thick deposition is seen on the experiments with $LiClO_4$ and $LiPF_6$, whereas only little deposition is observed in the case with $LiBF_4$. This leads to the conclusion that the SEI layer might be more compact in the case of $LiBF_4$ and will be further investigated with XPS.

To evaluate the FE carefully and not destroy the deposition on the WE, the electrolyte was first removed through a PTFE sampling tube that sits in the electrolyte in the cell and can be seen in Fig. 3.2 **D**, where the autoclave setup was described. After the electrolyte was removed, the pressure was released slowly into an acid solution to trap all the NH_3 in the gas phase. This procedure ensures that the deposit on the electrode stays intact and hence allows the determination of NH_3 in all the three phases, gas, liquid (electrolyte) and solid (deposition and SEI layer). The evaluation of the FE, NH_3 formation rates and NH_3 distribution is given in Fig. 5.12.

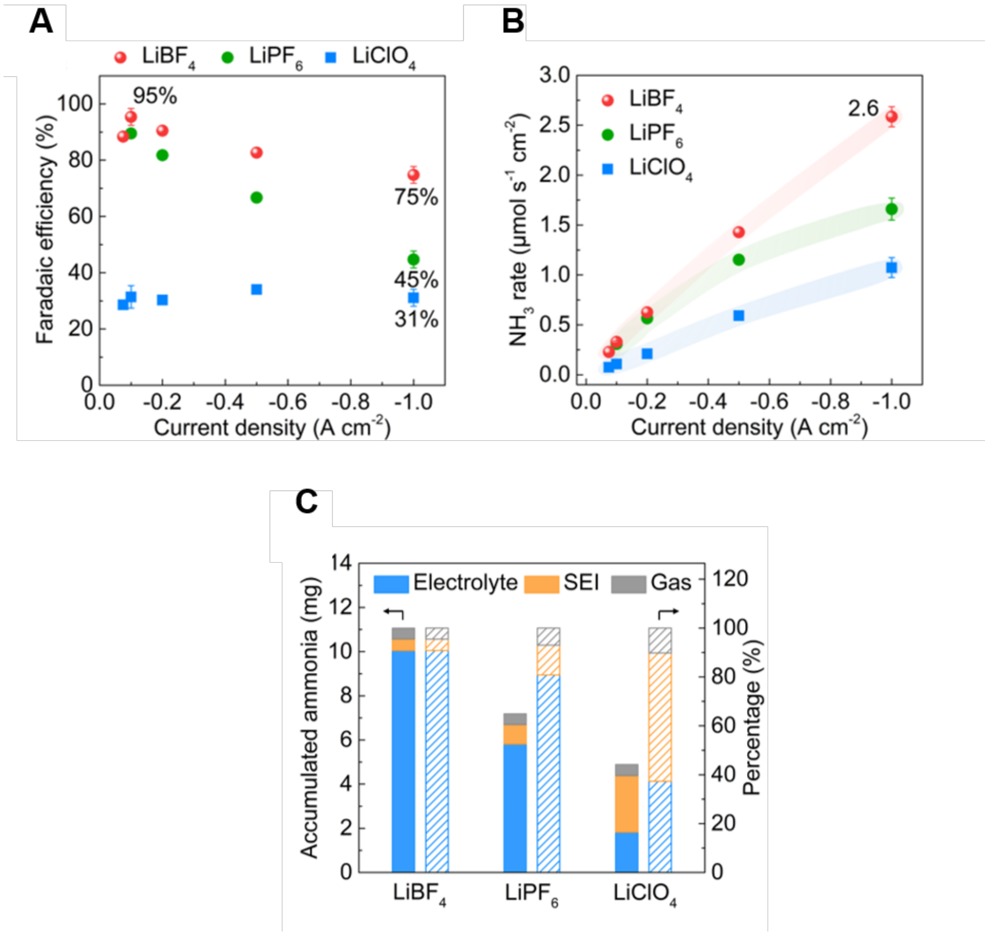

Figure 5.12: **A** FE and **B** NH_3 formation rates of HBTCuSS-5min in the LiMEAS at 20 bar at different current densities and with different Li-salts. **C** Distribution of formed NH_3 in the gas, liquid, and solid phase. Data obtained from Paper 5 [119].

As expected, the FE decreases with increasing current densities for the experiments with $LiBF_4$ and $LiPF_6$ as with increasing current the Li^+ deposition rate increases, which has a negative effect on the FE as predicted by micro-kinetic model. The sharper decrease for $LiPF_6$ is most likely due to its thermal instability, since increasing the current also heats the system through resistive heating. At -75 mA/cm^2_{geo} both exhibit a FE of around 90 %, which falls to 75 % for $LiBF_4$ and 45 % for $LiPF_6$. These high FE, especially in contrast to the FE with $LiClO_4$, prove that the F-containing salts indeed have a beneficial effect on the SEI and hence FE, as was foretold by theory. The highest obtained FE of 95 ± 3 % was achieved with $LiBF_4$ at -100 mA/cm^2_{geo}. Interestingly for $LiClO_4$, the FE stays constant at around 30 % for the experiments with $LiClO_4$ regardless of current densities. This makes us believe that with this specific SEI layer or decomposition products from $LiClO_4$ the Li-plating rate somehow does not play a significant role in FE. However, these are only speculations and need to be investigated further. Similarly, the NH_3 formation rates are the highest for $LiBF_4$ and the lowest for $LiClO_4$ with the highest overall rate of 2.5 ± 0.1 μmol/s $\cdot cm^{-2}_{geo}$ at -1 A/cm^2_{geo}, which gives an EE of 7.7 ± 0.3 %.

The NH_3 distribution in Fig. 5.12 **C** shows that little NH_3 is in the gas phase, probably due to the NH_3 being in form of NH_4^+ because of the acidification of our electrolyte [59]. For the F-containing salts, most NH_3 remains in the liquid phase with some of it trapped inside the deposit. Since the deposit is visually larger in the case of $LiPF_6$, more NH_3 also seems to be in the deposit of these experiments. The NH_3 distribution is totally different in the case of $LiClO_4$ with more than half of the actual produced NH_3 being in the deposition. This is an important finding, since not everyone measures the NH_3 content in the deposit, which in this case makes a big difference.

5.2.4 Investigation of the SEI Layer and Deposition at High Current Density

To investigate the SEI layer instead of the large deposits, only an LSV was performed until the current reached -1 A/cm^2_{geo}. The XPS measurement was then conducted the same way as the in the O_2 enhancement case, which prevented exposure to air and moisture. In this case, additional Ar sputtering was performed to see the depth profile. The XPS results for the three different salts is shown in Fig. 5.13. For the experimental details please see Paper 5 [119] in the Appendix B.2.

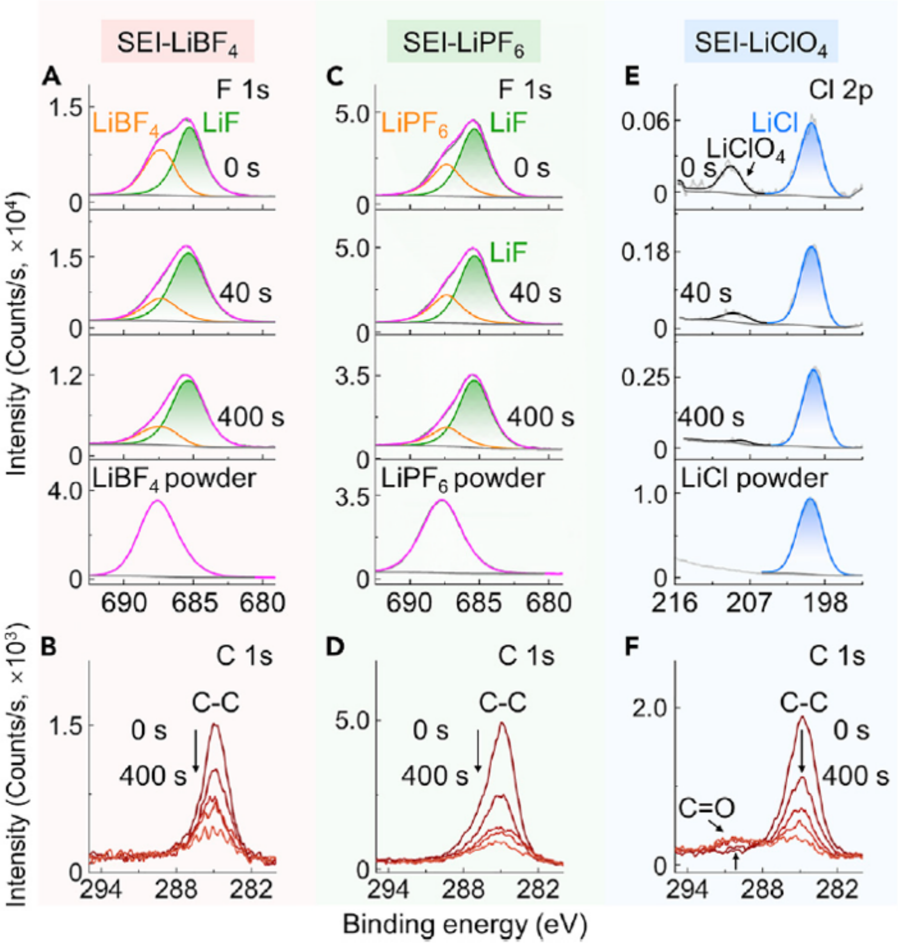

Figure 5.13: XPS spectra of the SEI layer at -1 A/cm$^2_{geo}$ ar 20 bar for **A-B** $LiBF_4$, **C-D** $LiPF_6$ and **E-F** $LiClO_4$. Data obtained from Paper 5 [119].

As predicted by theory, both the SEI layer of $LiBF_4$ and $LiPF_6$ exhibit a F 1s signal at 685.5 eV that is attributed to LiF according to values from literature [137]. In addition to that, another peak of the respective salts is also seen, which is probably due to residual dried salt from the electrolyte. These signals are diminished through consecutive Ar sputtering. A similar case is seen for the XPS spectra of the SEI with $LiClO_4$ with the salt itself being present in addition to a LiCl signal at 200 eV. All the C 1s spectra for the three salts show mostly C-C peaks that are also reduced upon sputtering. In the case of $LiClO_4$ a C=O peak develops upon sputtering, that could arise from Li_2CO_3 [138].

Next the deposit was also investigated by XPS. For that, standard experiments at -1 A/cm$^2_{geo}$ were performed until they reached 240 C, before transfer into the XPS chamber. The resulting data is presented in Fig. 5.14.

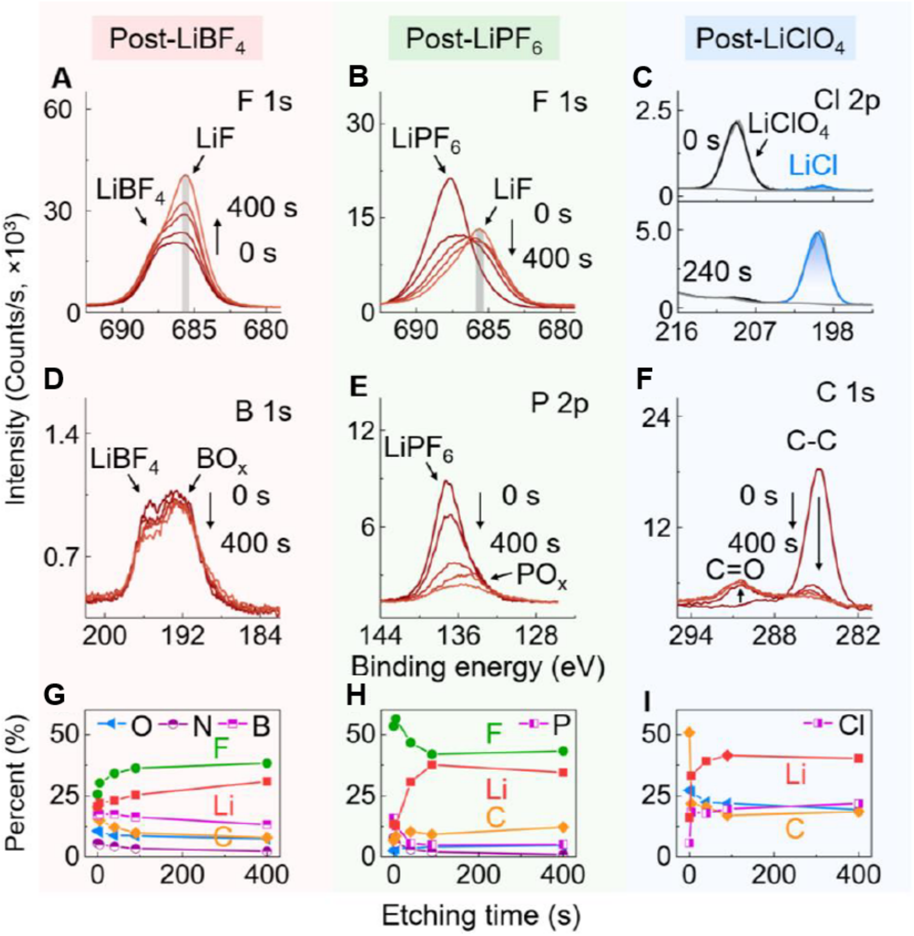

Figure 5.14: **A-F** XPS spectra of the deposit layer at -1 A/cm$^2_{geo}$ for the different Li-salts. **G-I** Elemental composition of the deposit layer at -1 A/cm$^2_{geo}$ at 20 bar for the different Li-salts. Data obtained from Paper 5 [119].

Again, a strong signal of LiF can be seen in the cases of $LiBF_4$ and $LiPF_6$ that stays constant even with Ar sputtering, hinting towards an even and rich LiF deposit. For $LiBF_4$ the B 1s spectra also shows a consistent BO_x signal, whereas the PO_x signal in the P 2p spectra for $LiPF_6$ depletes rapidly with Ar sputtering. This means that the deposit is mostly even in the case of $LiBF_4$ and uneven for $LiPF_6$, which makes sense given the instability of the latter. The Cl 2p and C 1s spectra of the $LiClO_4$ deposit show similar features as to their SEI equivalent, with signals of LiCl and Li_2CO_3.

The elemental depth composition was also measured and is seen in Fig. 5.14 **G-I**. The LiF rich deposit can be again confirmed for $LiBF_4$ and $LiPF_6$, with more Li signal in the case of $LiPF_6$ due to the over-plating of Li, as was seen from the size of the deposition. This is also the case for $LiClO_4$, where the Li signal far out-weights the Cl signal. Moreover, the relative high signal of C in the $LiClO_4$ case hints towards more solvent decomposition.

5.3 Summary

In this chapter we have proven the ability of porous Cu electrodes, made by HBT to reach high current densities in the LiMEAS. The initial conditions were improved with the help of theoretical predictions.

- High surface area Cu electrodes were successfully deposited on Ni foam as a substrate by the HBT method.

- The ability of HBTCu electrodes to increase current density was confirmed by initial testing at 20 bar N_2 and resulted in a FE and EE of 13.3 ± 2.0 % and 2.3 ± 0.3 %, respectively and a NH_3 formation rate of 46.0 ± 6.8 nmol/s $\cdot$cm$^{-2}{}_{geo}$.

- The electrolyte concentration needed to be increased to 2 M to increase the conductivity of the electrolyte as well as decrease the thickness of the EDL to probe the surface morphology of the high surface area electrodes.

- Increasing the concentration also improved the stability of the system, most likely through making a more inorganic-rich SEI layer.

- The substrate was changed from Ni foam to SS, which gives a mechanically more stable WE due to the more homogeneous current distribution. The times of deposition were also varied to achieve the maximum ECSA increase. At a deposition time of 5 min the roughness factor was determined by capacitive cycling to be 308.

- Theoretical calculation suggests that SEI components with good surface mobility but bad vertical Li^+ conductivity are preferential for high FE. LiF was predicted to be a beneficial constituent in the SEI layer due to its lower Li surface mobility barrier and lower Li^+ conductivity, which will lead to a more even Li plating behavior and better LiMEAS conditions.

- This hypothesis was tested at 20 bar with different Li salts ($LiClO_4LiBF_4LiPF_6$) in the electrolyte. Indeed, the F-containing salts were found to have higher FE with the highest FE of FE of 95 ± 3 % in 2 M $LiBF_4$ at a current density of -100 mA/cm$^2{}_{geo}$. The current density could further be increased to -1 A/cm$^2{}_{geo}$ which resulted in a NH_3 formation rate of 2.5 ± 0.1 μ mol/s $\cdot$cm$^{-2}{}_{geo}$ at a FE and EE of 71 ± 3 % and 7.7 ± 0.3 %, respectively.

- The NH_3 content was measured in all three different phases: gas, liquid and solid phase through a separation procedure. It was found that in $LiClO_4$ electrolytes half of the total NH_3 was trapped inside the deposition.

- The existence of LiF was confirmed in $LiBF_4$ and $LiPF_6$ electrolytes via air and moisture free XPS investigations.

6 Role of Ethanol in the Li-mediated Ammonia Synthesis

In this chapter the latest results regarding the several roles and importance of EtOH in our system will be discussed. Since these are relatively fresh results, they have not been polished and published yet. However, a manuscript is in preparation that is lead by my colleague Bjarke. In this chapter I will only present the experiments that I personally designed and conducted, which will be published in the future along with other complimentary data.
In the beginning, Tsuneto added EtOH mainly as a proton source, but since studying this system more closely the last few years, we have discovered that EtOH also has other roles such as leading to an improvement of electrolyte stability and also as an important constituent in the SEI layer. Interestingly, other groups also came to this conclusion with different experimental approaches, which makes us more confident [66].

6.1 Ethanol as Proton Source

As our electrolyte inherently has no protons, with the exception of minimal contamination of water (around 30 ppm measured by KFT before reaction). Tsuneto et al. added small amounts of EtOH as a proton source [52, 53]. Our group along with others have accepted EtOH as proton source and deemed it as a sacrificial proton source, since it is used up and not regenerated [55]. Confirming the proton source theory, several groups have reported that without added EtOH in the beginning no FE towards NH_3 can be observed and interestingly the electrolyte turns brown over time, hinting towards severe electrolyte degradation without EtOH [49, 66]. However, Krempl et al. [59] have shown in their publication that the proton source in the system can also be the solvent THF that gets oxidized at the anode to dihydrofuran and releases two protons. This dihydrofuran has been confirmed by GCMS in our group [60]. In (6.1) the structures of THF and dihydrofuran are shown to visualize where the protons come from THF.

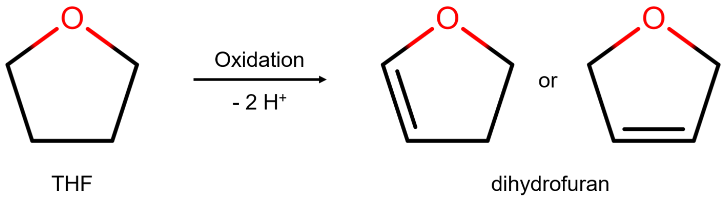

(6.1)

6.2 Ethanol as Stabilization Agent

As stated above, without EtOH the electrolyte turns brown after electrochemistry and over some time becomes viscous, hinting to the polymerisation of THF. With the same amount of charge passed with added EtOH in the system the electrolyte stays clear. This suggests that EtOH has a stabilizing effect towards hindering polymerization of THF. The onset of THF polymerization has been seen in literature at potentials of 4 V vs. Li/Li^+ [139] and has following mechanism seen in (6.2) according to [61]:

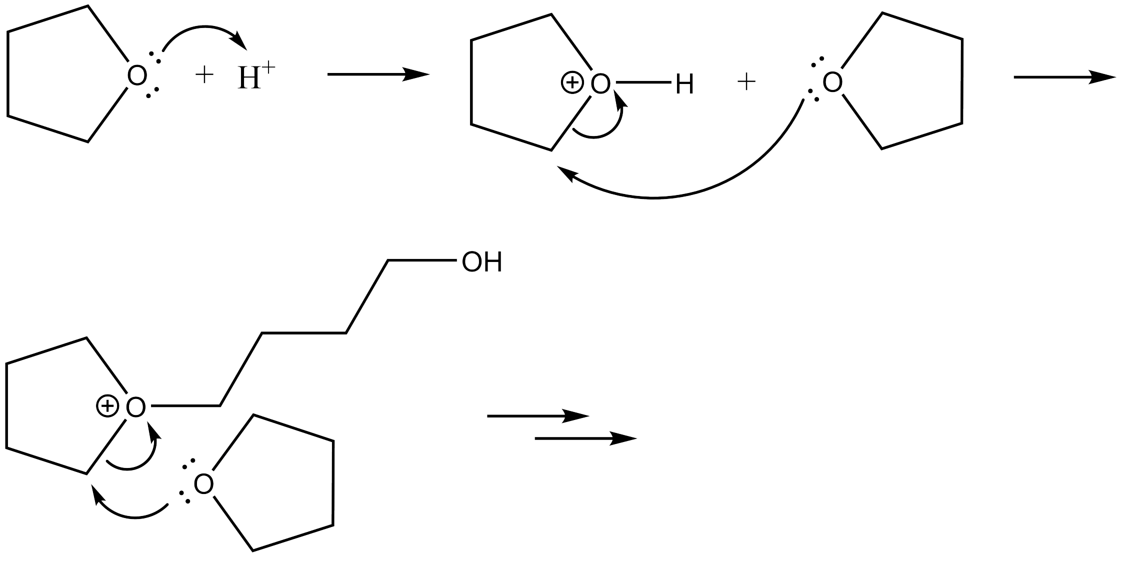

(6.2)

The polimerization is initiated by a proton, most likely from the dihydrofuran formation mentioned above. One of the lone pairs of O attacks the proton to form an oxonium ion, which is the basis for polymerization. Another THF molecule then attacks the C in ortho position of the oxonium ion and the ring opens.

EtOH is somehow able to prevent or more likely hinder the polymerization of THF. Several explanations are possible. For once, EtOH could be oxidized at the CE and therefore act as sacrificial oxidation agent. Another possibility is that EtOH, or its oxidated equivalents can interfere with the THF polimerization, either by stabilizing the oxonium ion or reacting with it faster than it can react with THF. Too little information is known at this point to speculate further, however, the oxidation of EtOH to acetic acid and acetaldehyde at the CE electrode has been proven by GC-MS measurements [60].

6.3 Ethanol as Part of the Solid Electrolyte Interface

Very recently another role of EtOH as a constituent of the SEI layer was developed, where Steinberg et. al investigated the SEI layer, with and without EtOH with cryo-TEM and found visibly different morphologies [66]. In parallel, we also found the importance for EtOH in the SEI layer with a different electrochemical approach.

For those experiments a single compartment glass cell was used in the glovebox with a standard electrolyte of 0.5 M $LiClO_4$ with 0.17 M EtOH in THF. The experiment consisted of a CP at –4 mA/cm^2 until 10 C were reached. Then the electrolyte was switched to an electrolyte with the same salt concentration but without EtOH, whereas the WE remained the same. Consequently, another CP was performed under the same conditions and the FE of both runs were then evaluated. A detailed description of the experimental procedure can be found in B.1.3.

It has to be noted that after removing the first electrolyte the cell was rinsed with pure THF to remove any residual EtOH for the second run. The EtOH concentration is estimated to be in the ppb levels at maximum. If any NH_3 is made in the second run without EtOH, it would mean that EtOH does not act as a proton source and is only important in the beginning of the experiment for SEI formation. The electrochemical results are presented in Fig. 6.1.

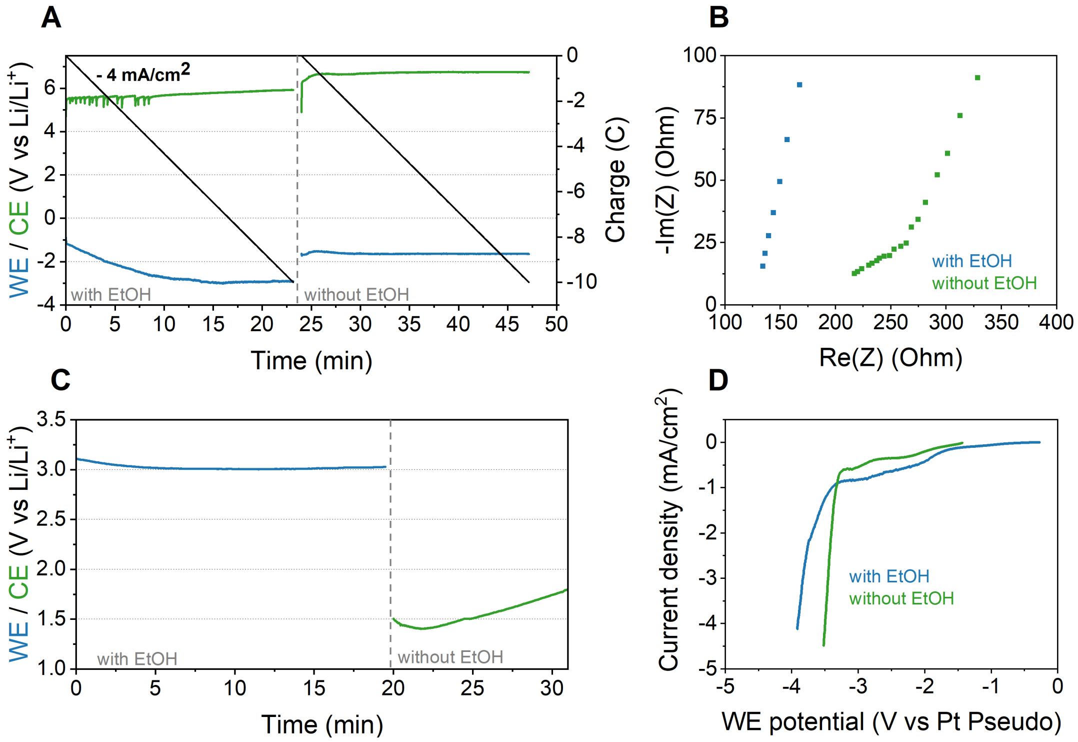

Figure 6.1: Electrochemical results of EtOH exchange experiments. **A** CP, **B** PEIS, **C** OCV and **D** LSV for experiments with and without EtOH. The WE was Mo, the CE and RE were Pt. The electrolyte was 0.5 M $LiClO_4$ + 0.17 M EtOH in THF.

The first part of the CP in Fig. 6.1 **A** shows that with EtOH the WE potential destabilizes over time, as is expected. Surprisingly, in the second run without EtOH the WE stays stable. This was seen in all repeat experiments and shows that it might be EtOH derived compounds that destabilize the WE potential. The potential vs Li/Li$^+$ was determined using the onset potential of Li plating from the recorded LSV that is shown in Fig. 6.1 **D**.The slightly higher cell potentials in the second run stem from uncompensated resistances, since without EtOH the electrolyte resistance is higher as is seen from the PEIS data in Fig. 6.1 **B**. To ensure that the SEI layer is maintained for the second run, OCV spectra were recorded before each CP as seen in Fig. 6.1 **C**. The OCV of the WE in the very beginning is around 3 V vs Li/Li$^+$, whereas before the second run it is distinctly more negative at 1.5 V vs Li/Li$^+$ but rising steadily. However, it was ensured that still some kind of deposit or SEI layer remained on the WE before starting the second CP. After evaluation of the FE, we found that without the EtOH more NH_3 is being formed than with EtOH. The FE in the first run with EtOH was 4.4 ± 1.7 % whereas in the second run it was 20.0 ± 2.1 %. These unexpected results confirm the assumption that EtOH is only important for the SEI formation in the beginning and THF can act as a proton source later on. The increase in FE can also be explained by the heatmap in Fig. 4.10. At atmospheric pressure the reaction is most definitely in the nitrogen limited regime, meaning a reduction in proton availability will increase the FE. However, the fact remains that EtOH is still important to stabilize the solvent.

As seen in Fig. 6.2, the electrolyte after the exchange to no EtOH still turns dark after passing charge.

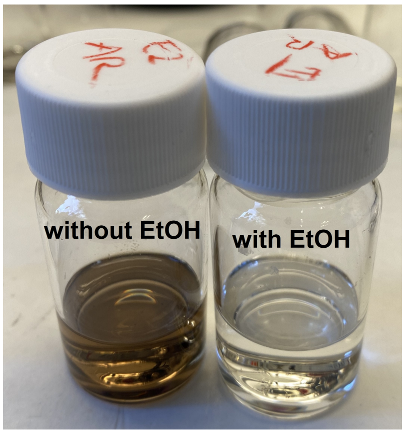

Figure 6.2: Electrolyte after electrochemistry with and without EtOH.

To investigate this interesting effect further, the next step was to vary the duration of the CP with and without EtOH. With this it is possible to evaluate when the SEI is formed and how long it is stable. Since with CP the passed charge is proportional to the time, three different charge distributions were chosen to compare to the standard 10/10 experiment: 5/10, 10/20 and 10/59. The results are listen in Fig. 6.3 and Tab. 6.1.

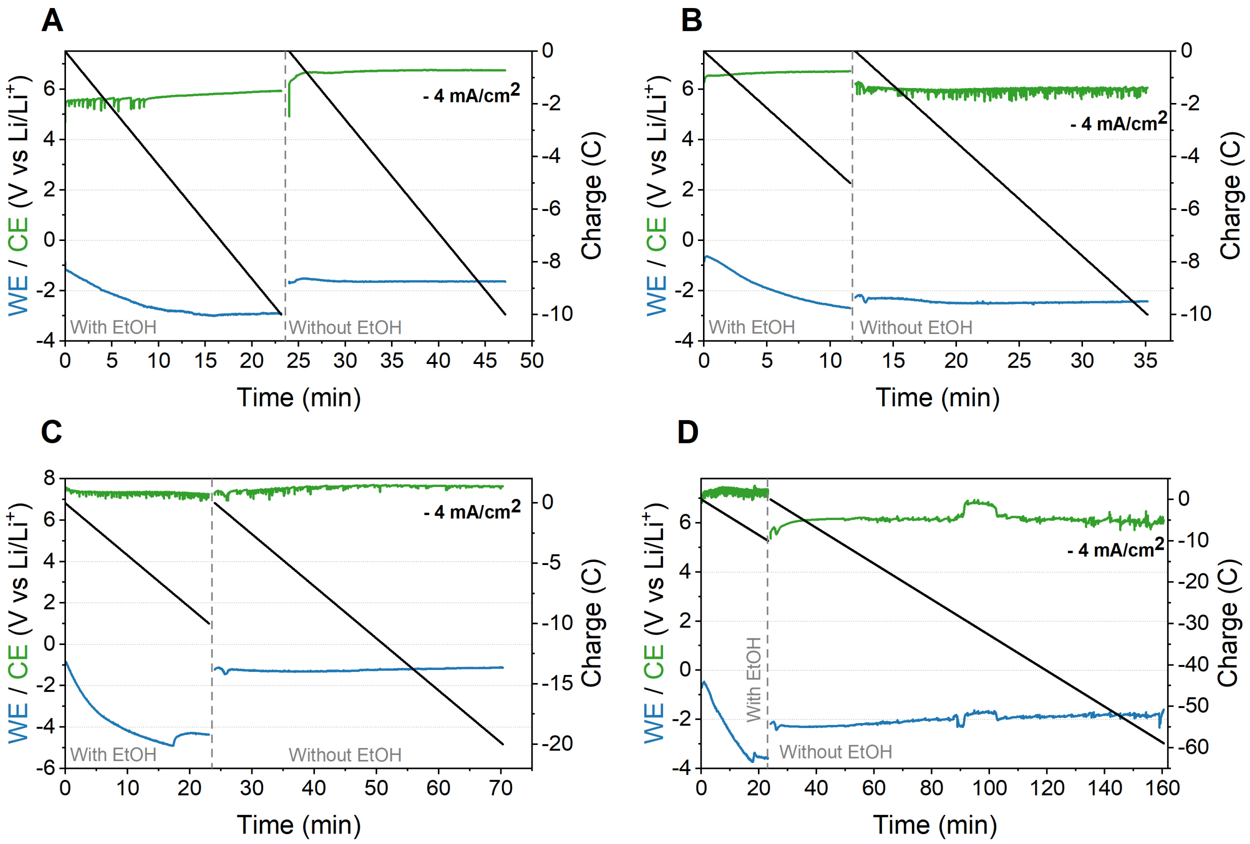

Figure 6.3: CPs of EtOH exchange experiments with different charge distribution of **A** 10/10, **B** 5/10, **C** 10/20 and **D** 10/59. The WE was Mo, the CE and RE were Pt. The electrolyte was 0.5 M $LiClO_4$ + 0.17 M EtOH in THF.

Table 6.1: FE of the EtOH exchange experiments with variation of charge passed with and without EtOH.

Charge with EtOH [C]	FE with EtOH [%]	Charge without EtOH [C]	FE without EtOH [%]
10	4.4 ± 1.7	10	20 ± 2.1
5	1.6	10	17
10	3.6	20	14.3
10	1.6	59	6.1

It has to be noted that for the values with no error bars, the experiments were only performed once. However, given the general good reproducibility of the experiments and the fact that we only want to observe trends it is still valuable information that we can gain from this.

The experiment with charge distribution of 5/10 shows that even when less charge is passed with EtOH the effect still holds, meaning the role of EtOH is in the very beginning, probably initial few minutes, like the SEI formation. With the second run without EtOH being longer in the 10/20 experiment it is still possible to make ammonia at higher FE but the value dropped by a bit to around 14 %. The dropping value could indicate that SEI layer is not stable but needs to consistently be replenished. This is further confirmed by the last 10/59 experiment where the FE dropped even further to 6 %.

Analysis of the SEI layer through impedance measurements

As already mentioned in the beginning of the chapter, these measurements show initial data and are not polished yet. Even though the following data was repeated three times and the same trend was observed, I would still advise to look at the data critically.

As EIS is a method to investigate the SEI layer and deposit *in-operando* in a simple experimental way, galvanostatic EIS (GEIS) were recorded before the CP to observe the development of the resistance in the beginning of a measurement, as well as after the CP. The GEIS were measured at the same current density as the CP to simulate reaction conditions. The resulting GEIS for the electrolyte with and without EtOH are both seen in Fig. 6.4.

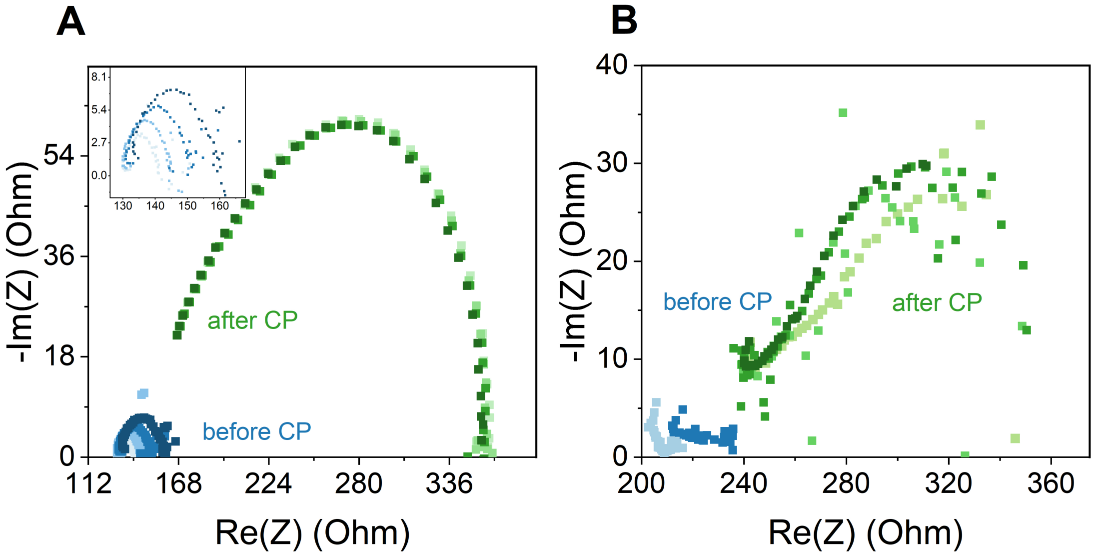

Figure 6.4: GEIS of LiMEAS in 0.5 M $LiClO_4$ **A** with and **B** without 0.17 M EtOH in THF at –4 mA/cm^2. The GEIS were recorded before the CP (blue) and after the CP (green). The lighter color represents earlier measurements and the darker colors represent later measurements.

Fig. 6.4 **A** shows the results of the measurement with added EtOH. The blue GEIS were recorded after the LSV and before the CP and the green ones were recorded after the CP. The different shades represent the number of repetitions, with a lighter shade being recorded earlier in time. The insert in Fig. 6.4 **A** shows that the charge transfer resistance is consistently growing over time, due to the development of the SEI layer in addition to Li deposition. After the CP the recorded GEIS were constant, meaning that the deposition has reached a steady state behavior. The GEIS spectra in Fig. 6.4 **B** without EtOH do not show such a nice trend. On the contrary, no informative spectra could be recorded. That itself must mean that the deposition is quite different from the one with EtOH. As was also observed by Steinberg et al. [66], without EtOH the deposition is quite uneven. By eye we could observe dendrites being formed and after reaction when taking out the electrolyte, the deposition fell off immediately leaving a blank Mo foil behind. This means that the Li on the Mo surface is not in strong contact to the electrode, which might result in these noisy GEIS spectra.

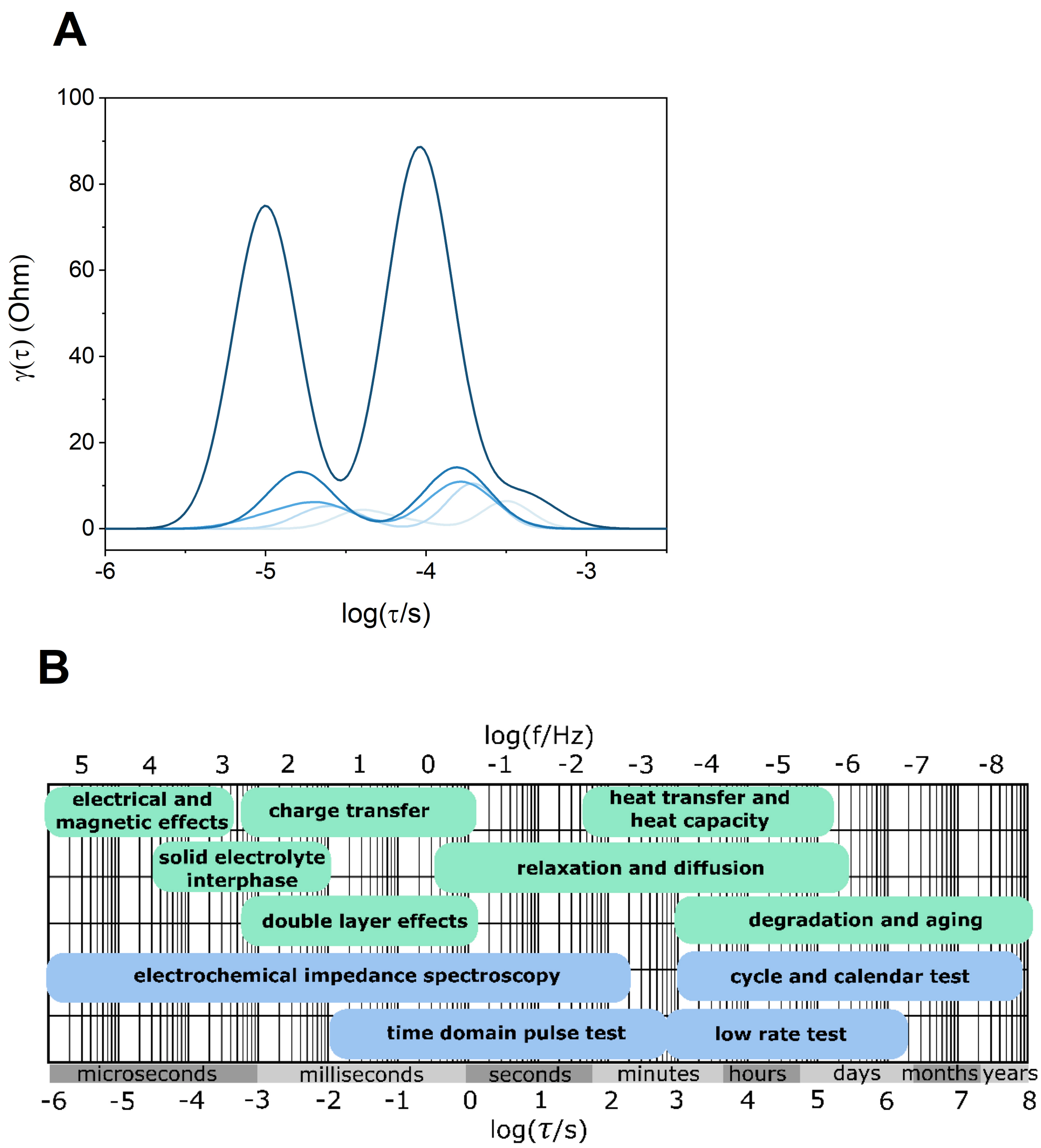

Figure 6.5: **A** DRT analysis of GEIS from measurement in 0.5 M $LiClO_4$ with 0.17 M EtOH in THF at −4 mA/cm^2. The lighter color represents earlier measurements and the darker colors represent later measurements. **B** Time constants of typical electrode processes. [73]

To gain even more knowledge from this data a distribution of relaxation time (DRT) analysis was carried out. This should give insights into how many processes are occurring with which time constants. One has to be very careful with DRT analysis since the results depend heavily on how one chooses the fitting parameters. A detailed description of the DRT analysis and the fitting parameters used is described in the Appendix B.1.3. The DRT analysis of the GEIS spectra shown in Fig. 6.4 **A** is given in Fig. 6.5 **A**.

Two distinct peaks can be observed that grow over time and shift towards lower τ/s values. When looking at the characteristic time constants of different processes in Fig. 6.5 **B**, the slower process, which starts at $10^{-3.5}$ s and shift to 10^{-4} s could be a charge transfer process whereas the faster one could be an SEI related phenomenon. Since the charge transfer reaction from Li^+ to Li is fast at these largely negative potentials these time constant values would make sense. If this DRT analysis is proven to be correct, it could be a valuable tool to both investigate the SEI layer as well as the Li plating behavior under different conditions such as electrolyte salt or pressure. Indeed, DRT analysis has been used in literature to investigate the Li plating and SEI in Li-ion batteries and as seen in Fig. 3.8 their determined time constants fit very well with the ones we measure here [76].

6.4 Summary

In this chapter the different roles of EtOH in the LiMEAS were discussed. Through the experimental design of changing the electrolyte from EtOH containing electrolyte to electrolyte without electrolyte, while maintaining the deposition on the WE, the following conclusions could be drawn:

- EtOH is needed in the beginning of the experiment, most likely for the SEI formation, but afterwards NH_3 can still form. Not only that, but the FE without EtOH is even higher, increasing from 4.4 ± 1.7 % with EtOH to 20 ± 2.1 % without EtOH. This is because the LiMEAS at ambient pressure is N-limited and hence a decrease in H^+ concentration would be preferential.

- These experiments also prove that EtOH can not be the (only) H^+ source, hence the H^+ can also come from THF oxidation to dihydrofuran, which was proven by GC-MS.

- With experiments running different amount of times, it is seen that this effect does not last forever, since the SEI might need to be replenished.

- EtOH also has a role in the stability of the electrolyte, since without EtOH the electrolyte turns brown and polymerizes after time.

- EIS measurements with subsequent DRT analysis detect two processes at the WE, which could be the charge transfer of Li plating and a SEI related phenomenon.

7 General discussion and conclusion

In this last chapter a summary of the last three chapters will be given along with a conclusion of this thesis and the key findings described here. Next, a general discussion of the LiMEAS will follow along with the upcoming challenges that need to be solved. This then will lead directly into the outlook and the thesis will be concluded there.

7.1 Summary and conclusion

The goal of this thesis was to improve the FE and current density of the LiMEAS. At the very start of the thesis in December 2019 the highest published FE value was from Tsuneto et al. in 1994 where they achieved 57.7 % at 50 bar at a current density of $-2\,\mathrm{mA/cm^2}$. These values were somehow questionable since they did not have gas cleaning and at 50 bar reaction pressure, a lot of NO_x contamination could be present. The next highest and more trustworthy result came from and Lazouski et al. where they presented a FE of 18.5 % at $-3\,\mathrm{mA/cm^2}$ [49].
Since the separate chapter were already summarized in their respective sections this will be kept short.

In chapter 4 the FE was increased from 24.7 ± 0.5 % to 78 ± 1.3 % at 20 bar trough the addition of small amounts of around 0.6 - 0.8 mol % O_2. This effect was explained by the modification of the SEI layer through O_2 that leads to more favorable conditions for Li to react with N_2. This hypothesis is supported by experimental and theoretical results as well as reports in literature.
Chapter 5 focused on increasing the current density through synthesis of high surface area Cu electrodes with the HBT method. After the initial verification at -100 $\mathrm{mA/cm^2}_{\mathrm{geo}}$ both the deposition conditions of HBT and the reaction electrolyte was modified to achieve optimal results. The optimization of the electrolyte was initiated by theoretical calculations that showed a beneficial role of LiF in the SEI layer. With using $LiBF_4$ as the electrolyte salt a current density of -1 $\mathrm{A/cm^2}_{\mathrm{geo}}$ was achieved with FE of 71 ± 3 %.
Chapter 6 was a more fundamental study on the role of EtOH in the LiMEAS. Contrary to initial believes, EtOH does not (only) act as a proton source, but also as an important constituent in

the SEI layer. This was confirmed through EtOH exchange experiments where a reaction as initiated with EtOH present and then continued without EtOH. The FE in these two consecutive runs increased from 4.4 ± 1.7 % with EtOH to 20 ± 2.1 % without EtOH, showing that EtOH is only needed in the beginning of the experiment to form the SEI layer.

7.2 Future of Li-mediated ammonia synthesis

Undoubtedly, the LiMEAS has seen a lot of improvement in the last 3 years, owing to the interest initiated by Andersen et al. [40] and the hard work in our group, as well as others [66, 67, 125] . Since only a few labs are working on this reaction, the steep improvement is astonishing. Now with the FE already close to 100 % [58] and current densities of -1 $A/cm^2{}_{geo}$ [119] it is easy to say that the LiMEAS has been mastered, which could not be further from the truth. There are still several issues that need to be addressed:

- Most of the experiment reporting these high numbers are done in batch type cells, which is very hard to up-scale [58, 119]. The only flow cell publication with GDE so far is by Lazouski et al. [56], however with high cell potentials and unstable operation. The goal here would be to have a continuous ammonia production in a flow-cell at ambient pressures and temperatures combined with high current density and FE. The reaction would be LiMEAS at the WE and HOR at the CE to produce the protons. This leads us to the second challenge of proton source.

- Until now several groups have tried to utilize HOR on the CE [55, 56], but they lack credibility, since their CE potential were still high at above 1 V vs Pt, which are already the potentials where THF can be oxidized to form protons [61]. The definite proof of HOR on the anode would be if the potentials are kept low and deuterium tests are performed, which results in formation of ND_3.

- Furthermore, THF which is the solvent of choice in most LiMEAS publications has a high vapor pressure and low boiling point, which makes it very volatile. Additionally, it is also very harmful to the environment and also suspected to cause cancer [140, 141]. All these factors makes it hard to be admitted in any food related application, like fertilizers. Ideally, another solvent should be found without these health risks. However, this will be an challenge, since the SEI layer, which plays a huge role in our process, should be heavily influenced by the solvent. Hence, all the optimization that was already performed for THF would need to be repeated if the solvent is changed.

- As of now, it seems that the LiMEAS in general is an unstable reaction that decomposes THF both on the CE as well as on the WE. A part of the decomposition is needed to form the SEI layer but the other decomposition pathways leading to the various compounds detected by GC-MS [60, 70] show that even in these short term experiments (< 5 h) significant electrolyte decomposition takes place. This is due to the large applied potential on both electrodes and high reactivity of metallic Li. The same challenge is probably faced in Li metal batteries where the cycling life is very limited. Addition of additives could be a way to tackle this challenge [142].

- This leads to the final challenge, which is probably the hardest to overcome, namely the large potentials. The whole idea of LiMEAS is to activate N_2 by metallic Li, but plating Li costs a large amount of energy, more than is theoretically needed to split the triple bond. In addition with the large resistances in the typical non-aqueous electrolytes this leads to very high cell potentials. Even at the most ideal condition of HOR at 0 V and no overpotential for Li plating the maximum achievable voltage efficiency would be $\frac{1.19V}{3.04V} = 39\%$, but more realistically it would be in the range of 25 %. One can then ask the question how relevant this process then is, but it has to be said that this is currently the only proven way to electrochemically make NH_3. So until a more energy efficient pathway is found the LiMEAS it still the best option for electrochemical NH_3 synthesis.

In addition to all these challenges, there is also still unanswered questions about the fundamentals of LiMEAS. Similar to the Li metal batteries, the Li plating behavior can be studied in more detail, like how the nucleation and growth process influences the stability and FE. Of course the SEI also still remains a mystery and can probably only truly be investigated *in-situ*.

7.3 Outlook

The goal of increasing the FE and current density was achieved in this thesis, however the challenge would be to combine these two factors in a setup that can produce NH_3 continuously. Furthermore, the long time performance of the LiMEAS should be carefully investigated, as there are worries about solvent degradation.

As for the last part of the thesis, I would have liked to investigate the GEIS data further by doing DRT analysis with different salts, pressures and O_2 contents to see if our predictions about the modification of SEI layer is also visible in the DRT. It would have been a direct prove if the charge transfer of Li plating is slowed down with the addition of O_2. In general, it seems to me that EIS, if used correctly, might be a powerful tool to investigate the SEI layer and Li plating *in-operando*.

I believe that after achieving high current densities and FE, the future of the LiMEAS will shift now from improving those numbers to more engineering related questions. How can the cell be modified to produce continuous ammonia and how can the resistance be decreased through cell design? Can we learn from CO_2 reduction, where they now apply membrane electrode assemblies? Also numbers like EE and cost per kilo NH_3 will be the next targets to improve upon as was correctly pointed out in [143].

If LiMEAS will continue to be a topic of interest or be deemed too expensive without real application value will depend heavily on the development in the next few years. This makes it a very interesting time to be in the field and me along with many others will look forward to observing and being part of this process.

A Bibliography

[1] A. Valera-Medina, H. Xiao, M. Owen-Jones, W. I. David, and P. Bowen, "Ammonia for power", Progress in Energy and combustion science **69**, 63–102 (2018).

[2] A. A. Lima, G. d. N. Leite, A. A. Ochoa, C. A. d. Santos, J. A. d. Costa, P. S. Michima, and A. M. Caldas, "Absorption refrigeration systems based on ammonia as refrigerant using different absorbents: review and applications", Energies **14**, 48 (2020).

[3] FAO-Food and A. O. o. t. U. Nations, "World fertilizer trends and outlook to 2020", (2017).

[4] F. Haber and G Van Oordt, "Ueber die bildung von ammoniak aus den elementen", Zeitschrift für anorganische Chemie **44**, 341–378 (1905).

[5] G. Soloveichik, "Electrochemical synthesis of ammonia as a potential alternative to the haber–bosch process", Nature Catalysis **2**, 377–380 (2019).

[6] F. Haber, "The synthesis of ammonia from its elements", Nobel Lecture **2** (1920).

[7] C. Bosch, "Ueber die entwicklung der chemischen hochdrucktechnik bei dem aufbau der neuen ammoniakindustrie", Nobel Lecture **21** (1932).

[8] J. W. Erisman, M. A. Sutton, J. Galloway, Z. Klimont, and W. Winiwarter, "How a century of ammonia synthesis changed the world", Nature Geoscience **1**, 636–369 (2008).

[9] C. Smith, A. K. Hill, and L. Torrente-Murciano, "Current and future role of haber–bosch ammonia in a carbon-free energy landscape", Energy and Environmental Science **13**, 331–344 (2020).

[10] A. Vojvodic, A. J. Medford, F. Studt, F. Abild-Pedersen, T. S. Khan, T Bligaard, and J. Norskov, "Exploring the limits: a low-pressure, low-temperature haber–bosch process", Chemical Physics Letters **598**, 108–112 (2014).

[11] C. J. Van der Ham, M. T. Koper, and D. G. Hetterscheid, "Challenges in reduction of dinitrogen by proton and electron transfer", Chemical Society Reviews **43**, 5183–5191 (2014).

[12] D. R. MacFarlane, P. V. Cherepanov, J. Choi, B. H. Suryanto, R. Y. Hodgetts, J. M. Bakker, F. M. F. Vallana, and A. N. Simonov, "A roadmap to the ammonia economy", Joule, 1186–1205 (2020).

[13] I. Hadjipaschalis, A. Poullikkas, and V. Efthimiou, “Overview of current and future energy storage technologies for electric power applications”, Renewable and sustainable energy reviews **13**, 1513–1522 (2009).

[14] N. Morlanés, S. P. Katikaneni, S. N. Paglieri, A. Harale, B. Solami, S. M. Sarathy, and J. Gascon, “A technological roadmap to the ammonia energy economy: current state and missing technologies”, Chemical Engineering Journal **408**, 127310 (2021).

[15] C. H. Christensen, T. Johannessen, R. Z. Sørensen, and J. K. Nørskov, “Towards an ammonia-mediated hydrogen economy?”, Catalysis Today **111**, 140–144 (2006).

[16] C Zamfirescu and I Dincer, “Using ammonia as a sustainable fuel”, Journal of Power Sources **185**, 459–465 (2008).

[17] J. Hansson, E. Fridell, and S. Brynolf, “On the potential of ammonia as fuel for shipping: a synthesis of knowledge”, (2020).

[18] Y. Bicer, I. Dincer, C. Zamfirescu, G. Vezina, and F. Raso, “Comparative life cycle assessment of various ammonia production methods”, Journal of Cleaner Production **135**, 1379–1395 (2016).

[19] B. Lee, L. R. Winter, H. Lee, D. Lim, H. Lim, and M. Elimelech, “Pathways to a green ammonia future”, ACS Energy Letters, 3032–3038 (2022).

[20] A. Buttler and H. Spliethoff, “Current status of water electrolysis for energy storage, grid balancing and sector coupling via power-to-gas and power-to-liquids: a review”, Renewable and Sustainable Energy Reviews **82**, 2440–2454 (2018).

[21] H. Zhang, L. Wang, F. Maréchal, and U. Desideri, “Techno-economic comparison of green ammonia production processes”, Applied Energy **259**, 114135 (2020).

[22] The Royal Society, "Ammonia: zero–carbon fertiliser, fuel and energy store", https://royalsociety.org/–/media/policy/projects/green–ammonia/green–ammonia–policybriefing.pdf (2020).

[23] Thyssenkrupp, https://www.thyssenkrupp-industrial-solutions.com/power-to-x/en/green-ammonia/.

[24] G. Qing, R. Ghazfar, S. T. Jackowski, F. Habibzadeh, M. M. Ashtiani, C.-P. Chen, M. R. Smith III, and T. W. Hamann, “Recent advances and challenges of electrocatalytic n2 reduction to ammonia”, Chemical reviews **120**, 5437–5516 (2020).

[25] E. Skulason, T. Bligaard, S. Gudmundsdóttir, F. Studt, J. Rossmeisl, F. Abild-Pedersen, T. Vegge, H. Jónsson, and J. K. Nørskov, “A theoretical evaluation of possible transition metal electro-catalysts for n 2 reduction”, Physical Chemistry Chemical Physics **14**, 1235–1245 (2012).

[26] G. Soloveichik, “Arpa-e refuel program: distributed production of ammonia and its conversion to energy”, in 2019 aiche annual meeting ().

[27] B. A. Rohr, A. R. Singh, and J. K. Nørskov, “A theoretical explanation of the effect of oxygen poisoning on industrial haber-bosch catalysts”, Journal of Catalysis **372**, 33–38 (2019).

[28]G. Hochman, A. S. Goldman, F. A. Felder, J. M. Mayer, A. J. Miller, P. L. Holland, L. A. Goldman, P. Manocha, Z. Song, and S. Aleti, "Potential economic feasibility of direct electrochemical nitrogen reduction as a route to ammonia", ACS sustainable chemistry and engineering **8**, 8938–8948 (2020).

[29]A. D. McNaught and A. Wilkinson, *Compendium of chemical terminology*, Vol. 1669 (Blackwell Science Oxford, 1997).

[30]Z. W. Seh, J. Kibsgaard, C. F. Dickens, I. Chorkendorff, J. K. Nørskov, and T. F. Jaramillo, "Combining theory and experiment in electrocatalysis: insights into materials design", Science **355**, eaad4998 (2017).

[31]A. Balandin, "Modern state of the multiplet theory of heterogeneous catalysis", Advances in catalysis **19**, 1–210 (1969).

[32]C. Hamann, A Hamnett, and W Vielstich, "Electrochemistry wiley", VCH: New York **17**, 121 (1998).

[33]A. J. Bard, L. R. Faulkner, and H. S. White, *Electrochemical methods: fundamentals and applications* (John Wiley and Sons, 2022).

[34]W. Schmickler and E. Santos, *Interfacial electrochemistry* (Springer, 2010).

[35]A. R. Singh, B. A. Rohr, M. J. Statt, J. A. Schwalbe, M. Cargnello, and J. K. Nørskov, "Strategies toward selective electrochemical ammonia synthesis", Acs Catalysis **9**, 8316–8324 (2019).

[36]J. Choi, B. H. Suryanto, D. Wang, H.-L. Du, R. Y. Hodgetts, F. M. Ferrero Vallana, D. R. MacFarlane, and A. N. Simonov, "Identification and elimination of false positives in electrochemical nitrogen reduction studies", Nature communications **11**, 1–10 (2020).

[37]J. H. Montoya, C. Tsai, A. Vojvodic, and J. K. Nørskov, "The challenge of electrochemical ammonia synthesis: a new perspective on the role of nitrogen scaling relations", ChemSusChem **8**, 2180–2186 (2015).

[38]A. R. Singh, B. A. Rohr, J. A. Schwalbe, M. Cargnello, K. Chan, T. F. Jaramillo, I. Chorkendorff, and J. K. Nørskov, "Electrochemical ammonia synthesis the selectivity challenge", (2016).

[39]S. S. Biswas, A. Saha, and M. Eswaramoorthy, "Facts or artifacts: pitfalls in quantifying sub-ppm levels of ammonia produced from electrochemical nitrogen reduction", ACS omega **7**, 1874–1882 (2022).

[40]S. Z. Andersen, V. Čolić, S. Yang, J. A. Schwalbe, A. C. Nielander, J. M. McEnaney, K. Enemark-Rasmussen, J. G. Baker, A. R. Singh, B. A. Rohr, M. J. Statt, S. J. Blair, S. Mezzavilla, J. Kibsgaard, P. Vesborg, M. Cargnello, S. F. Bent, T. F. Jaramillo, I. E. Stephens, J. K. Nørskov, and I. Chorkendorff, "A rigorous electrochemical ammonia synthesis protocol with quantitative isotope measurements", Nature **570**, 504–508 (2019).

[41] H. Iriawan, S. Z. Andersen, X. Zhang, B. M. Comer, J. Barrio, P. Chen, A. J. Medford, I. E. Stephens, I. Chorkendorff, and Y. Shao-Horn, “Methods for nitrogen activation by reduction and oxidation”, Nature Reviews Methods Primers **1**, 1–26 (2021).

[42] L. Li, C. Tang, D. Yao, Y. Zheng, and S.-Z. Qiao, “Electrochemical nitrogen reduction: identification and elimination of contamination in electrolyte”, ACS Energy Letters **4**, 2111–2116 (2019).

[43] J. Kibsgaard, J. K. Nørskov, and I. Chorkendorff, “The difficulty of proving electrochemical ammonia synthesis”, ACS Energy Letters **4**, 2986–2988 (2019).

[44] A. C. Nielander, J. M. McEnaney, J. A. Schwalbe, J. G. Baker, S. J. Blair, L. Wang, J. G. Pelton, S. Z. Andersen, K. Enemark-Rasmussen, and C. Viktor, “A versatile method for ammonia detection in a range of relevant electrolytes via direct nuclear magnetic resonance techniques”, ACS Catalysis **9**, 5797–5802 (2019).

[45] B. Hu, M. Hu, L. Seefeldt, and T. L. Liu, “Electrochemical dinitrogen reduction to ammonia by mo2n: catalysis or decomposition?”, ACS Energy Letters **4**, 1053–1054 (2019).

[46] H.-L. Du, T. R. Gengenbach, R. Hodgetts, D. R. MacFarlane, and A. N. Simonov, “Critical assessment of the electrocatalytic activity of vanadium and niobium nitrides toward dinitrogen reduction to ammonia”, ACS Sustainable Chemistry and Engineering **7**, 6839–6850 (2019).

[47] O. Westhead, R. Jervis, and I. E. Stephens, “Is lithium the key for nitrogen electroreduction?”, Science **372**, 1149–1150 (2021).

[48] I. E. L. Stephens, O. Westhead, A. Bagger, J. Barrio, Z. Shen, H. Yadegari, M. Spry, R. Jervis, M. Titirici, and M. Ryan, “(keynote) why is lithium uniquely able to reduce nitrogen to ammonia under ambient conditions?”, in Ecs meeting abstracts (), p. 1542.

[49] N. Lazouski, Z. J. Schiffer, K. Williams, and K. Manthiram, “Understanding continuous lithium-mediated electrochemical nitrogen reduction”, Joule **3**, 1127–1139 (2019).

[50] M. Titirici, S. G. Baird, T. D. Sparks, S. M. Yang, A. Brandt-Talbot, O. Hosseinaei, D. P. Harper, R. M. Parker, S. Vignolini, and L. A. Berglund, “The sustainable materials roadmap”, Journal of Physics: Materials **5**, 032001 (2022).

[51] F. Fichter, P. Girard, and H. Erlenmeyer, “Elektrolytische bindung von komprimiertem stickstoff bei gewoehnlicher temperatur”, Helvetica Chimica Acta **13**, 1228–1236 (1930).

[52] A. Tsuneto, A. Kudo, and T. Sakata, “Lithium-mediated electrochemical reduction of high pressure n2 to nh3”, Journal of Electroanalytical Chemistry **367**, 183–188 (1994).

[53] A. Tsuneto, A. Kudo, and T. Sakata, “Efficient electrochemical reduction of n2 to nh3 catalyzed by lithium”, Chemistry letters **22**, 851–854 (1993).

[54] R. Y. Hodgetts, H.-L. Du, T. D. Nguyen, D. MacFarlane, and A. N. Simonov, “Electrocatalytic oxidation of hydrogen as an anode reaction for the li-mediated n2 reduction to ammonia”, ACS Catalysis, 5231–5246 (2022).

[55] B. H. Suryanto, K. Matuszek, J. Choi, R. Y. Hodgetts, H.-L. Du, J. M. Bakker, C. S. Kang, P. V. Cherepanov, A. N. Simonov, and D. R. MacFarlane, “Nitrogen reduction to ammonia at high efficiency and rates based on a phosphonium proton shuttle”, Science **372**, 1187–1191 (2021).

[56] N. Lazouski, M. Chung, K. Williams, M. L. Gala, and K. Manthiram, “Non-aqueous gas diffusion electrodes for rapid ammonia synthesis from nitrogen and water-splitting-derived hydrogen”, Nature Catalysis, 463–469 (2020).

[57] X. Cai, C. Fu, H. Iriawan, F. Yang, A. Wu, L. Luo, S. Shen, G. Wei, Y. Shao-Horn, and J. Zhang, “Lithium-mediated electrochemical nitrogen reduction: mechanistic insights to enhance performance”, Iscience **24**, 103105 (2021).

[58] H.-L. Du, M. Chatti, R. Y. Hodgetts, P. V. Cherepanov, C. K. Nguyen, K. Matuszek, D. R. MacFarlane, and A. N. Simonov, “Electroreduction of nitrogen with almost 100 percent current-to-ammonia efficiency”, Nature **609**, 722–727 (2022).

[59] K. Krempl, J. B. Pedersen, J. Kibsgaard, P. C. Vesborg, and I. Chorkendorff, “Electrolyte acidification from anode reactions during lithium mediated ammonia synthesis”, Electrochemistry Communications **134**, 107186 (2022).

[60] R. Sažinas, S. Z. Andersen, K. Li, M. Saccoccio, K. Krempl, J. B. Pedersen, J. Kibsgaard, P. C. K. Vesborg, D. Chakraborty, and I. Chorkendorff, “Towards understanding of electrolyte degradation in lithium-mediated non-aqueous electrochemical ammonia synthesis with gas chromatography-mass spectrometry”, RSC Advances **11**, 31487–31498 (2021).

[61] A. Dey and E. Rudd, “Electroinitiated polymerization of tetrahydrofuran”, Journal of The Electrochemical Society **121**, 1294 (1974).

[62] S. Z. Andersen, M. J. Statt, V. J. Bukas, S. G. Shapel, J. B. Pedersen, K. Krempl, M. Saccoccio, D. Chakraborty, J. Kibsgaard, and P. C. Vesborg, “Increasing stability, efficiency, and fundamental understanding of lithium-mediated electrochemical nitrogen reduction”, Energy and Environmental Science **13**, 4291–4300 (2020).

[63] D Aurbach, M. Daroux, P. Faguy, and E Yeager, “Identification of surface films formed on lithium in propylene carbonate solutions”, Journal of The Electrochemical Society **134**, 1611 (1987).

[64] E. Peled, “The electrochemical behavior of alkali and alkaline earth metals in nonaqueous battery systems—the solid electrolyte interphase model”, Journal of The Electrochemical Society **126**, 2047 (1979).

[65] A. Dey, “Lithium anode film and organic and inorganic electrolyte batteries”, Thin Solid Films **43**, 131–171 (1977).

[66] K. Steinberg, X. Yuan, N. Lazouski, C. K. Klein, K. Manthiram, and Y. Li, “Imaging nitrogen fixation at lithium solid electrolyte interphases via cryo-electron microscopy”, (2022).

[67]S. J. Blair, M. Doucet, J. F. Browning, K. Stone, H. Wang, C. Halbert, J. Aviles Acosta, J. A. Zamora Zeledon, A. C. Nielander, and A. Gallo, "Lithium-mediated electrochemical nitrogen reduction: tracking electrode–electrolyte interfaces via time-resolved neutron reflectometry", ACS Energy Letters **7**, 1939–1946 (2022).

[68]N. Elgrishi, K. J. Rountree, B. D. McCarthy, E. S. Rountree, T. T. Eisenhart, and J. L. Dempsey, "A practical beginner's guide to cyclic voltammetry", Journal of Chemical Education **95**, 197–206 (2017).

[69]X. Fu, J. B. Pedersen, Y. Zhou, M. Saccoccio, S. Li, R. Sazinas, K. Li, S. Z. Andersen, N. H. Deissler, J. B. Mygind, C. Wei, J. Kibsgaard, P. Vesborg, J. Norskov, and I. Chorkendorff, "Electrosynthesis of ammonia from nitrogen reduction coupled with hydrogen oxidation in a continuous-flow reactor", Submitted (2022).

[70]R. Sazinas, K. Li, S. Z. Andersen, M. Saccoccio, S. Li, J. B. Pedersen, J. Kibsgaard, P. C. Vesborg, D. Chakraborty, and I. Chorkendorff, "Oxygen-enhanced chemical stability of lithium-mediated electrochemical ammonia synthesis", The Journal of Physical Chemistry Letters **13**, 4605–4611 (2022).

[71]S. Wang, J. Zhang, O. Gharbi, V. Vivier, M. Gao, and M. E. Orazem, "Electrochemical impedance spectroscopy", Nature Reviews Methods Primers **1**, 1–21 (2021).

[72]B.-Y. Chang and S.-M. Park, "Electrochemical impedance spectroscopy", Annual Review of Analytical Chemistry **3**, 207–229 (2010).

[73]M. A. Danzer, "Generalized distribution of relaxation times analysis for the characterization of impedance spectra", Batteries **5**, 53 (2019).

[74]E. Ivers-Tiffee and A. Weber, "Evaluation of electrochemical impedance spectra by the distribution of relaxation times", Journal of the Ceramic Society of Japan **125**, 193–201 (2017).

[75]T. H. Wan, M. Saccoccio, C. Chen, and F. Ciucci, "Influence of the discretization methods on the distribution of relaxation times deconvolution: implementing radial basis functions with drttools", Electrochimica Acta **184**, 483–499 (2015).

[76]D. E. Brown, E. J. McShane, Z. M. Konz, K. B. Knudsen, and B. D. McCloskey, "Detecting onset of lithium plating during fast charging of li-ion batteries using operando electrochemical impedance spectroscopy", Cell Reports Physical Science **2**, 100589 (2021).

[77]M Łukaszewski, M Soszko, and A Czerwiński, "Electrochemical methods of real surface area determination of noble metal electrodes–an overview", Int. J. Electrochem. Sci **11**, 4442–4469 (2016).

[78]S Trasatti and O. Petrii, "Real surface area measurements in electrochemistry", Pure and applied chemistry **63**, 711–734 (1991).

[79] Y. Yoon, B. Yan, and Y. Surendranath, “Suppressing ion transfer enables versatile measurements of electrochemical surface area for intrinsic activity comparisons”, Journal of the American Chemical Society **140**, 2397–2400 (2018).

[80] Y. Li, W.-Z. Jia, Y.-Y. Song, and X.-H. Xia, “Superhydrophobicity of 3d porous copper films prepared using the hydrogen bubble dynamic template”, Chemistry of Materials **19**, 5758–5764 (2007).

[81] H. Shin, J. Dong, and M. Liu, “Nanoporous structures prepared by an electrochemical deposition process”, Advanced Materials **15**, 1610–1614 (2003).

[82] B. J. Plowman, L. A. Jones, and S. K. Bhargava, “Building with bubbles: the formation of high surface area honeycomb-like films via hydrogen bubble templated electrodeposition”, Chemical Communications **51**, 4331–4346 (2015).

[83] H.-C. Shin and M. Liu, “Copper foam structures with highly porous nanostructured walls”, Chemistry of materials **16**, 5460–5464 (2004).

[84] K. Krempl, D. Hochfilzer, F. Cavalca, M. Saccoccio, J. Kibsgaard, P. C. Vesborg, and I. Chorkendorff, “Quantitative operando detection of electro synthesized ammonia using mass spectrometry”, ChemElectroChem **9**, 2196–0216 (2022).

[85] P. Bouguer, *Essai d optique, sur la gradation de la lumiere* (Claude Jombert, 1729).

[86] J. H. Lambert, *Photometria sive de mensura et gradibus luminis, colorum et umbrae* (sumptibus vidvae E. Klett, typis CP Detleffsen, 1760).

[87] R. Luther and A. Nikolopulos, “Ueber die beziehungen zwischen den absorptionsspektren und der konstitution der komplexen kobaltamminsalze”, Zeitschrift für Physikalische Chemie **82**, 361–384 (1913).

[88] T. G. Mayerhoefer, S. Pahlow, and J. Popp, “The bouguer-beer-lambert law: shining light on the obscure”, ChemPhysChem **21**, 2029–2046 (2020).

[89] S. Z. Andersen, “Electrochemical nitrogen reduction under (near) ambient conditions”, (2020).

[90] Y. Zhao, R. Shi, X. Bian, C. Zhou, Y. Zhao, S. Zhang, F. Wu, G. I. Waterhouse, L. Wu, and C. Tung, “Ammonia detection methods in photocatalytic and electrocatalytic experiments: how to improve the reliability of nh3 production rates?”, Advanced Science **6**, 1802109 (2019).

[91] C. Fisher and J. Guajardo, “Column properties that make an impact on ion chromatography”, Spectroscopy Asia **16**, 14–18 (2020).

[92] J. Weiss, *Handbook of ion chromatography*, Vol. 1 (John Wiley and Sons, 2016).

[93] H. Small, T. S. Stevens, and W. C. Bauman, “Novel ion exchange chromatographic method using conductimetric detection”, Analytical Chemistry **47**, 1801–1809 (1975).

[94] J. W. Niemantsverdriet, *Spectroscopy in catalysis: an introduction* (John Wiley and Sons, 2007).

[95] I. Chorkendorff and J. W. Niemantsverdriet, *Concepts of modern catalysis and kinetics* (John Wiley and Sons, 2017).

[96] R. Jenkins and R. L. Snyder, *Introduction to x-ray powder diffractometry (volume 138)* (Wiley Online Library, 1996).

[97] A. Baliyan, H. Imai, and V. Kumar, "Microscopy", in *Data processing handbook for complex biological data sources* (Elsevier, 2019), pp. 97–117.

[98] D. Shindo and T. Oikawa, "Energy dispersive x-ray spectroscopy", in *Analytical electron microscopy for materials science* (Springer, 2002), pp. 81–102.

[99] M. Hesse, H. Meier, and B. Zeeh, *Spektroskopische methoden in der organischen chemie* (Georg Thieme Verlag, 2005).

[100] D. Argoti, *Liquid chromatography-mass spectrometry for detection and characterization of dna biomarkers and reactive metabolites* (Northeastern University, 2008).

[101] K. Li, S. Z. Andersen, M. J. Statt, M. Saccoccio, V. J. Bukas, K. Krempl, R. Sazinas, J. B. Pedersen, K. Krempl, V. Shadravan, Y. Zhou, D. Chakraborty, J. Kibsgaard, P. C. Vesborg, J. Norskov, and I. Chornkendorff, "Enhancement of li-mediated ammonia synthesis by addition of oxygen", Science **374**, 1593–1597 (2021).

[102] K. Krempl, D. Hochfilzer, F. Cavalca, M. Saccoccio, J. Kibsgaard, P. C. Vesborg, and I. Chorkendorff, "Quantitative operando detection of electro synthesized ammonia using mass spectrometry", ChemElectroChem **9**, e202101713 (2022).

[103] E. Wang, S. Dey, T. Liu, S. Menkin, and C. P. Grey, "Effects of atmospheric gases on li metal cyclability and solid-electrolyte interphase formation", ACS Energy Letters **5**, 1088–1094 (2020).

[104] E. Wang, T. Insinna, and C. P. Grey, "Probing the li metal solid electrolyte interphase using a stable nitroxide radical", in (2022).

[105] T. Ludwig, A. R. Singh, and J. K. Nørskov, "Subsurface nitrogen dissociation kinetics in lithium metal from metadynamics", The Journal of Physical Chemistry C **124**, 26368–26378 (2020).

[106] J. M. McEnaney, A. R. Singh, J. A. Schwalbe, J. Kibsgaard, J. C. Lin, M. Cargnello, T. F. Jaramillo, and J. K. Nørskov, "Ammonia synthesis from n 2 and h 2 o using a lithium cycling electrification strategy at atmospheric pressure", Energy and Environmental Science **10**, 1621–1630 (2017).

[107] C. Liu, T. Li, H. Zhang, Z. Song, C. Qu, G. Hou, H. Zhang, C. Ni, and X. Li, "Dmf stabilized li3n slurry for manufacturing self-prelithiatable lithium-ion capacitors", Science Bulletin **65**, 434–442 (2020).

[108] Y. Sun, Y. Li, J. Sun, Y. Li, A. Pei, and Y. Cui, "Stabilized li3n for efficient battery cathode prelithiation", Energy Storage Materials **6**, 119–124 (2017).

[109] K. N. Wood and G. Teeter, “Xps on li-battery-related compounds: analysis of inorganic sei phases and a methodology for charge correction”, ACS Applied Energy Materials **1**, 4493–4504 (2018).

[110] C. Fang, J. Li, M. Zhang, Y. Zhang, F. Yang, J. Z. Lee, M.-H. Lee, J. Alvarado, M. A. Schroeder, and Y. Yang, “Quantifying inactive lithium in lithium metal batteries”, Nature **572**, 511–515 (2019).

[111] S.-K. Otto, Y. Moryson, T. Krauskopf, K. Peppler, J. Sann, J. Janek, and A. Henss, “In-depth characterization of lithium-metal surfaces with xps and tof-sims: toward better understanding of the passivation layer”, Chemistry of Materials **33**, 859–867 (2021).

[112] J. Zheng, Z. Ju, B. Zhang, J. Nai, T. Liu, Y. Liu, Q. Xie, W. Zhang, Y. Wang, and X. Tao, “Lithium ion diffusion mechanism on the inorganic components of the solid–electrolyte interphase”, Journal of Materials Chemistry A **9**, 10251–10259 (2021).

[113] R. S. Assary, J. Lu, P. Du, X. Luo, X. Zhang, Y. Ren, L. A. Curtiss, and K. Amine, “The effect of oxygen crossover on the anode of a li–o2 battery using an ether-based solvent: insights from experimental and computational studies”, ChemSusChem **6**, 51–55 (2013).

[114] C. W. Pan, K. Xia, S. A. Parker, and E. S. Tillman, “Identity of low-molecular-weight species formed in end-to-end cyclization reactions performed in thf”, Polymers **10**, 844 (2018).

[115] C. M. Gabardo, Y. Zhu, L. Soleymani, and J. M. Moran-Mirabal, “Bench-top fabrication of hierarchically structured high-surface-area electrodes”, Advanced Functional Materials **23**, 3030–3039 (2013).

[116] A. Verdaguer-Casadevall, C. W. Li, T. P. Johansson, S. B. Scott, J. T. McKeown, M. Kumar, I. E. Stephens, M. W. Kanan, and I. Chorkendorff, “Probing the active surface sites for co reduction on oxide-derived copper electrocatalysts”, Journal of the American Chemical Society **137**, 9808–9811 (2015).

[117] E. Bertheussen, A. Verdaguer-Casadevall, D. Ravasio, J. H. Montoya, D. B. Trimarco, C. Roy, S. Meier, J. Wendland, J. K. Norskov, and I. E. Stephens, “Acetaldehyde as an intermediate in the electroreduction of carbon monoxide to ethanol on oxide-derived copper”, Angewandte Chemie **128**, 1472–1476 (2016).

[118] K. Li, S. G. Shapel, D. Hochfilzer, J. B. Pedersen, K. Krempl, S. Z. Andersen, R. Sazinas, M. Saccoccio, S. Li, and D. Chakraborty, “Increasing current density of li-mediated ammonia synthesis with high surface area copper electrodes”, ACS Energy Letters **7**, 36–41 (2021).

[119] S. Li, Y. Zhou, K. Li, M. Saccoccio, R. Sazinas, S. Z. Andersen, J. B. Pedersen, X. Fu, V. Shadravan, and D. Chakraborty, “Electrosynthesis of ammonia with high selectivity and high rates via engineering of the solid-electrolyte interphase”, Joule (2022).

[120] S. Yesilkir-Baydar, O. N. Oztel, R. Cakir-Koc, and A. Candayan, “Evaluation techniques”, in *Nanobiomaterials science, development and evaluation* (Elsevier, 2017), pp. 211–232.

[121] C. Powell and A Jablonski, “Surface sensitivity of x-ray photoelectron spectroscopy”, Nuclear Instruments and Methods in Physics Research Section A: Accelerators, Spectrometers, Detectors and Associated Equipment **601**, 54–65 (2009).

[122] H. Boo, S. Park, B. Ku, Y. Kim, J. H. Park, H. C. Kim, and T. D. Chung, “Ionic strength-controlled virtual area of mesoporous platinum electrode”, Journal of the American Chemical Society **126**, 4524–4525 (2004).

[123] O. Westhead, M. Spry, A. Bagger, Z. Shen, H. Yadegari, S. Favero, R. Tort, M.-M. Titirici, M. P. Ryan, and R. Jervis, “The role of ion solvation in lithium mediated nitrogen reduction”, (2022).

[124] A. Bouibes, N. Takenaka, S. Saha, and M. Nagaoka, “Microscopic origin of the solid electrolyte interphase formation in fire-extinguishing electrolyte: formation of pure inorganic layer in high salt concentration”, The Journal of Physical Chemistry Letters **10**, 5949–5955 (2019).

[125] G. M. Girard, M. Hilder, D. Nucciarone, K. Whitbread, S. Zavorine, M. Moser, M. Forsyth, D. R. MacFarlane, and P. C. Howlett, “Role of li concentration and the sei layer in enabling high performance li metal electrodes using a phosphonium bis (fluorosulfonyl) imide ionic liquid”, The Journal of Physical Chemistry C **121**, 21087–21095 (2017).

[126] S Weisenberger and d. A. Schumpe, “Estimation of gas solubilities in salt solutions at temperatures from 273 k to 363 k”, AIChE Journal **42**, 298–300 (1996).

[127] F Gibanel, M. Lopez, F. Royo, J Santafe, and J. Urieta, “Solubility of nonpolar gases in tetrahydrofuran at 0 to 30 c and 101.33 kpa partial pressure of gas”, Journal of solution chemistry **22**, 211–217 (1993).

[128] E. Brunner, “Solubility of hydrogen in 10 organic solvents at 298.15, 323.15, and 373.15 k”, Journal of chemical and Engineering Data **30**, 269–273 (1985).

[129] F. M. Piller, P. Appukkuttan, A. Gavryushin, M. Helm, and P. Knochel, “Convenient preparation of polyfunctional aryl magnesium reagents by a direct magnesium insertion in the presence of licl”, Angewandte Chemie International Edition **47**, 6802–6806 (2008).

[130] S. Zhang, K Xu, and T. Jow, “A thermal stabilizer for lipf6-based electrolytes of li-ion cells”, Electrochemical and solid-state letters **5**, A206 (2002).

[131] R. Jasinski and S. Carroll, “Thermal stability of a propylene carbonate electrolyte”, Journal of The Electrochemical Society **117**, 218 (1970).

[132] G. Newman, R. Francis, L. Gaines, and B. Rao, “Hazard investigations of liclo4/dioxolane electrolyte”, Journal of The Electrochemical Society **127**, 2025 (1980).

[133] K. Xu, “Nonaqueous liquid electrolytes for lithium-based rechargeable batteries”, Chemical reviews **104**, 4303–4418 (2004).

[134] M. Ue, M. Takeda, M. Takehara, and S. Mori, "Electrochemical properties of quaternary ammonium salts for electrochemical capacitors", Journal of the Electrochemical Society **144**, 2684 (1997).

[135] S. S. Zhang, K. Xu, and T. R. Jow, "Study of libf4 as an electrolyte salt for a li-ion battery", Journal of the Electrochemical Society **149**, A586 (2002).

[136] M. Ue, M. Takeda, M. Takehara, and S. Mori, "Electrochemical properties of quaternary ammonium salts for electrochemical capacitors", Journal of the Electrochemical Society **144**, 2684 (1997).

[137] J. Hennessy and S. Nikzad, "Atomic layer deposition of lithium fluoride optical coatings for the ultraviolet", Inorganics **6**, 46 (2018).

[138] P. Lou, C. Li, Z. Cui, and X. Guo, "Job-sharing cathode design for li–o 2 batteries with high energy efficiency enabled by in situ ionic liquid bonding to cover carbon surface defects", Journal of Materials Chemistry A **4**, 241–249 (2016).

[139] S. Campbell, C Bowes, and R. McMillan, "The electrochemical behaviour of tetrahydrofuran and propylene carbonate without added electrolyte", Journal of electroanalytical chemistry and interfacial electrochemistry **284**, 195–204 (1990).

[140] J. Fowles, R. Boatman, J. Bootman, C. Lewis, D. Morgott, E. Rushton, J. van Rooij, and M. Banton, "A review of the toxicological and environmental hazards and risks of tetrahydrofuran", Critical reviews in toxicology **43**, 811–828 (2013).

[141] A. Gamer, R Jaeckh, E Leibold, W Kaufmann, C. Gembardt, R Bahnemann, and B Van Ravenzwaay, "Investigations on cell proliferation and enzyme induction in male rat kidney and female mouse liver caused by tetrahydrofuran", Toxicological Sciences **70**, 140–149 (2002).

[142] B. Liu, J.-G. Zhang, and W. Xu, "Advancing lithium metal batteries", Joule **2**, 833–845 (2018).

[143] M. C. Hatzell, "A decade of electrochemical ammonia synthesis", ACS Energy Letters **7**, 4132–4133 (2022).

B Appendix

B.1 Additional Information

B.1.1 Additional Figures for Chapter 4

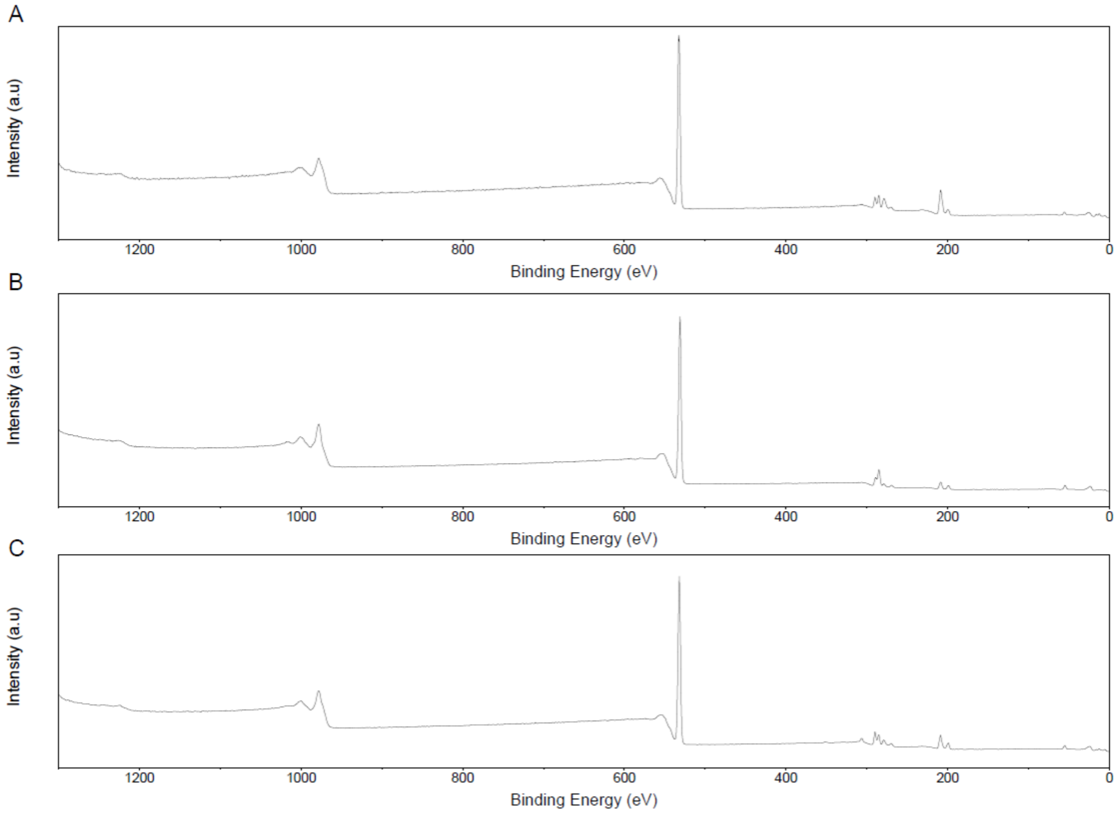

Figure B.1: XPS survey spectra of the Mo electrodes after electrochemistry at different O_2 contents.

B.1.2 Additional Figures for Chapter 5

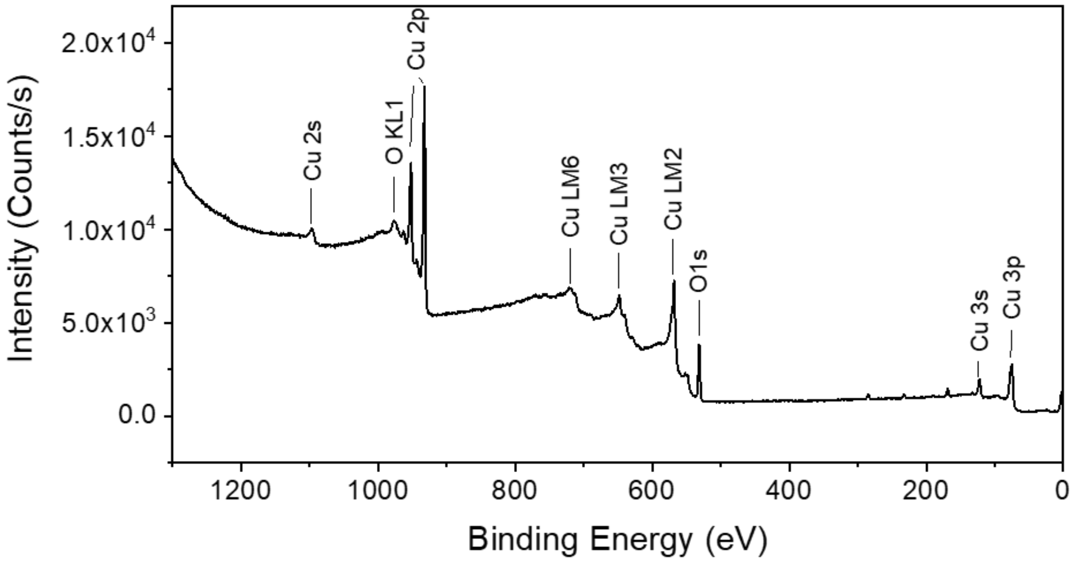

Figure B.2: XPS survey spectra of the HBTCu electrodes.

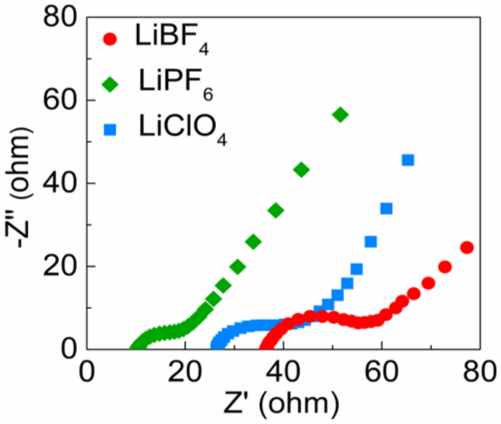

Figure B.3: PEIS measurements of different Li-salts used for electrolyte.

B.1.3 Additional Information for Chapter 6

Additional Experimental Information for Chapter 6

Experimental procedure for EtOH exchange experiments

All experiments were carried out in a single compartment glass cell inside an Ar glovebox. The WE was a 1.8 cm^2 Mo foil (+99.9 %, 0.1 mm thickness, Goodfellow) and the CE was a Pt mesh (99.9 %, 0.1 mm thickness, Goodfellow) and the RE was a Pt wire (99.99 %, 0.1 mm thickness, Goodfellow). The Pt electrodes were flame annealed before the measurement and The

Mo foil was cleaned in 2 % HCl and then rinsed in MilliQ water and EtOH. Afterward sit was polished with with SiC paper(CarbiMet, Buehler) and rinsed in EtOH again. The electrolyte was prepared in the glovebox and consisted of a 0.5 M $LiClO_4$ (99.99%, Sigma Aldrich) solution in THF (Sigma Aldrich, inhibitor free) with 0.17 M EtOH or without. 10 mL of the electrolyte with EtOH was introduced to the cell and then the cell was purged with purified (NuPure) N_2 (6.0, AirLiquide) for 20 min while the OCV was being recorded. Then a PEIS at OCV was recorded to determine the solution resistance. Afterwards a LSV at 20 mV/s was initiated until the desired current density of -4 mA/cm^2 was reached. Immediately after a GEIS was measured at the current density of -4 mA/cm^2 between 200 kHz and 10 Hz. This was then followed by a CP at -4 mA/cm^2 until 10 C was reached. After the CP another GIES was initiated to probe the deposition at the end of an measurement. Then the electrolyte was collected through a syringe without touching the electrodes. Then 10 mL of pure THF was introduced to the cell to rinse out all residual electrolyte. After removing the cleaning THF by syringe 10 mL of the electrolyte without EtOH was introduced and the cell was purged again with N_2 for at least 10 min whole recording OCV. After the purging, 0.5 mL of sample was taken as a blank to ensure no ammonia comes from the SEI layer being dissolved during the saturation time. Next, the same procedure of LSV, GEIS and CP was performed and the electrolyte afterwards measured for NH_3.

Analytical Procedure DRT Analysis

First of all the GEIS data was treated by removing some of the low frequency points that don't give valuable information. Then the DRT analysis was carried out with the software ©*Polarographica*, which is made by my very talented colleague Tim Trichter. He based the software on DRTtools, which is an open-access freeware. The calculations and transformation behind this tool are based on the publication by Wan et al. [75].

B.2 Publications in relation to this PhD

Paper 1

Enhancement of Li-mediated ammonia synthesis by addition of oxygen

K. Li*, S. Z. Andersen*, M. J. Statt*, M. Saccoccio, V. J. Bukas, K. Krempl, R. Sazinas, J. B. Pedersen, K. Krempl, V. Shadravan, Y. Zhou, D. Chakraborty, J. Kibsgaard, P. C. Vesborg, J. Nørsvov and I. Chorkendorff
Science, **2021**, 374, 1593-1597.

* these authors contributed equally

ELECTROCHEMISTRY

Enhancement of lithium-mediated ammonia synthesis by addition of oxygen

Katja Li[1]†, Suzanne Z. Andersen[1]†, Michael J. Statt[2]†, Mattia Saccoccio[1], Vanessa J. Bukas[1]‡, Kevin Krempl[1], Rokas Sažinas[1], Jakob B. Pedersen[1], Vahid Shadravan[1], Yuanyuan Zhou[1], Debasish Chakraborty[1], Jakob Kibsgaard[1], Peter C. K. Vesborg[1], Jens K. Nørskov[1]*, Ib Chorkendorff[1]*

Owing to the worrying increase in carbon dioxide concentrations in the atmosphere, there is a need to electrify fossil-fuel–powered chemical processes such as the Haber-Bosch ammonia synthesis. Lithium-mediated electrochemical nitrogen reduction has shown preliminary promise but still lacks sufficient faradaic efficiency and ammonia formation rate to be industrially relevant. Here, we show that oxygen, previously believed to hinder the reaction, actually greatly improves the faradaic efficiency and stability of the lithium-mediated nitrogen reduction when added to the reaction atmosphere in small amounts. With this counterintuitive discovery, we reach record high faradaic efficiencies of up to 78.0 ± 1.3% at 0.6 to 0.8 mole % oxygen in 20 bar of nitrogen. Experimental x-ray analysis and theoretical microkinetic modeling shed light on the underlying mechanism.

Ammonia (NH_3) is one of the most abundantly manufactured chemicals worldwide, with a yearly production of over 182 million tonnes (*1*). Its main use is as a synthetic fertilizer (~80%) and as the source of all activated nitrogen in the chemical industry, but it has recently also been considered as a carbon-free energy carrier (*2*–*4*). Currently, ammonia is produced from nitrogen and hydrogen through the thermally catalyzed Haber-Bosch process, which operates under harsh conditions (350° to 450°C, 100 to 200 bar), requiring large centralized plants and high capital investment (*5*, *6*). To satisfy the commercial demands, about ~1% of global energy consumption is used in the process (*7*). Additionally, the Haber-Bosch process is responsible for about 1.4% of the annual CO_2 emissions, as the supplied H_2 originates from steam reforming of methane (*8*–*10*). An alternative, environmentally sustainable way to produce ammonia is through an electrochemical pathway, with the electrical energy provided from renewable sources such as wind or solar power. Recently, efforts toward electrochemical synthesis of ammonia have increased substantially (*11*–*14*); however, the field has been hampered by various issues. One major concern in the literature is related to contamination of the input gases, chemicals, and catalysts by ammonia and other labile nitrogen compounds (*15*, *16*), which may result in an erroneously high reported faradaic efficiency (FE). Several protocols (*16*–*18*) have been published on proper contaminant identification and rigorous experimentation, and some of the erroneous reports are being corrected or withdrawn as scientists retest and reevaluate methods and systems (*19*, *20*). In a recent paper, Choi *et al.* investigated over 130 publications on electrochemical ammonia synthesis, concluding it highly likely that none of the aqueous systems produce ammonia and that the most reliable method presently is lithium-mediated nitrogen reduction (LiNR) in nonaqueous electrolytes (*16*). A similar lithium-mediated method was first published by Fichter *et al.* in 1930 (*21*) and later investigated with a near-aprotic solvent by Tsuneto *et al.* in the 1990s (*22*, *23*). Currently, the Tsuneto-based system has been revisited by several groups (*11*, *12*, *17*, *18*, *24*–*28*); however, the exact mechanism is still not fully understood. It is generally accepted that the LiNR takes place in three steps (*25*), the first one being the electrochemical reduction of Li^+ ions in the electrolyte to metallic Li, which is a very reactive material. This freshly plated Li is believed to then dissociate N_2, and the N at the surface is finally reduced in a series of electron and proton transfers to form NH_3 by using a suitable proton source, like ethanol (EtOH). An important component of the LiNR system is the solid electrolyte interface (SEI) that forms from decomposition products of an organic electrolyte during Li deposition on the cathode. The SEI provides a porous passivation layer over the electrode surface that is electronically insulating but ionically conducting. Its exact composition and mechanistic role in the LiNR process are still unclear and difficult to determine, because it is strongly dependent on experimental conditions and sensitive to air exposure. Nevertheless, the process reliably forms ammonia from N_2 and a proton source at ambient conditions, typically achieving a FE of around 5 to 20% (*17*, *25*, *29*), with a recent breakthrough in FE of up to 69% by Suryanto *et al.* (*11*) under 20-bar N_2. Lazouski *et al.* implemented this process using a gas diffusion electrode (GDE) setup with reported efficiencies of 30%, but the system was only stable for a few minutes and exhibited high cell potentials (*12*). Instability of this process was already described by Tsuneto *et al.* (*22*), and recently mitigated by Andersen *et al.* with a potential cycling strategy (*24*), which enabled stability over several days and increased the FE at 10-bar N_2 from 20% without cycling to 37% with cycling at an energy efficiency (EE) of 7%. However, the REFUEL program of the US Department of Energy set a target of 90% FE at 300 mA/cm^2 and an EE of 60% (*30*). The current state of the lithium-mediated process is clearly far from this target. Especially the EE is currently a major problem in the LiNR, because Li plating requires largely negative potentials (−3.04 V versus SHE). The overpotential losses of the LiNR are portrayed and discussed in fig. S1. If all overpotentials are minimized and hydrogen oxidation reaction (HOR) is utilized at the counter electrode (CE), the resulting EE would be 26%, assuming 80% FE.

Here we show that adding small amounts of O_2 to the feed gas has a positive effect on both the FE and the stability of the system. A FE of up to 78.0 ± 1.3% at 20-bar N_2 can be achieved by adding 0.5 to 0.8 mol % O_2, resulting in an EE of 11.7 ± 0.5% (calculation in supplementary materials). This EE calculation accounts for neither EtOH as sacrificial proton donor nor for the energy of pressurizing the system. We used this framework as a basis for comparison to results from literature (*24*, *25*). Using hydrogen oxidation at the CE in a GDE-type system has previously been shown to prevent solvent oxidation (*12*), and the use of a phosphonium proton shuttle has been experimentally verified to successfully shuttle the newly created protons to the working electrode while the phosphonium ylide becomes reprotonated at the anode (*11*), thereby circumventing the sacrificial ethanol issue. Our focus in this study lies on the finding that oxygen increases the FE and not on the sacrificial proton donor issue, but we expect that the previously reported solutions will also apply to our system. The positive effect of small amounts of oxygen is counterintuitive; one would expect oxygen to contaminate the active phase and result in loss of efficiency because of the oxygen reduction reaction (ORR). Indeed, early experiments by Tsuneto *et al.* showed that higher oxygen content in the gas feed (synthetic air with 20% O_2) lowered the FE considerably from ~50 to 0.1% at 50 bar (*23*). We investigated the origin of the oxygen promotion using a microkinetic model, suggesting that the higher FE is related to slower Li^+ diffusion through the SEI layer formed in the presence of O_2 as observed by Wang *et al.* in

---

[1] Department of Physics, Technical University of Denmark, Kongens Lyngby, Denmark. [2] SUNCAT Center for Interface Science and Catalysis, Department of Chemical Engineering, Stanford University, Stanford, CA, USA.
*Corresponding author. Email: jkno@dtu.dk (J.K.N.); ibchork@fysik.dtu.dk (I.C.)

†These authors contributed equally to this work.

‡Present address: Fritz-Haber-Institut der Max-Planck-Gesellschaft, 14195 Berlin, Germany.

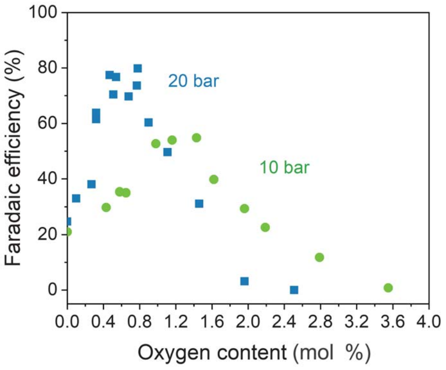

Fig. 1. Influence of oxygen content on the FE of the Li-mediated ammonia synthesis. Reactions were conducted at 10 (green) and 20 (blue) bar, where the added oxygen content inside the autoclave was determined by mass spectrometry. The reported pressure is the total pressure of N_2 and O_2 combined. All experiments were operated at a constant current of −4 mA/cm^2 until the system overloaded or reached 50 C (116 min to pass 50 C), unless stated otherwise.

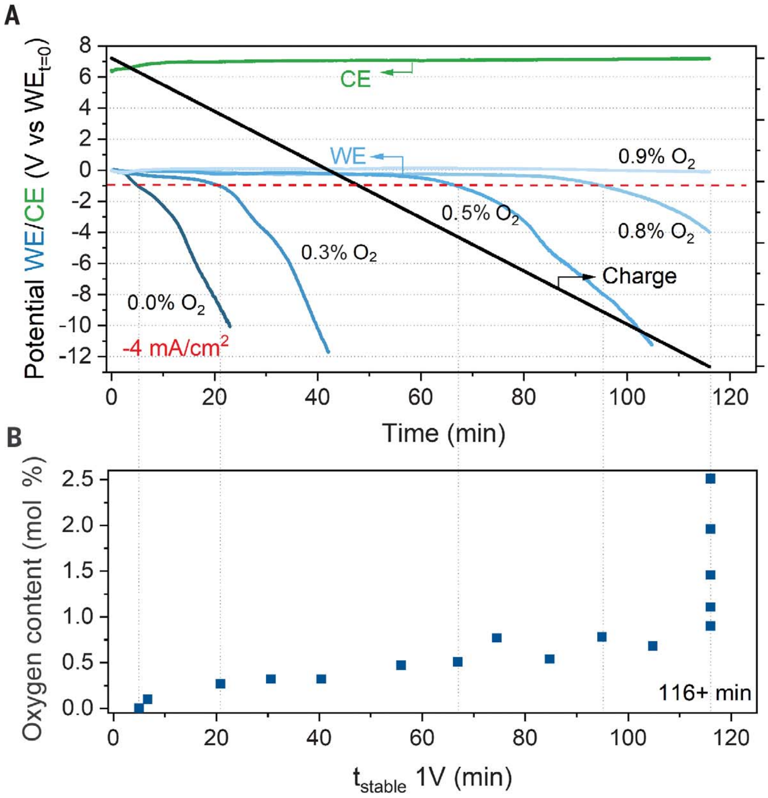

Fig. 2. Influence of oxygen content on the stability of the Li-mediated ammonia synthesis. (**A**) Chronopotentiometry with −4 mA/cm^2 applied at 20 bar N_2 with variable O_2 content. The potentials are normalized to the starting WE potential. A maximum of 50 C charge (black trace) is passed; however, some measurements overloaded before 50 C was reached, as seen from the sudden decrease in WE potential (blue traces) for low O_2 concentrations (all shown % O_2 are mol % O_2). A representative CE potential (green trace) is shown, which is stable throughout the measurement, even for experiments in which the WE overloaded. The dotted red line indicates the decrease of WE potential by 1 V. (**B**) The time until the WE potential decreased by 1 V (t_{stable}), as a function of O_2 content. All stable experiments were included in 116+ min.

studies of Li–air battery materials (*31*). We further tested this hypothesis by systematically investigating the effect of O_2 on the SEI layer through x-ray diffraction (XRD) and x-ray photoelectron spectroscopy (XPS).

Effect of oxygen on Faradaic efficiency

Systematic experiments with varying amounts of O_2 added at 10- and 20-bar total gas pressure were conducted. All experiments were performed in an in-house–fabricated autoclave based on the design by Wiberg *et al.* (*32*) and carried out in a glass cell containing ~30 ml of electrolyte (fig. S2). The gases used for the experiments were cleaned with purifiers (NuPure) to levels as low as parts per trillion by volume of nitrogen-containing impurities, and the flow was controlled by mass flow controllers (Brooks) to ensure proper gas mixing. This was important, as improper gas mixing affects the electrochemical reaction (figs. S3 and S4). The oxygen content was determined by a mass spectrometer (Pfeiffer, omnistar GSD 320) attached to the autoclave with a 1-μm orifice just above the electrochemical cell. A representative mass spectrum is shown in fig. S5. The electrolyte was 0.3 M $LiClO_4$ in tetrahyrofuran (THF) with 1.0 vol % EtOH, unless otherwise specified. The working electrode (WE) was a Mo foil of 1.8 cm$_{geo}^2$ area, the CE was a 1.8 cm$_{geo}^2$ Pt mesh, and the pseudo-reference electrode (RE) was a Pt wire. The potential scale was determined by calibrating the Pt pseudo-RE to the well-known Fc/Fc$^+$ couple (fig. S6). A constant-current density of −4 mA/cm^2 was applied, until the system either overloaded because of an increased total cell potential beyond the capacity of the potentiostat, or the experiment reached 50 C of total passed charge. A representative cyclic voltammetry is shown in fig. S7. Cycling experiments according to Andersen *et al.* (*24*) were also conducted, to show the beneficial coupling of the improved stability due to cycling with the increased FE from the addition of O_2. The FE was determined at the end of the experiment and therefore represents accumulated FE. A more detailed description of the experimental procedure and all experimental results can be found in the supplementary materials.

Figure 1 shows that small amounts of O_2 markedly increase the FE toward ammonia production at both 10 and 20 bar, showing peak behavior from 0.5 to 0.8 mol % O_2 in N_2 at 20 bar and 1.2 to 1.6 mol % at 10 bar. The optimum oxygen content at 10 bar is higher than at 20 bar by almost exactly a factor of 2, suggesting that the oxygen partial pressure, rather than the molar ratio of O_2 in N_2, is responsible for the increase in FE (fig. S8). The efficiency drops rapidly at higher amounts of O_2, in accordance with the much higher oxygen-content experiments (20% O_2, 50 bar) of Tsuneto *et al.* (*23*). An increase in the H_2O content of the electrolyte postelectrochemistry is observed with increasing O_2 content (fig. S9), suggesting that ORR is responsible for the decrease in FE. The decrease in the FE at higher O_2 content could also partly be due to the formation of passivating Li_2O species on the surface of the WE as seen later by XRD. As expected, the EE of the system follows a trend similar to that of the FE with peaks at 8.0 ± 1.8% and 11.7 ± 0.5% at optimal O_2 content under 10 bar and 20 bar, respectively (figs. S10 and S11).

Effect of oxygen on stability

In addition to the notable increase in the FE of the system because of added O_2, an increase in the apparent stability of the total cell potential was also observed. However, the electrochemistry will overload given enough time, and the only way to ensure stability in this system is through potential cycling (*24*). Figure 2A shows representative electrochemistry data of chronopotentiometry measurements at 20 bar, where it is clear that the WE potential remains stable for longer times with increasing O_2 content. The CE remains stable, even for experiments in which the WE is unstable. This excludes the possibility of oxygen having an appreciable influence on the CE. To compare the stabilities, we plotted the data against the starting WE potential of each individual experiment. The total time it takes for the WE potential to decrease by 1 V was taken as a measure of stability (t_{stable}). Because all experiments exceeding 0.8 mol % O_2 exhibited a WE potential that did not decrease by more than 1 V, t_{stable} was set to 116+ min for these experiments. t_{stable} is plotted as a function of the O_2 content in Fig. 2B, and a linear trend of increasing stability by increasing O_2 is observed. Stability remained high even for larger O_2 content when FE diminished. This relation can be visualized in fig. S10A and suggests that LiNR stability is qualitatively related to O_2 content but not to the FE. Cycling of the potential to prevent build-up of passivating lithium species is a previously proven method to achieve long-term stability (days) of the potential in the LiNR system (*24*). This method was applied for an experiment with optimal O_2 content (20 bar N_2, 0.67 mol % O_2) and one with suboptimal O_2 content (20 bar N_2, 0.26 mol % O_2), which would otherwise be unstable under constant Li deposition. We found that cycling the potential in the presence of O_2 retains the higher FE (fig. S9) while also stabilizing the WE during the 0.26 mol % O_2 experiment until (at least) 50 C of charge has been passed (figs. S12 and S13). In addition, the water content of these cycling experiment increased substantially compared to the constant-current experiments (table S1), owing to the constant ORR. However, because the FE seems to be unaffected by this result, it is believed that the increase in water on this scale is not detrimental to the system and that by applying cycling on the optimum oxygen content of 0.6 to 0.8 mol % at 20 bar, the reaction could be kept stable for longer (10 hours), as was shown previously (*24*).

Mechanistic role of O_2 in LiNR

We recently demonstrated that in the absence of oxygen, the LiNR system and its FE toward ammonia are largely controlled by mass transport limitations of the reactant species diffusing from the bulk electrolyte to the catalyst surface (*24*). By developing a kinetic model, we showed that the experimental FE is a simple function of the relative diffusion rates between incoming lithium ions (r_{Li}), protons (r_{H}), and nitrogen (r_{N_2}). Here, we assume a steady-state FE, although there might be dynamical changes especially initially where the SEI layer is formed. Our model considered a series of elementary steps and relied on the basic, yet reasonable, assumption that all diffusion steps are considerably slower than subsequent reaction steps taking place at the surface, i.e., they are overall rate-limiting. This assumption results from recognizing that (i) electrochemical surface steps are most likely very fast and driven irreversibly forward because of the extreme reducing potentials required to plate Li (*33*); (ii) the chemical (dissociative) adsorption of N_2 on metallic Li has a negligible kinetic barrier (*34*, *35*); and (iii) the SEI layer that forms during Li deposition in THF most likely leads to much slower diffusion as compared to that in aqueous media (*36*). Alongside rate-limiting diffusion, we further consider mass balance of the incoming protons toward either H_2 or NH_3 and thus distinguish between two possible mass-transfer limitations for the nitrogen reduction reaction (NRR): a limitation in nitrogen (N_{lim}), or a limitation in protons (H_{lim}). Within these two regimes, the steady-state rate of NH_3 production and resulting FE can be formulated in terms of only the three elementary (r_{Li}, r_{H}, r_{N_2}) diffusion rates. The heatmap of Fig. 3A shows how the predicted FE changes as a function of the relative-to-Li rates of incoming N_2 (x axis) and H^+ (y axis). A dashed green line marks the ideal r_{N_2} to r_{H} ratio that leads to the highest FE at the boundary between nitrogen- and proton-limited regimes.

When adding oxygen to the gas feed, it is intuitive to expect that the NRR will be suppressed because of additional competition from the ORR. The experimental improvement in FE at low O_2 content, however, is a counterintuitive result that is much harder to understand. As a first step toward this understanding, we extend our original kinetic model to incorporate the oxygen electrochemistry and examine its effect on the resulting FE. This involves not only the inclusion of the ORR that consumes protons and electrons at the catalyst surface, but also the probability that newly formed H_2O can itself act as a proton donor to further drive the catalysis. Derivation of the enhanced model can be found in the supplementary materials; we emphasize that none of the situations that we considered can account for an oxygen-induced improvement in FE as found experimentally. Indeed, we predict a (likely small) decrease in FE at low O_2 content because of the ORR competing as a parasitic side reaction, and a substantial drop to ≈0 when the more reactive oxygen species dominate all surface sites over nitrogen species at higher O_2 contents. This result suggests that O_2 must have another way of influencing the LiNR system.

What can increase the FE is a decrease in the Li diffusion rate (Fig. 3A). This is simply because Li electrodeposition also competes with the NRR for electrons. Ideally, one would want Li diffusion or deposition to be slow enough that it consumes a minimal number of electrons while still providing a full monolayer of clean, freshly plated Li that is reactive enough to dissociate nitrogen. Delayed Li diffusion as a result of oxygen-induced changes in the SEI layer has, indeed, been

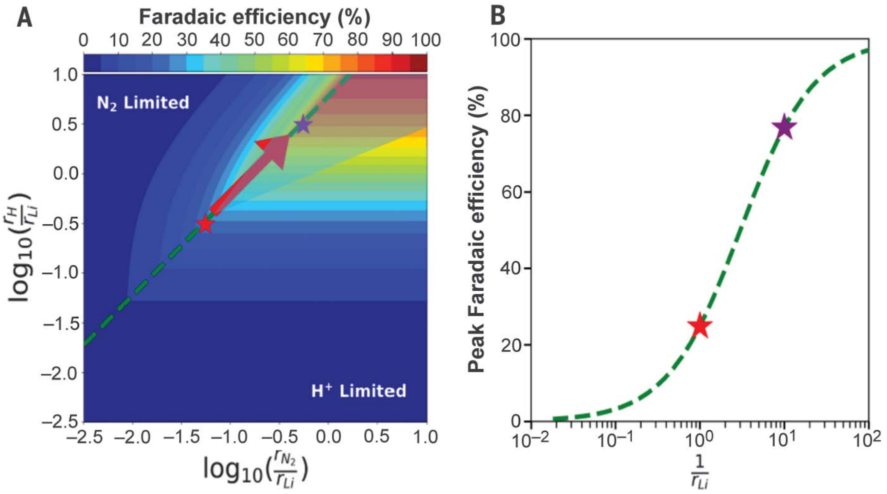

Fig. 3. Graphic illustration of the microkinetic model for Li-mediated ammonia synthesis. (**A**) Heatmap of the predicted FE as a function of the ratio of nitrogen to lithium (x axis) and proton to lithium (y axis) diffusion rates. The red star indicates the expected location of the 10-bar experiments without O_2 in the system. The purple star indicates the improvement in FE if r_{Li} were selectively lowered by an order of magnitude. The cone represents the uncertainty of the location of the purple star. (**B**) A one-dimensional plot of FE cut along the optimal r_{N_2}/r_{H} ratio (marked by the green dashed line in Fig. 3A) that clearly shows the marked FE improvement that can result from lowering r_{Li}. The x axis is normalized so that the red star corresponds to $1/r_{\mathrm{Li}} = 1$.

observed. Wang *et al.* recently showed that O_2 can specifically influence the SEI composition in nonaqueous lithium–air batteries, leading to increased SEI homogeneity as well as diminished Li$^+$ diffusivity (*31*). Such an effect on Li$^+$ diffusivity should have a substantial impact on the FE toward forming ammonia. If the rates of nitrogen and proton diffusion, r_{N_2} and r_H, remain unaffected by the oxygen content, a decrease in the Li$^+$ diffusion rate will move the operating point along the dashed diagonal in Fig. 3A, leading to a substantial increase in the FE. In reality, r_{N_2} and r_H may also change as a result of the oxygen-induced modification of the SEI layer, but as long as the decrease is less than that for r_{Li}, a net increase in the FE is expected, as indicated by the conical shaded area in Fig. 3A.

The improvement in FE, also shown in Fig. 3B, is much larger than what can be expected from moving either horizontally (by, e.g., changing N_2 pressure) or vertically (by, e.g., changing proton activity) across the plot. According to this picture, an optimal O_2 content should follow as a trade-off between FE increasing at low values because of restricted Li$^+$ diffusivity and decreasing at high values when the ORR starts dominating over the NRR. Furthermore, both the optimal O_2 content and resulting maximum FE should correlate directly with N_2 pressure when the NRR is in the nitrogen-limited regime. As seen from Fig. 3A, increasing N_2 pressure (i.e., moving horizontally to the right on the heatmap) increases FE until the NRR is pushed into the proton-limited regime. The optimal O_2 content is defined by the competition between NRR and ORR and, while increasing N_2 pressure in the nitrogen-limited regime, the maximum FE should occur at same absolute O_2 partial pressure or a proportionally lower O_2 content, exactly as observed experimentally (Fig. 1).

Compositional changes in the SEI layer in the presence of O_2 are also consistent with the observed improvement in stability. For Li-ion batteries, the addition of O_2 has been shown to form a more homogeneous and uniform SEI layer, leading to increased cyclability (*31*). A more homogeneous layer could lead to more uniform Li plating in the LiNR system, thereby keeping the total cell potential stable for longer. Supporting this hypothesis, we visually observed a change in the deposit on the WE from experiments without O_2 (0.0 mol % O_2), with added O_2 achieving optimum FE (0.5 to 0.8 mol % O_2), and with high O_2 concentrations yielding little to no ammonia (>2.6 mol % O_2). The Mo foil at optimum O_2 content showed a thick deposit on both sides, whereas in the other cases, only a thin deposit on the side facing the CE was observed (fig. S14). This again proves that O_2 affects the WE rather than the CE.

In conclusion, combining our model with a diminished Li$^+$ diffusivity through the SEI layer in the presence of oxygen explains our experimental observations and suggests that small amounts of O_2 can act as a beneficial SEI additive or modifier to greatly improve both the system's apparent stability and FE toward ammonia.

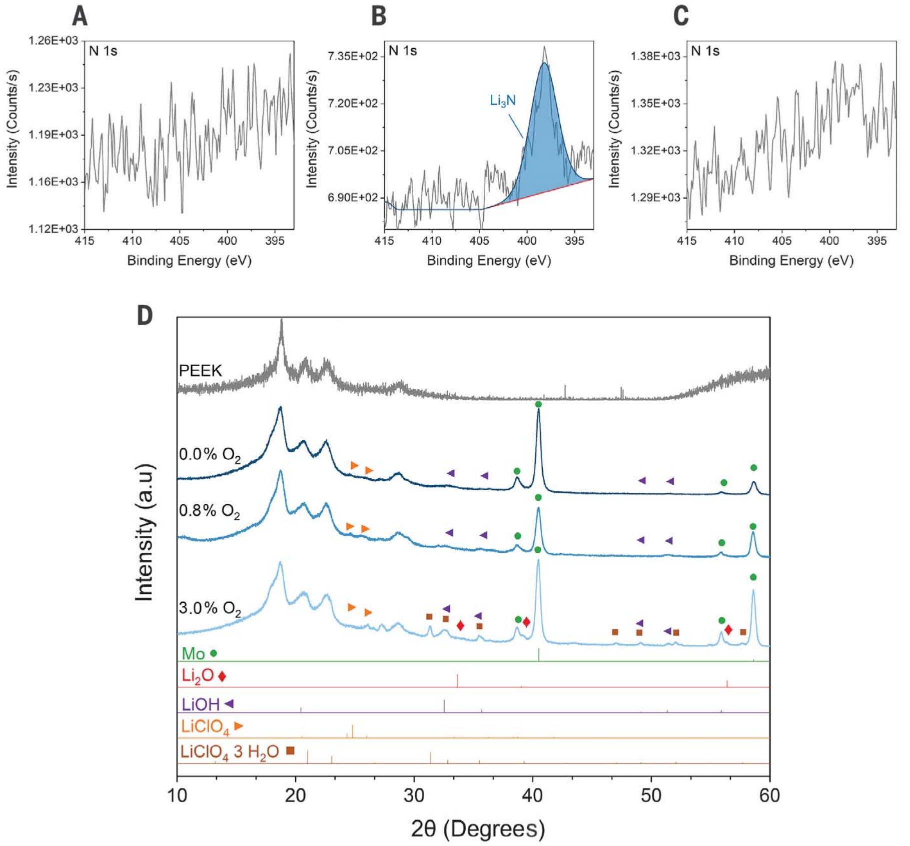

Fig. 4. XPS and XRD data of the working electrode after electrochemistry without exposure to air. Scans of three different WE foils postelectrochemistry with a constant −4 mA/cm^2 applied under 20-bar N_2 with varying amounts of O_2 present in the atmosphere. Foils were transferred without air exposure to the respective systems. (**A** to **C**) XPS spectra of N 1s scanning window for samples with 0.0 mol % (A), 0.8 mol % (B), and 3.0 mol % O_2 (C) in the reaction atmosphere. More high-resolution scans and full survey spectra are included in figs. S17 and S18. The N 1s peak at 0.8 mol % O_2 was seen in two independent measurements. (**D**) XRD diffractograms of samples with 0.0, 0.8, and 3.0 mol % O_2 in atmosphere and pattern of the PEEK dome transfer system, which creates reflections in the 15° to 30° region. Reference patterns for Mo (ICSD: 998-005-2267), Li_2O (ICSD: 98-017-3206), LiOH (ICSD: 98-002-6892), $LiClO_4$ (ICSD: 98-016-5579), $LiClO_4$ $3H_2O$ (ICSD: 98-003-2534), and Li_3N (ICSD: 98-003-4779) are included.

SEI layer investigation

The key conclusion of the model is that the high FE is a result of a SEI layer modified by the addition of oxygen. To determine the possible compositional effect of O_2 on the SEI layer, we carried out three representative electrochemical experiments at 20 bar with 0.0, 0.8, and 3.0 mol % O_2 in an autoclave kept inside an Ar glove box (fig. S2C). For XPS, the WE foils were loaded into a home-built vacuum transfer system, rapidly evacuated to pressures below 2 $\times 10^{-5}$ mbar, and then loaded into the XPS chamber having a base pressure below 9 $\times 10^{-10}$ mbar (fig. S15). For grazing incidence XRD, the samples were transported in an air-tight polyetheretherketone (PEEK) dome (fig. S16). Hence, both systems prevent air exposure, as the samples are only exposed to the glove box inert Ar atmosphere before loading into the respective transfer systems.

As seen from XPS in Fig. 4, A to C, and fig. S17, the most notable difference between the samples with varying O_2 content is for the sample with 0.8 mol % O_2, wherein a peak appears in the N 1s scanning window. On the basis of the proposed reaction mechanism, which suggests Li_3N as a precursor for ammonia (*25*), we attribute that peak to Li_3N. The peak position also fits well with previously reported spectra of Li_3N (*37*, *38*). The XRD pattern for Li_3N is not observed in Fig. 4 D, because the formed Li_3N is expected to be mainly a surface phase and would also react rapidly with protons to form ammonia. The

0 mol % O_2 sample shows many XPS peaks for Cl compounds, which are not observed in the higher O_2 samples (fig. S17), indicating that these additional species could cause the premature overloading of the system. The XRD diffractograms for the samples appear to increase in complexity with increasing O_2 content, as more compounds appear. For all three samples, the Mo foil is clearly visible, as well as LiOH and $LiClO_4$. The sample with 3.0 mol % O_2 additionally shows hydrated $LiClO_4$, as an increase in O_2 leads to an increase in the ORR (fig. S9 and tables S1 and S2). Furthermore, Li_2O is also faintly visible on this sample, as would be expected on a sample with increased O_2 exposure.

The counterintuitive results shown in this study focus attention on the effect of controlling the availability of competing H^+, N_2, and Li^+ ions at the catalyst surface. Our model suggests that oxygen can slow Li^+ diffusion through the SEI layer while keeping the optimal relationship between available H^+ and N_2 at the surface. The modification of the SEI layer through O_2 is well supported by Wang *et al.* (*31*) and the experimental data presented here. O_2 is shown to have an effect on the deposition behavior (fig. S14), as well as on the stability (Fig. 2). Because it was discussed previously that the increase in stability is caused by more uniform Li plating (*24*), both observations are evidence for O_2 influencing the deposition of Li through modification of the SEI layer. Further optimization of the LiNR system in future studies may direct design of an artificial SEI layer with improved transport-controlling properties, preferably even without using Li as one of the constituents to decrease the overall required cell potential.

We propose that the results presented here put into perspective all previous LiNR publications that did not conduct their experiments entirely in a glove box or with a fully controlled atmosphere. Some experiments could have small amounts of O_2 in the system, which would lead to higher efficiencies but perhaps also to large interexperimental variability (poor reproducibility). Because even very small amounts of O_2 can have such a critical effect, we strongly recommend that the atmospheric composition of the experiment be determined and stated in all future studies. Our findings should also lead to a substantial advantage in the scale-up of the process, because the LiNR will not require ultrapure nitrogen, unlike the Haber-Bosch process, in which even the smallest contamination by oxygen is detrimental to the catalyst (*39*). The separation of N_2 from air is industrially achieved by cryogenic separation in large facilities and is therefore prohibitively expensive for a decentralized system (*40*, *41*).

REFERENCES AND NOTES

1. United States Geological Survey (USGS), *Mineral Commodity Summaries 2020* (2020).
2. D. R. MacFarlane *et al.*, *Adv. Mater.* **32**, e1904804 (2020).
3. D. R. MacFarlane *et al.*, *Joule* **4**, 1186–1205 (2020).
4. C. H. Christensen, T. Johannessen, R. Z. Sørensen, J. K. Nørskov, *Catal. Today* **111**, 140–144 (2006).
5. F. Haber, R. Le Rossignol, *Z. Elektrochem. Angew. Phys. Chem.* **19**, 53–72 (1913).
6. J. W. Erisman, M. A. Sutton, J. Galloway, Z. Klimont, W. Winiwarter, *Nat. Geosci.* **1**, 636–639 (2008).
7. C. J. M. van der Ham, M. T. M. Koper, D. G. H. Hetterscheid, *Chem. Soc. Rev.* **43**, 5183–5191 (2014).
8. M. Capdevila-Cortada, *Nat. Catal.* **2**, 1055 (2019).
9. I. McPherson, J. Zhang, *Joule* **4**, 12–14 (2020).
10. S. T. Wismann *et al.*, *Science* **364**, 756–759 (2019).
11. B. H. R. Suryanto *et al.*, *Science* **372**, 1187–1191 (2021).
12. N. Lazouski, M. Chung, K. Williams, M. L. Gala, K. Manthiram, *Nat. Catal.* **3**, 463–469 (2020).
13. B. Yang, W. Ding, H. Zhang, S. Zhang, *Energy Environ. Sci.* **14**, 672–687 (2021).
14. H. Shen *et al.*, *Chem* **7**, 1708–1754 (2021).
15. J. Kibsgaard, J. K. Nørskov, I. Chorkendorff, *ACS Energy Lett.* **4**, 2986–2988 (2019).
16. J. Choi *et al.*, *Nat. Commun.* **11**, 5546 (2020).
17. S. Z. Andersen *et al.*, *Nature* **570**, 504–508 (2019).
18. H. Iriawan *et al.*, *Nat. Rev. Methods Primers* **1**, 56 (2021).
19. W. Yu *et al.*, *Sustain. Energy Fuels* **4**, 5080–5087 (2020).
20. S. Licht *et al.*, *Science* **369**, 780 (2020).
21. F. Fichter, P. Girard, H. Erlenmeyer, *Helv. Chim. Acta* **13**, 1228–1236 (1930).
22. A. Tsuneto, A. Kudo, T. Sakata, *Chem. Lett.* **22**, 851–854 (1993).
23. A. Tsuneto, A. Kudo, T. Sakata, *J. Electroanal. Chem. (Lausanne)* **367**, 183–188 (1994).
24. S. Z. Andersen *et al.*, *Energy Environ. Sci.* **13**, 4291–4300 (2020).
25. N. Lazouski, Z. J. Schiffer, K. Williams, K. Manthiram, *Joule* **3**, 1127–1139 (2019).
26. T. M. Pappenfus, K. Lee, L. M. Thoma, C. R. Dukart, *ECS Trans.* **16**, 89–93 (2009).
27. L.-F. Gao *et al.*, *Angew. Chem. Int. Ed.* **60**, 5257–5261 (2021).
28. R. Sažinas *et al.*, *RSC Advances* **11**, 31487–31498 (2021).
29. J. A. Schwalbe *et al.*, *ChemElectroChem* **7**, 1542 (2020).
30. G. Soloveichik, in *2019 AIChE Annual Meeting* (AIChE, 2019). https://arpa-e.energy.gov/technologies/programs/refuel
31. E. Wang, S. Dey, T. Liu, S. Menkin, C. P. Grey, *ACS Energy Lett.* **5**, 1088–1094 (2020).
32. G. K. H. Wiberg, M. J. Fleige, M. Arenz, *Rev. Sci. Instrum.* **85**, 085105 (2014).
33. A. R. Singh *et al.*, *ACS Catal.* **9**, 8316–8324 (2019).
34. J. M. McEnaney *et al.*, *Energy Environ. Sci.* **10**, 1621–1630 (2017).
35. T. Ludwig, A. R. Singh, J. K. Nørskov, *J. Phys. Chem. C* **124**, 26368–26378 (2020).
36. K. Xu, *Chem. Rev.* **114**, 11503–11618 (2014).
37. C. Liu *et al.*, *Sci. Bull.* **65**, 434–442 (2020).
38. K. N. Wood, G. Teeter, *ACS Appl. Energy Mater.* **1**, 4493–4504 (2018).
39. B. A. Rohr, A. R. Singh, J. K. Nørskov, *J. Catal.* **372**, 33–38 (2019).
40. W. F. Castle, *Int. J. Refrig.* **25**, 158–172 (2002).
41. S. Ivanova, R. Lewis, *Chem. Eng. Prog.* **108**, 38–42 (2012).
42. K. Li, S. Z. Andersen, I. Chorkendorff, DTU Data (2021).

ACKNOWLEDGMENTS

We thank the floor managers B. P. Knudsen and P. Strøm-Hansen for helping with the design of the autoclaves and the connection to the mass spectrometer. **Funding:** We gratefully acknowledge the funding by Villum Fonden, part of the Villum Center for the Science of Sustainable Fuels and Chemicals (V-SUSTAIN grant 9455), Innovationsfonden (E-ammonia grant 9067-00010B) and the European Research Council (ERC) under the European Union's Horizon 2020 research and innovation program (grant agreement no. 741860). **Author contributions:** Conceptualization: S.Z.A., K.K., I.C., J.K.N. Data curation: K.L., S.Z.A., M.J.S., M.S. Formal Analysis: K.L., S.Z.A., M.J.S., V.J.B., M.S. Investigation: K.L., S.Z.A., M.J.S., V.J.B., M.S. Methodology – Equipment design: S.Z.A., M.S., V.S. Visualization: K.L., S.Z.A., M.J.S., V.J.B. Supervision: I.C., J.K., P.C.K.V., D.C., J.K.N. Writing – original draft: K.L., S.Z.A., M.J.S., V.J.B. Writing – review and editing: K.L., S.Z.A., M.S., V.J.B., K.K., R.S., J.B.P., D.C., J.K., P.C.K.V., J.K.N., I.C. **Competing interests:** A patent application titled "Oxygen enhancement of lithium-mediated electrochemical nitrogen reduction" was submitted on 22 February 2021 regarding the reported increase in FE due to the addition of oxygen mentioned in the paper. Inventors: S.Z.A., K.L., V.J.B., M.S., K.K., R.S., J.B.P., J.K., M.S., P.C.K.V., D.C., J.K.N., and I.C. Institutions: DTU and Stanford University. US provisional application/DK priority-founding application. The authors declare no financial conflicts of interest. **Data and materials availability:** Additional information is provided in the supplementary materials, and the raw data are archived at the Technical University of Denmark (DTU) (*42*).

SUPPLEMENTARY MATERIALS

science.org/doi/10.1126/science.abl4300
Materials and Methods
Supplementary Text
Figs. S1 to S18
Tables S1 and S2
References (*43*–*45*)

9 August 2021; accepted 3 November 2021
10.1126/science.abl4300

Supplementary Materials for

Enhancement of lithium-mediated ammonia synthesis by addition of oxygen

Katja Li *et al.*

Corresponding authors: Jens K. Nørskov, jkno@dtu.dk; Ib Chorkendorff, ibchork@fysik.dtu.dk

Science **374**, 1593 (2021)
DOI: 10.1126/science.abl4300

The PDF file includes:

Materials and Methods
Supplementary Text
Figs. S1 to S18
Tables S1 and S2
References

Materials and Methods

Electrochemical experiments

Measurements were done in a 3-electrode single compartment glass cell enclosed in an electrochemical autoclave, placed in a fumehood. Electrolyte solution consisted of 0.3 M $LiClO_4$ (Battery grade, dry, 99.99 %, Sigma Aldrich) in 99 vol. % tetrahydrofuran (THF, anhydrous, >99.9 %, inhibitor-free, Sigma Aldrich) and 1 vol. % ethanol (EtOH, anhydrous, Honeywell) and was prepared in an Ar glovebox. Roughly, 30-40 p.p.m. of water contamination is measured in the electrolyte via Karl Fischer Titration (831 KF Coulometer and 728 Stirrer, Metrohm). The working electrode (WE) is a Mo foil (+99.9 %, 0.1 mm thick, Goodfellow) spot-welded with Mo wire (99.85 %, Goodfellow) for good electrical connection. Prior to electrochemical tests, the WE is dipped in 2 wt. % HCl (VWR Chemicals) to dissolve any surface species of Li, and rinsed in ultra-pure water (18.2 MΩ resistivity, Millipore, Synergy UV system) and EtOH. The WE is polished using Si-C paper (Buehler, CarbiMet P1200), and again rinsed thoroughly in EtOH. The counter electrode (CE) consists of a Pt mesh (99.9 %, Goodfellow), and the reference electrode (RE) is a Pt wire (99.99 %, Goodfellow). The CE and RE are both boiled in ultra-pure water, and dried overnight at 100 °C, then flame-annealed. The single compartment glass cell and a magnetic stirring bar (VWR, glass covered) is boiled in ultra-pure water, and dried overnight at 100 °C in air. The WE and CE are ~0.5 cm apart, and the surface area of the WE facing the CE is 1.8 cm^2. Prior to an electrochemical experiment, we introduce Ar gas (5.0, Air Liquide) into the empty assembled cell placed in the autoclave for at least 30 min. The denser Ar gas substantially displaces the atmospheric laboratory air, mainly consisting of N_2 and O_2, in the system, as measured via mass spectrometry. Next, we inject electrolyte solution into the cell in Ar atmosphere, and the autoclave is closed. The N_2 (6.0, Air Liquide) and synthetic air (20 % O_2 in N_2, 5.0, Air Liquide) used in the experiments are first cleaned by purifiers (NuPure, pptV cleaning of all labile N containing compounds) and the desired O_2 contents are controlled via mass flow controllers (Brooks Instrument). With this premixed gas, the pressure is increased to 10 bar and de-pressurized to 3 bar a total of 10 times, in order to flush out any remaining atmospheric contaminants, then filled to 10 or 20 bar for experiments. The system is left to rest for 20 min to equilibrate the atmosphere composition with the electrolyte, and afterwards the oxygen content is read off from the mass spectrometer signal (OmniStar GSD 320, Pfeiffer Vacuum). During the whole experiment, the electrolyte is stirred at 250 rpm. Subsequently, the electrochemical experiments, including potentiostatic electrochemical impedance spectroscopy (PEIS) to determine the resistance in our cell, a linear sweep voltammetry (LSV) from open circuit voltage (OCV) until lithium reduction is clearly seen, then chronopotentiometry (CP), followed by another impedance measurement to ensure that the resistance has not changed, are started. After the experiment, the water content is measured again. We determine the lithium reduction potential scale based on the LSV. The onset for lithium reduction is quite clear, and we can thereby denote the potential vs. Li/Li^+. During CP, either a steady current density of -4 mA/cm^2 is used (hereafter denoted deposition potential), or a cyclic method with -4 mA/cm^2 for 1 min, followed by 0 mA/cm^2 (hereafter denoted resting potential) for 2-7 min, depending on whether the WE potential needed to be increased, decreased, or stabilized. After 50 C of charge is passed the $LiClO_4$ concentration is reduced from 0.3 M to 0.28 M, if we assume 100 % FE towards Li plating. Since the consumption of Li^+ is so small we do not expect it to influence the measurements. We note that all experiments were conducted at room temperature.

Colorimetric quantification of ammonia

Synthesized ammonia was quantified by a modified colorimetric indophenol method, previously described*(17)*. The sample absorbance was analyzed by UV/Vis spectroscopy (UV-2600, Shimadzu) in the range from 400 nm to 1000 nm. The blank background solution is subtracted from each spectrum, and the difference between the peak around 630 nm and the trough at around 850 nm is used. A fitted curve of the difference between the peak and trough of each concentration showed a linear regression with an R^2 value of 0.998. We utilize this method, as opposed to the more common peak based method, because long experiments might have solvent breakdown, which can give a falsely high peak at the ammonia wavelength, due to interference from the evolved solvent background. For each measurement, four 0.5 mL samples were taken from the electrolyte. One sample from the electrolyte is used as a background, and the mean and standard deviation of the remaining 3 samples is reported in Table S1. The remaining samples were treated as described previously *(17),* to determine the ammonia concentration. If the expected concentration of ammonia exceeds the concentration limits of the indophenol method, the sample is accordingly diluted with ultra-pure water after drying. Since rigorous testing with quantitative isotope measurements were performed in our previous works in the same system, we did not repeat them in this work *(17).*

Analysis of Solid electrolyte interface

To analyze the effect of oxygen on the solid electrolyte interface the WE was characterized after electrochemistry with X-ray diffraction (XRD) and X-ray Photoelectron Spectroscopy (XPS). For both techniques the reaction was performed in an autoclave inside an Ar filled glovebox and a transfer system was used to minimize the exposure to air. For XRD a gas tight PEEK dome (Anton Paar, Fig. S11) was used to cover the sample on top of the XRD sample holder during the measurement. For XPS the sample was transported from the glovebox to the XPS via a vacuum suitcase seen in Fig. S12. XRD data was recorded running the Data Collector v5.4 software on a Malvern Pananalytical Empyrean X-ray diffractometer. On the incident beam path, a parallel beam X-ray mirror for Cu radiation, a fixed mask 10 mm, and a fixed slit 1/8° placed 140 mm from the sample were used. The diffracted beam path was equipped with a parallel plate collimator having an opening of 0.18°. The source was an Empyrean Cu LFF HR gun operated at 45 kV and 40 mA, with $K\alpha_1 = 1.540598$ Å. Grazing-incidence geometry was used to minimize the contribution of the substrate, i.e. the Mo foil, with an incident radiation beam fixed at a grazing angle of 1.0°. The data was analyzed with HighScore Plus v4.6a by Panalytical with reference patterns from the Inorganic Crystal Structure Database (ICSD). The data were not fitted and no quantitative analysis was performed since the peak intensities vary in GI-XRD measurements on thin films. Therefore, only qualitative are drawn from this data and stated in the main text. X-ray Photoelectron Spectroscopy was done using a ThermoScientific Thetaprobe instrument equipped with an Al Kα X-ray source and having a chamber base pressure below $9 \cdot 10^{-10}$ mbar . Survey spectra were recorded with 120 scans at 50 ms dwell time per 1 eV step. Elemental detail spectra were recorded with 25-250 scans in 0.1 eV steps with 50 ms dwell time. The lateral resolution was 400 μm and a value of pass energy of 200 eV was used. The chamber pressure was risen to $1.3 \cdot 10^{-7}$ mbar by flowing 6.0 Ar gas in order as required by the use of a flood gun, which was used in charge neutralization mode during the measurement. The data was acquired and analyzed using Thermo Advantage v5.9917 by Thermo Fischer Scientific. All data was fitted with the Powell fitting algorithm and the background determined by the Smart background option, which is based on the Shirley background.

Supplementary Text

Energy efficiency and Faradaic efficiency calculations

To calculate the Faradaic efficiency (FE), the concentration, c_{NH3}, of synthesized ammonia in the electrolyte is measured via either a colorimetric or isotope sensitive method, along with the total electrolyte volume, V, after each measurement. This is compared with the total charged passed, Q:

$$FE_{NH_3} = \frac{3 \cdot F \cdot c_{NH_3} \cdot V}{Q}$$

where F is Faraday's constant, and 3 is the number of electrons transferred during the reaction for each mole of NH_3. To estimate the energy efficiency, η, we considered the total amount of energy put into the system via the potentiostat, E_{in}, and compared that to the energy contained in the total amount of ammonia produced during the experiment, E_{out}. It should be noted that we do not include pressure and energy from EtOH in our calculations. We define E_{out} by the free energy of reaction of ammonia oxidation to N_2 and water times the amount of ammonia produced, while E_{in} is given by the total cell voltage between the counter electrode (CE) and working electrode (WE), multiplied by the current to get the instantaneous power, and integrated over time:

$$\eta = \frac{E_{out}}{E_{in}} = \frac{\Delta G_r \cdot m_{NH_3}}{\int V_{cell}(t) \cdot I(t) dt}$$

Paper 2

Increasing current density of Li-mediated ammonia synthesis with high surface area copper electrodes

K. Li, S. G. Shapel, D. Hochfilzer, J. B. Pedersen, K. Krempl, S. Z. Andersen, R. Sazinas, M. Saccoccio, S. Li, D. Chakraborty, J. Kibsgaard, P. C. Vesborg, J. Nørsvov and I. Chorkendorff, *ACS Energy Letters*, **2022**, 7, 36-41.

ACS Energy Letters
http://pubs.acs.org/journal/aelccp

Increasing Current Density of Li-Mediated Ammonia Synthesis with High Surface Area Copper Electrodes

Katja Li,[†] Sarah G. Shapel, Degenhart Hochfilzer, Jakob B. Pedersen, Kevin Krempl, Suzanne Z. Andersen, Rokas Sažinas, Mattia Saccoccio, Shaofeng Li, Debasish Chakraborty, Jakob Kibsgaard, Peter C. K. Vesborg, Jens K. Nørskov, and Ib Chorkendorff*

Cite This: *ACS Energy Lett.* 2022, 7, 36–41

Read Online

ACCESS | Metrics & More | Article Recommendations | Supporting Information

ABSTRACT: **The lithium-mediated ammonia synthesis is so far the only proven electrochemical way to produce ammonia with promising faradaic efficiencies (FEs). However, to make this process commercially competitive, the ammonia formation rates per geometric surface area need to be increased significantly. In this study, we increased the current density by synthesizing high surface area Cu electrodes through hydrogen bubbling templating (HBT) on Ni foam substrates. With these electrodes, we achieved high ammonia formation rates of 46.0 ± 6.8 nmol s^{-1} cm_{geo}^{-2}, at a current density of −100 mA/cm_{geo}^{-2} at 20 bar nitrogen atmosphere and comparable cell potentials to flat foil electrodes. The FE and energy efficiency (EE) under these conditions were 13.3 ± 2.0% and 2.3 ± 0.3%, respectively. Additionally, we found that increasing the electrolyte salt concentration improves the stability of the system, which is attributed to a change of Li deposition and/or solid electrolyte interphase.**

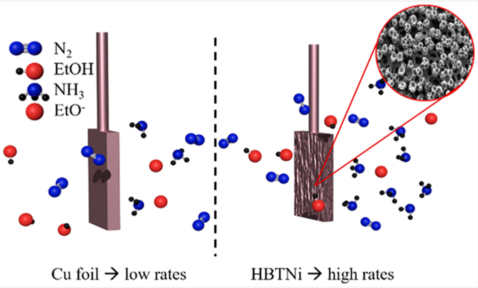

Global warming is arguably one of the biggest problems of our current society. It is caused by greenhouse gases such as CO_2, whose emissions are increasing constantly. To counteract this, all possible CO_2 emissions should be reduced. The ammonia production by itself is the cause of ∼1.4% of the global annual CO_2 emission, since it utilizes steam reforming to obtain H_2, which is then reacting with N_2 to form ammonia in the Haber-Bosch process.[1−5] This is not only harming the environment but is also heavily energy consuming (1% of total yearly energy consumption) because of its harsh conditions (100−200 bar, 350−450 °C).[6−8] Hence, finding a sustainable alternative to the Haber-Bosch process would be a huge step in mitigating climate change. One way to achieve this is by electrifying ammonia synthesis, since electricity can be acquired from renewable energy sources. Although the area of electrochemical ammonia synthesis has gained much scientific interest due to the large positive implications,[9−17] it still has some complications such as impurities in the gas feed or chemicals and selectivity issues, leading to erroneous reports and small faradaic efficiencies.[18−21] Recently, protocols of how to conduct experiments in this field and measure ammonia correctly were published, which will help move the research in the right direction.[18,22−24] So far it is believed that the only reliable way to make ammonia electrochemically is the Li-mediated ammonia synthesis which was initially developed by Fichter et al. in 1930[25] and later also studied by Tsuneto et al. over 60 years later.[4,5] This method uses a nonaqueous electrolyte to minimize the competing hydrogen evolution reaction (HER). The exact mechanism is yet to be elucidated, but most agree that it involves three main steps.[26] The first step is plating out metallic Li from a Li-salt, which then reacts in the second step with dissolved N_2 in the electrolyte, therefore splitting the stable triple bond and forming Li_3N or other N-containing compounds. Finally, ammonia is made after protonation by a suitable proton source like EtOH. Tsuneto et al. reported moderate faradaic efficiencies (FEs) of around 6% at ambient conditions and the inherent instability of the system,[4] but since the rediscovery of this process by many groups, the FE and the stability have increased.[11,18,26−30] Up to this point, the highest FE reported is 69% at 20 bar N_2,[27] where the sacrificial proton donor was replaced with an ionic liquid based proton shuttle.

Received: September 27, 2021
Accepted: November 19, 2021
Published: November 24, 2021

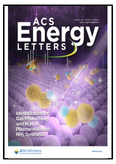

ACS Publications

https://doi.org/10.1021/acsenergylett.1c02104
ACS Energy Lett. 2022, 7, 36−41

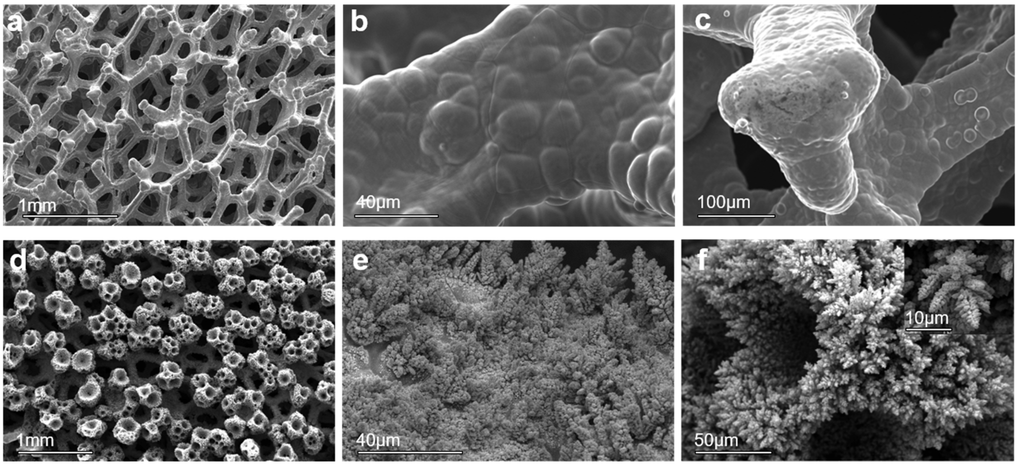

Figure 1. Representative SEM images of pristine Ni foam (a−c) and Cu electrodeposited on Ni foam with the HBT method (d−f).

This already comes quite close to the goal set by the REFUEL program of the US Department of Energy, who envision an FE and energy efficiency (EE) of 90% and 60% respectively, at current densities of 300 mA cm^{-2}.[31] The current density, however, has lagged behind with a recently set record of −25 mA cm_{geo}^{-2}, which was achieved by Lazouski et al. by applying the process to a gas diffusion electrode.[11] In this letter we report the successful fabrication of high surface area Cu electrodes, which achieved current densities of −100 mA cm_{geo}^{-2} in a glass cell setup inside an autoclave at 20 bar N_2 pressure.

It has to be noted that there are several definitions of surface area. In this study the term geometric surface area is used to describe the area that can be measured with a simple ruler, whereas the electrochemical surface area (ECSA) is the area of the working electrode that participates in the electrochemical reaction and has to be determined experimentally.

Tsuneto et al. tested several metals as working electrode material, and as long as the metal does not alloy with Li, it can be used.[4,5] Specifically Mo[18,28] and Cu[26,27] electrodes have been previously reported as suitable working electrode materials for the Li-mediated ammonia synthesis. Therefore, the aim was to make highly structured electrodes for one of these metals. The hydrogen bubble template (HBT) method was chosen to achieve this, since it is an easily up-scalable process. This technique creates porous metal structures by simultaneously plating a metal from a metal salt electrolyte while forming hydrogen through hydrogen evolution reaction (HER) at high overpotentials.[32] HBT is mostly utilized for Cu[33−35] but has also been used with other metals such as Pt,[36] Pd,[36] Ru,[37] and Co.[38] To the best of our knowledge, HBT has only been applied on flat substrates, but in this letter we used this method on Ni foam. This allows us to increase the surface area even further, by utilizing the already porous structure of Ni foam. With this technique, we managed to create highly structured Cu electrodes for the Li-mediated ammonia synthesis. The electrodes were characterized by scanning electron microscopy (SEM), energy dispersive X-ray analysis (EDX), and X-ray photoelectron spectroscopy (XPS). Furthermore, the electrochemical surface area was measured by capacitive cycling. Lastly, the performance of the working electrodes was tested at 20 bar N_2 in a home-built autoclave, where we achieved current densities of −100 mA/cm_{geo}^2 at similar cell potentials and FE compared to flat working electrodes.

For making the high surface area electrodes, we used a Ni foam of 0.5 cm^2 geometric surface area as substrate. The hydrogen bubble templating was performed in 0.4 M $CuSO_4$ dissolved in 1.5 M H_2SO_4 electrolyte with a split Pt mesh counter electrode to achieve homogeneous deposition on both sides. The Ni foam working electrode was placed in between the two Pt mesh counter electrodes with a separation of ∼1 cm between each of them, and a constant current of −5 A was applied for 15 s. Upon start of the deposition, heavy gas evolution was observed at the working electrode (HER) and counter electrodes (oxygen evolution reaction OER). The resulting hydrogen bubble templated Cu on Ni foam (HBTCu) was washed in EtOH, dried in vacuum for at least 1 h, and stored in an Ar glovebox before use, to prevent oxidation of Cu as much as possible. A more detailed description of the process and a real life image of HBTCu (Figure S1) can be found in the Supporting Information (SI).

When compared to the pure Ni foam (Figure 1a−c), the SEM images of the HBTCu (Figure 1 d−f) reveal a great increase of surface area. There are noticeably two different morphologies observed at the topmost exposed round (Figure 1 b, e) and the inner flat surface structures (Figure 1 c, f). A closer look and discussion of these two regions is provided in Figure S2. To ensure that the whole Ni surface is covered by Cu, SEM-EDX (Figure S3) and XPS (Figure S4) were carried out. Furthermore, cross sections of HBTCu were taken by SEM (Figure S5). All data show that the Ni foam structure is completely covered by Cu after the treatment, both on the outer surfaces and across its thickness. Since the resulting morphologies are heavily dependent on the deposition conditions (time and current), it is possible to modify and optimize the deposition, which will be a focus in future studies.

To determine the ECSA of the deposited HBTCu electrodes, capacitive cycling in 2 M $LiClO_4$ electrolyte was carried out to simulate the reaction conditions for ammonia synthesis. In previous Li-mediated ammonia synthesis publications, the electrolyte salt concentration was around 0.3−0.5 M,[11,18,26,28] but the concentration was increased to 2 M in this case to reduce the solution resistance and the double layer thickness. It has been shown previously that the double layer thickness scales with electrolyte salt concentration and therefore more surface area can be accessed with higher salt

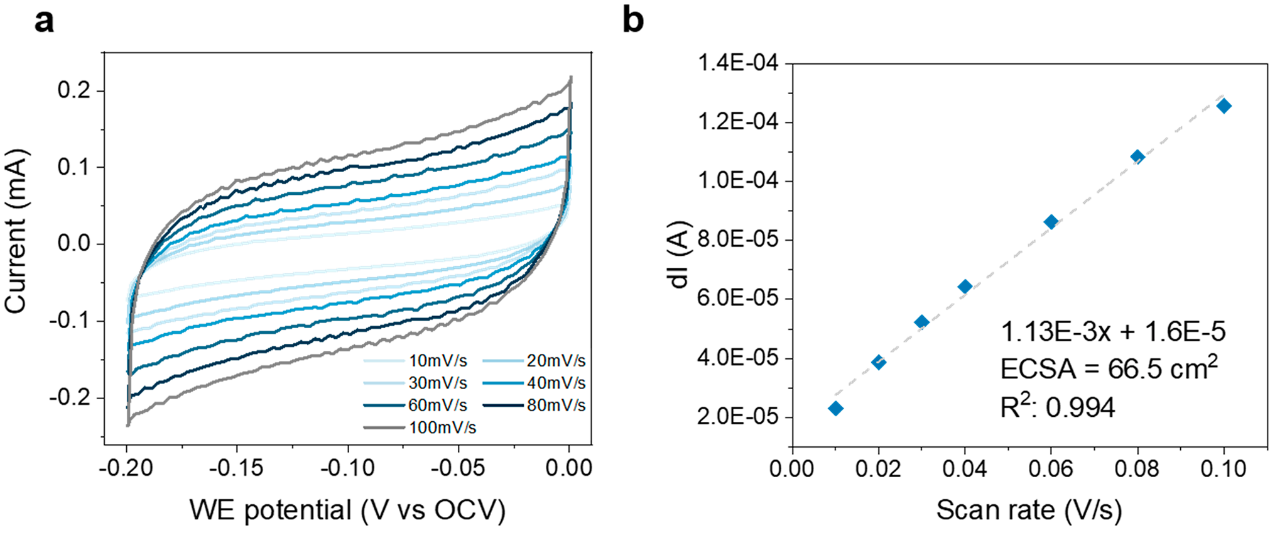

Figure 2. Representative capacitive cycling data of 0.5 cm_{geo}^2 HBTCu in 2 M $LiClO_4$. (a) Cyclic voltammetry at different scan rates (10−100 mV s^{-1}) from 0 to −0.2 mV vs OCV. (b) Change in current versus scan rate and calculated ECSA. The change in current was determined at −0.1 V vs OCV. The ECSA measurement was repeated on three independent HBTCu electrodes.

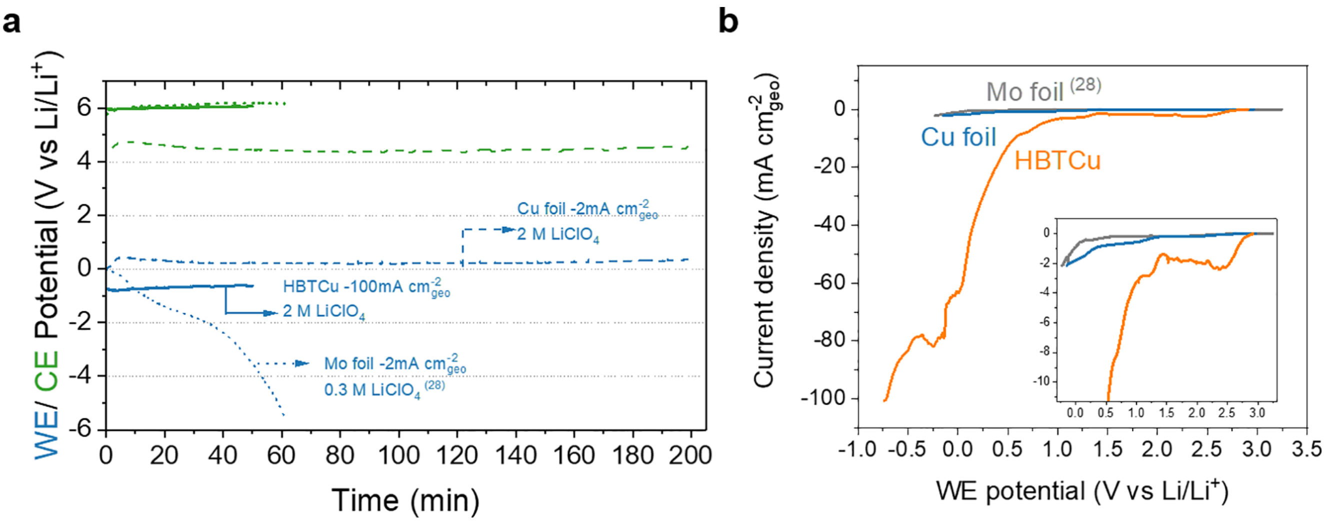

Figure 3. Representative chronopotentiometry (CP) (a) and linear sweep voltammetry (b) of Mo foil (−2 mA cm_{geo}^{-2}, 0.3 M $LiClO_4$, dotted),[28] Cu foil (−2 mA cm_{geo}^{-2}, 2 M $LiClO_4$, dashed) and HBTCu (−100 mA cm_{geo}^{-2}, 2 M $LiClO_4$, straight line) at 20 bar N_2 atmosphere. The CE potential of the Cu foil experiment was smoothed due to a loose connection. The unsmoothed raw data can be seen in Figure S10. All experiments were carried out three independent times.

concentrations.[39] For ECSA determination by capacitive cycling, the specific capacitance of the material in the respective electrolyte is needed. To obtain the specific capacitance of Cu in 2 M $LiClO_4$, a Cu stub of known surface area (0.2 cm^2) was polished with diamond paste until the geometric surface area was equal to the ECSA. Then cyclic voltammograms (CV) were carried out in 2 M $LiClO_4$ at different scan speeds (10−60 mV s^{-1}) from 0 to −0.2 mV vs OCV. With this, a specific capacitance of 0.017 mF cm^{-2} was determined for Cu. The electrochemical data and calculation methods can be found in the SI and Figure S6. After repeating the process with three independently synthesized HBTCu, an ECSA of 66.5 ± 7.1 cm^2 was determined as shown in Figure 2. If compared to the previously used current density of −2 mA cm_{geo}^{-2} [28] this electrode should theoretically be able to sustain a current density of around −130 mA cm_{geo}^{-2}, if scaled linearly.

To test the performance of the synthesized HBTCu, electrochemical synthesis of ammonia was carried out in a home-built autoclave (Figure S7) at 20 bar N_2. The N_2 (6.0, AirLiquide) was cleaned with purifiers (NuPure) to remove any traces of labile N-containing compounds. Pt mesh and Pt wire were used as the counter and pseudo reference electrode, respectively. The electrolyte consisted of 2 M $LiClO_4$ in tetrahydrofuran (THF) with 1 vol % of EtOH as the proton source. To directly compare the high surface area Cu electrodes to flat surfaces of the same material, two sets of experiments were conducted, using HBTCu and Cu foil as the working electrode, respectively. Additionally, reference experiments of pure Ni foil and HBT on Ni foil are included in the SI (Figure S10, Table S1). After 20 min at OCV, linear sweep voltammetry (LSV) was initiated from OCV until Li plating can be observed (Figure 3b). The ammonia was then synthesized at a constant current density of −2 mA cm_{geo}^{-2}

(Figure 3a) for Cu foil and −100 mA cm_{geo}^{-2} for HBTCu. SEM images were taken of the electrode after electrochemistry to test the physical stability in Figure S8. The image does not show big changes in the morphology, which suggests that the electrodes can be reused. Additional stability tests will be provided in future studies. The possibility of oxidation of ammonia at the CE was excluded since it was previously shown that ammonia oxidation does not occur at acidic conditions[40] and our electrolyte is believed to be acidic due to THF oxidation at the counter electrode.[30] The ammonia content was measured by a modified indophenol blue method (Figure S9). A more detailed description of the experimental procedure can be found in the SI.

The large differences in potential, especially on the CE side, stem from uncompensated resistances. The measured resistances for the measurements are given in Table S1, and the compensated CP is shown in Figure S10a. To compare to our previous work,[28] the LSV and CP of a Mo foil in 0.3 M $LiClO_4$ was inserted. Cu and Mo can be used interchangeably as working electrode materials, as is suggested by literature.[5,26] Figure 3b shows that HBTCu achieves much higher current densities at similar potentials due to its higher surface area, while Mo and Cu foil behave similarly, as expected. Interestingly, both the working electrode potentials for Cu foil and HBTCu (in 2 M $LiClO_4$ electrolyte) appear stable in the CP (Figure 3a), whereas Mo foil (in 0.3 M $LiClO_4$ electrolyte) starts destabilizing in the first few minutes of the experiment. This indicates that the high salt concentration is beneficial for stabilizing the working electrode potential. Since cycling the deposition current between OCV and negative currents, hence only plating a little Li at a time, also increases the stability,[28] it is believed that the destabilization arises from too much or uncontrolled Li deposition. This overplating of Li could lead to a passivation layer by decomposition products with metallic Li and therefore decreasing the working electrode to more negative potentials. The finding here suggests that the high salt concentration is limiting the reaction of metallic Li with the electrolyte by possibly surrounding the plated Li with other Li^+ ions and thus shielding it from THF or EtOH. A similar shielding of Li^+ ions from the solvent was also postulated in Li-ion battery studies, where Li salt based electrolytes of up to 21 M concentrations were utilized.[41] Additionally, the high salt concentration might have an influence on the solid electrolyte interphase (SEI) layer, which forms on metallic Li in organic solvents. It was previously discussed that this SEI layer influences the diffusion rates of the reactants and is therefore believed to be important for FE and also stability.[28] Further studies of the SEI layer at different electrolyte concentrations as well as flat and rough substrates are needed to provide a clear answer for the observed phenomenon. The FE and EE were comparable for both electrodes being 13.3 ± 2% and 2.3 ± 0.3% for HBTCu and 13.6% ± 1.0 and 3.9 ± 0.3% for Cu foil. However, the big benefit of HBTCu lies in the rate of ammonia formation with it being 46.0 ± 6.8 nmol s^{-1} cm_{geo}^{-2} for HBTCu and 1.0 ± 0.1 nmol s^{-1} cm_{geo}^{-2} for Cu foil, for three independent measurements. To compare the results with other studies in the Li-mediated ammonia synthesis area, Figure 4 shows the FE and current densities of previous publications.

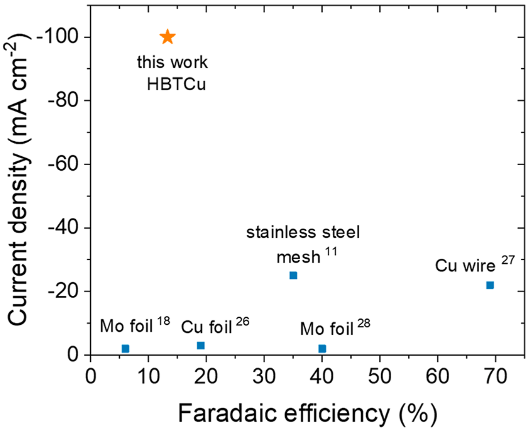

Figure 4. Current densities and FE of previous publications on the Li-mediated ammonia synthesis. The different working electrode geometries include Mo foil,[18,28] Cu foil,[26] stainless steel mesh,[11] and Cu wire.[27]

It is clear that the fabricated HBTCu electrodes presented in this study bring the field a big step further in terms of current densities and therefore scale-up potential. With the FE already approaching high values of around 70%,[27] more attention should now be given to increasing the current densities. The here obtained FEs are relatively low if compared to[28] where Andersen et al. achieved 25% in a comparable system. The only difference is that we used a 2 M electrolyte instead of a 0.3 M electrolyte, leading to the conclusion that the salt concentration has an influence on the FE. This might be due to the very reactive ClO_4^- anion or possibly to changes to the SEI. The thorough investigation of this salt effect will be a focus of future studies. Furthermore, we believe that the next step should be to remove the sacrificial proton source and implement hydrogen oxidation reaction (HOR) at the CE, similarly to Suryanto et al.[16] Only after that is achieved, we plan to optimize the FE of these high surface electrodes. We hope that this work encourages other scientists in the field to consider this area. If these high surface area electrodes are combined with other aspects that are believed to enhance the FE, the Li-mediated ammonia synthesis has a huge potential to mitigate a part of the Haber-Bosch process into a sustainable ammonia production.

In summary, we accomplished the synthesis of high surface area Cu electrodes through HBT on Ni foam substrates, which can be used for the Li-mediated ammonia synthesis. High current densities of −100 mA cm_{geo}^{-2} were achieved, leading to an increase of ammonia formation rate by a factor of 50 compared to flat Cu foil in the same system, based on geometric surface area. The FE and EE between HBTCu and Cu foil remain comparable (HBTCu: 13.3 ± 2.0% and 2.3 ± 0.3%; Cu foil: 13.6% ± 1.0 and 3.9 ± 0.3%), albeit with current densities of −100 mA cm_{geo}^{-2} and −2 mA cm_{geo}^{-2}, respectively. We believe additional optimization of the templating conditions and reaction electrolyte can further enhance the performance. Furthermore, it was observed that increased salt concentration in the electrolyte improves the stability of the system, by possibly inhibiting the formation of a passivating decomposition layer or changing the SEI layer composition. Hence, the findings shown here will not only bring us a big step further toward industrializing the electrochemical ammonia production but also provide scientific insight into the mechanism of the still elusive Li-mediated ammonia synthesis.

■ ASSOCIATED CONTENT

Supporting Information

The Supporting Information is available free of charge at https://pubs.acs.org/doi/10.1021/acsenergylett.1c02104.

> Information on experimental procedure, efficiency calculations, electrochemical active surface calculation and supplementary SEM, EDS and XPS data (PDF)

■ AUTHOR INFORMATION

Corresponding Author

Ib Chorkendorff − *Department of Physics, Technical University Denmark, 2800 Kongens Lyngby, Denmark*; orcid.org/0000-0003-2738-0325; Email: ibchork@fysik.dtu.dk

Authors

Katja Li − *Department of Physics, Technical University Denmark, 2800 Kongens Lyngby, Denmark*
Sarah G. Shapel − *Department of Physics, Technical University Denmark, 2800 Kongens Lyngby, Denmark*
Degenhart Hochfilzer − *Department of Physics, Technical University Denmark, 2800 Kongens Lyngby, Denmark*; orcid.org/0000-0003-3654-909X
Jakob B. Pedersen − *Department of Physics, Technical University Denmark, 2800 Kongens Lyngby, Denmark*
Kevin Krempl − *Department of Physics, Technical University Denmark, 2800 Kongens Lyngby, Denmark*; orcid.org/0000-0003-0031-8505
Suzanne Z. Andersen − *Department of Physics, Technical University Denmark, 2800 Kongens Lyngby, Denmark*
Rokas Sažinas − *Department of Physics, Technical University Denmark, 2800 Kongens Lyngby, Denmark*
Mattia Saccoccio − *Department of Physics, Technical University Denmark, 2800 Kongens Lyngby, Denmark*
Shaofeng Li − *Department of Physics, Technical University Denmark, 2800 Kongens Lyngby, Denmark*
Debasish Chakraborty − *Department of Physics, Technical University Denmark, 2800 Kongens Lyngby, Denmark*
Jakob Kibsgaard − *Department of Physics, Technical University Denmark, 2800 Kongens Lyngby, Denmark*; orcid.org/0000-0002-9219-816X
Peter C. K. Vesborg − *Department of Physics, Technical University Denmark, 2800 Kongens Lyngby, Denmark*; orcid.org/0000-0002-3761-4212
Jens K. Nørskov − *Department of Physics, Technical University Denmark, 2800 Kongens Lyngby, Denmark*

Complete contact information is available at:
https://pubs.acs.org/10.1021/acsenergylett.1c02104

Notes

The authors declare no competing financial interest.

■ ACKNOWLEDGMENTS

We gratefully acknowledge the funding by Villum Fonden, part of the Villum Center for the Science of Sustainable Fuels and Chemicals (V-SUSTAIN Grant 9455), Innovationsfonden (Eammonia grant 9067-00010B) and the European Research Council (ERC) under the European 430 Union's Horizon 2020 research and innovation programme (Grant Agreement No. 741860).

■ REFERENCES

(1) Capdevila-Cortada, M. Electrifying the Haber−Bosch. *Nature Catalysis* **2019**, *2* (12), 1055−1055.

(2) McPherson, I.; Zhang, J. Can Electrification of Ammonia Synthesis Decrease Its Carbon Footprint? *Joule* **2020**, *4* (1), 12−14.

(3) Wismann, S. T.; Engbæk, J. S.; Vendelbo, S. B.; Bendixen, F. B.; Eriksen, W. L.; Aasberg-Petersen, K.; Frandsen, C.; Chorkendorff, I.; Mortensen, P. M. Electrified methane reforming: A compact approach to greener industrial hydrogen production. *Science* **2019**, *364* (6442), 756−759.

(4) Tsuneto, A.; Kudo, A.; Sakata, T. Lithium-mediated electrochemical reduction of high pressure N2 to NH3. *J. Electroanal. Chem.* **1994**, *367* (1−2), 183−188.

(5) Tsuneto, A.; Kudo, A.; Sakata, T. Efficient electrochemical reduction of N2 to NH3 catalyzed by lithium. *Chem. Lett.* **1993**, *22* (5), 851−854.

(6) Haber, F.; Le Rossignol, R. Über die technische Darstellung von Ammoniak aus den Elementen. *Zeitschrift für Elektrochemie und angewandte physikalische Chemie* **1913**, *19* (2), 53−72.

(7) Erisman, J. W.; Sutton, M. A.; Galloway, J.; Klimont, Z.; Winiwarter, W. How a century of ammonia synthesis changed the world. *Nat. Geosci.* **2008**, *1* (10), 636−369.

(8) Van der Ham, C. J.; Koper, M. T.; Hetterscheid, D. G. Challenges in reduction of dinitrogen by proton and electron transfer. *Chem. Soc. Rev.* **2014**, *43* (15), 5183−5191.

(9) Christensen, C. H.; Johannessen, T.; Sørensen, R. Z.; Nørskov, J. K. Towards an ammonia-mediated hydrogen economy? *Catal. Today* **2006**, *111* (1−2), 140−144.

(10) Kim, K.; Chen, Y.; Han, J.-I.; Yoon, H. C.; Li, W. Lithium-mediated ammonia synthesis from water and nitrogen: a membrane-free approach enabled by an immiscible aqueous/organic hybrid electrolyte system. *Green Chem.* **2019**, *21* (14), 3839−3845.

(11) Lazouski, N.; Chung, M.; Williams, K.; Gala, M. L.; Manthiram, K. Non-aqueous gas diffusion electrodes for rapid ammonia synthesis from nitrogen and water-splitting-derived hydrogen. *Nature Catalysis* **2020**, *3*, 463−469.

(12) Schwalbe, J. A.; Statt, M. J.; Chosy, C.; Singh, A. R.; Rohr, B. A.; Nielander, A. C.; Andersen, S. Z.; McEnaney, J. M.; Baker, J. G.; Jaramillo, T. F. A Combined Theory-Experiment Analysis of the Surface Species in Lithium-Mediated NH3 Electrosynthesis. *ChemElectroChem* **2020**, *7* (7), 1542−1549.

(13) Abghoui, Y.; Garden, A. L.; Hlynsson, V. F.; Björgvinsdóttir, S.; Ólafsdóttir, H.; Skúlason, E. Enabling electrochemical reduction of nitrogen to ammonia at ambient conditions through rational catalyst design. *Phys. Chem. Chem. Phys.* **2015**, *17* (7), 4909−4918.

(14) MacFarlane, D. R.; Cherepanov, P. V.; Choi, J.; Suryanto, B. H.; Hodgetts, R. Y.; Bakker, J. M.; Vallana, F. M. F.; Simonov, A. N. A Roadmap to the Ammonia Economy. *Joule* **2020**, *4*, 1186−1205.

(15) MacFarlane, D. R.; Choi, J.; Suryanto, B. H.; Jalili, R.; Chatti, M.; Azofra, L. M.; Simonov, A. N. Liquefied sunshine: transforming renewables into fertilizers and energy carriers with electromaterials. *Adv. Mater.* **2020**, 32 (18), 1904804.

(16) Suryanto, B. H.; Kang, C. S.; Wang, D.; Xiao, C.; Zhou, F.; Azofra, L. M.; Cavallo, L.; Zhang, X.; MacFarlane, D. R. Rational electrode−electrolyte design for efficient ammonia electrosynthesis under ambient conditions. *ACS Energy Letters* **2018**, *3* (6), 1219−1224.

(17) Iriawan, H.; Andersen, S. Z.; Zhang, X.; Comer, B. M.; Barrio, J.; Chen, P.; Medford, A. J.; Stephens, I. E.; Chorkendorff, I.; Shao-Horn, Y. Methods for nitrogen activation by reduction and oxidation. *Nature Reviews Methods Primers* **2021**, *1* (1), 1−26.

(18) Andersen, S. Z.; Čolić, V.; Yang, S.; Schwalbe, J. A.; Nielander, A. C.; McEnaney, J. M.; Enemark-Rasmussen, K.; Baker, J. G.; Singh, A. R.; Rohr, B. A. A rigorous electrochemical ammonia synthesis protocol with quantitative isotope measurements. *Nature* **2019**, *570*, 504−508.

(19) Choi, J.; Du, H.-L.; Nguyen, C. K.; Suryanto, B. H. R.; Simonov, A. N.; MacFarlane, D. R. Electroreduction of Nitrates, Nitrites and Gaseous Nitrogen Oxides: A Potential Source of

Ammonia in Dinitrogen Reduction (NRR) Studies. *ACS Energy Letters* **2020**, *5* (6), 2095−2097.

(20) Singh, A. R.; Rohr, B. A.; Schwalbe, J. A.; Cargnello, M.; Chan, K.; Jaramillo, T. F.; Chorkendorff, I.; Nørskov, J. K. Electrochemical Ammonia Synthesis— The Selectivity Challenge. *ACS Catal.* **2017**, *7*, 706−709.

(21) Hu, B.; Hu, M.; Seefeldt, L.; Liu, T. L. Electrochemical Dinitrogen Reduction to Ammonia by Mo2N: Catalysis or Decomposition? *ACS Energy Letters* **2019**, *4* (5), 1053−1054.

(22) Choi, B. N.; Seo, J. Y.; Kim, B.; Kim, Y. S.; Chung, C.-H. Electro-deposition of the lithium metal anode on dendritic copper current collectors for lithium battery application. *Appl. Surf. Sci.* **2020**, *506*, 144884.

(23) Greenlee, L. F.; Renner, J. N.; Foster, S. L. The use of controls for consistent and accurate measurements of electrocatalytic ammonia synthesis from dinitrogen. *ACS Catal.* **2018**, *8*, 7820−7827.

(24) Nielander, A. C.; McEnaney, J. M.; Schwalbe, J. A.; Baker, J. G.; Blair, S. J.; Wang, L.; Pelton, J. G.; Andersen, S. Z.; Enemark-Rasmussen, K.; Čolić, V. A Versatile Method for Ammonia Detection in a Range of Relevant Electrolytes via Direct Nuclear Magnetic Resonance Techniques. *ACS Catal.* **2019**, *9*, 5797−5802.

(25) Fichter, F.; Girard, P.; Erlenmeyer, H. Elektrolytische Bindung von komprimiertem Stickstoff bei gewöhnlicher Temperatur. *Helv. Chim. Acta* **1930**, *13* (6), 1228−1236.

(26) Lazouski, N.; Schiffer, Z. J.; Williams, K.; Manthiram, K. Understanding continuous lithium-mediated electrochemical nitrogen reduction. *Joule* **2019**, *3* (4), 1127−1139.

(27) Suryanto, B. H.; Matuszek, K.; Choi, J.; Hodgetts, R. Y.; Du, H.-L.; Bakker, J. M.; Kang, C. S.; Cherepanov, P. V.; Simonov, A. N.; MacFarlane, D. R. Nitrogen reduction to ammonia at high efficiency and rates based on a phosphonium proton shuttle. *Science* **2021**, *372* (6547), 1187−1191.

(28) Andersen, S. Z.; Statt, M. J.; Bukas, V. J.; Shapel, S. G.; Pedersen, J. B.; Krempl, K.; Saccoccio, M.; Chakraborty, D.; Kibsgaard, J.; Vesborg, P. C. Increasing stability, efficiency, and fundamental understanding of lithium-mediated electrochemical nitrogen reduction. *Energy Environ. Sci.* **2020**, *13*, 4291−4300.

(29) Schwalbe, J. A.; Statt, M. J.; Chosy, C.; Singh, A. R.; Rohr, B. A.; Nielander, A. C.; Andersen, S. Z.; McEnaney, J. M.; Baker, J. G.; Jaramillo, T. F. A Combined Theory-Experiment analysis of the Surface Species in Lithium Mediated NH3 Electrosynthesis. *ChemElectroChem* **2020**, *7*, 1542−1549.

(30) Sažinas, R.; Andersen, S. Z.; Li, K.; Saccoccio, M.; Krempl, K.; Pedersen, J. B.; Kibsgaard, J.; Vesborg, P. C. K.; Chakraborty, D.; Chorkendorff, I. Towards understanding of electrolyte degradation in lithium-mediated non-aqueous electrochemical ammonia synthesis with gas chromatography-mass spectrometry. *RSC Adv.* **2021**, *11* (50), 31487−31498.

(31) Soloveichik, G. *ARPA-E REFUEL Program: Distributed Production of Ammonia and its Conversion to Energy*, 2019 AIChE Annual Meeting, AIChE: 2019.

(32) Plowman, B. J.; Jones, L. A.; Bhargava, S. K. Building with bubbles: the formation of high surface area honeycomb-like films via hydrogen bubble templated electrodeposition. *Chem. Commun.* **2015**, *51* (21), 4331−4346.

(33) Najdovski, I.; O'Mullane, A. P. The effect of electrode material on the electrochemical formation of porous copper surfaces using hydrogen bubble templating. *J. Electroanal. Chem.* **2014**, *722*, 95−101.

(34) Zhang, H.; Ye, Y.; Shen, R.; Ru, C.; Hu, Y. Effect of bubble behavior on the morphology of foamed porous copper prepared via electrodeposition. *J. Electrochem. Soc.* **2013**, *160* (10), D441.

(35) Li, Y.; Jia, W.-Z.; Song, Y.-Y.; Xia, X.-H. Superhydrophobicity of 3D Porous Copper Films Prepared Using the Hydrogen Bubble Dynamic Template. *Chem. Mater.* **2007**, *19* (23), 5758−5764.

(36) Liu, J.; Cao, L.; Huang, W.; Li, Z. Direct electrodeposition of PtPd alloy foams comprised of nanodendrites with high electrocatalytic activity for the oxidation of methanol and ethanol. *J. Electroanal. Chem.* **2012**, *686*, 38−45.

(37) Oppedisano, D. K.; Jones, L. A.; Junk, T.; Bhargava, S. K. Ruthenium electrodeposition from aqueous solution at high cathodic overpotential. *J. Electrochem. Soc.* **2014**, *161* (10), D489.

(38) Jović, V. D.; Maksimović, V.; Pavlović, M. G.; Popov, K. I. Morphology, internal structure and growth mechanism of electrodeposited Ni and Co powders. *J. Solid State Electrochem.* **2006**, *10* (6), 373−379.

(39) Boo, H.; Park, S.; Ku, B.; Kim, Y.; Park, J. H.; Kim, H. C.; Chung, T. D. Ionic strength-controlled virtual area of mesoporous platinum electrode. *J. Am. Chem. Soc.* **2004**, *126* (14), 4524−4525.

(40) Lee, G.; Kim, K.; Chung, J.; Han, J.-I. Electrochemical ammonia accumulation and recovery from ammonia-rich livestock wastewater. *Chemosphere* **2021**, *270*, 128631.

(41) Suo, L.; Borodin, O.; Gao, T.; Olguin, M.; Ho, J.; Fan, X.; Luo, C.; Wang, C.; Xu, K. Water-in-salt" electrolyte enables high-voltage aqueous lithium-ion chemistries. *Science* **2015**, *350* (6263), 938−943.

Supplementary Information for

Increasing current density of Li-mediated ammonia synthesis with high surface area copper electrodes

Katja Li [a†], *Sarah G. Shapel* [a], *Degenhart Hochfilzer* [a], *Jakob B. Pedersen* [a], *Kevin Krempl* [a], *Suzanne Z. Andersen* [a], *Rokas Sažinas* [a], *Mattia Saccoccio* [a], *Shaofeng Li* [a], *Debasish Chakraborty* [a], *Jakob Kibsgaard* [a], *Peter C. K. Vesborg* [a], *Jens K. Nørskov* [a]*, *and Ib Chorkendorff* [a]*

[a] Department of Physics, Technical University Denmark, 2800 Kongens Lyngby, Denmark

* Corresponding author email: ibchork@fysik.dtu.dk

Experimental Methods

Synthesis of Cu hydrogen bubble templated Ni foam

The Ni foam (99.5 %, porosity: 95 %, pores/ cm: 20, Goodfellow) or Ni foil (99.99+ %, Goodfellow) was cut into 0.5 cm^2 pieces, cleaned in H_3PO_4 (85 %, Supelco) and sonicated three times in ethanol (EtOH). Afterwards, they were attached to a Cu wire (99.98+ %, Goodfellow) and used as the working electrode. Two Pt meshes (A_{geo}= ~2 cm^2, 99.9 %, Goodfellow), were electrically connected and used as a split counter electrode, where the Ni foam working electrode was positioned in the middle during deposition. As electrolyte a 0.4 M $CuSO_4$ (Merck) in 1.5 M H_2SO_4 (99.999%, Sigma Aldrich) solution was used. In this two-electrode setup a constant current of -5 A was applied for 15 s to create the porous Cu deposit on the Ni foam. After the deposition process the electrodes were cleaned in EtOH and dried in vacuum before being stored in an Ar glovebox to prevent oxidation of Cu.

Characterization by SEM-EDX and XPS

The deposited samples were characterized with several different techniques. Scanning Electron Microscopy (SEM) images were taken with a Quanta FEG 250 SEM from FEI, equipped with an Oxford Instruments 80 mm^2 X-Max silicon drift EDX detector for elemental mapping. The morphology of the samples shown in Figure 3 was recorded with an ETD detector for secondary electrons at 20 kV. The cross section of HBTCu and Ni foam were measured by cutting the electrode in half and putting them vertically on the sample holder. X-ray Photoelectron Spectroscopy was done using a ThermoScientific Thetaprobe instrument equipped with an Al Kα

X-ray source and having a chamber base pressure below $9 \cdot 10^{-10}$ mbar. Survey spectra were recorded with 20 scans at 50 ms dwell time per 1 eV step. Elemental detail spectra were recorded with 20 scans in 0.1 eV steps with 50 ms dwell time. The lateral resolution was 400 µm and a pass energy of 200 eV was used. The data was acquired and analyzed using Thermo Advantage v5.9917 by Thermo Fischer Scientific. All data was fitted with the Powell fitting algorithm and the background determined by the Smart background option, which is based on the Shirley background.

Surface area measurement by capacitive cycling

To get the specific capacitance of Cu in 2 M $LiClO_4$ (Battery grade, dry, 99.99 %, Sigma Aldrich) in tetrahydrofuran (THF, anhydrous, >99.9 %, inhibitor-free, Sigma Aldrich) a Cu stub ($0.2 cm^2$) was first mechanically polished with diamond paste (DP-Pase M, 3 µm) on a micro-fibre cloth and subsequently electropolished in 66 % H_3PO_4 at 2 V vs Cu for 2 min. Then cyclic voltammetry was performed in an Ar glovebox in a glass cell with Pt mesh as a counter electrode and Pt wire as a pseudo reference electrode in 2 M $LiClO_4$ in THF. The setup was first purged with Ar (5.0, Air Liquide) for at least 20 min to remove any trace O_2 and N_2 and then an equilibration time of at least 20 min at open circuit voltage was set. After a stable OCV was obtained CVs were performed at 0 to -200 mV vs OCV at scan rates between 10 – 60 mV/s. To measure the electrochemical active surface area of the deposited HBTCu samples the same experimental procedure was followed, substituting the Cu stub with a HBTCu sample. The calculation of the ECSA is shown below in supplementary text and calculations.

Electrochemical ammonia synthesis

Measurements were done in a 3-electrode single compartment glass cell enclosed in an electrochemical autoclave, placed in a fumehood. Electrolyte solution consisted of 2 M $LiClO_4$ in 99 vol. % THF and 1 vol. % EtOH (anhydrous, Honeywell) and was prepared in an Ar glovebox. The working electrode (WE) is a Cu foil (+99.9 %, 0.1 mm thick, Goodfellow), Ni foil or the synthesized HBTCu (on Ni foam and Ni foil) both attached to a Cu wire for electrical contact. The counter electrode (CE) consists of a Pt mesh (99.9 %, Goodfellow), and the reference electrode (RE) is a Pt wire (99.99 %, Goodfellow). The CE and RE are both boiled in ultra-pure water, and dried overnight at 100 °C, then flame-annealed. When Cu foil (99.999 %, Puratonic) was used as the working electrode it was electro-polished beforehand in 66 % H_3PO_4 (85 %, Supelco) for 3 min at 2 V vs. Cu. The single compartment glass cell and a magnetic stirring bar (VWR, glass covered) is boiled in ultra-pure water, and dried overnight at 100 °C in air. The WE and CE are ~0.5 cm apart, and the surface area of the WE facing the CE is 0.5 cm_{geo}^2. Prior to an electrochemical experiment, we introduce Ar gas (5.0, Air Liquide) into the empty assembled cell placed in the autoclave for at least 30 min. The denser Ar gas substantially displaces the atmospheric laboratory air, mainly consisting of N_2 and O_2, in the system, as measured via mass spectrometry. Next, we inject electrolyte solution into the cell in Ar atmosphere, and the autoclave is closed. The N_2 (6.0, Air Liquide) used in the experiments is cleaned by purifiers (NuPure, pptV cleaning of all labile N containing compounds) and the pressure is increased to 10 bar and de-pressurized to 3 bar a total of 10 times, in order to flush out any remaining atmospheric contaminants, then filled to 20 bar for experiments. The system is left to rest for 20 min to equilibrate the atmosphere composition with the electrolyte. During the whole experiment, the electrolyte is stirred at 250 rpm. Subsequently, the electrochemical experiments, including potentiostatic electrochemical impedance spectroscopy (PEIS) to determine the resistance in our cell, a linear sweep voltammetry (LSV) from open circuit voltage (OCV) until lithium reduction is clearly seen, then chronopotentiometry (CP), followed by another impedance measurement to ensure that the resistance has not changed, are started. We determine the lithium reduction potential scale based on the LSV. The onset for lithium reduction is quite clear, and we can thereby denote the potential vs. Li/Li^+. The onset potential for the representative LSVs in Fig 3b and Fig 10b are -3.16 V, -3.59 V, -3.47 V, -3.3 V, -3,25 V vs Pt. Pseudo for HBTCu, Cu foil, Mo foil, HBT on Ni foil and Ni foil, respectively. During CP, either a steady current density of -2 mA/cm_{geo}^2 is used for the Cu foil experiments, or -100 mA/cm_{geo}^2 for the HBTCu experiments. We note that all experiments were conducted at room temperature.

Quantification of ammonia

Synthesized ammonia was quantified by a modified colorimetric indophenol method, previously described[1]. The sample absorbance was analyzed by UV/Vis spectroscopy (UV-2600, Shimadzu) in the range from 400 nm to 1000 nm. The blank background solution is subtracted from each spectrum, and the difference between the peak around 630 nm and the trough at around 850 nm is used. A fitted curve of the difference between the peak and trough of each concentration showed a linear regression with an R^2 value of 0.998. We utilize this method, as opposed to the more common peak based method, because long experiments might have solvent breakdown, which can give a falsely high peak at the ammonia wavelength, due to interference from the evolved solvent background. For each measurement, four 0.5 ml samples were taken from the electrolyte. One sample from the electrolyte is used as a background, and the mean and standard deviation of the remaining 3 samples is reported in Table S1. The remaining samples were treated as described previously[1], to determine the ammonia concentration. If the expected concentration of ammonia exceeds the concentration limits of the indophenol method, the sample is accordingly diluted with

Paper 3

Towards understanding of electrolyte degradation in lithium-mediated non-aqueous electrochemical ammonia synthesis with gas chromatography-mass spectrometry
R. Sažinas, S. Z. Andersen, K. Li, M. Saccoccio, K. Krempl, J. B. Pedersen, J. Kibsgaard, P. C. K. Vesborg, D. Chakraborty and I. Chorkendorff
RSC Advances, **2021**, 11, 31487-31498.

RSC Advances

ROYAL SOCIETY OF CHEMISTRY

PAPER

View Article Online
View Journal | View Issue

Check for updates

Cite this: *RSC Adv.*, 2021, **11**, 31487

Towards understanding of electrolyte degradation in lithium-mediated non-aqueous electrochemical ammonia synthesis with gas chromatography-mass spectrometry†

Rokas Sažinas, Suzanne Zamany Andersen, Katja Li, Mattia Saccoccio, Kevin Krempl, Jakob Bruun Pedersen, Jakob Kibsgaard, Peter Christian Kjærgaard Vesborg, Debasish Chakraborty and Ib Chorkendorff*

Received 6th August 2021
Accepted 8th September 2021

DOI: 10.1039/d1ra05963g

rsc.li/rsc-advances

Lithium-mediated electrochemical ammonia synthesis (LiMEAS) in non-aqueous media is a promising technique for efficient and green ammonia synthesis. Compared to the widely used Haber–Bosch process, the method reduces CO_2 emissions to zero due to the application of green hydrogen. However, the non-aqueous medium encounters the alkali metal lithium and organic components at high negative potentials of electrolysis, which leads to formation of byproducts. To assess the environmental risk of this synthesis method, standardized analytical methods towards understanding of the degradation level and consequences are needed. Here we report on the implementation of an approach to analyze the liquid electrolytes after electrochemical ammonia synthesis *via* high-resolution gas chromatography-mass spectrometry (GCMS). To characterize the molecular species formed after electrolysis, electron ionization high-resolution mass spectrometry (EI-MS) was applied. The fragmentation patterns enabled the elucidation of the mechanisms of byproduct formation. Several organic electrolytes were analyzed and compared both qualitatively and quantitatively to ascertain molecular composition and degradation products. It was found that the organic solvent in contact with metallic electrodeposited lithium induces solvent degradation, and the extent of this decomposition to different organic molecules depends on the organic solvent used. Our results show GCMS as a suitable technique for monitoring non-aqueous electrochemical ammonia synthesis in different organic electrolytes.

Introduction

Lithium-mediated electrochemical ammonia synthesis (LiMEAS) is a promising alternative to the traditional complex thermochemical Haber–Bosch process,[1–5] which predominantly requires high temperatures (400–500 °C) and pressures (150–200 bar) coupled with a steam reforming plant for hydrogen (H_2) production.[6] On the other hand, the LiMEAS is thermodynamically driven by an electrical potential instead of high temperatures and pressures, and the chemical reactivity of lithium towards nitrogen gas (N_2).[7] By utilization of green electricity from *e.g.* wind or solar energy sources, the process can be considered a renewable alternative. This enables softer operation conditions in a modular fashion, similar to a flow reactor,[8] and leads to lower capital costs for the process without greenhouse gas emissions compared to the 1.4% of global CO_2 emissions for ammonia (NH_3) production by the Haber–Bosch process. The LiMEAS could be operated on a local level *e.g.* individual farms or greenhouses, thereby further eliminating the need for transportation and storage. This alternative decentralized NH_3 production method turns against the centralized nature of Haber–Bosch making ammonia accessible at a local scale and employing renewable energy sources *e.g.* wind or solar. The production of H_2 (for example, water splitting) may overcome some of the issues associated with the traditional Haber–Bosch process, such as the large amount of CO_2 from steam reforming[9] emissions and high cost.[2]

A typical LiMEAS cell consists of a noble metal anode *e.g.* platinum (Pt) and transition metal cathode which does not interact or alloy with lithium (Li) *e.g.* molybdenum (Mo).[10,11] The electrodes are usually submerged in the non-aqueous organic electrolyte with or without a membrane or separator. The electrolyte is composed of a conducting Li salt and a solvent, typically lithium perchlorate ($LiClO_4$)[12] and tetrahydrofuran (THF), respectively.[10,13] Other mostly ether-based solvents, such as dimethoxyethane (DME) or diethyleneglycol dimethyl ether or diglyme (DG) can also be used for LiMEAS. Thus, the influence

---

Department of Physics, Technical University of Denmark, Kongens Lyngby, 2800, Denmark. E-mail: ibchork@fysik.dtu.dk

† Electronic supplementary information (ESI) available. See DOI: 10.1039/d1ra05963g

Paper 4

Oxygen-Enhanced Chemical Stability of Lithium-Mediated Electrochemical Ammonia Synthesis

R. Sažinas, K. Li, S. Z. Andersen, M. Saccoccio, S. Li, J. B. Pedersen, J. Kibsgaard, P. C. K. Vesborg, D. Chakraborty and I. Chorkendorff

The Journal of Physical Chemistry Letters, **2022**, 13, 4605-4611.

THE JOURNAL OF
PHYSICAL CHEMISTRY
LETTERS
A JOURNAL OF THE AMERICAN CHEMICAL SOCIETY

pubs.acs.org/JPCL

Letter

Oxygen-Enhanced Chemical Stability of Lithium-Mediated Electrochemical Ammonia Synthesis

Rokas Sažinas, Katja Li, Suzanne Z. Andersen, Mattia Saccoccio, Shaofeng Li, Jakob B. Pedersen, Jakob Kibsgaard, Peter C. K. Vesborg, Debasish Chakraborty, and Ib Chorkendorff*

Cite This: *J. Phys. Chem. Lett.* 2022, 13, 4605−4611

Read Online

ACCESS | Metrics & More | Article Recommendations | Supporting Information

ABSTRACT: Although oxygen added to nonaqueous lithium-mediated electrochemical ammonia synthesis (LiMEAS) enhances Faradaic efficiency, its effect on chemical stability and byproducts requires understanding. Therefore, standardized high-resolution gas chromatography−mass spectrometry and nuclear magnetic resonance were employed. Different volatile degradation products have been qualitatively analyzed and quantified in tetrahydrofuran electrolyte by adding some oxygen to LiMEAS. Electrodeposited lithium and reduction/oxidation of the solvent on the electrodes produced organic byproducts to different extents, depending on the oxygen concentration, and resulted in less decomposition products after LiMEAS with oxygen. The main organic component in solid-electrolyte interphase was polytetrahydrofuran, which disappeared by adding an excess of oxygen (3 mol %) to LiMEAS. The total number of byproducts detected was 14, 9, and 8 with oxygen concentrations of 0, 0.8, and 3 mol %, respectively. The Faradaic efficiency and chemical stability of the LiMEAS have been greatly improved with addition of optimal 0.8 mol % oxygen at 20 bar total pressure.

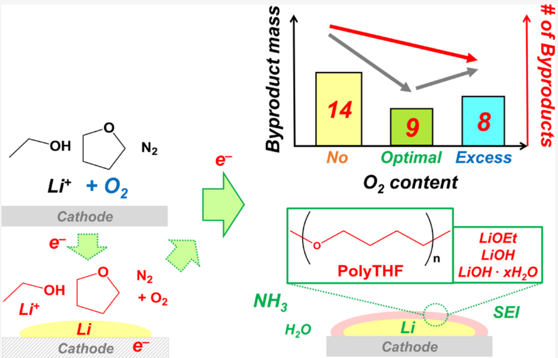

Thermodynamically driven by an electric potential at ambient temperature and pressure, lithium-mediated electrochemical ammonia synthesis (LiMEAS) can potentially compete with the traditional thermochemical Haber−Bosch process[1−3] with its high temperatures (400 °C) and pressures (150−200 bar). This method of ammonia (NH_3) production is responsible for the emission of a large amount of CO_2 (around 1%) associated with steam reforming emissions and is characterized by high capital costs related to the high-pressure and high-temperature requirements of the Haber−Bosch process.[3] On the other hand, the nitrogen reduction reaction (N2RR) between lithium (Li) and nitrogen (N_2) is driven by the affinity and chemical reactivity of Li toward N_2 through the formation of lithium nitride, Li_3N, or other N-containing Li materials at ambient temperature and pressure.[4] LiMEAS can be even fully powered by renewable energies; it thus offers CO_2-free operation, and because of its milder process conditions, it can be decentralized in smaller and less capital-intensive plants.

Even though it seems simple and is effective, LiMEAS is a chemically complicated process performed in an electrochemical cell by application of the potentials close to Li deposition. The LiMEAS mechanism is not fully understood to date, although the literature has some speculative models.[5] For an assembly of a typical LiMEAS cell, a noble metal anode, e.g., platinum (Pt), and a transition metal cathode which does not interact and alloy with Li, e.g., molybdenum (Mo) or copper (Cu), are employed.[6−8] The desired product, i.e., NH_3, is synthesized when the electrodes are submerged in the nonaqueous organic electrolyte, which consists of a conducting salt, e.g., lithium perchlorate ($LiClO_4$);[9] an organic solvent, e.g., tetrahydrofuran (THF);[6,10] and a potential proton source, such as alcohol or hydrogen (H_2).[5−7] The charge is usually passed at high overall cell potentials (>5 V). Our recent study described the stability of LiMEAS with the emphasis on the evolution of the electrolyte degradation products and showed that prolonged constant current reaction may lead to significant changes in the electrolyte composition and SEI, presumably deteriorating the efficiency of the whole LiMEAS.[11] The decomposition reactions which have been identified are hydrolysis, ring-opening, and oxidation products of the electrolyte.[11] There are many reports regarding the aging behavior of lithium ion batteries (LIB) cells with various approaches, including gas chromatography−mass spectrometry (GCMS).[12−14] Our recent work on stability of LiMEAS monitored using GC with high-resolution MS for chemical and

Received: March 15, 2022
Accepted: May 5, 2022
Published: May 19, 2022

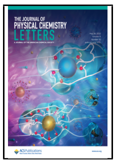

https://doi.org/10.1021/acs.jpclett.2c00768
J. Phys. Chem. Lett. 2022, 13, 4605−4611

structural elucidation is a pioneering approach toward stability of LiMEAS in different organic electrolytes.[11,14]

Taking into consideration that Li metal is very reactive chemically, one would assume that its instability and reactivity with traces of moisture (H_2O); O_2; and organic solvent components, such as ethanol (EtOH) and THF, should deteriorate LiMEAS.[15] However, this is not the case; it has been reported recently by our group that small amounts of O_2 boost the LiMEAS.[16] It is very important to mention that the electrochemical reduction of the electrolyte on the negative electrode of LIB results in the formation of the solid electrolyte interphase (SEI),[12] which must be considered in LiMEAS as well. Both inorganic and organic components of this SEI are required for long-term performance if it is permeable for Li ions, thus protecting the highly reactive cathode against unwanted reductive side reactions.[17−19] The SEI layer on the working electrode (WE) in LiMEAS would be different from LIBs affecting the nature and amount of byproducts, which dissolve in the electrolyte and stay as part of the SEI.[20−23] The nature of the SEI is distinct to prevent further electrolyte decomposition, improving the synthesis process, and would depend on the conditions and various aspects and parameters of LiMEAS.

In the current study we demonstrate that small amounts of oxygen (O_2) present together with N_2 gas enhance not only the FE but also the stability of the electrolyte in LiMEAS. For analyzing and identifying mainly organic degradation products or byproducts in both the electrolyte and SEI, high-resolution GCMS and nuclear magnetic resonance (NMR) were employed. We compared the outcome and stability of LiMEAS with different O_2 concentrations in nonaqueous LiMEAS both qualitatively and quantitatively. It has been shown that 0.8 mol % of O_2 is an optimal amount for promotion of LiMEAS toward NH_3 with improved stability of the nonaqueous organic electrolyte based on THF.[8,16]

Typical electrochemical results obtained for LiMEAS in an autoclave (see Figure S1) at elevated total pressure (20 bar) and ambient temperature with Mo WE of 1.8 cm^2 area are shown in Figure 1. A total amount of 50 C charge was passed in 116 min with current density of -4 mA cm^{-2}. The regular LiMEAS in THF without O_2 (Figure 1a) shows an unstable voltage profile where the WE potential drops significantly after 10 min. In contrast, the electrolyte with optimal O_2 content of 0.8 mol % demonstrates a more stable WE potential (Figure 1b). In addition, the most stable WE potential is seen with excess (3.0 mol %) of O_2 (Figure 1c). The more oxygen in the system, the greater the electrochemical stability. This can be attributed to the complete reaction of Li with O_2 forming oxide materials and suppressed accessibility for N_2 to reach the metallic Li for N2RR as the Faradaic efficiency (FE) of LiMEAS drops as well. Moreover, the WE potential with excess O_2 is the most stable. This could be attributed to the most stable SEI and permeability of Li ions in the SEI. The presence of O_2 minimizes the decomposition products as supported by the GCMS/NMR data. Consequently, most of the further reduction occurs either as hydrogen evolution reaction (HER) or electrolyte decomposition. Thus, the LiMEAS run with 0.8 mol % O_2 in the gas feed shows intermediate WE stability that is markedly better than that observed in the absence of O_2. The electrochemical behavior observed for the experiments of this work is in line with results we reported previously.[8,10,16,24] One difference can be seen in the linear sweep voltammmetry (LSV), shown in Figure S2, where a clear feature at -1.5 V vs Pt pseudoreference (Pt_{pseudo}) can be seen with the presence of O_2, which represents oxygen reduction reaction according to the literature.[19] For all of the cases in Figure 1, the counter electrode (CE) potential is around 2 V vs Pt_{pseudo}. The noises and some instability of CE were most likely due to mechanical contact issues. We assume that the main reason for such a high CE potential is electrolyte (THF and EtOH) oxidation and formation of the products reported elsewhere.[11]

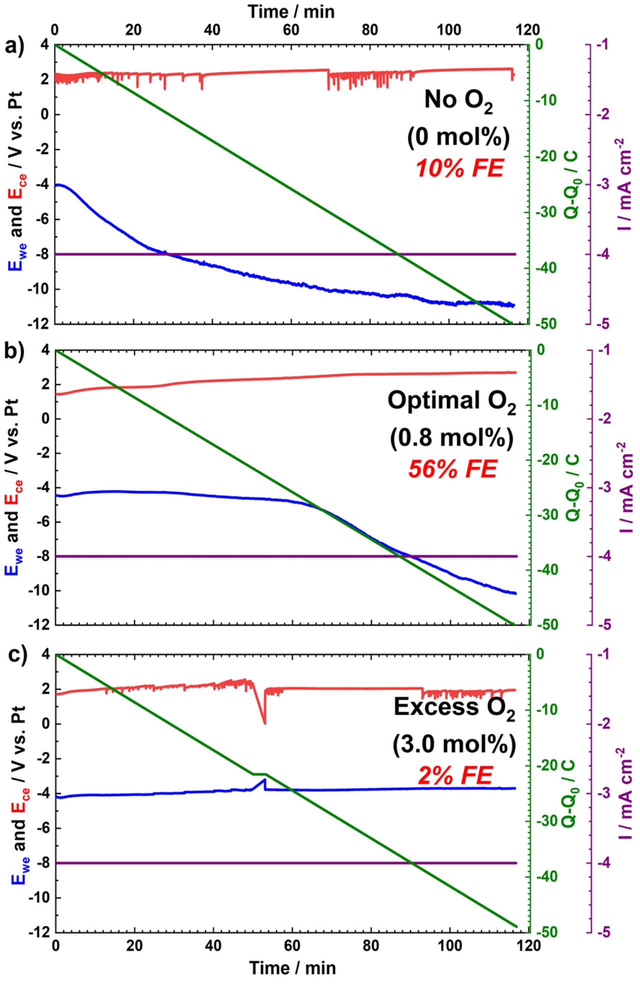

Figure 1. Chronopotentiometry (CP) results of LiMEAS with the presence of (a) 0, (b) optimal 0.8, and (c) excess 3 mol % of O_2 added. All the experiments were performed at 20 bar (N_2 ± O_2) and at -4 mA cm^{-2} with 50 C of charge passed.

The FE of LiMEAS in THF electrolytes was evaluated using an indophenol method described in more detail in the Supporting Information.[25,26] The LiMEAS resulted in FE of 10%, 56%, and 2% (all <1% error within 3 different measurements) with 0, 0.8, and 3.0 mol % of O_2, respectively. The advantages of adding a small amount of O_2 to the system over typical non-O_2 reaction can be clearly seen. Therefore, the optimal amount of O_2 enhances the FE and electrochemical stability of the system (Figure 1).

Several images of the WE in the Ar-filled glovebox after LiMEAS for 2 h in THF are shown in Figure S3. Even though the experimental conditions were the same, the images are difficult to analyze. The WE with 0 and excess of 3 mol % O_2 show only a thin deposit on the front side that is facing the CE. A slightly thicker deposit is observed for the optimum O_2 content of 0.8 mol %, both on the front and back sides of the electrode. It should be noted that the formation of the dendrites was not observed on the surface of the electrodes, and the yellow color is due to image quality, not a yellow deposit. A slightly more homogeneous surface was obtained for the case of LiMEAS with optimal 0.8 mol % O_2 concentration, especially in the peripheral shinny metallic part of the electrode. The effect of O_2 on the FE and the WE potential was investigated in detail in the literature.[16]

Herein, we investigate the effect of O_2 on the stability of the electrolyte with GCMS and NMR. For the GCMS analysis, all the samples were analyzed for 20 min each with repeated injections, and the temperature program used is shown in the Supporting Information (Figure S4). Overall GCMS results are shown in Figure 2 and Figures S5 and S6 in the Supporting Information as 3D chromatograms after 2 h of constant current LiMEAS in THF-based electrolytes with different O_2 concentrations. The freshly obtained electrolytes were transferred to the GCMS after LiMEAS followed by immediate analysis of the electrolytes to limit reaction of the electrolyte with air and moisture. The experimental details regarding the GCMS experiments and analysis of the samples are described in brief in the Supporting Information and were reported by us in detail in ref 11. Longer GCMS recording time did not reveal any eluents from the samples, and all the byproducts of LiMEAS eluted in less than 15 min. It can be seen that the increase of the O_2 content in the system reduces the number and the amount of the byproducts formed during LiMEAS. The thorough analysis of the organic volatile species in the electrolytes after LiMEAS resulted in 10, 5, and 5 compounds detected by GCMS for the 0, 0.8, and 3 mol % O_2, respectively. The results are shown in Tables S1−S3 of the Supporting Information. As shown in Figure 2 and summarized in Figure 3, the total number of organic volatile species detectable with GCMS decreases with increasing O_2 content; the sum of the total amounts (organic and nonorganic), however, increases because of the permanent increase of H_2O, which is caused by the oxygen reduction reaction (ORR). On the other hand, the addition of excess O_2 does not have an effect on the structure of the byproducts introducing some novel or different compounds, only the number and the amount of them. The chromatograms become cleaner from organic species with increasing O_2 (Tables S1−S3). The quantity and mass of the decomposition products and their concentration measured in the electrolytes decrease when the optimal 0.8 mol % O_2 is added. On the other hand, the excess of O_2 induces much less decomposition products than that without O_2. This suggests that denser or thicker surface films are formed on the basis of inorganic Li compounds on the surface of the electrodes because of reaction between Li and O_2. Consequently, these inorganic Li materials are not involved in further decomposition reactions of the electrolyte.

The decomposition extent of the THF-based electrolyte after LiMEAS with addition of O_2 to the system is exhibited in Figure 3. The LiMEAS without O_2 leads to all the compounds shown by green arrows (10). However, the addition of O_2 to LiMEAS reduces the number of the byproducts formed during the electrolysis represented by blue arrows (5), and the mass of organic decomposition products decreases as shown in Figure 3a,b. The detected compounds were characterized and their amounts were evaluated as summarized in Tables S1−S3. It can be seen that O_2 added to the LiMEAS electrochemical system significantly improves FE for ammonia and stability of the system. We hypothesize that this is due to the changes in the formation and stabilization of the SEI layer which inhibit further decomposition of the electrolyte compared to LiMEAS with only N_2 present, which gives relatively better stability of the electrolyte and better protection of the electrode. The second argument is that some O_2 present suppresses the HER reaction from EtOH by employing it in oxidation reactions toward acetaldehyde and acetic acid on the transition metal−transition metal oxide surface, as has been reported previously in the literature.[27,28] We have observed that EtOH at less than 1 vol %, as used in this study, increases FE but decreases stability of the system; that is, more dendrites are formed and more flakes are seen in the electrolyte (not reported in this study). The LiMEAS demonstrates enhanced performance and stability with the addition of the optimal amount of O_2.

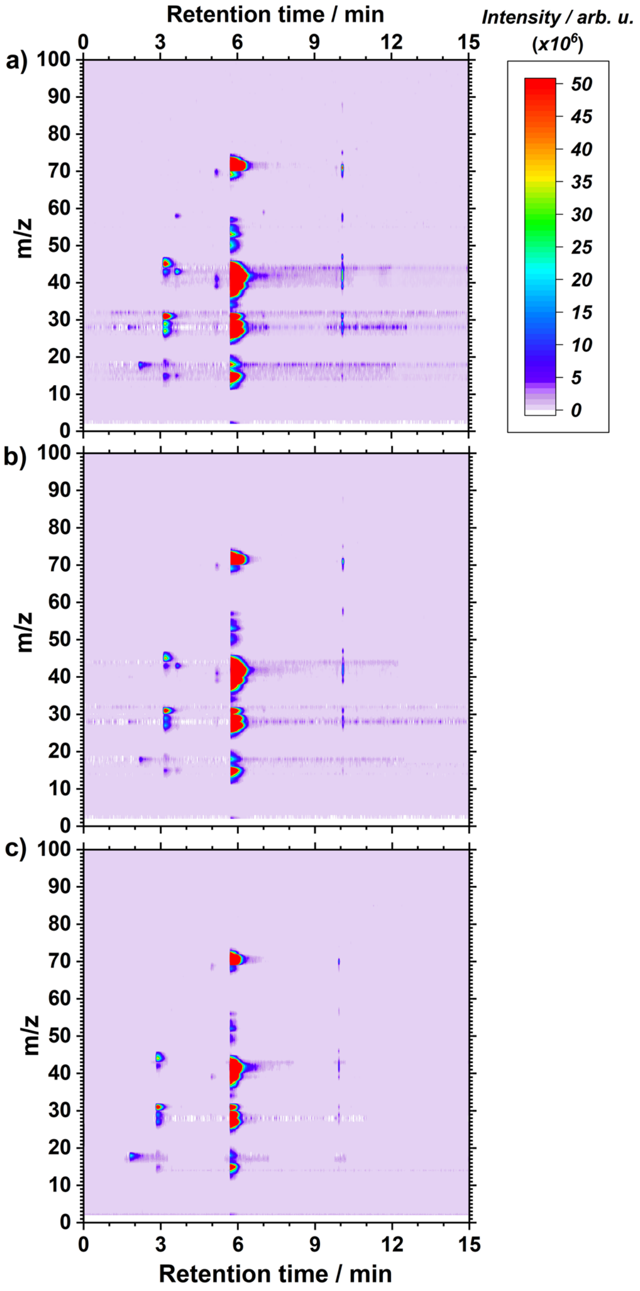

Figure 2. GCMS contour chromatograms visualizing electrolyte composition after LiMEAS with the presence of (a) 0, (b) 0.8, and (c) 3.0 mol % of O_2 added to the system.

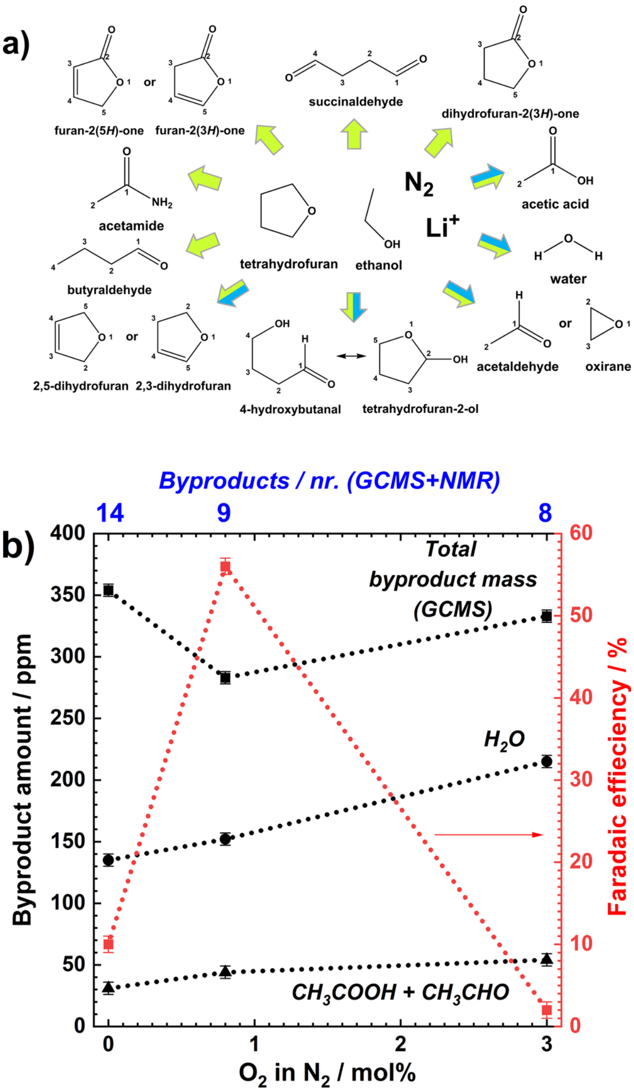

Figure 3. GCMS results. (a) The spectrum of volatile byproducts detected by GCMS in THF-based electrolyte after LiMEAS without (green) and with (blue) addition of O_2; (b) total number (blue scale), concentration of byproducts, H_2O, acetic acid/acetaldehyde (CH_3COOH/CH_3CHO) (black), and Faradaic efficiency (red) vs O_2 content. The error bars represent three separate measurements of the same experiment.

As can be seen in Figure 3b, the total amount of the organic decomposition products detected by GCMS shown in Figure 3a is decreases from 0 to 0.8 mol % and increases from 0.8 to 3 mol % of O_2, respectively. In total, the amount of H_2O and EtOH oxidation products, i.e., acetic acid and acetaldehyde, increases with addition of O_2.

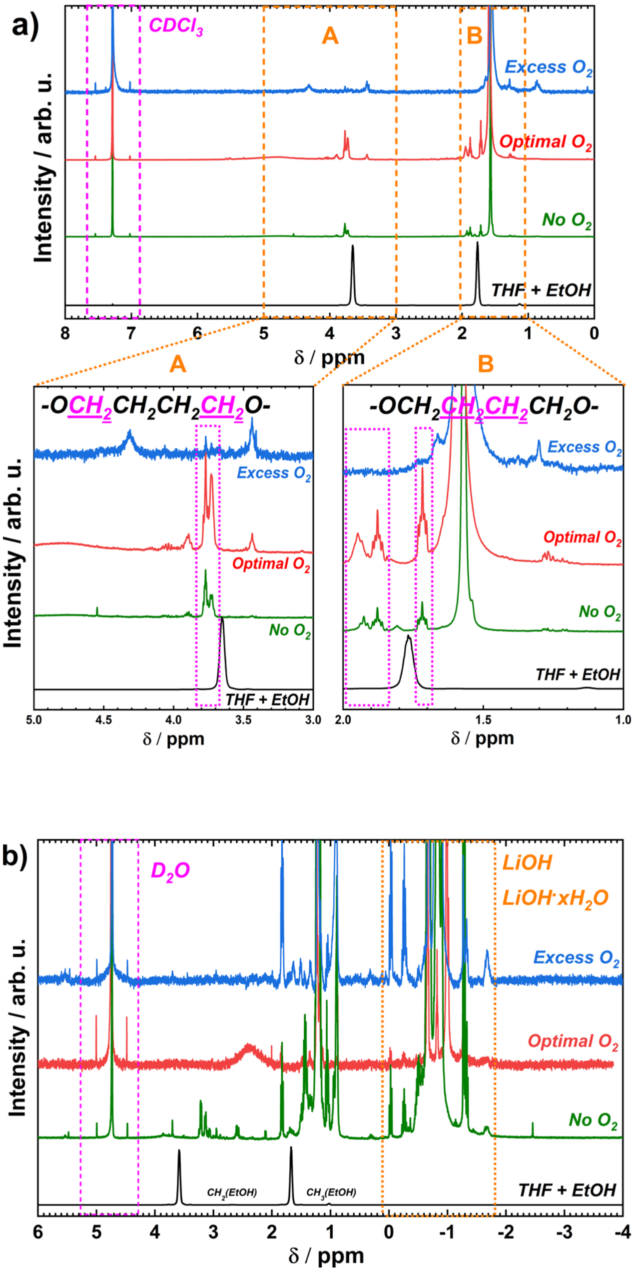

Figure 4. ^1H NMR results of the surface species on the working electrode (WE) washed with $CDCl_3$ after LiMEAS with different O_2 content in the feed gas. A and B show magnified parts of the spectra for specific aliphatic protons of the polyTHF. (b) The ^1H NMR results of the surface species on the WE washed with D_2O after LiMEAS with different O_2 content in the feed gas. A and B represent selected regions in the spectrum.

Our NMR study after LiMEAS involves two main types of samples: (i) solid residual on the WE and (ii) solid residual from dried electrolyte. For the former, the WE was dried in the glovebox atmosphere overnight and then washed with two different deuterated solvents, i.e., $CDCl_3$ and D_2O; for the latter, the used electrolyte was first dried at 60 °C to evaporate THF and EtOH, then the solid residual was dissolved in deuterated solvent. Figure 4a presents NMR spectra of the dry residue on the working electrode after LiMEAS washed with $CDCl_3$. As expected, no obvious signal of THF and EtOH is visible as they were removed by drying the sample prior to NMR analysis. This seems to be sufficient for removing most of the volatile solvent because there are no obvious signals of the electrolyte components. On the other hand, the main organic component of the solid film on the surface of the WE is the THF polymerization product, polytetrahydrofuran (polyTHF), according to the chemical shifts and multiplicity of the peaks.[29,30] This polymer is the main organic and polymeric constituent of the SEI in LiMEAS together with inorganic species reported previously,[8,10,24] which is formed on the surface of the WE and responsible for mass transport in and out of the electrode surface. The characteristic signals at

3.7−3.8 ppm belong to the protons of the methylene groups attached to the carbon close to the heteroatom, i.e., oxygen in $-O\underline{CH_2}CH_2CH_2\underline{CH_2}O-$ chains.[30] The chemical shifts at 1.8−2.0 and 1.7 ppm belong to different protons attached to the carbons between other carbon atoms ($-OCH_2\underline{CH_2}\underline{CH_2}CH_2O-$) of polyTHF. The higher the chemical shift, the closer the proton is attached to the heteronucleus, i.e., oxygen in the chain. The latter polymer has been reported and characterized in the literature as a substance produced in acid-treated polymerization of THF;[31] however, it has not been reported in any electrochemical systems or as an SEI component to date. PolyTHF forms on the surface of WE with or without O_2 added to the system. However, with excess O_2 (3 mol %), the surface of the electrode is most likely completely dominated by hydrated lithium oxide materials ($Li_xO_yH_z$) because of increased reaction of electroplated Li and O_2, as can be seen in Figure S7 of the Supporting Information. For other types of protons in the materials, no aromatic or unsaturated protons have been detected in the samples, as there are no peaks at 6−8 ppm and higher chemical shifts, indicating that polyTHF is the main organic matrix of the SEI. Only some additional peaks can be seen in Figure 4a, which are very difficult to attribute to some structure of the molecules, and we speculate that according to their chemical shifts, they belong to lithium ethoxide ($LiOCH_2CH_3$ or LiOEt). The ^1H NMR spectrum of the WE after LiMEAS with excess (3.0 mol %) O_2 is relatively clean with respect to protons detected in organic molecules including polyTHF, indicating less organic decomposition products. Overall, the NMR results lead to the conclusion that excess O_2 reacts with electroplated Li and stops its activity toward electrolyte decomposition on the WE but also shut down the ammonia synthesis.

The ^1H NMR investigation of the chemical species on the WE soluble in H_2O with different O_2 content in the feed gas is shown in Figure 4b. For this purpose, D_2O was used as a solvent, and the results were identical for all three O_2 concentrations. The main components of materials formed on the surface of the WE are lithium hydroxide, LiOH, and lithium hydroxide hydrates ($LiOH \cdot xH_2O$). No lithium hydride (LiH) was detected ((−5) to (−20) ppm), as this would react with any traces of H_2O to form LiOH. We have previously reported and described these materials as SEI components in LiMEAS using XRD and XPS,[10] and they have also been reported as components of SEI in LIBs.[32] Also, aliphatic protons belonging to most likely deuterated ethanol (DOEt) can be seen.

The ^1H NMR spectra of the residue after LiMEAS dried at 60 °C from THF and EtOH and dissolved in $CDCl_3$ are shown in Figure S7. The main components are a mixture of materials recorded and already identified by GCMS and the polyTHF described above and in Figure 4. Moreover, the aliphatic region of the NMR spectra seems to be similar without and with optimal 0.8 mol % of O_2. On the other hand, the excess of O_2 reduces the amount of signals with distinct chemical shifts, indicating that less organic species are formed as byproducts of LiMEAS, confirming the results discussed above and previously.[11] The samples with no and optimal oxygen contain unsaturated carbons because of protons detected at 5−6.5 ppm (Figure S7). This supports the GCMS findings shown in Figure 3 when it comes to byproducts of the oxidation of the solvent containing double or triple carbon bonds (Figure S7). No signals at 7−8 ppm could be detected except $CDCl_3$, which indicates no aromatic protons.

It is therefore important to mention that we cannot evaluate the whole extent of decomposition as the byproduct spectrum after LiMEAS because other inorganic substances, such as Li_2CO_3 and lithium chloride, LiCl, are not detectable by GCMS and ^1H or ^{13}C NMR. The latter methods, as with many in the field, have to be supplemented by, e.g., XRD or XPS. Thus, the "real" amount of byproducts would be different than assumed here because of nonmeasurable inorganic species. We have seen and reported several inorganic phases before by XRD and XPS,[8,10,16,24] and they are reproducible.

In summary, the stabilizing effect of oxygen in LiMEAS was demonstrated in THF-based electrolyte by GCMS and NMR analysis. It was shown that adding O_2 to the gas feed suppresses the electrolyte degradation and chemical side reactions, leading to a more efficient and stable LiMEAS process and enhancing the chemical stability of the system. A stable voltage profile for more than 2 h at a current density of -4 mA cm^{-2} and the least amount of the organic byproducts is achieved with excess O_2, however at the expense of reduced FE. The total number of byproducts detected by GCMS and NMR decreased with increasing O_2 and was 14, 9, and 8 with O_2 concentration of 0, 0.8, and 3 mol %, respectively. The 0.8 mol % oxygen is optimal for very efficient and stable LiMEAS. The high performance of LiMEAS with optimal amount of O_2 presented in this work was attributed to the formation of a stable and efficient SEI on the surface of the working electrode run in THF-based electrolyte and the subsequent suppression of hydrogen evolution reaction from the proton source, EtOH or THF, in LiMEAS. The use of O_2 in the THF-based electrolyte is very promising as it makes it possible to obtain more efficient and stable LiMEAS, while simultaneously reducing the costs associated with purifying air to N_2.

■ ASSOCIATED CONTENT

Supporting Information

The Supporting Information is available free of charge at https://pubs.acs.org/doi/10.1021/acs.jpclett.2c00768.

Experimental section; supplementary methods and calculations; Figures S1−S7 showing the setup and the electrodes after LiMEAS, LSV results, GCMS temperature program, and additional GCMS and NMR results; and Tables S1−S3 which summarize and quantify the byproducts with different O_2 content added to LiMEAS system (PDF)

Transparent Peer Review report available (PDF)

■ AUTHOR INFORMATION

Corresponding Author

Ib Chorkendorff − *Department of Physics, Technical University of Denmark, 2800 Kongens Lyngby, Denmark;* orcid.org/0000-0003-2738-0325; Email: ibchork@fysik.dtu.dk

Authors

Rokas Sažinas − *Department of Physics, Technical University of Denmark, 2800 Kongens Lyngby, Denmark;* orcid.org/0000-0002-4422-890X

Katja Li − *Department of Physics, Technical University of Denmark, 2800 Kongens Lyngby, Denmark*

Suzanne Z. Andersen − *Department of Physics, Technical University of Denmark, 2800 Kongens Lyngby, Denmark*
Mattia Saccoccio − *Department of Physics, Technical University of Denmark, 2800 Kongens Lyngby, Denmark*
Shaofeng Li − *Department of Physics, Technical University of Denmark, 2800 Kongens Lyngby, Denmark*
Jakob B. Pedersen − *Department of Physics, Technical University of Denmark, 2800 Kongens Lyngby, Denmark*
Jakob Kibsgaard − *Department of Physics, Technical University of Denmark, 2800 Kongens Lyngby, Denmark;* orcid.org/0000-0002-9219-816X
Peter C. K. Vesborg − *Department of Physics, Technical University of Denmark, 2800 Kongens Lyngby, Denmark;* orcid.org/0000-0002-3761-4212
Debasish Chakraborty − *Department of Physics, Technical University of Denmark, 2800 Kongens Lyngby, Denmark*

Complete contact information is available at:
https://pubs.acs.org/10.1021/acs.jpclett.2c00768

Notes

The authors declare no competing financial interest.

■ ACKNOWLEDGMENTS

We gratefully acknowledge the funding by Villum Fonden, part of the Villum Center for the Science of Sustainable Fuels and Chemicals (V-SUSTAIN grant 9455), Innovationsfonden (Eammonia grant 9067-00010B), and the European Research Council (ERC) under the European 430 Union's Horizon 2020 Research and Innovation Programme (grant agreement No 741860). We thank the floor managers and the whole SurfCat research group at DTU Physics for being together and helping with some equipment and experiments. The NMR measurements were performed at the NMR Center at DTU Chemistry. Therefore, we acknowledge Kasper Enemark-Rasmussen and Charlotte Held Gotfredsen for assistance with NMR.

■ REFERENCES

(1) Chen, J. G.; Crooks, R. M.; Seefeldt, L. C.; Bren, K. L.; Bullock, R. M.; Darensbourg, M. Y.; Holland, P. L.; Hoffman, B.; Janik, M. J.; Jones, A. K.; Kanatzidis, M. G.; King, P.; Lancaster, K. M.; Lymar, S. V.; Pfromm, P.; Schneider, W. F.; Schrock, R. R. Beyond fossil fuel-driven nitrogen transformations. *Science (New York, N.Y.)* **2018**, *360*, eaar6611.

(2) Li, C.; Wang, T.; Gong, J. Alternative Strategies Toward Sustainable Ammonia Synthesis. *Transactions of Tianjin University* **2020**, *26*, 67−91.

(3) Garagounis, I.; Vourros, A.; Stoukides, D.; Dasopoulos, D.; Stoukides, M. Electrochemical Synthesis of Ammonia: Recent Efforts and Future Outlook. *Membranes* **2019**, *9*, 112.

(4) McFarlane, E. F.; Tompkins, F. C. Nitridation of lithium. *Trans. Faraday Soc.* **1962**, *58*, 997−1007.

(5) Lazouski, N.; Schiffer, Z. J.; Williams, K.; Manthiram, K. Understanding Continuous Lithium-Mediated Electrochemical Nitrogen Reduction. *Joule* **2019**, *3*, 1127−1139.

(6) Tsuneto, A.; Kudo, A.; Sakata, T. Lithium-mediated electrochemical reduction of high pressure N_2 to NH_3. *J. Electroanal. Chem.* **1994**, *367*, 183−188.

(7) Tsuneto, A.; Kudo, A.; Sakata, T. Efficient Electrochemical Reduction of N_2 to NH_3 Catalyzed by Lithium. *Chem. Lett.* **1993**, *22*, 851−854.

(8) Li, K.; Shapel, S. G.; Hochfilzer, D.; Pedersen, J. B.; Krempl, K.; Andersen, S. Z.; Sažinas, R.; Saccoccio, M.; Li, S.; Chakraborty, D.; Kibsgaard, J.; Vesborg, P. C. K.; Nørskov, J. K.; Chorkendorff, I. Increasing Current Density of Li-Mediated Ammonia Synthesis with High Surface Area Copper Electrodes. *ACS Energy Lett.* **2022**, *7*, 36−41.

(9) Marom, R.; Haik, O.; Aurbach, D.; Halalay, I. C. Revisiting $LiClO_4$ as an Electrolyte for Rechargeable Lithium-Ion Batteries. *J. Electrochem. Soc.* **2010**, *157*, A972−A983.

(10) Andersen, S. Z.; Colic, V.; Yang, S.; Schwalbe, J. A.; Nielander, A. C.; McEnaney, J. M.; Enemark-Rasmussen, K.; Baker, J. G.; Singh, A. R.; Rohr, B. A.; Statt, M. J.; Blair, S. J.; Mezzavilla, S.; Kibsgaard, J.; Vesborg, P. C. K.; Cargnello, M.; Bent, S. F.; Jaramillo, T. F.; Stephens, I. E. L.; Norskov, J. K.; Chorkendorff, I. A rigorous electrochemical ammonia synthesis protocol with quantitative isotope measurements. *Nature* **2019**, *570*, 504−508.

(11) Sažinas, R.; Andersen, S. Z.; Li, K.; Saccoccio, M.; Krempl, K.; Pedersen, J. B.; Kibsgaard, J.; Vesborg, P. C. K.; Chakraborty, D.; Chorkendorff, I. Towards understanding of electrolyte degradation in lithium-mediated non-aqueous electrochemical ammonia synthesis with gas chromatography-mass spectrometry. *RSC Adv.* **2021**, *11*, 31487−31498.

(12) Heiskanen, S. K.; Kim, J.; Lucht, B. L. Generation and Evolution of the Solid Electrolyte Interphase of Lithium-Ion Batteries. *Joule* **2019**, *3*, 2322−2333.

(13) Liu, D.; Shadike, Z.; Lin, R.; Qian, K.; Li, H.; Li, K.; Wang, S.; Yu, Q.; Liu, M.; Ganapathy, S.; Qin, X.; Yang, Q. H.; Wagemaker, M.; Kang, F.; Yang, X. Q.; Li, B. Review of Recent Development of In Situ/Operando Characterization Techniques for Lithium Battery Research. *Adv. Mater.* **2019**, *31*, 1806620.

(14) Stenzel, Y. P.; Horsthemke, F.; Winter, M.; Nowak, S. Chromatographic Techniques in the Research Area of Lithium Ion Batteries: Current State-of-the-Art. *Separations* **2019**, *6*, 26.

(15) Zhuang, G. R.; Wang, K.; Chen, Y.; Ross, P. N. Study of the reactions of Li with tetrahydrofuran and propylene carbonate by photoemission spectroscopy. *J. Vacuum Sci. & Technol. A: Vacuum, Surfaces, and Films* **1998**, *16*, 3041−3045.

(16) Li, K.; Andersen, S. Z.; Statt, M. J.; Saccoccio, M.; Bukas, V. J.; Krempl, K.; Sažinas, R.; Pedersen, J. B.; Shadravan, V.; Zhou, Y.; Chakraborty, D.; Kibsgaard, J.; Vesborg, P. C. K.; Nørskov, J. K.; Chorkendorff, I. Enhancement of lithium-mediated ammonia synthesis by addition of oxygen. *Science* **2021**, *374*, 1593−1597.

(17) Wang, L.; Menakath, A.; Han, F.; Wang, Y.; Zavalij, P. Y.; Gaskell, K. J.; Borodin, O.; Iuga, D.; Brown, S. P.; Wang, C.; Xu, K.; Eichhorn, B. W. Identifying the components of the solid-electrolyte interphase in Li-ion batteries. *Nat. Chem.* **2019**, *11*, 789−796.

(18) Aurbach, D.; et al. Identification of Surface Films Formed on Lithium in Propylene Carbonate Solutions. *J. Electrochem. Soc.* **1987**, *134*, 1611−1620.

(19) Aurbach, D.; Daroux, M.; Faguy, P.; Yeager, E. The electrochemistry of noble metal electrodes in aprotic organic solvents containing lithium salts. *J. Electroanal. Chem. and Interface Electrochem.* **1991**, *297*, 225−244.

(20) Schultz, C.; Vedder, S.; Streipert, B.; Winter, M.; Nowak, S. Quantitative investigation of the decomposition of organic lithium ion battery electrolytes with LC-MS/MS. *RSC Adv.* **2017**, *7*, 27853−27862.

(21) Kraft, V.; Weber, W.; Grützke, M.; Winter, M.; Nowak, S. Study of decomposition products by gas chromatography-mass spectrometry and ion chromatography-electrospray ionization-mass spectrometry in thermally decomposed lithium hexafluorophosphate-based lithium ion battery electrolytes. *RSC Adv.* **2015**, *5*, 80150−80157.

(22) Gourdin, G.; Collins, J.; Zheng, D.; Foster, M.; Qu, D. Spectroscopic Compositional Analysis of Electrolyte during Initial SEI Layer Formation. *J. Phys. Chem. C* **2014**, *118*, 17383−17394.

(23) Yang, L.; Smith, C.; Patrissi, C.; Schumacher, C. R.; Lucht, B. L. Surface reactions and performance of non-aqueous electrolytes with lithium metal anodes. *J. Pow. Sour.* **2008**, *185*, 1359−1366.

(24) Andersen, S. Z.; Statt, M. J.; Bukas, V. J.; Shapel, S. G.; Pedersen, J. B.; Krempl, K.; Saccoccio, M.; Chakraborty, D.; Kibsgaard, J.; Vesborg, P. C. K.; Nørskov, J.; Chorkendorff, I. Increasing stability, efficiency, and fundamental understanding of

Supplementary Information

Oxygen-Enhanced Chemical Stability of Lithium-Mediated Electrochemical Ammonia Synthesis

*Rokas Sažinas, Katja Li, Suzanne Z. Andersen, Mattia Saccoccio, Shaofeng Li, Jakob B. Pedersen, Jakob Kibsgaard, Peter C. K. Vesborg, Debasish Chakraborty and Ib Chorkendorff**

Department of Physics, Technical University Denmark, Kongens Lyngby, Denmark

*Corresponding author:

Ib Chorkendorff, email: ibchork@fysik.dtu.dk

Experimental Methods

Electrochemical ammonia synthesis

All the electrochemical experiments were conducted in a 3-electrode single compartment glass cell placed in a home-built electrochemical autoclave inside an Ar glovebox. The setup is shown in Figure S1. The regular electrolyte solution was prepared in an inert argon-filled (Ar) glovebox from 0.3 M $LiClO_4$ (Battery grade, Sigma Aldrich) in 99 vol. % tetrahydrofuran (THF, anhydrous, inhibitor-free, Sigma Aldrich) and 1 vol. % ethanol (EtOH, anhydrous, Honeywell). As a working electrode (WE), molybdenum (Mo) foil (+99.9 %, 0.1 mm thick, Goodfellow) attached by spot-welding to a Mo wire for electrical contact was used. The WE was cleaned in 2% HCl (VWR Chemicals), rinsed in ultra-pure water (miliQ, 18.2 MΩ cm^{-1}) and EtOH and polished with SiC paper (CarbiMet, Buehler). Afterwards it was again rinsed in EtOH and dried before usage. The counter electrode (CE) was made of a platinum (Pt) mesh (99.9 %, Goodfellow), and the reference electrode (RE) was a Pt wire (99.99 %, Goodfellow). The CE and RE were boiled in ultra-pure water (miliQ, 18.2 MΩ cm^{-1}), dried overnight at 100 ˚C and finally flame-annealed before the experiments. The single compartment glass cell and a magnetic stirring bar (VWR, glass covered) are boiled in ultra-pure water, washed with EtOH for 3 times and dried overnight at 100 ˚C in air. The WE and CE are ~0.5 cm apart, and the surface area of the WE facing the CE is 1.8 cm_{geo}^2. The cell is brought into the glovebox straight from the oven while it is still hot, to limit H_2O sticking to the walls. The electrodes are mounted in the cell, and it is placed inside the autoclave in the Ar atmosphere of the glovebox, and the autoclave is closed off. The N_2 (6.0, Air Liquide) and synthetic air (20 % O_2 in N_2, 6.0, Air Liquide) used in the experiments was additionally cleaned by purifiers (NuPure, pptV impurities of H_2O and N-containing contaminants removed). To set the molar ratio of O_2 in N_2 the flow of the N_2 and synthetic air was adjusted with mass flow controllers (Brooks). The pressure in the autoclave was increased to 10 bar and de-pressurized to 3 bar 10 times with the gas mixture in order to remove any remaining Ar. Afterwards, the setup was filled with O_2/N_2 to 20 bar for the main experiments, and the ratio of gasses were measured using a micron-sized orifice and a mass spectrometer (Pfeiffer Vacuum, OmniStar™, Gas Analysis System). The system was usually left for 20 min at open circuit potential to allow the gasses to equilibrate. The electrolyte was stirred at 250 rpm throughout the whole experiment to increase the mass transport in the system and triple-phase boundaries (gas-liquid-solid). The electrochemical experiments included the potentiostatic electrochemical impedance spectroscopy (PEIS) to determine the resistance in the electrolyte, a linear sweep voltammetry (LSV) from open circuit voltage (OCV) until clear and distinct lithium ion reduction, and a chronopotentiometry (CP). After CP, another PEIS was run to ensure the changes in the resistance. The LSV was run before CP in every experiment to determine the Li reduction potential scale, and the values were reported versus platinum pseudo reference electrode (Pt_{Pseudo}). During CP, a steady current density of –4 mA/cm^2 is used for all the experiments. It is important to note that all experiments were conducted at ambient temperature in summer. Consequently, the FE values obtained are lower compared to the values previously reported in our group[1-4] due to the increase in temperature (measured to be ~40 C with thermocouple in the glovebox),, which is detrimental to the reaction since nitrogen solubility is inversely proportional to the temperature. After all the LiMEAS experiments the electrolytes were colorless and transparent and did not change in time.

Quantification of ammonia

In all the experiments, the synthesized ammonia (NH_3) was quantified by a modified colorimetric indophenol method, previously described.[5] As has previously been reported,[6] the GCMS could be used to evaluate the concentration of NH_3 in the electrolytes after LiMEAS. However, the specially designed program has to be applied to the ex situ measurements. The sample absorbance was analyzed by ultraviolet-visible light (UV/Vis) spectroscopy using UV-2600 (Shimadzu) spectroscope in the range 400-1000 nm. The blank background solution was subtracted from each spectrum, and then the difference in absorbance at the peak around 630 nm and through around 860 nm is used. A fitted curve of the difference between the peak and trough of each concentration showed a linear regression with an R^2 value of 0.998. This method is more advantageous opposed to the more common peak based methods because long-time experiments might have solvent breakdown, which can give a falsely high peak at the ammonia wavelength, due to interference from the evolved solvent mixture background. For each measurement, 4 samples of 0.5 mL were taken from the electrolyte. One sample from the electrolyte is used as a background, and the mean and standard deviation of the remaining 3 samples is reported as error bars in Figure 3c. The remaining samples were treated as described previously[5-6], to determine the NH_3 concentration. In the case when the expected concentration of NH_3 exceeds the concentration limits of the indophenol method, the sample is accordingly diluted with ultra-pure water after drying.

Gas chromatography – mass spectrometry (GCMS)

All of the gas chromatography-mass spectrometry (GCMS) measurements in this study were done with an Agilent 6890N gas chromatograph with manual liquid sample injection. All the samples were analyzed immediately after LiMEAS by injecting each of them (0.1 µL) to an inlet at 200 °C and electron-ionized with 30 eV in order to form positive ions (e.g., M^+). The injection volume of 0.1 µl was optimized to get reliable intensities of the peaks without overloading the detector. As a carrier gas, helium (N5.0 purity, Air Liquide) was used with 5 mL min^{-1} flow through the column and 5 mL min^{-1} purge flow. As a filter and collector, a cotton fiber in the inlet was used to avoid deposition of lithium perchlorate ($LiClO_4$) or any other non-volatile species present in the electrolyte in the column upon evaporation of the injected liquid sample. The setup of 2 columns connected in series was used in this study: a non-polar Agilent CP-Volamine (30 m x 0.32 mm x 0.32 µm) and non-polar Agilent HP-5MS UI (30 m x 0.32 mm x 0.25 µm). The temperature program is represented in Figure S4. The GCMS experiments started at 50 °C which was held for 3 min. The ramping of the temperature with 10 °C min^{-1} until 100 °C was performed with dwell time at each temperature of 1 min. The temperature was held for 3 min at 100 °C, then ramped to 120 °C with 20 °C min^{-1}, held for 1 min, ramped to 150 °C with 30 °C min^{-1}. Finally, the system was heated to 190 with 40 °C min^{-1}, held for 3 min, and cooled down to room temperature. The overall measurement time was around 25 min screening the mass range from 1–200 m/z with an event time of 0.1 s in scan mode. It is very important to mention that before the GCMS experiments, the blank electrolyte was injected in order to check for there was any in situ decomposition reactions in GCMS. No volatile compounds except the components of the electrolyte were detected –the initial electrolytes were clean with no side reactions in the hot GC inlet.

EI-MS Analysis

The GC was interfaced with a sector mass spectrometer (Autospec v4.0 mass spectrometer, Waters Corporation). A very high mass resolution of ~30000 and mass accuracy of 1−2 ppm were achieved. Initially, the chromatograms and mass spectra were monitored and analyzed with MassLynx v4.0 (Waters Corporation) software. The mass spectrometer was run in the electron impact ionization (EI) mode with the following parameters: the temperature of the ion source together with the GC inlet was set to 200 °C, and the filament was operated at a voltage of 30 eV. The detector voltage was set relative to the respective tuning results. Compound identification and corresponding structural formulae were assigned relying upon the National Institutes of Standards (NIST) library[7] and most of them including the more detailed description were reported previously.[6] A full scan mode ranging from m/z 1 to 200 was applied to the instrument. The compounds were confirmed with their retention time and fragment patterns of in-house made standards from commercially available compounds (Sigma Aldrich). The compound of 100 ppm was dissolved in THF and injected into GCMS. Before each run, a mixture of ethanol and THF was used to rinse the lines and analyzed at the same time to generate a background spectrum. Every recorded GCMS data set was processed and mass-by-mass analyzed in order to evaluate the molecular masses of the molecular ions and fragmentation patterns using the OpenChrom and MassLynx 4.0 software. As the initial data, the total ion current (TIC) chromatograms were collected. However, each sample was thoroughly analyzed by m/z values as extracted ion chromatograms (XIC or EIC). In a reconstructed-ion chromatogram (RIC), one or more m/z values of interest are recovered taken and represented in time from the entire data set for a chromatographic run,[8] revealing species if any at specific retention time of the chromatograms, which were not visible in TIC. The total sum intensity, in other words called the base peak intensity, within a mass tolerance range of interest around m/z of a particular compound is plotted at every point in the analysis. The size of the mass tolerance range typically depends on the mass accuracy and mass resolution of the data collecting instrument. XIC is generated by focusing upon the ions of interest with specific m/z in the whole data set containing the full mass spectrum over time after the fact. More discussion on the methods is given elsewhere.[6]

The area of the most intense XIC fragment of the eluting compound was integrated and compared to the main peaks of THF and EtOH. After integration, the relative amount of compound was estimated and compared to the appropriate in-house made 100 ppm concentration standard in THF. The integration of the XICs method for other compounds is in a good agreement with the experimental standards and confirms the evaluated amount of the compound molecule. Further description of the method is given elsewhere.[6]

The GCMS data was analyzed with super user-friendly open source software OpenChrom.[9] It is highly recommended for all the GCMS users.

NMR Analysis

The NMR spectra were acquired using an AVANCE III HD 400 MHz spectrometer equipped with a 5 mm Prodigy probe with either deuterium oxide (D_2O) or deuterated chloroform ($CDCl_3$). Prior to NMR, the electrodes were kept in the Ar-filled glovebox overnight. In addition, the reference THF+EtOH represents the 1 vol% EtOH solution in THF, and contains 4 main peaks belonging to different protons of EtOH and THF. The proton on the oxygen is drifting and might not be seen in general in the spectrum. As can be seen from Figure 4, this was enough to get rid of all the THF and EtOH. All the chemical shifts of the samples were normalized to tetramethylsilane (TMS). The very little variation of chemical shift of the NMR signals could appear due to slight differences in the pH, volume, and/or temperature of the samples. The data was analyzed with Topspin 4.0.8 software. The concentration of the material from the surface of the WE was very small in order to obtain ^{13}C NMR spectrum. However, the latter is not useful in the specific application of this study with organic multicomponent systems from multicomponent electrolytes and surfaces of the electrodes. ^{15}N NMR spectrum was recorded additionally, however did not reveal any additional information.

Faradaic efficiency calculation

In order to calculate the Faradaic efficiency (FE), the molar concentration, c_{NH3} (mol L^{-1}), of synthesized NH_3 in the electrolyte is measured via an indophenol colorimetric UV/Vis along with the total electrolyte volume, V (L), after each electrochemical measurement, and is compared to the total charged passed, Q:

$$FE_{NH_3} = \frac{3 \cdot F \cdot c_{NH_3} \cdot V}{Q} \qquad (1)$$

where F is Faraday's constant of 96485 C mol^{-1}, and the number 3 represents the electrons transferred during the reaction for each mole of NH_3 as shown in the following equation,

$$1/2N_2\,(g) + 3H^+ + 3e^- \rightarrow NH_3\,(g) \qquad (2)$$

Paper 5

Electrosynthesis of ammonia with high selectivity and high rates via engineering of the solid-electrolyte interphase
S. Li*, Y. Zhou*, K. Li, M. Saccoccio, R. Sažinas, S. Z. Andersen, J. B. Pedersen, X. Fu, V. Shadravan, D. Chakraborty, J. Kibsgaard, P. C. Vesborg, J. Nørskov and I. Chorkendorff
Joule, **2022**, 3, 2083-2101.
* these authors contributed equally

Joule

CellPress
OPEN ACCESS

Article

Electrosynthesis of ammonia with high selectivity and high rates via engineering of the solid-electrolyte interphase

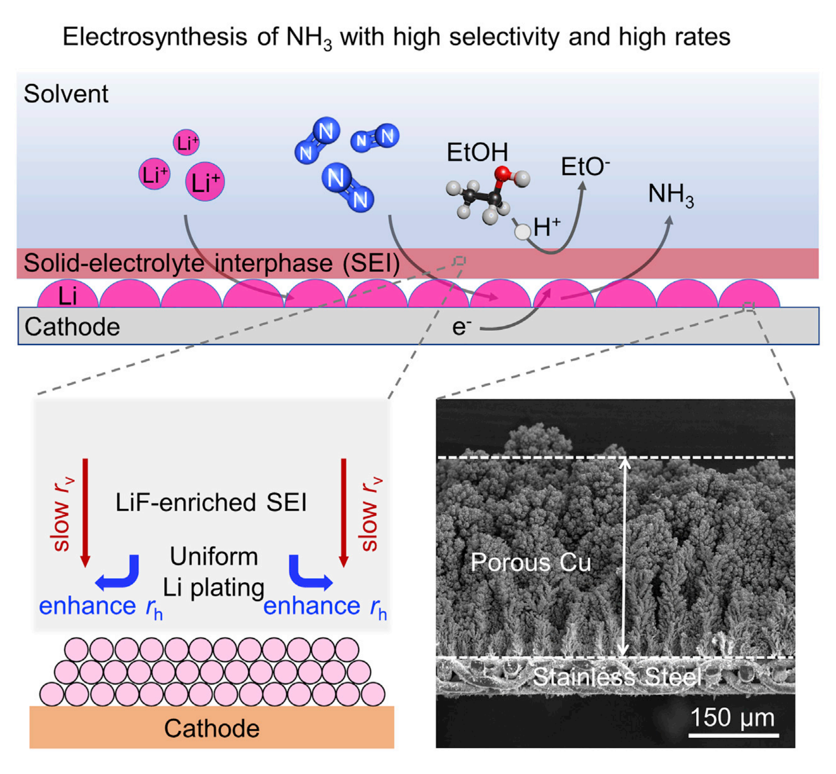

Achieving high selectivity at a commercially relevant current density holds the key to the practical applications of electrochemical NH_3 synthesis. Here, a record selectivity and NH_3 production rate at a current density of -1.0 A cm_{geo}^{-2} under 20 bar N_2 are achieved through a combination of highly porous Cu electrode and $LiBF_4$-based electrolyte. Theoretical calculations and experimental analysis suggest that a compact and uniform LiF-enriched SEI layer facilitates even lithium plating and suppresses the undesired electrolyte decomposition.

Shaofeng Li, Yuanyuan Zhou, Katja Li, ..., Peter C.K. Vesborg, Jens K. Nørskov, Ib Chorkendorff

jkno@dtu.dk (J.K.N.)
ibchork@fysik.dtu.dk (I.C.)

Highlights

LiF-enriched SEI layer is beneficial to achieve high selectivity

$LiBF_4$ electrolyte induces the formation of a compact and uniform LiF-enriched SEI layer

Porous Cu electrode combined with $LiBF_4$ realizes both high selectivity and high rates

NH_3 distribution in different phases is highly dependent on the lithium salts used

Li et al., Joule 6, 2083–2101
September 21, 2022
Published by Elsevier Inc.
https://doi.org/10.1016/j.joule.2022.07.009

Joule

CellPress
OPEN ACCESS

Article

Electrosynthesis of ammonia with high selectivity and high rates via engineering of the solid-electrolyte interphase

Shaofeng Li,[1,2] Yuanyuan Zhou,[1,2] Katja Li,[1] Mattia Saccoccio,[1] Rokas Sažinas,[1] Suzanne Z. Andersen,[1] Jakob B. Pedersen,[1] Xianbiao Fu,[1] Vahid Shadravan,[1] Debasish Chakraborty,[1] Jakob Kibsgaard,[1] Peter C.K. Vesborg,[1] Jens K. Nørskov,[1,*] and Ib Chorkendorff[1,3,*]

SUMMARY

Ammonia is a large-scale commodity essential to fertilizer production, but the Haber-Bosch process leads to massive emissions of carbon dioxide. Electrochemical ammonia synthesis is an attractive alternative pathway, but the process is still limited by low ammonia production rate and faradaic efficiency. Herein, guided by our theoretical model, we present a highly efficient lithium-mediated process enabled by using different lithium salts, leading to the formation of a uniform solid-electrolyte interphase (SEI) layer on a porous copper electrode. The uniform lithium-fluoride-enriched SEI layer provides an ammonia production rate of 2.5 ± 0.1 μmol s^{-1} cm_{geo}^{-2} at a current density of -1 A cm_{geo}^{-2} with 71% ± 3% faradaic efficiency under 20 bar nitrogen. Experimental X-ray analysis reveals that the lithium tetrafluoroborate electrolyte induces the formation of a compact and uniform SEI layer, which facilitates homogeneous lithium plating, suppresses the undesired hydrogen evolution as well as electrolyte decomposition, and enhances the nitrogen reduction.

CONTEXT & SCALE

Lithium-mediated nitrogen reduction (LiNR) is a promising pathway to produce ammonia (NH_3) in a modular and distributed manner, but the process is still limited by low NH_3 production rate and selectivity. Herein, we establish a theory modeling approach to screen lithium salts for the LiNR process and find that fluorine-based electrolytes are beneficial to achieve a high selectivity due to the presence of lithium fluoride (LiF) in the solid-electrolyte interphase (SEI) layers. We demonstrate that a record selectivity and NH_3 production rate at a current density of -1.0 A cm_{geo}^{-2} under 20 bar N_2 are achieved by using lithium tetrafluoroborate electrolyte in combination with a highly porous copper electrode. Experimental analysis uncovers that a compact and uniform LiF-enriched SEI layer facilitates even lithium deposition and suppresses the uncontrolled electrolyte degradation. These findings provide new insights into the development of an industrially feasible route for electrochemical NH_3 synthesis.

INTRODUCTION

Ammonia (NH_3) is one of the most abundantly produced chemicals, with an annual production exceeding 182 million tonnes.[1] Around 80% of the synthesized NH_3 is used in the fertilizer industry, but it is also regarded a promising carbon-free energy carrier to replace fossil fuels.[2,3] Currently, the Haber-Bosch process is the predominant pathway to produce NH_3 by passing N_2 and H_2 over an iron-based catalyst at high temperatures (350°C–450°C) and high pressures (150–200 bar).[4,5] The process consumes more than 1% of the global energy supply and leads to about 1.3% of the global CO_2 emission,[6,7] mainly associated with the production of H_2 from hydrocarbon feedstocks. In addition, considering the extreme operating conditions and the required on-site hydrogen production, this process requires large industrial plants, which are capital intensive. Alternatively, electrochemical NH_3 synthesis in principle provides a simple route that can be based on renewably generated electricity, which will reduce the CO_2 footprint, and is also compatible with small-scale facilities that produce NH_3 in a modular and distributed manner.

Currently, the only known reliable method of electrochemical NH_3 synthesis at ambient temperature is lithium-mediated nitrogen reduction (LiNR), which was first reported by Fichter et al. in 1930[8] and later studied by Tsuneto et al. in the 1990s.[9,10]

There have been many claims of synthesizing NH_3 from N_2 electrochemically in this field, but most of those reports were highly questionable, due to a lack of scientific rigor necessary to prove that the NH_3 originated from activated N_2.[11,12] Solid evidence with a method for validating that the N_2 is activated for this process was first provided by our group by using a proper gas cleaning procedure and $^{14}N_2$ and $^{15}N_2$ isotopes.[11] Although the accurate mechanisms are still not entirely understood, it is broadly believed that this LiNR process relies on the metallic lithium reduced from Li^+ to dissociate N_2 followed by a sequence of electron and proton transfers to form NH_3 with suitable proton donors or so-called sources (Figure 1A).[13,14] The LiNR process was revisited by several groups recently,[11,13–20] and the typical reported faradaic efficiency (FE) is around 5%–20% at ambient conditions with NH_3 production rate less than 0.01 μmol s^{-1} cm_{geo}^{-2}.[11,14,16,17] Recently, Suryanto et al. has reported 69% FE at a current density of −0.022 A cm_{geo}^{-2} and an NH_3 production rate of 0.053 μmol s^{-1} cm_{geo}^{-2} by using phosphonium salt as a proton carrier under 20 bar pressure.[18] Our recent work has demonstrated 78% FE at a current density of −0.004 A cm_{geo}^{-2} achieved by adding 0.6 to 0.8 mol % oxygen to the 20 bar N_2 atmosphere, which is attributed to the modification of the solid-electrolyte interphase (SEI) layer formed between the active (lithium) surface and the electrolyte during operation.[21]

The SEI layer over the electrode surface is mainly composed of electrolyte decomposition products, including various inorganic and organic components, known in the lithium-ion battery field to be ion conducting but electron insulating.[22,23] This passivation layer is likely a crucial player in determining the stability and performance of the LiNR process. First, it may help improve the system's stability by avoiding excess electrolyte decomposition and lithium dendrite formation. Second, the SEI layer is a vital factor in determining the relative diffusion rates of Li^+, H^+, and N_2 (r_{Li}, r_H, r_{N2}), which are the critical variables determining the rate and selectivity (Figure 1A).[13,21] However, the exact composition and functionality of the SEI layer in the LiNR process remains largely unexplored. Further, our group has found that modifying the SEI layer by the addition of oxygen in the N_2 feed can dramatically increase the FE up to 78%.[21] To overcome the gap of low current density, we also proposed increasing the current density (e.g., −0.1 A cm_{geo}^{-2}) by the use of high surface area copper electrodes.[24] The challenge still remains to achieve high FE and a commercially relevant current density (i.e., around −1.0 A cm_{geo}^{-2}) in a single system.

This is the challenge we address in this work by modifying the SEI layer and improving the accessible surface area (per geometric surface area) simultaneously. We concentrate on determining the dynamic changes of the SEI under different experimental conditions and understanding how the SEI layer improves the performance of the LiNR process by tuning the ionic conductivity. We study several electrolytes and suggest that a fluorine-based electrolyte is the best. In combination with a highly porous Cu electrode, we demonstrate 95% ± 3% FE at a current density of −0.1 A cm_{geo}^{-2} under 20 bar N_2. In addition, we show a FE of 71% ± 3% is achievable at a current density of −1.0 A cm_{geo}^{-2}, delivering an NH_3 production rate of 2.5 ± 0.1 μmol s^{-1} cm_{geo}^{-2}. The new results are attributed to the uniform lithium fluoride (LiF)-enriched SEI layer that facilitates even lithium deposition and suppresses the uncontrolled electrolyte degradation. The different SEI layers were characterized with X-ray photoelectron spectroscopy (XPS) and X-ray diffraction (XRD), where we confirmed the presence of LiF. Moreover, we also found that the produced NH_3 does not only exist in the electrolyte but also in the gas phase and in the deposited layer with SEI, and the NH_3 concentration distribution in different phases is highly related to the lithium salt used.

[1]Department of Physics, Technical University of Denmark, Kongens Lyngby, Denmark

[2]These authors contributed equally

[3]Lead contact

*Correspondence: jkno@dtu.dk (J.K.N.), ibchork@fysik.dtu.dk (I.C.)

https://doi.org/10.1016/j.joule.2022.07.009

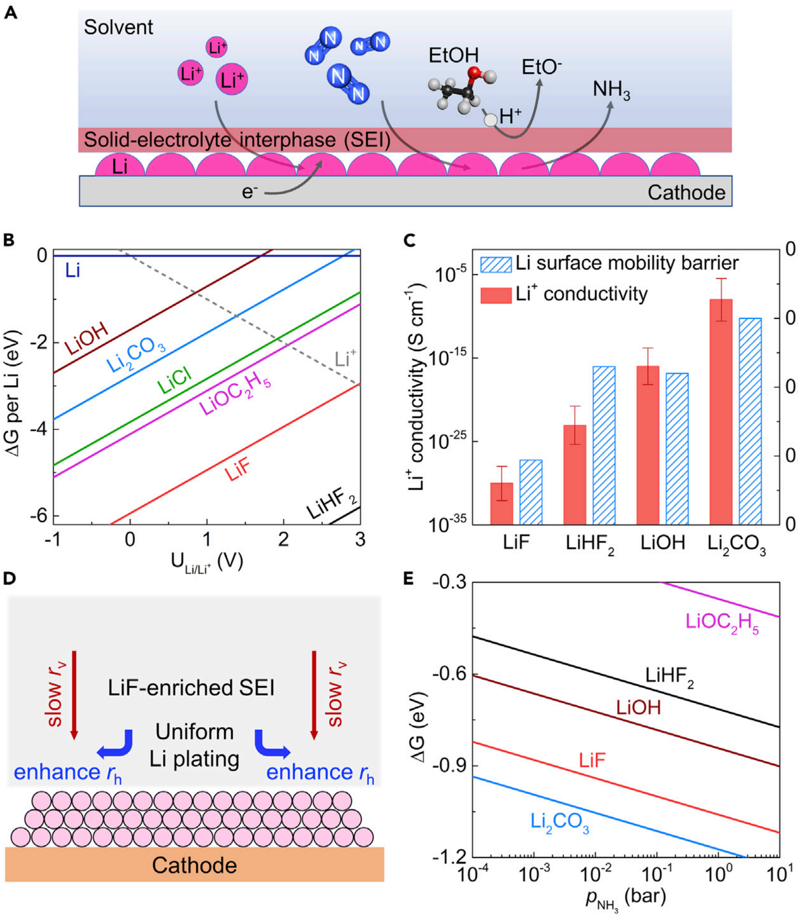

Figure 1. Theoretical investigation of the SEI layer by using different lithium salts

(A) Schematic of the mechanism for Li-mediated ammonia synthesis. Although the accurate mechanisms are still not entirely understood, it is broadly believed that this LiNR process relies on the metallic lithium reduced from Li^+ to dissociate N_2 followed by a sequence of electron and proton transfers to form NH_3 with suitable proton donors.

(B) Calculated Gibbs formation free energy of Li-containing compounds as a function of voltage (versus Li/Li^+).

(C) The Li^+ conductivity and energy barrier of Li surface mobility for the Li_2CO_3, LiOH, $LiHF_2$, and LiF at the operating voltage ($U_{Li/Li+} = 0$ V). The error bars represent the uncertainty of calculated Li^+ conductivity.

(D) Schematic illustration of proposed Li diffusion model for a LiF-enriched SEI layer during the LiNR process.

(E) The Gibbs adsorption free energy of NH_3 on different Li-containing compounds.

RESULTS

Theoretical investigation of the SEI layer

We first present an analysis of the thermodynamic stability of different Li-containing compounds that form in the SEI layer. In the following discussion, we only focus on the most stable compounds that are not soluble in tetrahydrofuran (THF), since these are likely to be the main components in the SEI, thereby determining the intrinsic properties. Other phases could also be part of the SEI, but most likely not in large quantities compared with the most stable materials. Figure 1B shows the free energy (Pourbaix diagram) versus potential of the 6 most stable phases that could form in the SEI layer at different potentials based on experimental stability data.[25] The full Pourbaix diagram including all possible experimentally reported Li-containing compounds is shown in Figure S1. The two most stable phases using $LiClO_4$ as the lithium salt and pure N_2 gas are $LiOC_2H_5$ and Li_2CO_3, since LiCl is soluble in THF.[26] This is in agreement with the literature for Li-ion batteries,[27] where it is found that organic salts (e.g., $LiOC_2H_5$) near the SEI/electrolyte interface are porous, so that Li^+ can be transported with other anions through this organic outer layer of the SEI, whereas a dense inorganic layer (e.g., Li_2CO_3) blocks further anion diffusion. Therefore, the transport mechanism of Li^+ in the inorganic layer is most likely based on Li defect formation and defect diffusion. As shown in Figure 1B, when using $LiBF_4$ instead of $LiClO_4$ as the lithium salt in the electrolyte, the two most stable solid phases in the SEI are $LiHF_2$ and LiF. Although $Li_2B_6O_{10}$, $Li_2B_4O_7$, and $NH_3 \cdot BF_3$ are even more stable than $LiHF_2$ and LiF (Figure S1), they are more soluble in THF.[28]

The elementary steps in the LiNR include the diffusion of Li^+, H^+, and N_2 species from bulk electrolyte through SEI toward the electrode surface followed by Li deposition, H_2 formation, and NH_3 formation. Due to the presence of the SEI, the diffusion of these three species is rather slower than that of H_2 and NH_3 formation at extreme operating potential (~ -3 V).[13,21] Therefore, the diffusion rates of Li^+, H^+, and N_2 species in the SEI are the overall rate-limiting steps in the LiNR.[13,21] For Li^+ transport properties, we conducted a comprehensive first-principles study of possible Li point-defect formation energies in Li_2CO_3, LiOH, $LiHF_2$, and LiF (Figure S2) and identify the dominating defects at the applied voltage range. The Li^+ conductivity is related to the defect concentration and the diffusivity via the Nernst-Einstein equation.[29] Based on random-walk theory,[29] the diffusivity is determined by the migration barrier, which we calculate by the climbing image nudged elastic band (CI-NEB) method,[30] whereas defect concentration depends on the defect formation energy (see experimental procedures). As shown in Figure 1C, at the operating voltage (0 V versus Li/Li^+), the calculated Li^+ conductivity in $LiHF_2$ and LiF is several orders of magnitudes lower than that of Li_2CO_3. The presence of LiF results in a decrease of r_{Li} relative to Li_2CO_3. The diffusion rates of proton and N_2 are estimated via Fick's first law. Consider the case of linear (one-dimension) diffusion of proton from bulk electrolyte through SEI approaching the electrode surface, the flux of proton $J_{H^+}(x,t)$ at given position x at a time t is proportional to the concentration gradient C_{H^+}, that is, $J_{H^+}(x,\ t) = D_{H^+}\frac{\partial C_{H^+}(x,\ t)}{\partial x}$. Since the N_2 reduction and H_2 evolution reactions are fast enough at the very negative potential (<-3 V), the proton and N_2 concentration at electrode surface ($x = L$) is approximated to be zero. Therefore, the diffusion rates of proton and nitrogen are estimated by $D_{H^+} = \frac{3J_{NH_3}}{FE}\frac{L}{C_{H^+}(0,\ t)}$ and $D_{N_2} = J_{NH_3}\frac{L}{C_{H^+}(0,\ t)}$, where L is the thickness of the SEI chosen to be 10–100 nm.[31] As shown in Table S1, there is a small change of r_H and r_{N2} at different experimental conditions (i.e., different main components of the formed SEI) relative to r_{Li}. Therefore, the decreased r_{Li} caused by the presence of LiF should lead to a considerable FE increase according to the microkinetic modeling reported in our previous work.[13,21] The reason is that fewer electrons are "wasted" depositing Li relative to electrons used in reducing nitrogen. A similar phenomenon is also observed in our previous work, where by adding small amounts of oxygen,[21] the formation of LiOH competes with that of Li_2CO_3 in the SEI using a $LiClO_4$ salt (Figure S3), leading to a FE increase from 25% to 78%. The resulting FE due to the changes of Li diffusion rates in different SEI components are summarized in Figure S4.

In the beginning, the Li^+ transporting through bulk electrolyte is reduced to Li metal immediately and deposited on the electrode surface. The active Li metal will spontaneously decompose electrolyte, resulting in the growth of SEI. An ideal SEI is electron insulating to prevent continuous electrolyte decomposition, yet ion conducting to lithium ions. In the presence of the SEI, the Li^+ that go through the SEI is deposited as metallic Li on the electrode surface. The deposition of metallic Li results in the formation of the Li dendrite if the two-dimensional Li mobility parallel to the SEI and the electrode surface is rather low, leading to a poor homogeneity of the SEI.[32] Here, we investigated the Li mobility in the surfaces of Li_2CO_3, LiOH, $LiHF_2$, and LiF. The most probable/stable surfaces for each species are selected based on the surface phase diagram (see Figures S5–S8). As shown in Figure 1C, LiF exhibits a 0.09 eV migration barrier for Li surface mobility, which is lower than that of LiOH (0.22 eV) and Li_2CO_3 (0.3 eV). Therefore, the LiF-enriched SEI could improve an uneven electrodeposition of lithium by enhancing Li surface mobility, thus a more homogeneous SEI, and the similar phenomenon is also observed in Li-ion batteries.[33] Furthermore, LiF is more electrically insulating and has a wider electrochemical stability window than Li_2CO_3 (see Figure S9), thus creating a better passivated electrode surface to prevent undesired side reactions between deposited lithium and electrolyte.

Figure 1D is a schematic illustration of our proposed Li^+ diffusion model for a LiF-enriched SEI layer during the LiNR process. The r_{Li} consists of diffusion rates in two directions, i.e., vertical and horizontal, and denoted as r_v (Li^+ diffusion rate through the SEI, v: vertical) and r_h (Li^+ diffusion rate on the surface, h: horizontal), respectively. The model suggests that by decreasing r_v while enhancing r_h, the LiF-enriched SEI layer enables a homogeneous Li^+ flux and suppresses Li dendrite formation, thus leading to a further increase in FE. In addition, as shown in Figure 1E, we find that NH_3 molecules can easily be absorbed in the bulk and the surface of different Li-containing phases, e.g., $LiOC_2H_5$, Li_2CO_3, LiOH, $LiHF_2$, and LiF, which suggests that the produced NH_3 could be possibly trapped in the SEI layer. It also should be noted that the NH_3 formed using $LiBF_4$ as lithium salt can be trapped as $NH_3 \cdot BF_3$, which is easily soluble in THF and ethanol. As shown in Figure S1, the Gibbs formation free energy of $Li_xH_yN_z$ (Li_3N, Li_2NH, and $LiNH_2$) species per Li atom is several eV (at least 6 eV at the operation voltage) higher than that of $LiHF_2$, LiF, and $NH_3 \cdot BF_3$, so the portion of $Li_xH_yN_z$ in the SEI is much less than that of $LiHF_2$, LiF, and $NH_3 \cdot BF_3$. It indicates that the produced NH_3 may mainly exist in the electrolyte rather than in the SEI layer by using $LiBF_4$ as lithium salt.

Experimental demonstration

Motivated by theoretical results, we choose two typical fluorine-based lithium salts, i.e., $LiBF_4$,[14,15,18,20] $LiPF_6$, and the widely used $LiClO_4$,[9,10,16,21] as the model systems. It should be noted that Lazouski et al. have first reported 18% FE by using $LiBF_4$ under ambient pressure,[14] and then, $LiBF_4$ was also used by different groups in this field.[18,20] However, the comprehensive investigations on the effect of different lithium salts on the SEI layer are unexplored. In contrast to our previous study, a stainless steel (SS) mesh was used as substrate rather than a Ni foam,[15] in order to allow the controlled growth of porous Cu using the hydrogen bubble template method.[24] The geometrical surface area was defined as the front of a 0.5 × 0.4 cm^2 SS mesh or Cu foil. The detailed procedures of Cu deposition on the SS mesh are shown in the experimental procedures. The Cu was chosen as the electrode material here because Cu has difficulties alloying with lithium electrochemically in organic electrolyte.[9,10,34] Scanning electron microscopy (SEM) images show that highly structured Cu with well-ordered pores self-assemble on the SS mesh (Figures 2B–2D). The high-resolution SEM image in Figure 2C shows that the highly structured Cu consists of connected Cu particles with a diameter of ~1 to 3 μm. As shown in Figures 2D and S10A, the thickness of the deposited Cu can be well controlled and tuned from 110 to 470 μm by changing the deposition time. It should be noted that changing other deposition parameters, e.g., applied current (Figure S11), could also change the deposition thickness and the porous structure.

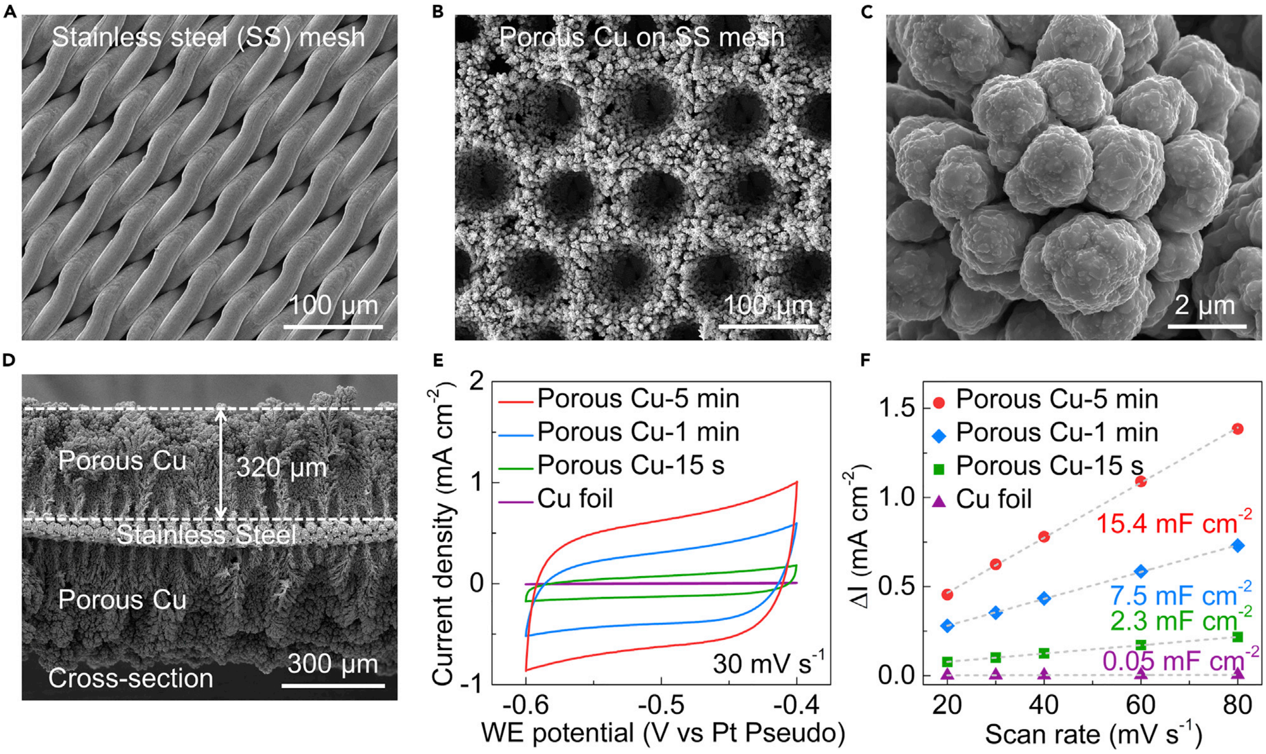

Figure 2. Fabrication of porous Cu electrodes for Li-mediated ammonia synthesis

(A–C) Representative SEM images of the stainless steel (SS) mesh (A) and porous Cu electrode (B and C).

(D) Cross-section SEM images of the porous Cu electrode.

(E) Cyclic voltammetry of different porous Cu electrodes at scan rate of 30 mV s^{-1}.

(F) Current density change versus scan rate of different porous Cu electrodes and the calculated specific capacitances. The change in current density was determined at −0.5 V versus reference electrode.

We also would like to point out that the porous electrode can also be made by other transition metals using the hydrogen bubble template method, such as Ni, Co, etc.,[35–38] which could potentially also used for LiNR process. To determine the electrochemical surface area (ECSA) of the porous Cu synthesized with different deposition time, i.e., 15 s, 1 min, and 5 min (denoted as porous Cu-15 s, porous Cu-1 min, and porous Cu-5 min), capacitive cycling was employed to measure the specific capacitances. The cycling voltammetry (CV) curves of the as-made porous electrodes and the Cu foil at various scan rates are shown in Figures 2E and S12. It can be seen that current density and the average area of the porous Cu electrodes are much higher than the Cu foil, implying a much higher specific capacitance and ECSA. As shown in Figure 2F, the porous Cu electrodes displays much higher current densities at the same scan rates compared with the Cu foil. The calculated specific capacitance of the porous Cu-5 min is 15.4 mF $\text{cm}_{\text{geo}}^{-2}$, which is 300 times higher than the Cu foil (0.05 mF $\text{cm}_{\text{geo}}^{-2}$). Therefore, the ECSA of 308 cm^2 was determined for the porous Cu-5 min electrode with geometric area of 1 cm^2, and such a considerable increase of ECSA is attributed to the deposited porous Cu with high surface area.

In order to investigate the current density achievable, porous Cu-15 s, porous Cu-1 min, and porous Cu-5 min were selected for the standard test using the widely used $LiClO_4$ electrolyte. As shown in Figures 3A–3D, all the experiments were carried out in a custom-designed autoclave with a glass cell containing 30 mL electrolyte under 20 bar N_2. The electrolyte was 2 M lithium salt in THF containing 1 vol %

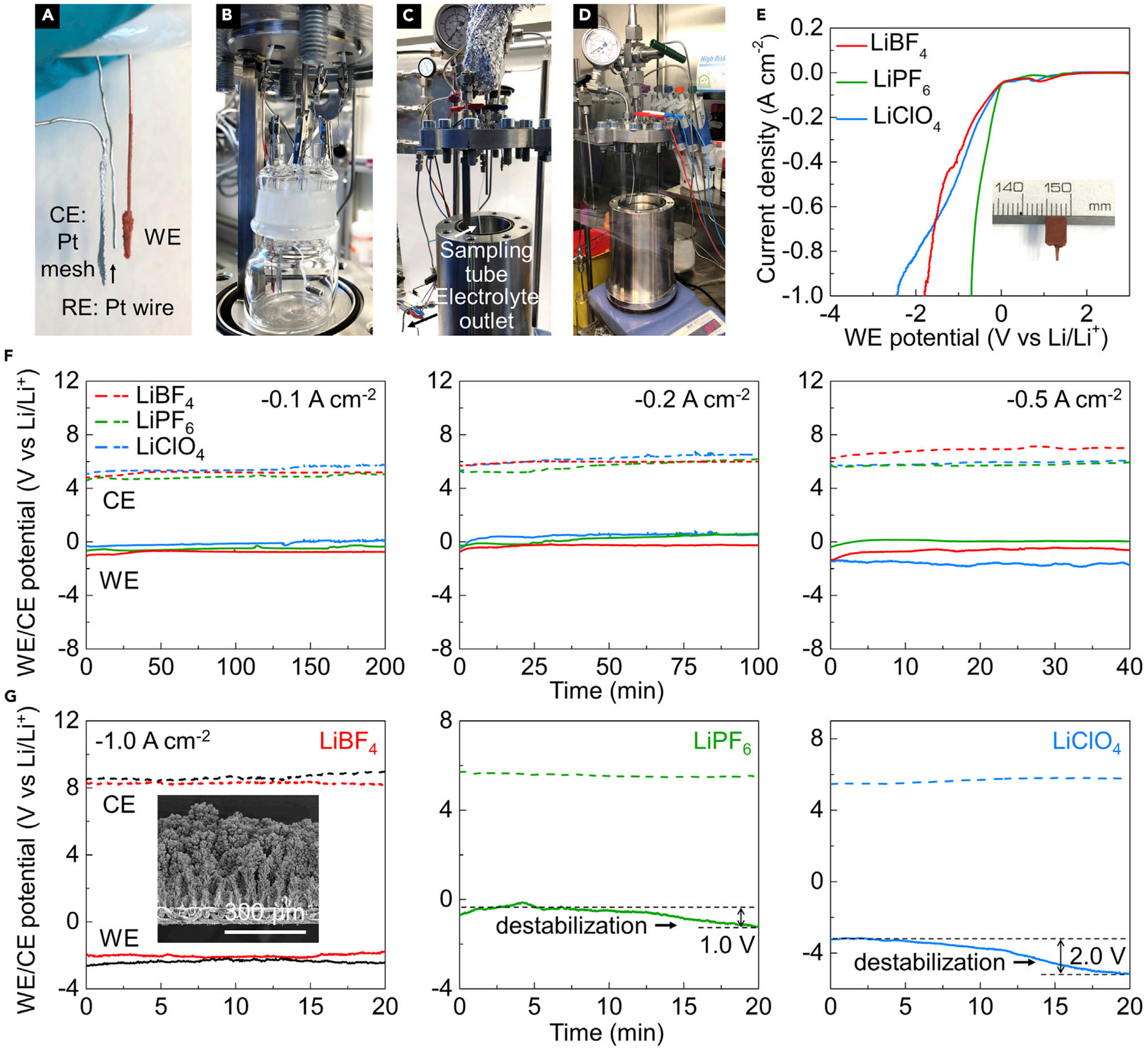

Figure 3. Electrochemical performance of Li-mediated ammonia synthesis

(A and B) Digital photos of the setup for working, counter, and reference electrodes (A) and the glass cell sitting in the autoclave (B). The distance between WE and RE was fixed around 0.5 cm for all the experiments.

(C and D) Digital photos of the autoclave sitting in the fume hood (C) and Ar glovebox (D).

(E) LSV of the porous Cu electrode using different lithium salts. Inset in (E) is a digital photo of the porous Cu electrode (0.2 cm_{geo}^2).

(F and G) Chronopotentiometry (CP) of the porous Cu electrode at current densities of −0.1, −0.2, and −0.5 A cm_{geo}^{-2} (F) and −1.0 A cm_{geo}^{-2} (G) with different lithium salts. Inset in (G) is the cross-section SEM image of the porous Cu electrode without porous Cu on the backside. The black lines represent the data of the porous Cu electrode without porous Cu on the backside. All the experiments here were using the porous Cu electrodes that were synthesized at the same condition, and 2 M lithium salt in tetrahydrofuran solutions containing 1 vol % ethanol under 20 bar N_2. A total charge of 240 C was passed for the CP measurements at varied current densities.

ethanol (0.17 M ethanol). The N_2 used in the experiments was 99.9999% pure and additionally cleaned with purifiers (NuPure) to reduce the nitrogen-containing impurities to parts per trillion levels. The as-prepared porous Cu electrode (0.2 cm_{geo}^2), Pt mesh (1 cm_{geo}^2), and Pt wire were used as working electrode (WE), counter electrode (CE), and pseudo-reference electrode (RE), respectively (Figure 3A). As shown in the linear sweep voltammetry (LSV, Figure S13), current densities of -0.1, -0.3, and -1.0 A $\text{cm}_{\text{geo}}^{-2}$ were achieved by using the porous Cu-15 s, porous Cu-1 min, and porous Cu-5 min, respectively. Therefore, systematic experiments with different lithium salts were further conducted using the porous Cu-5 min electrode that achieved a current density of −1.0 A $\text{cm}_{\text{geo}}^{-2}$. As shown in Figure 3E, the current density of −1.0 A $\text{cm}_{\text{geo}}^{-2}$ can also be reached by using the fluorine-based electrolyte, i.e., $LiBF_4$ and $LiPF_6$. Potentiostatic electrochemical impedance spectroscopy (PEIS) was employed to measure the bulk electrolyte resistance (Figure S14). The electrolyte resistance for the three electrolyte formulations in descending order is thus as follows: $LiBF_4 > LiClO_4 > LiPF_6$.

Constant-current densities from −0.1 to −1.0 A $\text{cm}_{\text{geo}}^{-2}$ were applied for the chronopotentiometry (CP) measurements when using different lithium salts, until the total passed charge reached 240 C. As shown in Figure 3F, the WE and CE potentials are quite stable for all the lithium salts at various constant-current densities from −0.1 to −0.5 A $\text{cm}_{\text{geo}}^{-2}$ within the investigated time period. In contrast, the WE potential of the porous Cu electrode using $LiPF_6$ and $LiClO_4$ exhibits destabilization during CP measurement at a current density of −1.0 A $\text{cm}_{\text{geo}}^{-2}$, although the WE potential using $LiBF_4$ is stable in that period (Figure 3G). Specifically, the WE potential shows a drop of ~1.0 and 2.0 V for the porous Cu electrode using $LiPF_6$ and $LiClO_4$, respectively, which is indicative of unstable SEI layers and severe electrolyte decomposition. We have here chosen to define the geometric area as only one side of the SS mesh. Nevertheless, one should be aware that the porous Cu was deposited on both sides as seen in Figure 2D. In order to investigate the influence of the porous Cu deposit on the backside of the electrode, we removed the Cu deposit on the backside (inset in Figures 3G and S10B) and tested this electrode again at current density of 1 A $\text{cm}_{\text{geo}}^{-2}$. It also shows the similar stability (black lines in Figure 3G), which indicates that the backside does not significantly influence the electrochemical stability. After CP measurement at a current density of −1.0 A $\text{cm}_{\text{geo}}^{-2}$, the similar morphology as the pristine electrode is shown for the porous Cu electrode using $LiBF_4$ (Figure S15), indicative of a stable porous structure during the electrochemical tests. In addition, as shown in Figure S16, the calculated specific capacitance of the porous Cu electrode using $LiBF_4$ after the CP measurements is 15.2 mF $\text{cm}_{\text{geo}}^{-2}$, which is also similar to the pristine electrode (15.4 mF $\text{cm}_{\text{geo}}^{-2}$).

As shown in the Figure S17, both $LiPF_6$ and $LiClO_4$ electrolytes turn black after CP measurements at −1.0 A $\text{cm}_{\text{geo}}^{-2}$, whereas the $LiBF_4$ electrolyte only shows a mild color change. In addition, the black electrolyte became highly viscous within a few hours post-electrochemistry (Figure S18), which is ascribed to the serious electrolyte decomposition (Figure S19), specifically THF oxidation that might lead to production of polymers.[39] The changes of the electrolyte color at varied constant-current densities from −0.1 to −1.0 A $\text{cm}_{\text{geo}}^{-2}$ are shown in Figure S20. This shows the general instability of the electrolyte under these experimental conditions, which is particularly prominent for the $LiPF_6$ and $LiClO_4$ salts. Moreover, it is obviously seen that the electrolyte color of $LiClO_4$ darkens as the current density increases, which can be attributed to the high CE potential at high current density that might lead to more THF oxidation reactions. However, the $LiBF_4$ only show a mild color change after CP measurements even at −1.0 A $\text{cm}_{\text{geo}}^{-2}$. We believe that lowering the CE potential below THF oxidation by utilizing hydrogen oxidation reaction (HOR) at the CE will help to solve this issue, which is desirable for the follow-up study. Another difference seen in the images is the huge variances of the deposited layers over the porous Cu electrode using different lithium salts (Figure S17). The deposited layer using $LiBF_4$ looks much thinner than that of $LiPF_6$ and $LiClO_4$, which

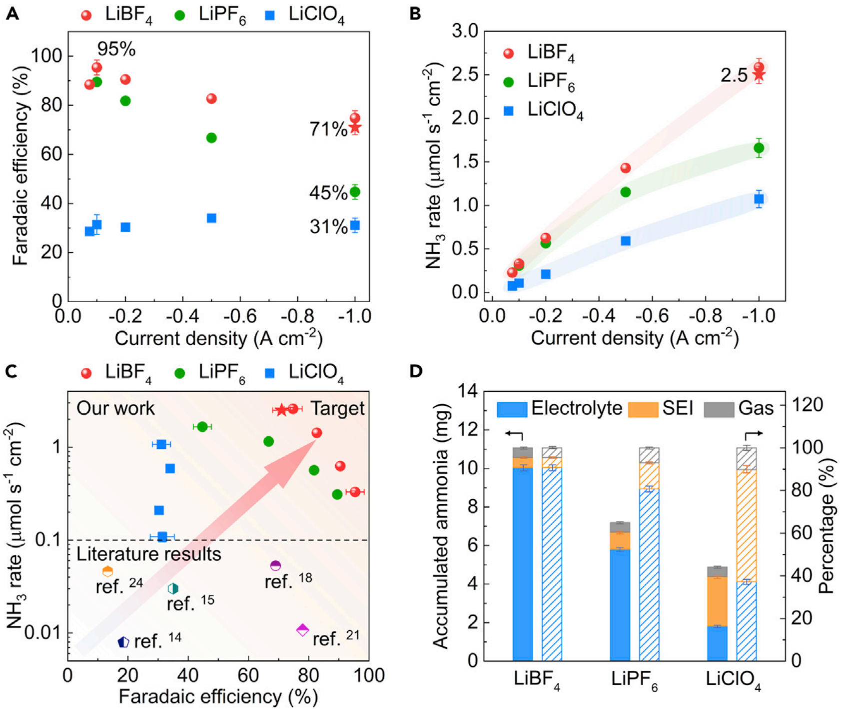

Figure 4. Efficiency of the Li-mediated ammonia synthesis

(A and B) Faradaic efficiencies (A) and NH_3 production rates (B) of the porous Cu electrode using different lithium salts at current densities ranging from −0.075 to −1.0 A cm_{geo}^{-2}. The shadows in (B) are guides to the eye.

(C) A comparison of NH_3 production metrics at ambient temperature between our work and reported highest rates in non-aqueous electrolytes in the literature.

(D) Accumulated NH_3 in the electrolyte, deposited layer including SEI, and gas phases using different lithium salts at −1.0 A cm_{geo}^{-2}. The left and right y axis in (D) represents the weight and corresponding percentage of NH_3, respectively. The calculated faradaic efficiencies and NH_3 production rates at current densities ranging from −0.1 to −1.0 A cm^{-2} are based on the experiments shown in Figure 3. The error bars represent the standard deviation of independent repeats of the same experiment (n ≥ 3).

indicates a compact SEI layer without excess organic components. We also point out that the deposited layers shown in this work is without damages from degassing and air exposure. This is an advantage of the modified autoclave placed inside an Ar glovebox (Figure 3D), which enables separation of the electrode from the electrolyte prior to depressurization, such that the SEI remains intact. This is important, as the depressurization from 20 bar and subsequent air exposure destroys the structure and composition of the SEI layer, which precludes the following XPS investigations on the different SEI layers and deposits.

Efficiency of the Li-mediated ammonia synthesis

The FE was determined at the end of the experiment, where the accumulated NH_3 was detected in the electrolyte solutions by a modified indophenol blue method.[11] More details can be found in the experimental procedures. Figure 4A shows the FE of the porous Cu electrode using different lithium salts for different CP measurements with current densities ranging from −0.075 to −1.0 A cm_{geo}^{-2}. The porous Cu electrode with $LiBF_4$ salt exhibits a remarkable 95% ± 3% FE at a current density of −0.1 A cm_{geo}^{-2}. Furthermore, it is striking that a relatively high FE of 75% ± 3% is achieved at a current density of −1.0 A cm_{geo}^{-2}, which is far higher than that using

$LiPF_6$ (45% ± 3% FE) and $LiClO_4$ (31% ± 3% FE) salts. The porous Cu electrode without porous Cu on the backside also shows a similar FE (71% ± 3%, star in Figure 4A) to the porous Cu electrode with Cu on the two sides (75% ± 3%, sphere in Figure 4A) by using $LiBF_4$ salt, which indicates that the backside does not significantly influence the FE. The FE drops rapidly at high current densities for the $LiPF_6$ salt, i.e., from 90% FE at -0.1 A cm_{geo}^{-2} to the aforementioned 45% ± 3% FE at -1.0 A cm_{geo}^{-2}, whereas that using $LiClO_4$ salt shows a relative stable FE around 31% ± 3% at varied current densities. The rapid FE drop when using $LiPF_6$ salt at high current densities is attributed to the severe electrolyte decomposition and unstable SEI layers, considering the poor thermal stability of $LiPF_6$ and the potentially produced joule heat at high current densities. It has been widely investigated and proven within the Li-ion battery field that $LiPF_6$-based electrolyte has poor stability at elevated temperatures, e.g., 60°C, and the SEI layer is unstable at elevated temperature, especially in the presence of $LiPF_6$.[40–43] In addition, we also ran the CP measurements using Cu foil (1.8 cm^2) with different salts at -4 mA cm^{-2} until the total passed charge reached 50 C (Figure S21). The standard Cu foil electrode with $LiBF_4$ salt exhibits 65% FE, which is also higher than that $LiClO_4$, which only achieved 20% FE.

Accordingly, the NH_3 production rate of the porous Cu electrode using different lithium salts at varied current densities is shown in Figure 4B. The porous Cu electrode using $LiBF_4$ exhibits an NH_3 production rate of 2.5 ± 0.1 μmol s^{-1} cm_{geo}^{-2} at a current density of -1.0 A cm_{geo}^{-2} based on 71% ± 3% FE of the electrode with the backside deposited Cu removed. Therefore, the backside Cu does not significantly affect the electrochemical stability, FE production rate, and NH_3 production rate. As show in Figure 4C, the FE and NH_3 production rates when using $LiBF_4$ at a current density of -0.1 A cm_{geo}^{-2} (95% ± 3% and 0.33 ± 0.01 μmol s^{-1} cm_{geo}^{-2}) are, to the best of our knowledge, the highest ever reported for the LiNR process.[14,15,18,21,24] More importantly, the reported NH_3 production rate of 2.5 ± 0.1 μmol s^{-1} cm_{geo}^{-2} at a current density of -1.0 A cm_{geo}^{-2} is more than one order of magnitude higher than all published literature results.[18] Although the energy efficiency (EE) is currently also a major concern in the LiNR process, considering Li plating requires large negative potentials (-3.04 V versus standard hydrogen electrode). Based on our previous work,[21] if all overpotentials are minimized and HOR is utilized at the CE, the optimized resulting EE would be 26%, assuming 80% FE. Thus, as pointed out in our previous publications,[13,21,24] the EE reported here is artificial as it does not take into account the sacrificial proton source. We want to point out here that initially in the 1950s the Haber-Bosch process also exhibited low energy efficiencies of 36% and only reached 62% in the 1990s.[44] It also should be clarified here that NH_3 production rate per geometric surface area rather than NH_3 production rate per ECSA is pursued in this work, which is more relevant to the industrial application.

The EE of the porous Cu electrode using $LiBF_4$ at a current density of -1.0 A cm_{geo}^{-2} is 7.7% (Table S2), which is well beyond the previously reported value of 2.8% for a 6 min experiment,[15] 1.5% for a 40 min experiment,[14] and 2.3% in literature.[24] In addition, regarding to the long-term stability, the single-compartment cell was used in this work with a sacrificial proton source. There are substantial energy losses related to the anode in the single-compartment cell. Ideally, a two-compartment setup, such as flow cell, should be used for better control of the anode reaction, which allow the HOR to use H_2, instead of consuming a sacrificial proton source. We also believe that further improvements to the electrolyte conductivity in future can also improve the EE, considering the energy losses from the large electrolyte resistance. The in-depth investigation of the long-term stability of the LiNR system by using flow cell is the subject of our ongoing work, whereas the goal of this work is to demonstrate the remarkable NH_3 production rates and FE at -1.0 A cm_{geo}^{-2} that are possible by modifying the SEI layer using and improving the accessible surface area (per geometric surface area). It is also noteworthy that in our previous work, we have developed a potential cycling procedure that greatly extend the lifetime of the LiNR system, and continuous operation for 125 h was demonstrated.[13]

Additionally, inspired by the theoretical modeling regarding the possibility of NH_3 being trapped in the SEI layer, we further conducted a separation procedure in the glovebox. First, right after the end of the CP measurements conducted at -1.0 A cm_{geo}^{-2}, we extracted the electrolyte from the glass cell through a polytetrafluoroethylene (PTFE) sampling tube, whereas the system is still pressurized at ~20 bar in the autoclave (Figure 3C). Next, degas the system although using an acid trap to collect all the NH_3 in the gas phase, and finally, open the autoclave and remove the WE with the intact deposited layer. For a comparison, as shown in Figure S22, there is no obvious thick deposit shown on the porous Cu electrode after depressurization from 20 bar without separation procedure, and most of the deposit was broken into pieces and floated on the electrolyte due to the degassing with electrolyte. This indicates that without separation procedure to extract the electrolyte first, the deposited layer can be easily damaged by degassing from 20 bar. Such a separation procedure ensures the SEI layer is damaged as little as possible, which is very important for the following SEI investigations. All the experiments toward investigating of the SEI layer were conducted in an autoclave placed inside an Ar glovebox to avoid air exposure, although completely avoiding O_2 and H_2O exposure can never be obtained by such methods as typical H_2O and O_2 content in Ar glovebox are in the <0.5 and <0.1 ppm range, respectively. More detailed information about the separation procedure can be found in the experimental procedures.

As shown in Figure 4D, it is clearly seen that the produced NH_3 is not only present in the electrolyte but also in the gas phase, as well as the deposited layer, which is a composite of the SEI layer and excess deposited species. The distribution of the accumulated NH_3 in the different phases is strongly dependent on the type of lithium salt used. Particularly, ~50% of the synthesized NH_3 was trapped in the deposited layer using $LiClO_4$, which is much higher than both $LiPF_6$ (~10%) and $LiBF_4$ (~5%). We would like to point out that the synthesized NH_3 trapped in the deposited layer could also include the intermediate nitrogen species (reduced from N_2) that can be easily converted to NH_3 during the collection step using HCl to dissolve the deposited layer (see experimental procedures). The high amount of NH_3 trapped in the deposited layer when using $LiClO_4$ was possibly caused by the massively thick SEI layer and deposit, which is a sign of severe electrolyte decomposition, especially of the organic components.[39] The smaller amount of NH_3 trapped in the deposited layer using $LiBF_4$ can be possibly ascribed to the high solubility of $NH_3 \cdot BF_3$ in THF and ethanol, which is also revealed by the theoretical results (Figure 1E). Most of the produced NH_3 is distributed in the electrolyte when using $LiBF_4$ salt in the single-compartment cell. However, the flow cell-based system with continuous N_2 gas flow can be used to potentially change the NH_3 distribution, leading to more of the produced NH_3 in the gas phase, which would be ideal for convenient collection and further utilization. It is also noteworthy that the total accumulated NH_3 reported here are all at the milligram level (Figure 4D), rather than the microgram level reported most commonly in the literature. For example, ~11 mg NH_3 was synthesized in a single experiment at different current densities by using 30 mL $LiBF_4$-based electrolyte with passed charge of 240 C. Considering the LiNR process has been well established by different groups,[11,14,15,18,21] we would like to point out

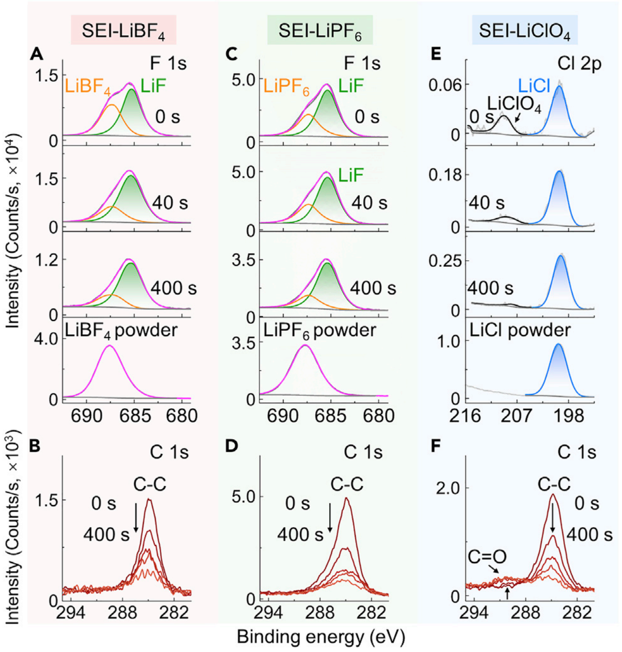

Figure 5. XPS investigation on the SEI layers without degassing damage and air exposure

(A and B) Depth-profiling XPS spectra of F 1s (A) and C 1s (B) for the SEI-LiBF$_4$.

(C and D) Depth-profiling XPS spectra of F 1s (C) and C 1s (D) for the SEI-LiPF$_6$.

(E and F) Depth-profiling XPS spectra of Cl 2p (E) and C 1s (F) for the SEI-LiClO$_4$. The commercial LiBF$_4$, LiPF$_6$, and LiCl powder were used as reference samples.

that when produced NH_3 in this milligram range and using the well-described precautions,[11] it is not necessary to conduct isotope measurements.

SEI layer investigations

To further elucidate the effect of different lithium salts on the SEI layer, we purposely designed the short electrochemical experiments in the Ar glovebox using $LiBF_4$, $LiPF_6$, and $LiClO_4$ salts. As shown in Figure S23A, we conducted the LSV measurements for the porous Cu electrodes using different lithium salts and stopped the reaction after the working potential passed lithium plating and reached a current density of -0.1 A cm_{geo}^{-2}. Then, we followed the same procedures as the separation procedure and collected the electrodes with the intact SEI layers. These short electrochemical experiments are supposed to build only a thin SEI layer without severe electrolyte decomposition (Figure S23B), which is more relevant to the theory insights. All the porous Cu electrodes with deposited layers were loaded into a home-built transfer arm inside an Ar glovebox and evacuated to pressures below 5×10^{-6} mbar, followed by a transfer into the XPS chamber with a base pressure below 9×10^{-10} mbar (Figure S24). Depth-profiling XPS with different etching times using Ar ions was engaged to probe the elemental composition, chemical state, and depth profile of the SEI layer.

As shown in the F 1s spectra of the SEI layer formed using $LiBF_4$ (denoted as SEI-$LiBF_4$, Figure 5A), the peak centered at 685.5 eV is attributed to LiF,[45] and the peak at 687.5 eV is well matched with $LiBF_4$. Additionally, the ratio of the LiF signal increases as the etching time increases, which indicates a LiF-enriched SEI layer on the porous Cu electrode using $LiBF_4$ and confirms the theoretical suggestion. As shown in Figure 5C, similar phenomena were also observed for the SEI layered formed using $LiPF_6$ (denoted as SEI-$LiPF_6$). Figure 5E shows the Cl 2p spectra of the SEI layer formed using $LiClO_4$ (denoted as SEI-$LiClO_4$), and the peak centered at 200.0 and 209.5 eV is attributed to LiCl and $LiClO_4$, respectively. It is clearly seen that LiCl is derived from the reduced product of $LiClO_4$ and is enriched in the SEI-$LiClO_4$, which also implies that solvent oxidation might already happened at the beginning of the reaction due to the strongly oxidizing property of $LiClO_4$. In addition, as shown in the C 1s spectra (Figures 5B, 5D, and 5F), compared with the SEI-$LiBF_4$ and SEI-$LiPF_6$, the SEI-$LiClO_4$ exhibits a new peak after etching that is well matched with the C=O bond and possibly attributed to the presence of Li_2CO_3.[46]

Moreover, the different deposits (shown in Figure S17) on the porous Cu electrodes after CP measurements at a current density of -1.0 A cm_{geo}^{-2} were also investigated in the same manner to reveal the possible changes of the deposit after reaction. As shown in Figure S25, the LiF remain enriched in the deposits formed using $LiBF_4$ and $LiPF_6$ (denoted as Post-$LiBF_4$ and Post-$LiPF_6$, respectively), and the XRD pattern shown in Figure S26 further confirmed the presence of LiF phase in both Post-$LiBF_4$ and Post-$LiPF_6$. The signal intensity of the P 2p reduces rapidly compared with that of B 1s during etching (Figures S25B and S25E), indicating the inhomogeneous composition of the Post-$LiPF_6$, which could be caused by the serious electrolyte decomposition at high current density due to the poor thermal stability of $LiPF_6$. In addition, the C 1s spectra shown in Figures S25H and S27 exhibit that the deposits formed using $LiClO_4$ (denoted as Post-$LiClO_4$) has a strong peak assigned to the C=O bond, which might indicate more Li_2CO_3 accumulated inside. As shown in the N 1s spectra (Figure S28), both Post-$LiBF_4$ and Post-$LiClO_4$ have a peak centered at 398.6 eV, which is attributed to organic nitrogen species[47,48] rather than Li_3N, as is seen from the Li_3N reference spectrum. The depth profile of the elemental composition for the different SEI layers clearly shown that F and Li are the predominant elements inside of the Post-$LiBF_4$ and Post-$LiPF_6$ (Figures S25C, S25F, and S25I), which also indicates the LiF-enriched deposit. However, Li is the main element inside of the Post-$LiClO_4$, and more Li is shown inside of the Post-$LiPF_6$ compared with Post-$LiBF_4$, which could indicate the uncontrolled Li plating using $LiPF_6$ and $LiClO_4$ at a current density of -1.0 A cm_{geo}^{-2}. Besides, more C is also shown inside of the Post-1A-$LiClO_4$, which further implies the severe electrolyte decomposition at a current density of -1.0 A cm_{geo}^{-2}.

Therefore, based on the investigations on the different SEI layers formed at the beginning and the deposits formed after CP measurements at a current density of -1.0 A cm_{geo}^{-2}, the huge FE differences by using $LiBF_4$, $LiPF_6$, and $LiClO_4$ are explained as following: (1) the high FE achieved by using $LiBF_4$ and $LiPF_6$ at relatively low current densities are ascribed to the LiF-enriched SEI layers that result in a decreased r_{Li} with a smaller change of r_H and r_{N2} and promote the LiNR process, which is revealed by the theory modeling results. LiF is beneficial to the uniform lithium plating and builds a better interface to prevent too much undesired side reactions between deposited lithium and the electrolyte. (2) The high FE of 71% ± 3% achieved at a current density of -1.0 A cm_{geo}^{-2} by using $LiBF_4$ instead of $LiPF_6$ and $LiClO_4$ is not only attributed to LiF-enriched SEI layer but also due to increased thermal and chemical stabilities of $LiBF_4$, which suppresses severe electrolyte decomposition. Particularly, the poor thermal stability of $LiPF_6$ and strongly oxidizing property of $LiClO_4$ results in a disastrous electrolyte decomposition, which could potentially destroy and complicate the SEI layer formed at the beginning and result in the uncontrolled lithium plating.

DISCUSSION

In summary, we utilize a theory modeling approach to screen the lithium salts for the LiNR process and find that fluorine-based electrolytes are beneficial to achieve a high

FE due to the presence of LiF in the SEI layer. Through systematic experimental demonstrations, the $LiBF_4$-based electrolyte is observed as the most stable and promising electrolyte to realize a highly efficient LiNR process. We demonstrate that combined with a highly porous Cu electrode, record FE of 71% ± 3% and NH_3 production rate of 2.5 ± 0.1 μmol s^{-1} cm_{geo}^{-2} at a current density of -1.0 A cm_{geo}^{-2} under 20 bar N_2 are achieved using $LiBF_4$-based electrolyte. The good LiNR performance can be explained by the formation of a compact and uniform LiF-enriched SEI layer and the better thermal and chemical stability of $LiBF_4$, which enables even lithium plating and suppresses uncontrolled electrolyte degradation. We also find that the NH_3 distribution in the gas, electrolyte, and deposited layer with SEI is highly dependent on the lithium salts used. We anticipate that our findings offer new insights on developing an industrially feasible pathway for electrochemical NH_3 synthesis.

EXPERIMENTAL PROCEDURES

Resource availability

Lead contact

Further information and requests for resources and materials should be directed to and will be fulfilled by the lead contact, Ib Chorkendorff (ibchork@fysik.dtu.dk).

Materials availability

The materials in this study will be made available upon reasonable request.

Data and code availability

The datasets generated in this study are available from the lead contact upon reasonable request.

Preparation of porous Cu electrode

The SS mesh (SS316, 325 × 2,300, McMASTER-CARR) was cut into 0.2–1 cm_{geo}^2 pieces and then spot welded with Cu wire (≥99.98%, Goodfellow) for electrical connection and used as WE. Two Pt mesh (1.5 cm_{geo}^2, 99.9%, Goodfellow) electrodes were connected and used as a split CE. The WE was located in the middle of the two Pt meshes. Prior to electrodeposition, the WE was dipped in 0.06 M HCl (VWR Chemicals) and rinsed with Milli-Q water and ethanol. The electrolyte was made of 0.4 M $CuSO_4$ (98%, Merck) in 1.5 M H_2SO_4 (99.999%, Sigma Aldrich). A constant current of −2 A with applied time ranging from 15 s to 7 min was set for the porous Cu deposition on SS mesh. The electrode was cleaned with Milli-Q water and ethanol several times and dried under vacuum after electrodeposition. The excess deposited Cu on the Cu wire and the edge of SS mesh were removed to keep the constant geometric area of the WE at different experimental conditions (Figure S29). All the WEs were stored in an Ar glovebox before use.

Electrochemical experiments

A three-electrode single-compartment glass cell in an electrochemical home-made autoclave placed in a fume hood was used for all the electrochemical experiments. The same electrochemical autoclave in an Ar glovebox was specifically used for the SEI investigation. Electrolyte solution (30 mL) was prepared in an Ar glovebox, which consists of 2 M lithium salts (99.99%, Sigma Aldrich) in 99 vol % THF (anhydrous, >99.9%, inhibitor-free, Sigma Aldrich) and 1 vol % ethanol (anhydrous, Honeywell). The glass cell, the magnetic stirring rotor (glass covered), CE (1.5 cm_{geo}^2 Pt mesh, 99.9%, Goodfellow), and RE (Pt wire, 99.99%, Goodfellow) were boiled in Milli-Q water and dried overnight at 100°C in air. The CE and RE are both flame-annealed before use, and the distance between WE and RE was fixed around 0.5 cm for all the experiments. Considering the convenience of running the experiment in the fume hood, which showed the same performance as those obtained from the autoclave inside the Ar glovebox, only the experiments associated with the investigation of the SEI layer were conducted in an autoclave placed inside an Ar glovebox to avoid air exposure. The Ar gas (99.999%, Air Liquide) was introduced into the assembled cell in the autoclave sitting in the fume hood for at least 30 min before the electrochemical experiment. Then, the electrolyte solution was injected into the cell in an Ar atmosphere, followed by the closing of the autoclave. Afterward, the pressure in the autoclave was increased to 10 bar using N_2 (99.9999%, Air Liquide) and de-pressurized to 3 bar for 10 times in order to flush out any remaining air contaminants, followed by filling to 20 bar for the experiments. The N_2 gas used here was cleaned by commercial purifiers (NuPure, pptV cleaning of all labile N containing compounds). The electrochemical measurements were started from an open circuit voltage (OCV) for 20 min to equilibrate the atmosphere composition in the electrolyte. Then, the PEIS, LSV, and CP, followed by another PEIS was applied for the measurements (Bio-Logic SP-200). The LSV was used to see a clear onset for lithium reduction, thereby denoting the potential versus Li/Li^+ and confirming that the target current was reached before CP. During CP, varied constant-current densities from -0.075 to -1.0 A $cm_{geo}{}^{-2}$ were applied until the total passed charge reached 240 C. All the experiments were performed with the electrolyte stirred at 250 rpm at room temperature. The porous Cu electrodes with geometric surface area of 0.2 $cm_{geo}{}^2$ were used for all the electrochemical experiments considering the current and potential limit of the potentiostat. The porous Cu electrodes with 1.0 $cm_{geo}{}^2$ were used for the CP measurements at a current density of -0.1 A $cm_{geo}{}^{-2}$, which remains within the current and potential range of the potentiostat, and exhibit a FE similar to that of the electrodes with smaller geometric surface area.

Separation procedure

All the separation procedures were conducted in an autoclave placed inside an Ar glovebox to ensure no exposure to air. Typically, after the electrochemical experiments, we took out the electrolyte through a sampling tube while the system was still pressurized at 20 bar, degassed the system through an acid trap (0.06 M HCl) to collect all the NH_3 in the gas phase, and then removed the WE with the intact SEI layer in the end. To quantify the produced NH_3 in the SEI layer, the WE was dipped into 10 mL of 0.06 M HCl to gradually dissolve the SEI layer.

Colorimetric quantification of NH_3

The produced NH_3 was quantified by a modified colorimetric indophenol method.[11] The calibration solutions consisted of known concentrations of NH_4Cl in the dilute aqueous solution containing lithium salts (Figure S30). 500 μL of alkaline hypochlorite solution (A1727, Sigma Aldrich) was added to a 2 mL sample with NH_4Cl, followed by the addition of 500 μL of phenol nitroprusside solution (P6994, Sigma Aldrich). The solution was then mixed and left in the dark for 30 min at room temperature, followed by the measurement of absorbance using UV-vis spectroscopy (UV-2600, Shimadzu) from 400 to 1,000 nm. The fitted calibration curve that shows a linear regression with an R^2 value of 0.9999 was used for the quantifications (Figure S30). It is clearly shown that a high Li salt concentration ($\geq$250 mM) has an obvious effect on the indophenol reaction. For example, a concentration of 0.5 M $LiClO_4$ in the sample leads to a much lower slope in the calibration curve, which indicates that a falsely high FE might be calculated without proper dilution and calibration to eliminate the effect of the lithium salts concentration. Considering the produced NH_3 at milligram level in this work, all the as-obtained samples after electrochemical experiments were diluted with Milli-Q water as needed to keep the measured absorbance located in the range of the calibration curve. For the sample from the electrolyte, 10 μL of 4 M HCl (37%, VWR Chemicals) was added to 500 μL of electrolyte and then diluted as required (ranging from 200 to 800 times). For the sample from the SEI and gas phase, the corresponding acid solutions were also diluted as needed (ranging from 10 to 200 times). All the FE were calculated by the following equation:

$$FE = 3 \times F \times c_{NH3} \times V/Q \qquad \text{(Equation 1)}$$

where 3 is the number of electrons transferred for each mole of NH_3, F is the Faraday constant, c_{NH3} is the concentration of produced NH_3, V is the total electrolyte volume, and Q is the total passed charge.

To estimate the EE, we considered the total amount of energy put into the system via the potentiaostat, E_{in}, and compared that with the energy contained in the total amount of NH_3 produced during the experiment, E_{out}. It should be noted that we do not include the pressure and energy from EtOH in our calculations. All the EE were calculated by the following equation:

$$EE = \frac{E_{out}}{E_{in}} = \frac{\Delta G_r \cdot m_{NH3}}{\int V_{cell}(t) \cdot I(t) dt} \qquad \text{(Equation 2)}$$

where E_{out} was defined by the free energy (ΔG_r) of reaction of NH_3 oxidation to N_2 and water times the amount of NH_3 produced (m_{NH3}), and E_{in} is given by the total cell voltage (V_{cell}) between the CE and WE, multiplied by the current (I) to get the instantaneous power, and integrated over time.

SEI investigation

XPS and XRD were used to investigate the SEI after electrochemistry. XPS was conducted on a ThermoScientific Thetaprobe instruments with an Al Kα X-ray source and base pressure below 9.0×10^{-10} mbar. The ion gun in etching mode and flood gun in charge neutralization mode were used during the measurement with a chamber pressure of 2.0×10^{-7} mbar by flowing Ar gas (99.9999%, Air Liquide). The ion gun was run using 4 kV and 1 μA mode with scanning size of 2 × 2 mm^2. The spot size of 400 μm was used. All the survey spectra were recorded with step size of 1.0 eV and dwell time of 50 ms at pass energy of 200 eV (Figures S31 and S32). High-resolution elemental spectra were recorded with step size of 0.1 eV and dwell time of 50 ms at pass energy of 200 eV. All the spectra were acquired and analyzed by Thermo Avantage (v5.9925) by Thermo Fisher Scientific. All the background was determined using Shirley mode and fitted using Powell algorithm. To analyze all the powder samples with XPS, all the commercial powders were shaped to pellets with 7 mm diameter and 0.5–1 mm thickness in an Ar glovebox. The pellets were loaded in a custom-made sample holder in transfer arm. For the XRD measurements, the deposited layer was scraped off the electrode and loaded into the holder inside an Ar glovebox with an air-tight polyetheretherketone (PEEK) dome and then transferred to the XRD instrument without air exposure (Figure S33). XRD patterns were recorded on a Malvern Panalytical Empyrean X-ray diffractometer. The source was an Empyrean Cu LFF HR gun ($K\alpha_1$ = 1.540598 Å) operated at 45 kV and 40 mA.

Capacitive cycling experiment

The capacitive cycling experiments were conducted at ambient pressure using 2 M $LiClO_4$ with the same electrode setup as the autoclave experiments. The CV measurements of different porous Cu electrodes and Cu foil were conducted at scan rates of

20–80 mV s^{-1}. The specific capacitance (C_{spec}, F cm^{-2}) is the slope of the current density change (ΔI) versus scan rates shown in Figure 2F. The ΔI were calculated by the following equation:

$$\Delta I = (I_a\text{-}I_c)/2 \qquad \text{(Equation 3)}$$

where I_a and I_c is the anodic and cathodic current density at −0.5 V versus Pt pseudo-reference electrode, respectively.

Theory calculations

Our calculations are based on density functional theory (DFT) within the generalized Kohn-Sham scheme,[49] using the Vienna *ab initio* simulation package (VASP),[50] as implemented in atomic simulation environment (ASE).[51] We use the beef-vdw exchange-correlation functional[52] to model adsorption properties as well as van der Waals interactions. We employ the Heyd-Scuseria-Ernzerhof (HSE06)[53] with 25% mixing of short-range Hartree-Fock exchange to estimate the valence-band maximum (VBM) and conduction-band minimum (CBM). Projector augmented wave (PAW) potentials[54,55] are used with a plane-wave cutoff of 600 eV. The smallest spacing between k points is chosen as 0.15 Å. The Li $1s^22s^1$, N $2s^22p^3$, O $2s^22p^4$, C $2s^22p^2$, F $2s^22p^5$, Cl $3s^23p^5$, and H $1s^2$ electrons are treated explicitly as valence. Calculations of migration barriers are based on the CI-NEB method.[30]

Defect calculations

To calculate defect properties, supercells are constructed with dimensions $2\mathbf{a} \times 2\mathbf{b} \times 2\mathbf{c}$ for Li_2CO_3, $3\mathbf{a} \times 3\mathbf{b} \times 2\mathbf{c}$ for LiOH, $3\mathbf{a} \times 3\mathbf{b} \times \mathbf{c}$ for $LiHF_2$, and $2\mathbf{a} \times 2\mathbf{b} \times 2\mathbf{c}$ for LiF. Different Li defects are investigated, including Li vacancies in different charge states and Li interstitials in different charge states. The E_f formation energy of a specific defect is calculated as follows:[56]

$$E_f = E_q - E_{bulk} + n\mu_{Li} + qE_F + \Delta_{corr} \qquad \text{(Equation 4)}$$

Here, E_q represents the total energy of a supercell containing Li defect in charge state q, E_{bulk} is the total energy of a supercell containing no defect, n represents the number of Li atoms added ($n < 0$) or removed ($n > 0$) from the system, μ is the chemical potential of Li, E_F is the Fermi level that is a variable with values ranging from VBM to CBM, and Δ_{corr} is a finite-size correction factor[57,58] neglected in this study.

Ionic conductivity

The ionic conductivity, σ, is calculated from the Nernst-Einstein equation:[29]

$$\sigma = \frac{F^2q^2DS}{RT} = \frac{D_0e^2N_{sites}}{k_BT}\exp\left(\frac{-(E_f+E_m)}{k_BT}\right) \qquad \text{(Equation 5)}$$

Here, $D_0 = \alpha\nu a^2\exp\left(\frac{\Delta S}{k_B}\right)$, where α is a geometry-related factor often close to unity, ν is the hopping frequency around a typical phonon frequency, a is the distance between sites, the entropy term ΔS is neglected in this study, and E_m is the migration barrier. The estimation error in Li conductivity is due to the general prediction error of the exchange-correlation functional.[59]

SUPPLEMENTAL INFORMATION

Supplemental information can be found online at https://doi.org/10.1016/j.joule.2022.07.009.